

Organic Semiconductors For Photoelectrochemical Applications

Présentée le 10 février 2022

Faculté des sciences de base
Laboratoire d'ingénierie moléculaire des nanomatériaux optoélectroniques
Programme doctoral en chimie et génie chimique

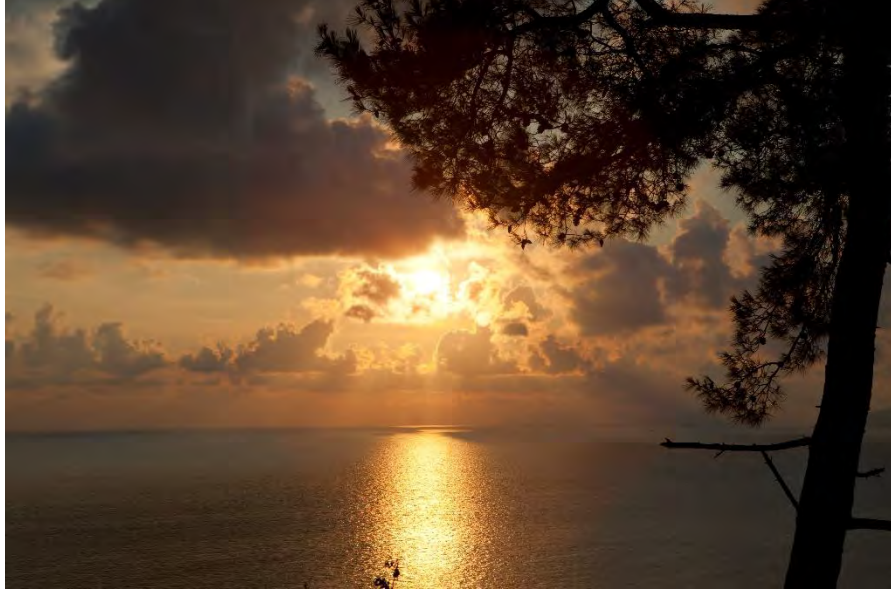
pour l'obtention du grade de Docteur ès Sciences

par

Arvinth SEKAR

Acceptée sur proposition du jury

Prof. M. K. Nazeeruddin, président du jury
Prof. K. Sivula, directeur de thèse
Dr A. Ruggi, rapporteur
Dr E. D. Glowacki, rapporteur
Prof. A. Boghossian, rapporteuse



सूर्याद्भवन्ति भूतानि सूर्येण पालितानि तु ।
सूर्ये लयं प्राप्नुवन्ति यः सूर्यो सोहम् एव च ॥

“O Resplendent one! You exist for the welfare of the whole world

O Sun! May I acquire the opportunity to merge with You who is the
embodiment of the ultimate reality.”

- *Surya Upanishad, Atharvaveda, 1200 BCE*

From the Sun arise all beings.
The Sun sustains them all.
Into the Sun they all vanish.
What the Sun is,
that I am.

More important than any one new application is the new 'materials' concept itself. It marks a shift from concern with substances to concern with structures, a shift from artisan to scientist as man's artificer, a shift from chemistry to physics as the basic discipline, and a shift, above all, from the concrete experience of the workshop to abstract mathematics, a shift from starting with what nature provides to what man wants to accomplish.

-The Age of Discontinuity, 1969 — **Peter F. Drucker**

We speak erroneously of "artificial" materials, "synthetics", and so forth. The basis for this erroneous terminology is the notion that Nature has made certain things which we call natural, and everything else is "man-made", ergo artificial. But what one learns in chemistry is that Nature wrote all the rules of structuring; man does not invent chemical structuring rules; he only discovers the rules. All the chemist can do is find out what Nature permits, and any substances that are thus developed or discovered are inherently natural. It is very important to remember that.

— **R. Buckminster Fuller**

Acknowledgements

I take this opportunity to thank my supervisor Prof. Kevin Sivula for offering me an opportunity to spend a long period in the Laboratory for Molecular Engineering of Optoelectronic Nanomaterials (LIMNO). He has invested a lot of time and resources on me, and I always hope that my work measures to his expectations. He gave me a long leash and encouraged me to explore any idea that catered to my skills, due to which I believe I have grown as a person. Always providing perspectives to my ridiculous propositions, his insightful advice and comments were always welcome.

My second family would be the past and present LIMNO members. I came to this lab in 2016 when I was first very intimidated by Dr. Aiman Rahmanuddin, who was my project and MSc thesis supervisor. I would credit him as the mold to the organic chemist that I am today. I still remember the discussions we had in the lab and enjoyed watching him perform MMA in the ring. Dr. Liang Yao was the Yin to Aiman's Yang for me: a lot of thought going on behind that calm demeanor. Since we shared common research projects, I would daresay that I was merely trying to mirror his actions and experiments in many cases! I also have mad respect for my other seniors in the lab: Dr. Mathieu Prevot and Dr. Xavier Jeanbourquin, with whom had not interacted much, but their presence was felt in the lab everywhere as they set protocols for literally every experiment.

When it comes to Dr. Nestor Guijarro, I can write pages after pages, but I will restrict myself to one paragraph here. I barely spoke more than 2 sentences with him till about 4 months after I started working in LIMNO, but I am proud to say that from then he has been forever, a much-wanted spirit in my life: Thank you, sir!! Your deep insights into how one must *science*, as opposed to how people *science*, overview on life other than the lab, motivation to get me to learn new things both in lab and outside, I believe were well accepted and implemented.

My colleagues are always helpful and there for everyone and looking back maybe I should have spent more time with you all outside the lab too. I thank Dr. Yongpeng Liu for being the ideal office mate, sharing science, technology, anime, entertainment, and gaming

information – all of which we have in common. Barbara Alexandra for being kindred souls in the lab – long hours with meticulous *sciencing*, but with limited publishable content. I also am indebted to you for trying out different experiments together, helping me with PL and AFM, trying wild ideas which probably wouldn't have worked anyway, and for the lunch sessions hosted at your wonderful house with our colleagues.

As a successor to Dr. Liang Yao, Dr. Han-Hee Cho was the second guiding light in the lab for me. We had many fruitful discussions, similar ideas, failures, and inability to stably generate oxygen from water: fun times. I also loved his effort to cook delicious Korean meals for us in the lab. I am also indebted to Dr. Yum Jun-Ho, who, despite his busy schedule found time for my requests to perform measurements on my substrates, and for offering suggestions and improvements during group meetings.

I have high hopes for the future of our lab with vibrant and intelligent people like Rebekah Wells, Nukorn and Marina Caretti working hard in the lab. Rebekah, it was wonderful to see you do a lot of things at the same time and would love to have your multi-tasking ability and energy in the lab. I thank Marina for helping me with any issues with French in the lab, and for being an overall positive person, which was much needed. It was always interesting to hear Nukorn give a presentation, and I try to imbibe his flair for the dramatic to create a neat impression on others.

I wish to thank and encourage the new blood of LIMNO: Connor, Simon, Luc and Colin, all the very best!! Connor, it was fun to have you around in the lab, and to listen to your choice of music. Simon was a good listener to my unwanted organic chemistry suggestions, and I must also thank him for letting me hijack his fume hood without permission for a long time. And last but not the least, I thank you, Juan Manuel, for being my student and helping me out with a bunch of experiments ranging from synthesis to applications. I hope you learnt something useful during your time here from me. I also thank Dan Zhang for kindly lending her time and electrodes for my experiments.

At this point, a big thank you to my jury members: Prof. Mohammad Nazeeruddin (EPFL, *Jury President*), Dr. Albert Ruggi (University of Fribourg), Dr. Eric D. Glowacki (Brno

University of Technology) and Prof. Ardemis Boghossian (EPFL), who, in their busy schedule found time to evaluate my thesis.

We are no one without our family, and I must also thank my parents for their immense faith in me, unconditional love and for their patience. At times, we hadn't seen each other for years together, so I hope they forgive me for this. *Hare Krsna, ee thesis meeku maru devudu ku samarpanam.*

Abstract

The capture and conversion of solar energy into other useful forms has been the topic of discussion for the past few decades, accentuated by the need to combat climate change and face the challenge of non-renewability of conventional sources of fuel for our rising energy demands. Photoelectrochemical (PEC) fuel generation from sources like water is a promising method to achieve a carbon free path towards cleaner energy. As this method combines multiple physico-chemical processes: light harvesting, charge generation and fuel generation in one component, it is easier and inexpensive to make and use.

Usable solar energy is mostly concentrated in the near visible to near infrared region of the spectrum, and due to bandgap and other material considerations, a single photoabsorbing semiconductor system has made way for dual absorbing PEC semiconductors, which work in tandem to carry out the reduction (photocathode) and oxidation (photoanode) halves of a redox splitting reaction.

While the use of inorganic semiconductors in photoelectrodes is well established, to overcome their inherent drawbacks organic semiconductors (OSCs) are being touted as possible replacements. Indeed, the field of organic photovoltaics has demonstrated how OSCs are quite superior in many aspects, especially due to our ability to tune their properties based on their chemical structures. Therefore, many researchers around the globe are focusing towards OSCs for PEC applications. While photocathodic OSCs have indeed been successfully demonstrated to have competing performance and stability, OSCs in photoanodes is at its nascent stage.

This arises due to the inherent difficulties in photooxidation itself: the use of harsh electrolytic conditions, high oxidative potentials placing strain on the components of photoanode etc. In this thesis, a complete overview of how an OSC based photoanode can be designed: right from the molecular level to the final device fabrication and optimization is elaborated. In the first chapter, an introduction to this area of research, its motivation and context is provided, with details from previous peer-reviewed research along with a bit of

theoretical insight. The second chapter briefly discusses the materials, methods and techniques involved in this thesis. The third chapter is based on the Quaterrylene di-imide (*QDI*) molecule, its chosen reason, synthesis, and practical difficulties in implementing a workable photoanode using it. After realizing that neat OSCs themselves probably would not make good photoanodes, a transition to using bulk heterojunction (BHJ) type photoanodes is looked at. The fourth chapter discusses the donors: their synthesis, analytical and initial PEC characterization, while the fifth chapter deals with acceptors for similar aspects. Moving to BHJ, the sixth chapter elaborates optimizations and characterization of thin film BHJs and delves deep into techniques to obtain high performance and stability. The seventh chapter involves possible applications for these optimized photoanodes, and how these can be used for unassisted solar fuel generation.

Keywords

Organic Semiconductors (OSCs), photoelectrochemical (PEC) oxidation reactions, rylene di-imides (RDIs), tin oxide, Bulk Heterojunctions (BHJs), tandem devices.

Resume

La capture et la conversion de l'énergie solaire en d'autres formes utiles a été le sujet de discussion au cours des dernières décennies, accentuée par la nécessité de lutter contre le changement climatique et de faire face au défi de la non-renouvelabilité des sources conventionnelles de carburant pour nos demandes énergétiques croissantes. La génération de combustible photoélectrochimique (PEC) à partir de sources telles que l'eau est une méthode prometteuse pour parvenir à une voie sans carbone vers une énergie plus propre. Cette méthode combinant plusieurs processus physico-chimiques tels que la récupération de la lumière, la génération de charge et la génération de carburant en un seul composant, est plus facile et peu coûteuse à fabriquer et à utiliser.

L'énergie solaire utilisable est principalement concentrée dans la région du spectre proche du visible au proche infrarouge, et en raison de la bande interdite et d'autres considérations matérielles, un seul système semi-conducteur photoabsorbant a fait place à des semi-conducteurs PEC à double absorption, qui fonctionnent en tandem pour effectuer la réduction (photocathode) et l'oxydation (photoanode) de l'eau respectivement..

L'utilisation de semi-conducteurs inorganiques dans les photoélectrodes étant bien établie, pour surmonter leurs inconvénients inhérents, les semi-conducteurs organiques (OSC) sont présentés comme leurs remplaçants possibles. En effet, le domaine du photovoltaïque organique a démontré à quel point les OSC sont effectivement supérieures à bien des égards, notamment en raison de notre capacité à ajuster leurs propriétés en fonction de leurs structures chimiques. Par conséquent, de nombreux chercheurs du monde entier se concentrent sur les OSC pour les applications PEC. Alors qu'il a en effet été démontré avec succès que les OSC photocathodiques ont des performances et une stabilité semblables, les OSC dans les photoanodes en sont à leurs balbutiements.

Cela est dû aux difficultés inhérentes à la photo-oxydation elle-même : l'utilisation de conditions électrolytiques difficiles, des potentiels d'oxydation élevés exerçant une contrainte sur les composants de la photoanode, etc. Dans cette thèse, un aperçu complet de la façon dont une photoanode à base d'OSC peut être conçue sera exposé: du niveau

moléculaire à la fabrication et à l'optimisation du dispositif final. Dans le premier chapitre, une introduction à ce domaine de recherche, sa motivation et son contexte est fournie, avec des détails de recherches antérieures évaluées par des pairs, ainsi qu'un peu de vision théorique. Le deuxième chapitre présente brièvement les matériaux, les méthodes et les techniques impliqués dans cette thèse. Le troisième chapitre est basé sur la molécule de Quaterrylene di-imide (QDI), la justification de son choix, sa synthèse et les difficultés pratiques pour mettre en œuvre une photoanode exploitable en l'utilisant. À l'heure actuelle, nous avons des raisons de croire que les OSC seraient pas des photoanodes performantes, et passeraient à l'utilisation de photoanodes de type à hétérojonction en vrac (BHJ). Le quatrième chapitre traite des donneurs: leur synthèse, leur caractérisation analytique et initiale du PEC. Le cinquième chapitre traite des accepteurs avec des aspects similaires. Passant à BHJ, le sixième chapitre élabore des optimisations et une caractérisation des BHJ à couches minces et approfondit les techniques permettant d'obtenir des performances et une stabilité élevée. Le septième chapitre concerne les applications possibles de ces photoanodes optimisées et la manière dont nous pouvons les utiliser pour la production de combustible solaire sans assistance.

Mots clés

Semi-conducteurs organiques (OSC), réactions d'oxydation photoélectrochimique (PEC), di-imides de rylène, oxyde d'étain, hétérojonctions en vrac (BHJ), dispositifs en tandem.

Abbreviations & Symbols

^{13}C	Carbon isotope with molecular mass 13
^1H	Hydrogen with molecular mass 1
A1	5,6,12,13-tetrachloro-2,9-bis(2-ethylhexyl)anthra[2,1,9-def:6,5,10-d'e'f'] diisoquinoline-1,3,8,10(2H,9H)-tetraone
A2	2,3,13,14-tetrachloro-6,10,17,21-tetrakis(2-ethylhexyl)pyranthreno[6,7,8-def:14,15,16-d'e'f':3,4,5-d''e''f'g':11,12,13-d'''e'''f'''g''']tetraisoquinolin-5,7,9,11,16,18,20,22(6H,10H,17H,21H)-octaone
A2b	12,12',13,13'-tetrachloro-2,2',9,9'-tetrakis(2-ethylhexyl)-[5,5'-bianthra [2,1,9-def:6,5,10-d'e'f']diisoquinolin]- 1,1',3,3',8,8',10,10'(2H,2'H,9H,9'H)-octaone
A4a_{xx}/A4b	Heavier dimers of A2
AFM	Atomic Force Microscopy
BBL	poly(benzimidazobenzophenanthroline)
BHJ	Bulk Heterojunction
CB	Chlorobenzene
CF	Chloroform
CV	Cyclic Voltammetry
D:A	Donor:Acceptor
DPPD	Dynamic Potential-pH Diagram
DSC	Differential Scanning Calorimetry
DS-PEC	Dye-Sensitized Photoelectrochemical Cells
DSSC	Dye-Sensitized Solar Cells
EIS	Electrochemical Impedance Spectroscopy
ETL	Electron Transport Layer
GC	Gas Chromatography
GPC	Gel Permeation Chromatography
HOMO	Highest Occupied Molecular Orbital

IPCE	Incident Photon to Converted Electron Efficiency
J _{ph}	Photocurrent Density
LIMNO	The Laboratory of Molecular Engineering for Optoelectronic Nanomaterials
LUMO	Lowest Unoccupoied Molecular Orbital
MALDI-TOF	Matrix Assisted Laser Desorption Ionization – Time of Flight
MO	Molecular Orbitals
mSnO ₂	mesoporous tin oxide
NMR	Nuclear Magnetic Resonance
O/HERC	Oxygen/Hydrogen evolution reaction catalyst
OFET	Organic Field Effect Transistor
OPV	Organic Photovoltaic
OSC	Organic Semiconductor
P1	<i>pBDTTTPD</i> / poly[(5, 6- dihydro- 5- octyl- 4, 6- dioxo- 4H- thieno[3, 4- c] pyrrole- 1, 3- diyl) (4, 8- bis[5- (2- ethylhexyl) - 2- thienyl] benzo[1, 2- b:4, 5- b'] dithiophene- 2, 6- diyl)]
P2	<i>pBDTTCITPD</i> / poly[(5, 6- dihydro- 5- octyl- 4, 6- dioxo- 4H- thieno[3, 4- c] pyrrole- 1, 3- diyl) (4,8-Bis(4-chloro-5-(2-ethylhexyl)thiophen-2-yl) benzo[1,2-b:4,5-b']dithiophene-2,6-diyl)]
P3HT	poly(3-hexyl thiophene)
PC ₆₁ BM	[6,6]-Phenyl C61 butyric acid methyl ester
PCE%	Power Conversion Efficiency percentage
PDI-DIP	Perylene 2,9-bis(2,6-diisopropylphenyl) imide
PEC	Photoelectrochemisty/Photoelectrochemical
PL	Photoluminescence
pSnO ₂	planar tin oxide
PTB7-Th	poly([2,6'-4,8-di(5-ethylhexylthienyl)benzo[1,2-b;3,3-b] dithiophene] {3-fluoro-2[(2-ethylhexyl)carbonyl]thieno[3,4-b]thiophenediyl})
QDI_{xx}	Quaterrylene di-imide <i>derivatives</i>
R _f	Retention Factor
R _q	Roughness Factor

SAM	Self Assembled Monolayer
SEM	Scanning Electron Microscopy
TF-PEC	Thin Film Photoelectrochemical Cells
TFT	Thin Film Transistor
THF	Tetrahydrofuran
TPD	Thiophene Dicarboximide
TWh	Terawatt hours
TWy	Terawatt years
UV-Vis	Ultraviolet-Visible (Absorption Spectroscopy)

Contents

Acknowledgements	vi
Abstract.....	x
Keywords	xi
Resume.....	xiii
Mots clés	xiv
Abbreviations & Symbols.....	xvi
Contents.....	xx
Chapter 1. Introduction	1
1.1. Challenges.....	2
1.2. Solar Energy.....	5
1.3. Solar Spectrum	6
1.4. Solar Energy Harvesting.....	7
1.5. Water Splitting Thermodynamics	8
1.6. Photoelectrochemical Water Splitting [†]	10
1.7. Organic Semiconductors for PEC Water Oxidation [†]	13
1.7.1. DS-PECs: Literature Overview	15
1.7.2. TF-PECs: Literature Overview	22
1.8. Thesis Goals	27
1.9. Conclusion and Thesis Overview	28
1.10. References.....	28
Chapter 2. Methods	38
2.1. Overview	39
2.2. General Methods & Instrumentation	40
2.2.1. Synthetic methods.....	40
2.2.2. Gel Permeation Chromatography	40
2.2.3. Nuclear Magnetic Resonance characterization	40
2.2.4. Mass spectrum characterization.....	40
2.2.5. UV-Vis and Photoluminescence Spectroscopy.....	41
2.2.6. (Photo)Electrochemical Studies.....	41
2.2.7. Miscellaneous Instrumentation.....	41

2.2.8.	Electrolyte Preparation.....	42
2.2.9.	Substrate Preparation	42
2.3.	OSC Characterization	44
2.3.1.	Mass Spectroscopy	45
2.3.2.	Cyclic Voltammetry.....	45
2.3.3.	Thin Film Transistors: Hole Mobility	47
2.3.4.	Ultraviolet-Visible Absorption Spectroscopy.....	49
2.3.5.	Differential Scanning Calorimetry.....	50
2.4.	Thin Film: Binary Mixtures Characterization.....	51
2.4.1.	Photoluminescence Spectroscopy.....	51
2.4.2.	Atomic Force Microscopy.....	52
2.5.	Photoelectrochemistry (PEC).....	53
2.5.1.	PEC instrumentation	53
2.5.2.	Xenon Lamp Calibration	54
2.5.3.	PEC experiments.....	56
2.5.4.	Incident Photon to Converted Electron (IPCE) studies.....	57
2.6.	References	58
Chapter 3.	Quaterrylene Di-imide.....	59
3.1.	Motivation.....	60
3.2.	Synthesis	61
3.3.	Characterization.....	63
3.3.1.	NMR.....	63
3.3.2.	UV-Vis Absorption.....	64
3.3.3.	Cyclic Voltammetry.....	65
3.4.	PEC Characterization	66
3.4.1.	Effect of pH	66
3.4.2.	Amount of <i>QDI</i> sprayed.....	67
3.4.3.	Effect of mSnO ₂ underlayer	67
3.4.4.	Effect of Annealing	68
3.4.5.	Effect of Applied Potential	69
3.5.	Modifications to <i>QDI</i>	70
3.5.1.	Drawbacks of <i>QDI</i>	70
3.5.2.	Structural Changes.....	71

3.6.	Conclusion	75
3.7.	Supporting Information.....	75
3.7.1.	Methods	75
3.7.2.	Miscellaneous NMR.....	80
3.7.3.	MALDI-TOF.....	84
3.7.4.	Miscellaneous UV-Vis Absorption Spectra	85
3.8.	References	86
Chapter 4.	Donors [†]	88
4.1.	Motivation.....	89
4.2.	Synthesis	90
4.3.	Characterization.....	91
4.3.1.	NMR.....	91
4.3.2.	UV-Vis Absorption.....	92
4.3.3.	Cyclic Voltammetry.....	93
4.3.4.	TFT: Mobility	94
4.4.	PEC performance	94
4.5.	Conclusion	96
4.6.	Supporting Information.....	96
4.6.1.	Synthesis.....	96
4.7.	References	97
Chapter 5.	Acceptors [†]	98
5.1.	Motivation.....	99
5.2.	Synthesis	101
5.2.1.	Optimizing oligomerization pathway	101
5.2.2.	Cu- promoted vs Pd- catalyzed coupling reactions.....	101
5.3.	Characterization.....	104
5.3.1.	NMR.....	104
5.3.2.	MALDI-TOF.....	107
5.3.3.	UV-Vis Absorption.....	108
5.3.4.	Cyclic Voltammetry.....	110
5.3.5.	Effect of Cl- substitution	110
5.4.	PEC characterization.....	112
5.5.	Conclusion	113

5.6.	Supporting Information.....	113
5.6.1.	Synthesis.....	113
5.7.	References	120
Chapter 6.	BHJ Blends [†]	123
6.1.	Introduction	124
6.2.	Architecture Optimization.....	124
6.3.	Donor:Acceptor Weight Ratio Optimization.....	127
6.4.	Annealing Optimization	128
6.4.1.	AFM images of BHJ	128
6.4.2.	PEC validation	130
6.4.3.	Photoluminescence Studies	132
6.5.	IPCE	133
6.6.	Effect of Electrolytic pH	134
6.6.1.	Electrochemical Impedance Spectroscopy.....	134
6.6.2.	Dynamic Potential pH Diagram	135
6.7.	Solvent Choice: Chloroform or Chlorobenzene?	136
6.7.1.	Morphology	136
6.7.2.	PEC Performance	138
6.8.	Advantage over Traditional OSCs.....	138
6.9.	Supporting Information.....	139
6.9.1.	Electron Microscopy.....	139
6.9.2.	Miscellaneous PEC data	140
6.10.	Conclusion.....	141
6.11.	References.....	141
Chapter 7.	Applications	142
7.1.	Motivation.....	143
7.2.	BHJ (re-)optimization	144
7.2.1.	Acceptor modification	144
7.2.2.	SAM modification.....	144
7.3.	Halide PEC oxidation.....	146
7.3.1.	PEC Performance	146
7.3.2.	Tandem PEC for HI splitting	149
7.3.3.	Faradaic Efficiency Calculations.....	150

7.4. Water Oxidation – Catalysts.....	152
7.5. Conclusion	153
7.6. Supporting Information.....	153
7.6.1. Photocathode description.....	153
7.6.2. UV-Vis Calibration of Triiodide Solutions.....	154
7.7. References	154
Chapter 8. Conclusion	156
8.1. Final Overview	156
Curriculum Vitae.....	158
Résumé.....	162

Chapter 1. Introduction

The field of PEC solar fuel generation is an emerging area of focus for ongoing research. An interesting concept to improve the performance of the photoelectrodes is to implement organic semiconductors in place of inorganic semiconductors, which suffer from a few intrinsic limitations. While OSC based photocathodes have been demonstrated earlier with reasonable performance and stabilities, OSC based photoanodes are still in a very nascent stage of research. This chapter gives an insight into OSC based photoanodes, the scope and challenges it faces. The two major device architectures: DS-PECs and TF-PECs are discussed with a compilation of involved components in previously published, peer-reviewed reports and their performance parameters. Based on this investigation, we infer the need for alternate OSCs, which are traditionally not used in OPVs due to structural and energetic reasons as possible candidates to obtain high performance and stable photoanodes.

1.1. Challenges

Since the Industrial revolution in the 18th century, there has been a constant increase in the demand for energy by humans.^[1] The latter half of the 20th century saw relative worldwide peace and bolstered by improved living conditions and science and technology; this period resulted in a dramatic increase in human population. According to the *United Nations*, it is estimated that by 2050, over 9 billion humans would compete for resources on earth (Figure 1.1.1).^[2]

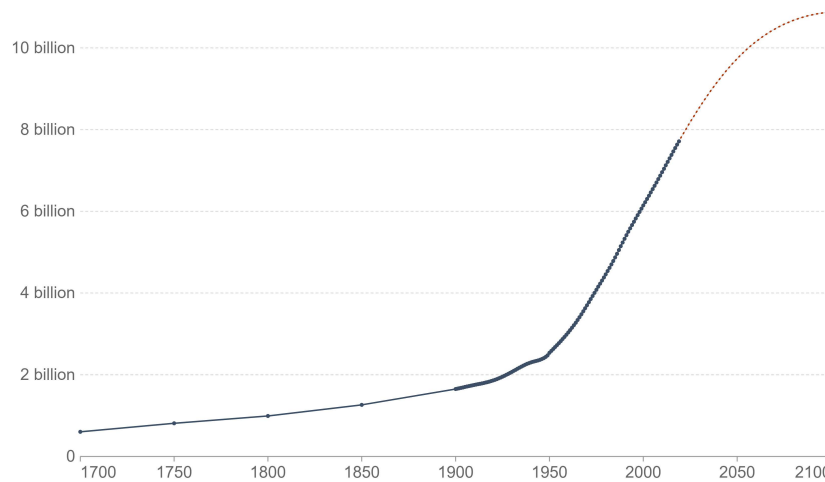


Figure 1.1.1: Trend of world human population. Notice the immense population growth in the 1900s – early 2000s, leading to about 10 billion populations by 2100.^[3]

Improved standards of living in “developing countries”, which have the higher population densities than the “developed countries”, combined with lengthened life expectancies leads to a burgeoning middle class, who are avid consumers of energy collectively. More technologies are increasingly globalized, and as these are often aimed at consuming energy and resources than harnessing or storing, there is an urgent need for alternate technologies to help humankind survive.

Energy is at the core of everyday human life, and progress of mankind. In 2019, the total energy requirement was 173,340 TWh (Figure 1.1.2a) and is only expected to rise with the population. Also, the rapidly developing countries in Asia, have led to a surge in energy consumption.^[4–6]

However, the conventional sources of energy used to cater to the major energy demands of the world have been fossil fuels, like coal and petroleum products. Most of today’s technologies consume these sources directly or indirectly, by means of engines, generators, or power plants.

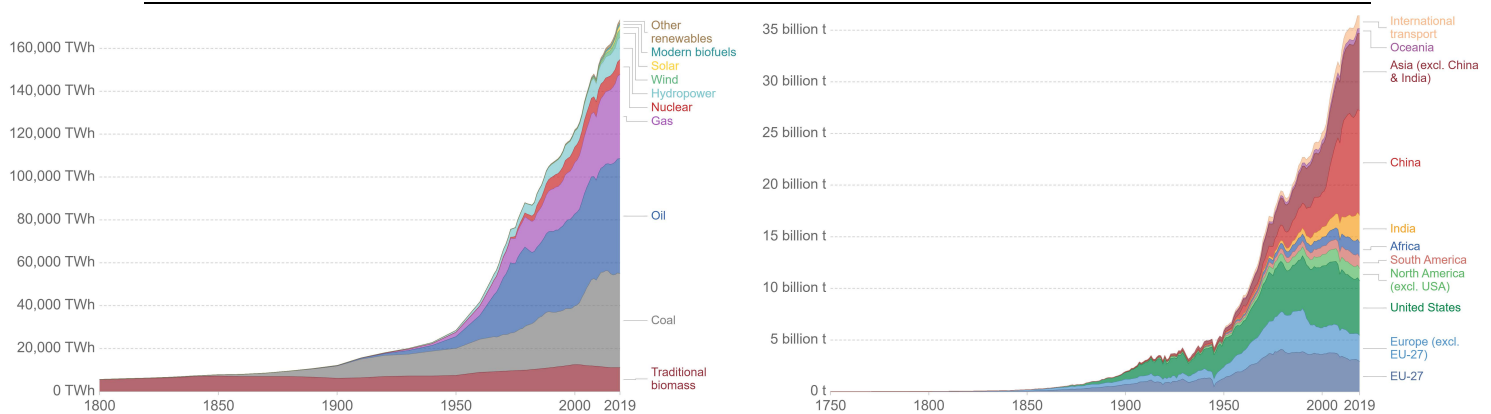


Figure 1.1.2: Chronological evolution of a) (Left) Global primary energy demand by source,^[5,7] b) (Right) CO₂ emissions from fossil fuels and industrial production by region.^[8,9]



“Top Ten Problems of Humanity for the Next 50 Years.” (descending order of concern)

- | | |
|----------------|--------------------|
| 1. Energy | 6. Terrorism & war |
| 2. Water | 7. Disease |
| 3. Food | 8. Education |
| 4. Environment | 9. Democracy |
| 5. Poverty | 10. Population |

- Richard E. Smalley (late Nobel laureate) at Woodrow Wilson Institute, Washington, DC., 10/6/2003

Over the years, despite fluctuating oil prices, multiple wars and crises, petroleum and natural gas have been primary energy resources. This indiscriminate use of fossil fuels has led to a host of problems, including climate change and rise of sea levels following the melting of polar ice caps.^[10] This occurs due to the rise in greenhouse gases in the atmosphere due to human activities involving fossil fuels (Figure 1.1.2b). Specifically, CO₂ and CH₄, lead to trapping of the incoming solar radiation within the atmosphere and cause an overall increase in the temperature of the earth over time^[11] (Figure 1.1.3). As of 2019, about 36.4 billion tons of CO₂ have been emitted by human activities alone, which is double the amount emitted in 1977, indicating that rapid human progress and development in a mere span of about four decades is at the cost of the environment.

Therefore, an urgent need to alleviate the strain on the environment exists, so that human development, progress and rise of technology is not stifled. This calls for sustainable development, but also an alternate, greener source of energy to replace fossil fuels.

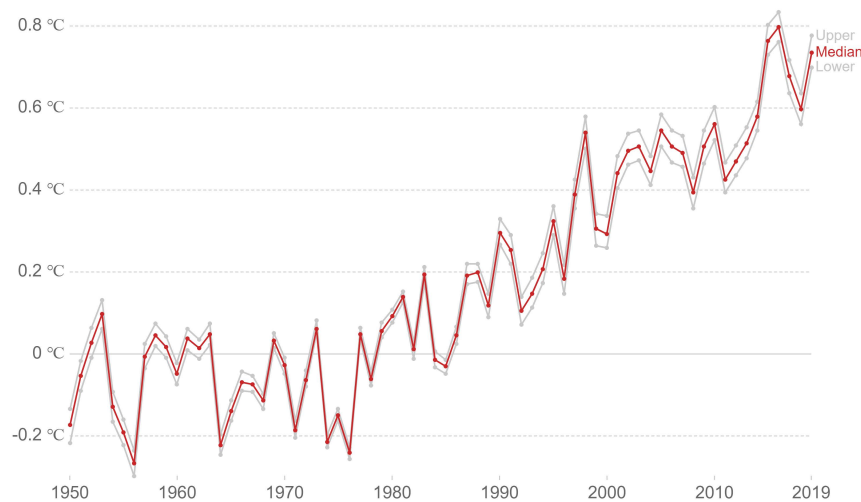


Figure 1.1.3: Chronological evolution of average global temperature anomaly.^[11]

Mapping out energy resources according to their available quantity, it is clearly seen that solar energy is the champion, with over 23000 TWy/year.^[12] Comparing this with the overall human energy requirement of about 32 TWy/year (as of 2018),^[13] it is evident that the use of solar power would be more than sufficient to satiate overall human energy needs for centuries, and other energy resources dwarf in terms of availability (Figure 1.1.4).

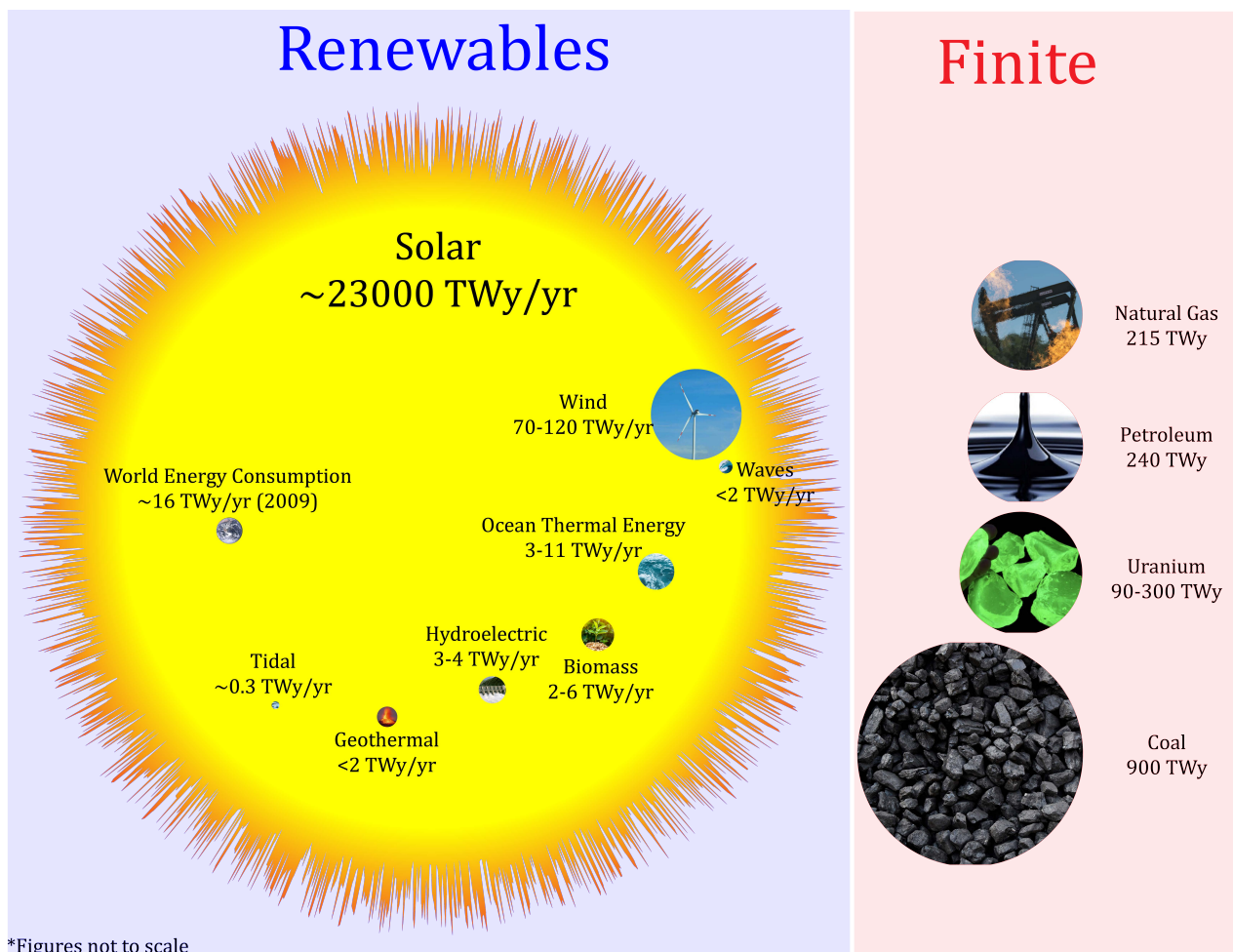


Figure 1.1.4: Available energy resources, showing renewable and finite non-renewable distinction. Mankind is primarily using finite resources and needs to switch to renewables. Data from IEA, 2009.^[12]

1.2. Solar Energy

If the root cause of most sources of energy is traced out, it can be found that the sun is the answer. Till the early Industrial revolution, it was primarily wood or wood-charcoal that was being used as fuels.^[13] Chemical energy stored in wood, which is harnessed by combustion converts the biomass into usable energy in the form of heat. However, this chemical energy buildup in wood occurs because of photosynthesis, wherein atmospheric carbon dioxide is sequestered by plants and photosynthesized energy is eventually stored in wood. This process can be dated back to the Carboniferous era (300,000,000 years ago) where photosynthesizing algae, moss and dense forests were buried and compressed, resulting in what is today known as coal.^[14] Similarly, the wind, hydroelectric, tidal, ocean thermal and other sources of energy also trace their origins to the sun, apart from direct solar irradiation.

The Sun is a G-type main sequence star, based on its size and electromagnetic emission. As with other stars, the main source of its energy is nuclear fusion at 10^7 K in the sun's core, where four protons fuse into one helium nucleus due to extreme thermal kinetic energy.^[15] However, most of this energy is absorbed by H ions closer to the surface of the sun where heat is transferred by convection,^[16] and finally at the surface of the sun, a temperature of 5778 K is maintained.

On average, the distance between the Sun and the earth is 1 AU or 1.5×10^{11} m. The photosphere, which is the outermost surface, being opaque and ionized, almost acts as a black body, and hence, the solar energy radiated into space from the sun can be estimated from Stefan-Boltzmann equation:

$$P_{emit} = A\sigma\epsilon(T_{surface}^4 - T_{space}^4)$$

where,

A: surface area of the sun

σ : Stefan-Boltzmann constant

ϵ : Emissivity of the solar surface

$T_{surface}$: Solar surface temperature

T_{space} : average space temperature (2.7 K)

Only a fraction of this power reaches the earth, corresponding to the solid angle subtended by the earth's surface at the sun's core ($\frac{\pi(\text{Earth's radius})^2}{4\pi(\text{Earth-Sun distance})^2} = \frac{6396^2}{4(149600000)^2} \approx 10^{-8} \%$), and this corresponds to approximately 175000 TW solar irradiation, or 1367 W.m⁻². Assuming reasonable energy losses and harness-able energy fractions, a working solar conversion efficiency of 10% would provide enough energy for humankind. And since the sun is a renewable resource, its usage would not directly have an adverse impact on the environment.

1.3. Solar Spectrum

As mentioned before, since the surface of the sun can be approximated as a black body electromagnetic radiator, Planck's radiation law can be used to estimate the emitted spectra of the sun:

$$E_{\lambda,T} = \frac{2hc^2}{\lambda^5} \frac{1}{\left(e^{\frac{hc}{\lambda k_B T}} - 1\right)}$$

where, h : Planck's constant, c : speed of light in vacuum, k_B : Boltzmann constant, $E_{\lambda,T}$: Energy per unit area, per unit time, per unit wavelength (emitted as a function of λ :wavelength and T :Temperature).

However, this spectrum is only observed at the edge of the earth's atmosphere, uncontaminated by any absorptive interference by air. *Air Mass Coefficient* is useful in characterizing solar spectrum on earth, wherein the direct optical path length ratio with respect to the zenith is the coefficient. AM1.5G refers to the solar spectrum obtained at a zenith angle of 48.2° and includes both direct and diffuse irradiation, averaged to 1000 W.m⁻² and is usually taken as the standard value for solar cell testing conditions (Figure 1.3.1). Another difference between AM1.5G and AM0 spectra is the absence of certain fingerprint wavelengths corresponding to vibrational absorption with atmospheric gases like O₂, CO₂ and H₂O in AM1.5G.

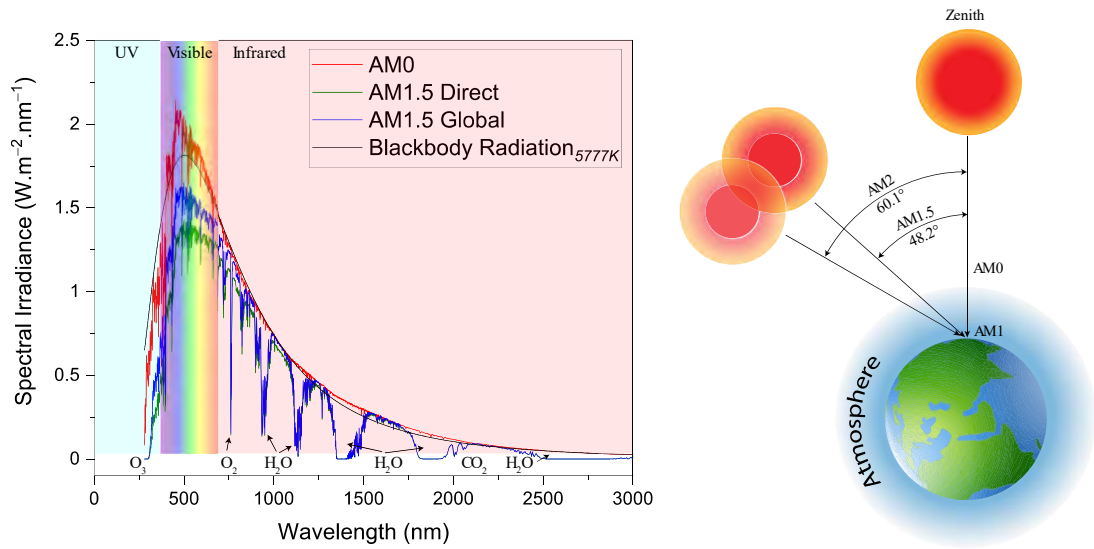


Figure 1.3.1: (Left) Various solar irradiation spectra and Blackbody radiation at 5777K for reference, data from NREL,^[18] (Right) Air Mass Coefficient Illustration.

1.4. Solar Energy Harvesting

While it is evident that the solar energy would solve most of our energy demand, an average $1000 \text{ W} \cdot \text{m}^{-2}$ solar irradiation is obtained at the earth's surface. This would imply an overall land area of around 500000 sq.km covered by solar panels with a conversion efficiency of 20% power conversion efficiency,^[17] based on 2009 IEA estimates (Figure 1.4.1a), is sufficient to cover the worldwide energy requirements.

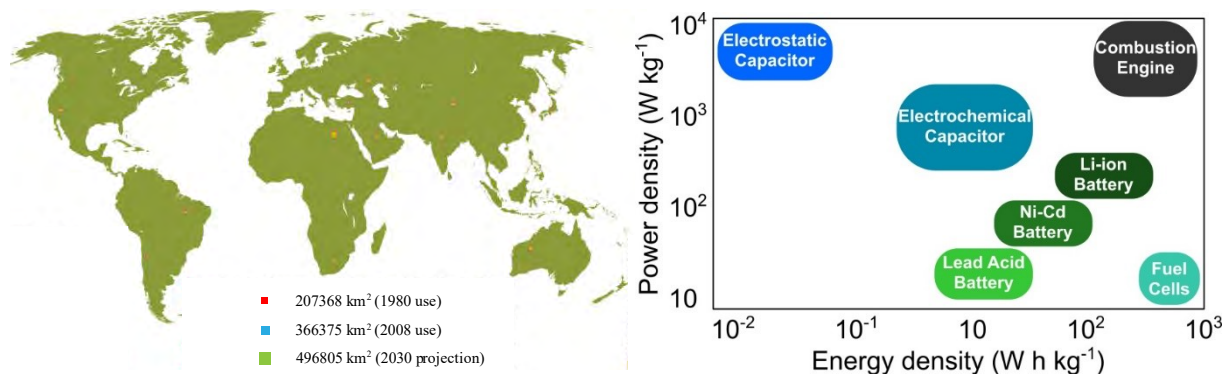


Figure 1.4.1: a) Estimated land area under solar panels for world energy consumption,^[19] b) Power and energy densities by various storage technologies.^[20]

However, due to the major problem of intermittency, due to weather, cloud cover, pollution and the night-day cycle, the integration of solar energy with the existing electricity grid is also made difficult, as it requires a regular, stable power source which results in alternating current.^[21] Even for standalone, off-grid photovoltaic systems, continuous power output is not possible. This necessitates storage of harnessed solar power in some form to use later, when irradiation is absent. The traditional method is to

use batteries or capacitors, which are charged when sunlight is available by solar photovoltaic cells (PVs) and discharged when required. However, they have low energy densities^[20], which makes its use application specific, like for powering up small electronic gadgets, etc. For industrial or automotive purposes, it is often an advantage to use fuels,^[22–24] as it is more economical and needs no new infrastructures (Figure 1.4.1.b).

But these fuels should be solar generated, as opposed to conventional fossil fuels. The process of obtaining solar fuels is also known as artificial photosynthesis, as it mimics the natural phenomena, wherein, plants and chlorophyll containing algae convert ambient CO₂ and water into hydrocarbons and energy. Various fuels could be candidates for this purpose. When carbon dioxide is used as the source, fuels like CO^[25] and methanol,^[26] and even gases like methane^[27] or longer chain hydrocarbons^[28] can be produced by reduction using solar energy. However, the most promising solar fuel is hydrogen, produced by reducing water. In these fuels, solar energy is converted to chemical energy in the form of covalent bonds in the fuel molecules, which could then be harnessed either by combustion, or electrochemically.

1.5. Water Splitting Thermodynamics

Water splitting is the chemical reaction, where water molecules are broken down to hydrogen and oxygen molecules. The energetics of the reaction is:^[29]

$$\begin{aligned}
 & \mathbf{H_2O \rightarrow H_2 + \frac{1}{2}O_2} \\
 & \Delta H_{f,H_2O} = -285.83 \frac{kJ}{mol}; \Delta H_{f,H_2} = \Delta H_{f,O_2} = 0 \frac{kJ}{mol} \\
 & \Delta S_{H_2O} = 69.91 \frac{J}{mol.K}; \Delta S_{H_2} = 130.68 \frac{J}{mol.K}; \Delta S_{O_2} = 205.14 \frac{J}{mol.K} \\
 & \Delta G_{298 K} = \Delta(H - TS)_{298 K} = (285.83 - 48.7) \frac{kJ}{mol} = \mathbf{237.1 \frac{kJ}{mol}}
 \end{aligned}$$

This process occurs spontaneously at high temperatures of ~800°C or higher ($\Delta G < 0$), where the covalent bonds of H₂O break down, however, the kinetics are slow, which warrant higher temperatures for reasonable reaction rate. Such high temperatures put constraints on the materials used and often, catalysts^[28] are used to accelerate the process or solar irradiation is concentrated to split water thermally.^[31]

However, the easier approach is to electrochemically break down water into its components. This process is easily explained when the reaction is split into two half reactions as explained in Table 1.1.

When water is split electrochemically and the source of energy to drive the reaction is the sun, the process is called solar driven water splitting, and whose various methods are detailed in the next subsection.

Table 1.1: Thermodynamics of Water Splitting

Reduction Half-Reaction ^[29]	Oxidation Half-Reaction ^[29]
In acidic conditions, $4H^+ + 4e^- \rightarrow 2H_2$	$2H_2O \rightarrow O_2 + 4H^+ + 4e^-$
In alkaline conditions, $4H_2O + 4e^- \rightarrow 4OH^- + 2H_2$	$4OH^- \rightarrow O_2 + 4e^- + 2H_2O$
$E_{H_2O \text{ reduction}}^0 = 0.00 V_{RHE}$	$E_{H_2O \text{ oxidation}}^0 = +1.229 V_{RHE}$

$$E_{Cell}^0 = E_{H_2O \text{ reduction}}^0 - E_{H_2O \text{ oxidation}}^0$$

$$= -1.229 V \text{ at } 25^\circ C \text{ and } 1 atm$$

E_{cell} changes with different parameters based on the Nernst Equation:

$$E_{cell} = E_{Cell}^0 - \frac{RT}{zF} \ln\left(\frac{a_{Red}}{a_{Ox}}\right)$$

E_{Cell} : Half-Cell Reduction Potential

E_{Cell}^0 : Standard Half-Cell Reduction Potential

R : Universal Gas Constant

T : Temperature (K)

F : Charge of 1 mol of e^- in C

a_i : Activity of species "i"

1.6. Photoelectrochemical Water Splitting†

Broadly, the major types of solar-driven technologies to split water into H_2 and O_2 can be divided into three types: Photovoltaic-Electrolysis (PV-E), Photoelectrochemical (PEC), and Photocatalytic reactors (PC) (Figure 1.6.1).

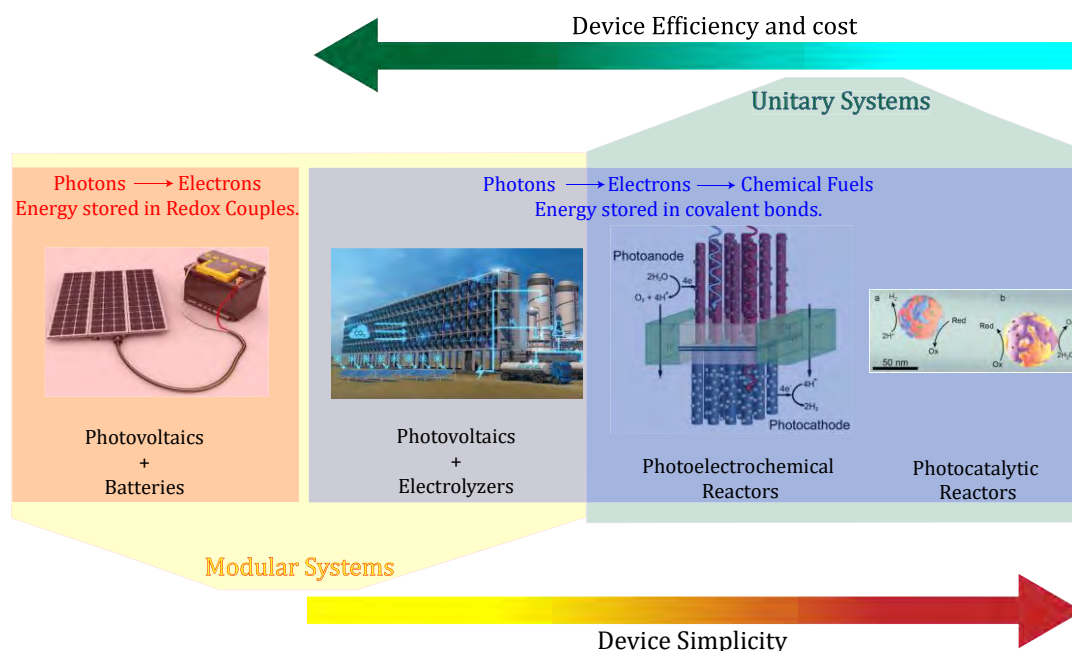


Figure 1.6.1: Scheme showing simplicity and efficiency differences in the 3 major technologies for solar fuel generation.

Photovoltaic-Electrolysis (PV-E) technology simply couples available photovoltaic systems with water splitting electrolyzers. The photovoltaic component uses a semiconductor-based device to convert solar photons to excited electrons (driving an electrical current in an external circuit) and the electrolyzer device uses this electrical power to drive the two water-splitting half-reactions: water (or proton, H^+) reduction on the cathode to form H_2 and hydroxide (or water) oxidation on the anode to make O_2 . Effectively in PV-E, the photon-to-electron and electron-to-fuel conversions occur using different components that are electronically connected. Individually, as both technologies themselves are quite well established on a large scale, this method of producing hydrogen has been demonstrated with high efficiency^[32,33] and can be easily implemented at different scales. Unfortunately, as previously mentioned the price of the H_2 produced is not yet economically competitive with conventional H_2 production techniques, so a common goal in research is to increase the Solar-to-Hydrogen (STH) efficiency of PV-E systems. However, systems with high STH efficiency require multiple junction PV-devices and

†: This section is adapted and used from a review article, titled “Organic Semiconductors as Photoanodes for Solar-driven Photoelectrochemical Fuel Production” (A. Sekar and K. Sivula, *Chim. Int. J. Chem.* **2021**, 75, 169–179)

concentrated solar irradiation,^[34] which are typically very expensive. As a benchmark example of a simple PV-E implementation under 1 sun illumination, the highest STH of 20.6% has been reported by Tae Nam and coworkers^[35] which used an AlGaAs as a PV device coupled to an electrolyzer (membrane electrode assembled configuration) with IrO_x as the oxygen evolution reaction catalyst (OERC) on the anode and Pt on nanocrystalline carbon as the hydrogen evolution reaction catalyst (HERC) on the cathode. About 78% of the electrical energy generated by the PV was effectively converted to hydrogen. Despite the progress with PV devices and the PV-E approach, many researchers look for an alternative approach that could produce H₂ at a significantly reduced cost.

Photoelectrochemical (PEC) water splitting combines light harvesting and chemical fuel generation into a single component: the semiconductor (SC) photoelectrode. SCs which either self-catalyze the water oxidation/reduction reactions directly using their surface or use electrocatalysts deposited at the SC-water interface form the photoanode and photocathode in PEC water splitting. The advantages of this technology can be lower device complexity and potentially lower cost. Working photoelectrodes can easily be immersed in electrolytes to produce chemical fuels without any complicated electronic connections. The simplicity of the device architecture is visible from Figure 1.6.2, where the scheme of a PEC tandem cell is shown. Here the HERC/photocathode (SC1) and OERC/photoanode (SC2) are wirelessly connected via an Ohmic contact and immersed in a water-based electrolyte. SC1 and SC2 absorb complementary portions of the solar spectrum and build sufficient photopotential to drive the overall water-splitting reactions.

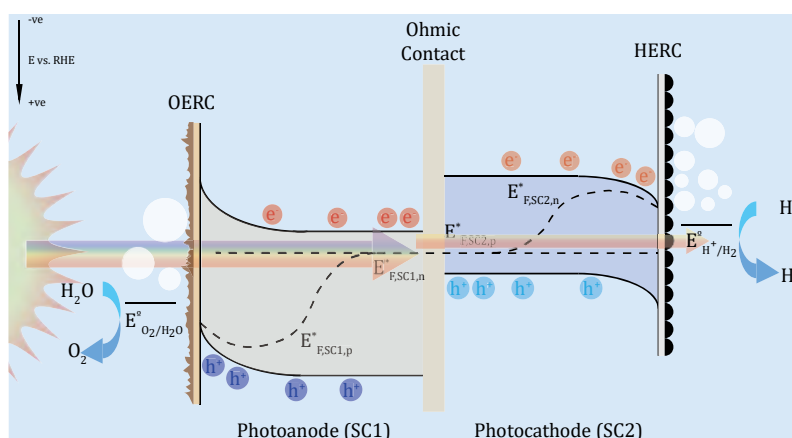


Figure 1.6.2: Scheme of tandem PEC electrodes splitting water, showing Fermi and quasi Fermi levels upon illumination.

The thermodynamic driving force for the electrolysis of water is 1.23 eV per molecule of H₂O. In addition to the thermodynamic energy, accounting for energy losses

due to charge recombination and catalytic overpotential of the materials, the valence band of the SC in the photoanode needs to be more positive than 1.23 V vs. the *Reversible Hydrogen Electrode* (V_{RHE}) and the conduction band of the photocathode needs to be more negative than 0 V_{RHE} . While the *Fermi* levels represent the average energy of electrons present in the semiconductor, the quasi *Fermi* levels show the influence of photopotential as well. Upon illumination, the quasi *Fermi* level of minority charge carriers equilibrate, $E_{F,SC2p}^* \approx E_{F,SC1,n}^*$ while the quasi *Fermi* level of SC1 at the electrolyte/semiconductor interface is sufficient to transfer holes to OERC and oxidize water ($E_{F,SC1,p}^* > E_{O_2/H_2O}^o$) while the quasi *Fermi* level of SC2 at the electrolyte/semiconductor interface is sufficient to transfer electrons to HERC and reduce water ($E_{F,SC2,n}^* < E_{H^+/H_2}^o$). The band bending in SC1 and SC2 results in an internal electric field which causes holes drifting towards OERC and electrons drifting towards HERC for overall water splitting.

Photocatalytic (PC) systems comprise the simplest of the three device architectures. SCs with appropriate energy band levels are suspended as micro- or nanoparticles in water, and upon illumination the photogenerated electrons and holes are used by HERCs and OERCs on the surface of the particles or in solution to produce hydrogen and oxygen. The ease of this system configuration however comes with drawbacks. A lack of a driving force for charge carrier separation, poor STH efficiencies (around 1%), and the requirement of sacrificial electron shuttles to afford overall water-splitting, to name a few, make this method of splitting water the least performant.^[36] However, from an economic perspective PC water splitting can potentially produce the most cost-effective H_2 if the STH can be raised to the level of the PEC or PV-E devices. Moreover, like PEC water splitting, the PC approach employs a direct SC/water interface, the further study of photoelectrodes with various semiconductors can help to gain insight into the limitations of the PC water splitting approach and further develop both systems towards viable commercial application.

Considering the SC materials that can be suitable for PEC or PC water splitting, the direct SC/water interface places harsh demands on the stability. The seminal report of PEC water splitting is often cited as Fujishima and Honda in 1972,^[37] where n-type TiO_2 , a wide energy gap, E_g , SC material was used as a photoanode to directly oxidize water on its surface under illumination. However, TiO_2 cannot harness much of the incoming solar spectrum due to its wide E_g of 3.1 eV. Similar wide E_g SCs like $SrTiO_3$ ($E_g > 3.2$ eV) and $KTaO_3$

($E_g > 3.6$) have good relative performance based on the light that they can absorb, but they are limited to $STH < 2\%$.^[38,39]

More recently, smaller E_g SC materials in PC systems and as photocathodes and photoanodes capable of much higher STH which can be used in a tandem cell have been developed. A few examples of photocathodes with high performance include p-Si(001) based photocathodes with epitaxially grown $SrTiO_3$ and a nanostructured HERC (Pt)^[40] reaching a 1-Sun photocurrent density, J_{ph} , of 15 mA cm^{-2} at $0 V_{RHE}$ and inexpensive Sb_2Se_3 sublimed into compact, well-oriented films protected by TiO_2 and with RuO_x HERC deposited photoelectrochemically^[41] giving $J_{ph} \sim 30 \text{ mA cm}^{-2}$ at $0 V_{RHE}$.

While the photocathodes have almost reached the SC's theoretical maximum J_{ph} , photoanodes however, typically perform more poorly. The state-of-the-art photoanode materials are metal oxides and oxynitrides. For example, $LaTiO_2N$ ^[42] gives (unstable) J_{ph} of $8.9 \text{ mA}\cdot\text{cm}^{-2}$ at $1.23 V_{RHE}$, $BiVO_4$ gives stable J_{ph} of $1.7 \text{ mA}\cdot\text{cm}^{-2}$ at $1.2 V_{RHE}$, etc. These materials suffer from low J_{ph} due to crystallographic disorders, high internal recombination states due to traps, low absorption coefficients, low carrier hole mobilities and lifetimes of the SC. Moreover, these materials often require expensive processing techniques like vapor deposition which severely limit the scalability of the photoelectrode devices.^[43–46] Thus, there is a clear need for the development of new high performance photoanode materials.

1.7. Organic Semiconductors for PEC Water Oxidation[†]

Carbon-based organic semiconductors (OSCs) have been widely demonstrated in organic photovoltaics (OPVs) and dye sensitized solar cells (DSSCs) and have various advantages over the typically used inorganic SCs used in photoanodes. Most of the OSCs used in OPVs and DSSCs are solution processable, which facilitates large area fabrication of devices using printing techniques capable of high Power Conversion Efficiency (PCE).^[47–50] With relatively high charge mobilities and high light absorption properties, even thin films of OSCs lead to high PCEs (up to 17% in OPVs and 14% in DSSCs).^[51–54] Accordingly, the use of OSCs for solar-driven water splitting has been recently considered. OPVs coupled with electrolyzers as PV-E systems have been demonstrated, usually with multijunctions to obtain high open circuit potentials ($> 1.23 \text{ V}$) and expensive fabrication methods, and scalability issues with respect to surface area of electrolyzer vs. solar cell.^[55–57]

Alternatively, OSCs have been employed with a direct OSC/water interface in photocathodes for H₂ production. For example, a bulk heterojunction (BHJ) of PTB7-Th donor and PDI-V acceptor polymers^[58] (Figure 1.7.1) over MoO₃ as the hole-selective transport layer (HTL) and RuO_x as HERC resulted in a J_{ph} of 8.2 mA·cm⁻² at 0 V_{RHE}, retaining 85% of the initial J_{ph} after 8 hours of operation.

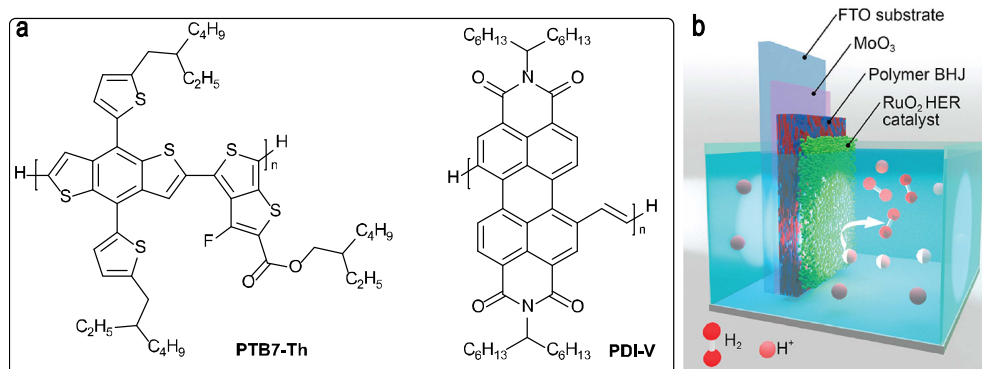


Figure 1.7.1: a) Polymers used in a recently reported OSC-based photocathode, b). A schematic of the employed photocathode which uses a F-doped tin oxide (FTO) substrate, the polymers in a bulk heterojunction (BHJ) and a direct contact of the OSCs/catalyst with the water-based electrolyte. Reproduced with permission from ref. ^[45] © 2020 American Chemical Society.

While the use of OSCs as high performance and stable photocathodes have been demonstrated successfully,^[58–63] their use as photoanodes has been somewhat restrained. A major issue is likely the harsh oxidative electrochemical conditions. At such high applied potentials, the OSC should be functionally stable to oxidize water instead of decomposing. Due to synthetic ease of tuning energy levels in OSCs, many OSCs are reported that possess suitable energy levels to oxidize water under illumination and do remain stable in the harsh environment of a photoanode, at least temporarily. In the next section the details of device architectures that make functional photoanodes based on OSCs and the progress made recently using OSCs as photoanodes for the water oxidation reaction is reported. It is important to note that the OSC inherently only performs the light absorption, exciton generation and charge separation and charge transport processes.^[64–66] Unlike inorganic metal oxide photoanodes, the photogenerated hole at the OSC/water interface almost always requires the use of a water oxidation heterogeneous catalyst or a molecular catalyst (OERC) deposited on the photoanode to oxidize water, due to the kinetic complexity of the water oxidation reaction.

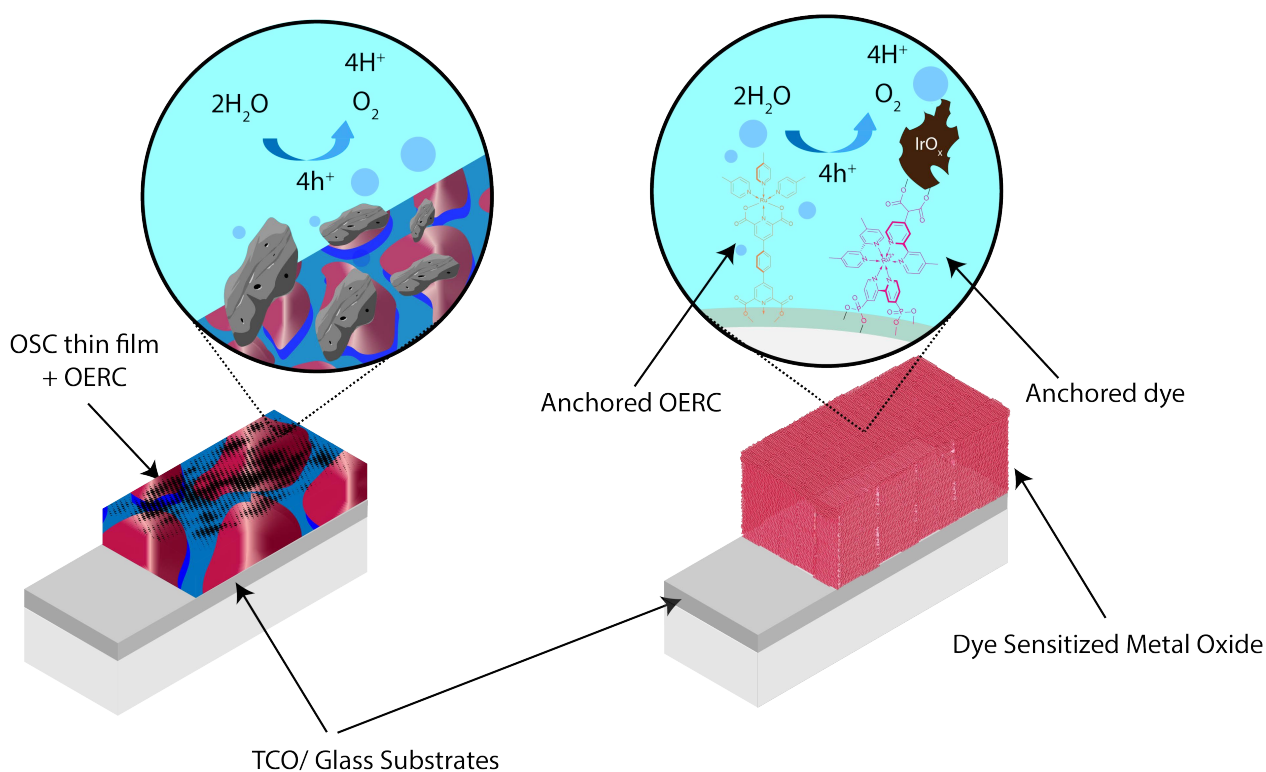


Figure 1.7.2: Schematic Diagram of TF-PEC (left) and DS-PEC (right). While the TF-PEC uses a heterogeneous OERC, in the DS-PEC, two ways of anchoring an OERC are shown. A molecular OERC (Ru complex in orange) is directly anchored on the metal oxide, or a heterogeneous OERC can be anchored via the dye (Ru complex in magenta).

Overall, there are two major strategies in which OSCs are used as photoanodes. The first borrows the device architecture from DSSCs and incorporates a mesoporous metal oxide layer over a conducting substrate onto which a monolayer of dye is sensitized. Light absorption by the dye leads to ultrafast injection of a photogenerated electron from the dye into the mesoporous metal oxide's conduction band, leaving the photogenerated hole on the dye and available to oxidize a species in the electrolyte. When these dye-sensitized photoelectrochemical cells (DS-PECs) are placed in contact with an aqueous electrolyte the hole can oxidize water if it can be transferred to an OERC first. The second strategy employing OSCs in photoanodes involves replacing the dye sensitized mesoporous metal oxide with a thin film OSC and can be called a thin film photoelectrochemical cell (TF-PEC). In this case, the OSC acts both as a medium for light harvesting and photogenerated charge transport. Figure 1.7.2 illustrates schematics of the two different photoanode architectures.

1.7.1. DS-PECs: Literature Overview

Broadly, the DS-PECs can be further classified as those using metal-organic complexes as dye sensitizers (MC DS-PECs), and those which utilize chromophores without metal centers i.e., "metal-free" (MF DS-PECs).

The metal-organic-complex-based dyes inherently are more expensive, based on raw materials, and likely more toxic. Hence MC DS-PECs could have limitations in terms of scalability and processability.^[51] Synthetically, modifying the energy levels of these complexes is also limited by the substituents on the ligands, leading to constraints in terms of band gap and energy level tuning.^[65,67,68] The demonstrated metal-organic complexes used in MC DS-PECs usually follow a similar molecular template. A Ruthenium central ion ligated by aromatic N-heterocycles like bipyridines with anchoring groups like phosphonates is the primary photoabsorber (Figure 1.7.3a shows dye molecular structures, which will be discussed below), and which is anchored to a thick (7-12 μm) mesoporous electron accepting metal oxide scaffold. Reports of photoanodes using this concept and other DS-PECs are summarized in Table 1.2 with typical performance parameters.^[69-76]

Another known template for DS-PECs uses porphyrin derivatives as macromolecular dyes: both with metal centers,^[77] and as metal free (sub)porphyrins.^[78-81] While these Ru- dyes and metal porphyrins are efficient photo-absorbers; their onset wavelength is limited to $< 700\text{ nm}$, leading to limited light capture in the near infrared region of the solar spectrum. To extend the light harvesting, researchers have more recently employed alternate OSCs: robust intrinsic n-type OSCs like rylene di-imide derivatives,^[82,83] Donor- π conjugation-Acceptor moieties (D- π - A),^[84,85] or metal free (sub)porphyrins.^[78,79,86] Figure 1.7.3b shows the structures of the D- π - A dyes employed in DS-PEC photoanodes where the incorporation of electronic push-pull phenomena at the molecular level in their conjugation length can be noticed. Triphenyl amine-based dyes with cyanoacrylic acid anchoring groups have been successfully demonstrated in DS-PEC as photosensitizers. For example, in 2015, Sun and coworker^[84] managed to make an organic tandem DS-PEC with both photocathode and photoanode sensitized by OSCs. The photoanode in use involved L0 dye (Figure 1.7.3b) sensitized on TiO_2 over Fluorine doped Tin Oxide (FTO) using RuWOC4 sensitized on TiO_2 as the OERC (the structures of the OERCs used for DS-PECs are shown in Figure 1.7.4). Slightly modifying this dye, Meyer and coworkers^[85] in 2016, used the P-A- π -D dye (Figure 1.7.3b) on TiO_2 coated SnO_2 as the photoanode. While P-A- π -D-based photoanodes worked well in sacrificial conditions (20 mM hydroxyquinone, H_2Q), giving stable sacrificial $J_{\text{ph,sac}}$ of $\sim 2.5\text{ mA cm}^{-2}$ at 0.66 V_{RHE} in pH 7, with the OERC RuWOC6 (Figure 1.7.4a) in absence of sacrificial electron donors, J_{ph} was significantly lower.

An interesting example of an n-type OSC dye is from Bignozzi and coworkers in 2015, who used an organic di-cation PDI (Figure 1.7.3d) as the photoabsorber.^[82] In this study, multiple metal oxides like TiO₂, SnO₂ and WO₃ were sensitized over long periods, when PDI was adsorbed on the nanocrystalline metal oxide. Spun-coat and air-dried IrO₂ nanoparticles on PDI-sensitized WO₃ was used as the photoanode. Other examples of n-type OSC dyes include photoanodes by Wasielewski and coworkers^[87] and Finke and Kirner.^[88] PMI and PMPDI (Figure 1.7.3d) were the dyes investigated, using IrWOC3 (Figure 1.7.4b) and CoO_x as catalysts respectively. Interestingly, Kirner and Finke also investigated their photoanodes with sacrificial electron donors (20 mM H₂Q), reaching stable $J_{ph,sac}$ of 1.1 mA cm⁻² at 0.61 V_{RHE} in pH 7. Unfortunately, with the OERC, J_{ph} for water oxidation was in the μ A cm⁻² scale.

Examples of metal-free (sub)porphyrin photoanodes include PPor–OPh–COOH anchored to SnO₂ and SP anchored to TiO₂ (Figure 1.7.3c) by van der Est and coworkers^[86] and Imahori and co-workers.^[79] With IrWOC3 and RuWOC4 as OERCs (Figure 1.7.4a-b) respectively, these photoanodes fared rather poorly in terms of performance and stability. Indeed, stability is a critical issue for the practical application of OSC-based photoanodes.

From Table 1.2, it can be observed that engineering OERCs plays a major role in the device performance and stability. In all the cases, illumination was from the side of the back contact: F-doped SnO₂ (FTO) or Sn-doped In₂O₃ (ITO), and OERC was in contact with the electrolyte to oxidize water. Moreover, Mallouk and coworkers initially used hydrated IrO_x-bound to-dye-bound to-TiO₂ as the photoanode in 2009^[70] and in 2012, used ligand modified IrO_x (IrWOC2, Figure 1.7.4b)^[71] in which J_{ph} marginally increased to 0.2 mA·cm⁻² but was not very stable;^[85,89] there was a 50% reduction in J_{ph} after just 95 seconds of operation.

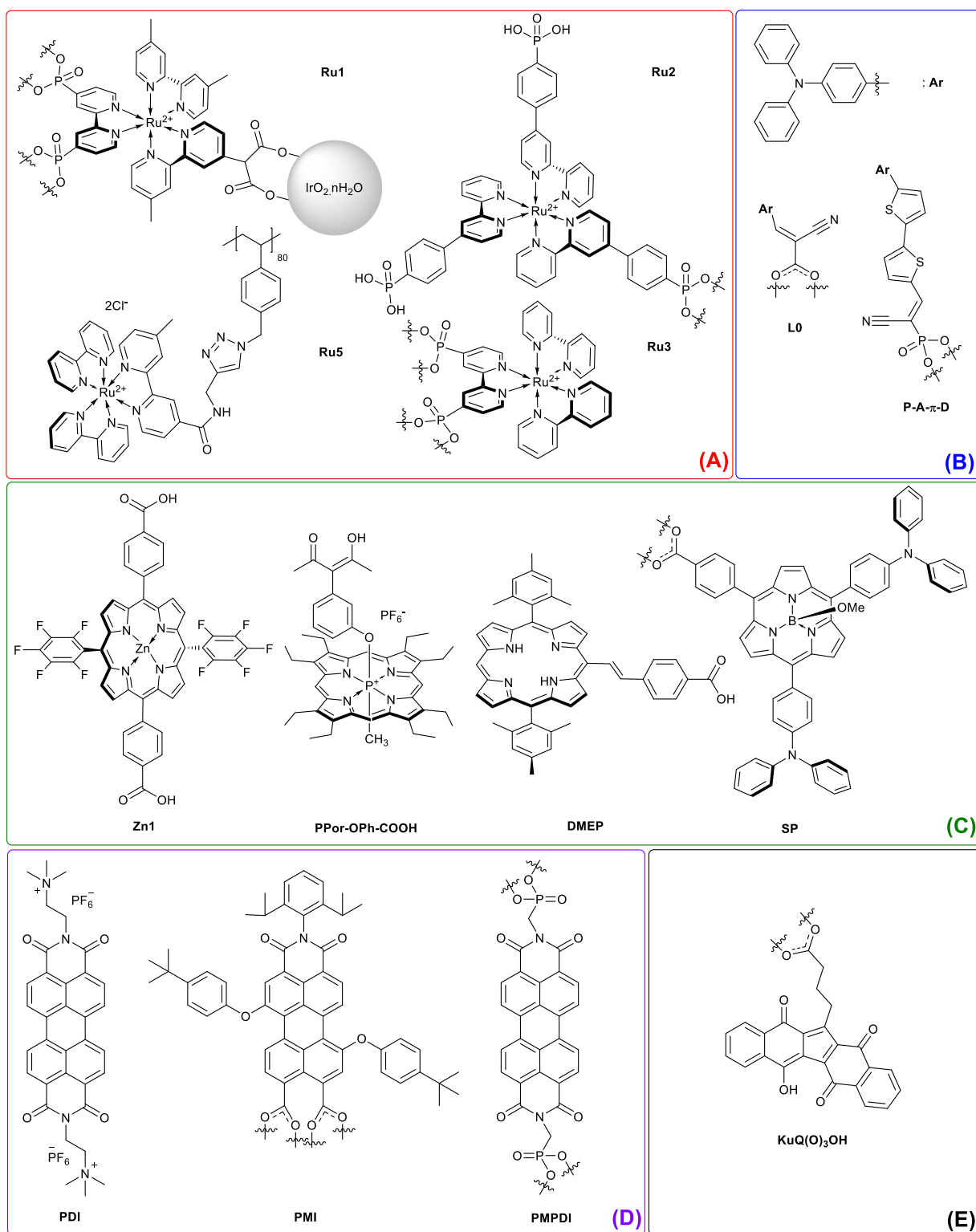


Figure 1.7.3: Subtypes of Dyes in DS-PECs: A) Ru- based dyes (red box), B) D- π -A dyes (blue box), C) porphyrin derivatives (green box), D) n-type OSC dyes (purple box, E) miscellaneous dyes (black box). Anchoring groups are bound to metal oxides.

layer along with Ru3 (Figure 1.7.3a) resulted in $J_{ph} \sim 2.5 \text{ mA}\cdot\text{cm}^{-2}$, which dropped to $0.7 \text{ mA}\cdot\text{cm}^{-2}$ after 100 seconds of operation.^[69] In another study, binuclear RuWOC2 (Figure 1.7.4a) with a phosphonate group anchored to TiO_2 showed $\sim 83\%$ higher J_{ph} than its mono

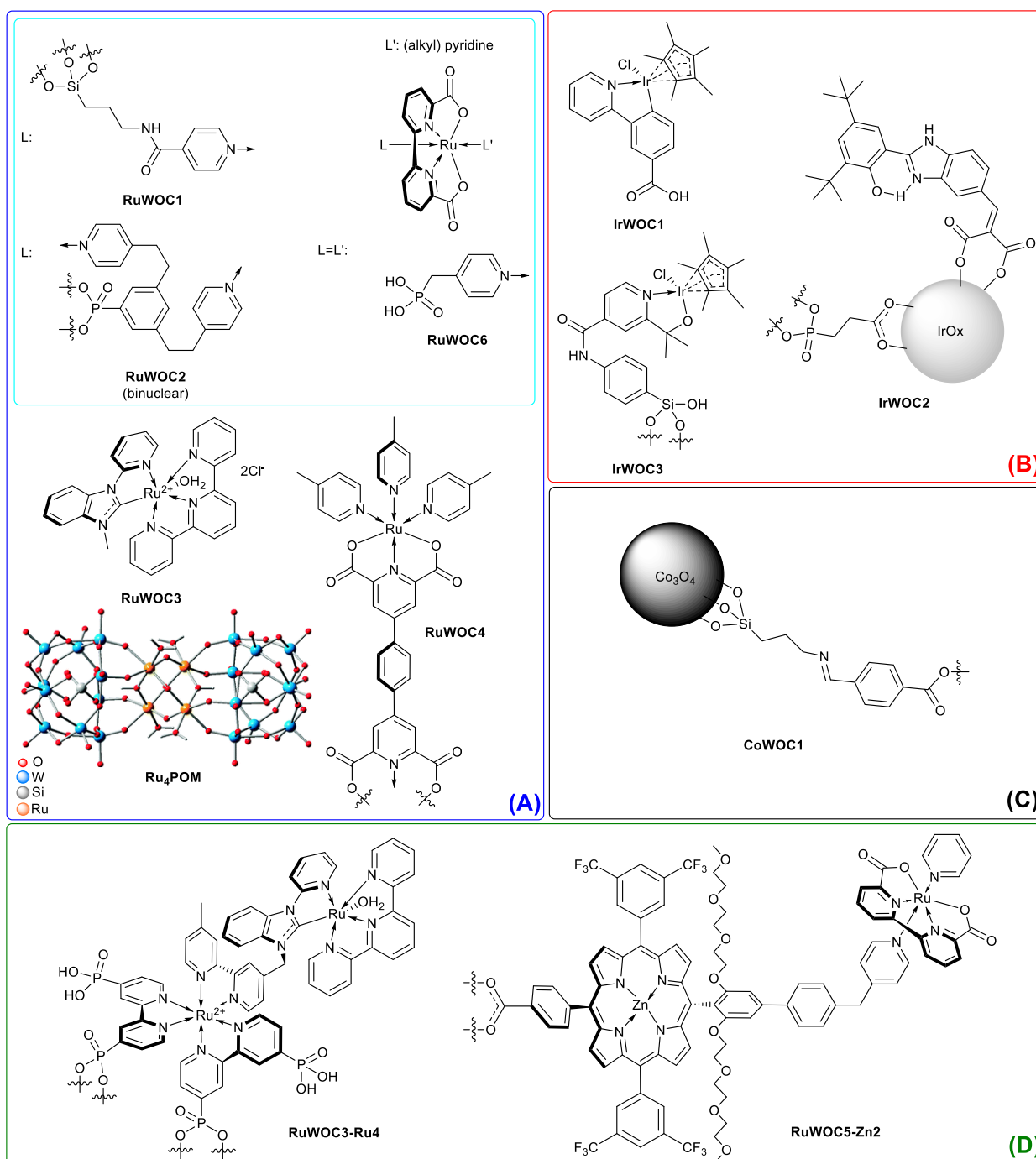


Figure 1.7.4: Subtypes of OERCs: A) Ru- molecular catalysts (blue box), B) Ir- catalysts (red box), C) non-noble metal catalyst (black box), D) bifunctional (photosensitizer + molecular OERC) binuclear metal complexes (green box).

-nuclear variant,^[72] however losing ~37% of its initial J_{ph} within 100 seconds of operation. Binuclear bifunctional molecules^[73,90] (RuWOC3-Ru4 and RuWOC5-Zn2) were also sensitized onto metal oxides, wherein two metal organic complexes, one a photosensitizer and another a molecular OERC which are covalently bonded (Figure 1.7.4d) resulted in poor stability. More recently in 2020, Sartorel and coworkers reported their DS-PEC photoanode which utilized a tetraruthenium polyoxometalate OERC (Ru₄POM with 1%

Nafion, Figure 1.7.4a) showing oxygen evolution for 90 minutes^[91] with a pentacyclic dye KuQ(O)₃OH (Figure 1.7.3e), albeit with a modest J_{ph} . An overarching observation is that using Ruthenium based molecular catalysts always led to poor Faradaic efficiencies for oxygen evolution (lowest:^[85] 8.2%, highest:^[69] 83%), compared to heterogeneous oxide nanoparticles (lowest:^[71] $\geq 85\%$, highest:^[78] $102 \pm 5\%$) and low stability (the best performing unprotected photoanode was operational for < 2 minutes).

In addition to the OERC, another factor which affected the stability was the photosensitizer itself. It is hypothesized that in DS-PECs, the loss of stability is primarily due to detachment of the dye from the metal oxide^[92,93] or the oxidative decomposition of the chromophore.^[85,89] To address these issues, additional protective overlayers were used to enhance the stability. However, these overlayers are intrinsically insulating in nature for hole transport (e.g. Al₂O₃,^[73] polyacrylic acid (PA)^[76]) and therefore lower the J_{ph} . The longest functioning DS-PEC with a molecular OERC was demonstrated by Murray and coworkers^[74] in 2015. A thin layer of TiO₂ by atomic layer deposition (ALD) over the mesoporous nanoITO ensured stable sorption of the dye and oxygen evolution for 2 hours of operation (with $\sim 80\%$ loss in J_{ph}) was measured.

Table 1.2: DS-PECs and operating parameters, observed J_{ph} and stability with faradaic efficiencies.

Type	Overlayers (if any)/ OERC and Photo-absorber ^a / Electron Transport Layer / Electrode	Illumination & Filters (λ : cutoff wavelength)	J_{ph} ($A \cdot cm^{-2}$) @ Applied Potential (V_{RHE})	Stability (J_{ph} , in $A \cdot cm^{-2}$ after time, in seconds)	Electrolyte	Faradaic Efficiency for O ₂ generation (%)
MC DS-PECs	IrO_x.nH₂O/ Ru1/ porous nanocrystalline TiO ₂ film (9 μm)/ FTO [70]	$\lambda > 410$ nm	$\sim 7.5 \times 10^{-7}$ @ 0.54	$\sim 1.7 \times 10^{-7}$ after 60	Na ₂ SiF ₆ -NaHCO ₃ buffer at pH 5.75; 0.5 M Na ₂ SO ₄	-
	IrWOC1/ Zn1/ P25 TiO ₂ nanoparticles film (10 μm)/ FTO [77]	200 mW.cm ⁻² ; $\lambda > 400$ nm	$\sim 3.3 \times 10^{-7}$ @ 0.91	$\sim 3.0 \times 10^{-7}$ after 60	M Na ₂ SO ₄ at pH 7	-
	IrWOC2+Ru2/ TiO ₂ film (7 μm)/FTO [71]	$\lambda > 410$ nm	1.8×10^{-4} @ 0.54	$\sim 9.0 \times 10^{-5}$ after 95	Na ₂ SiF ₆ -NaHCO ₃ buffer at pH 5.8; 0.1 M LiClO ₄	$\geq 85\%$
	RuWOC1+Ru3/ nano TiO ₂ film (12 μm)/FTO [69]	300 mW.cm ⁻² ; $\lambda > 400$ nm	$\sim 2.5 \times 10^{-3}$ @ 0.67	$\sim 7.0 \times 10^{-4}$ after 100	phosphate buffer at pH 6.8	83%
	RuWOC2^b+Ru3/ TiO ₂ film (12 μm)/FTO [72]	300 mW.cm ⁻² ; $\lambda > 400$ nm	$\sim 1.1 \times 10^{-3}$ @ 0.61	$\sim 7.0 \times 10^{-4}$ after 100	0.1 M Na ₂ SO ₄ at pH 7	75%
	Al ₂ O ₃ (0.3 nm)/ RuWOC3-Ru4/ TiO ₂ (6.6 nm)/ SnO ₂ ^c / FTO [73]	455 nm LED at 46.2 mW/cm ²	$\sim 5.0 \times 10^{-4}$ @ 0.6 V vs. Pt ^{d,e}	$\sim 7.0 \times 10^{-5}$ after ~ 1300	0.1 M phosphate buffer at pH 7	41%
	IrO_x.nH₂O/ Ru3/ TiO ₂ (6.6 nm)/ nanoITO (3.2 \pm 0.5 μm)/ FTO [74]	455 nm LED at 14.5 mW/cm ²	$> 6.0 \times 10^{-4}$ @ 0.61	1.1×10^{-4} after 7200	Na ₂ SiF ₆ -NaHCO ₃ buffer at pH 5.8; 0.1 M LiClO ₄	-
	RuWOC5-Zn2/ TiO ₂ (12 μm)/FTO [90]	35 mW.cm ⁻² ; $\lambda > 380$ nm	$\sim 1.7 \times 10^{-4}$ @ 0.23	7.0×10^{-5} after 60	0.1 M phosphate buffer at pH 7.3	33%
	CoWOC1+Ru3/ TiO ₂ ^c / FTO [75]	100 mW.cm ⁻² ; $\lambda > 400$ nm	$\sim 1.3 \times 10^{-4}$ @ 0.9	$< 4.0 \times 10^{-5}$ after 120	phosphate buffer at pH 6.8	-
	(PA- RuWOC3) ₅ ~(Ru5) ₅ ^f / TiO ₂ (6.6 nm)/ SnO ₂ ^c / FTO [76]	100 mW.cm ⁻² ; $\lambda > 400$ nm	$\sim 1.8 \times 10^{-5}$ @ 0.85	$\sim 6.0 \times 10^{-6}$ after 600	0.1 M phosphate buffer at pH 7	22%
MF DS-PECs	IrWOC1 + PPor-OPh-COOH^g/ SnO ₂ film (10 μm)/ FTO [86]	200 mW.cm ⁻² ; $\lambda > 400$ nm	$\leq 2.0 \times 10^{-5}$ @ 0.91	$\leq 2.0 \times 10^{-5}$ after 300	0.1 M Na ₂ SO ₄ at pH 7	-
	IrO_x + DMEP^h / TiO ₂ film (4 μm)/ FTO [78]	$\lambda > 410$ nm	$\sim 8.0 \times 10^{-5}$ @ 0.70	$\sim 1.0 \times 10^{-5}$ after 600	0.1 M sodium phosphate buffer at pH 6.8	102 \pm 5%
	IrO₂/ PDI/ nanocrystalline WO ₃ ^h film (0.7 μm)/ FTO [82]	AM 1.5 G; $\lambda > 435$ nm	$< 7.0 \times 10^{-5}$ @ 0.77	Chrono-coulometry ⁱ	0.1 M NaClO ₄ at pH 3	-
	RuWOC4 + L0 / TiO ₂ (8 μm)/ FTO [84]	White LED at 100 mW.cm ⁻² ; $\lambda > 400$ nm	$\sim 5.0 \times 10^{-4}$ @ 0.41	$\sim 2.0 \times 10^{-4}$ after 400	0.05 M phosphate buffer at pH 7	73%
	RuWOC6 + P-A-π-D/ TiO ₂ (3 nm)/ SnO ₂ (8 μm)/ FTO [85]	100 mW.cm ⁻² ; $\lambda > 400$ nm	$\sim 1.4 \times 10^{-3}$ @ 0.85 ^e	$\sim 1.0 \times 10^{-4}$ after 600	0.1 M phosphate buffer at pH 7; 0.5 M KNO ₃	8.2%
	RuWOC4 + SP/ TiO ₂ film (2 μm)/ FTO [79]	LED at 100 mW.cm ⁻² ; $\lambda > 420$ nm	$\sim 8.0 \times 10^{-4}$ @ 0.64	$\sim 6.0 \times 10^{-5}$ after 30	0.1 M NaF at pH 7	64%
	IrWOC3^b / Al ₂ O ₃ (5 ALD cycles)/ PMI/ TiO ₂ (10 nm)/ FTO [87]	200 mW.cm ⁻² ; $\lambda > 410$ nm	$\sim 1.7 \times 10^{-4}$ @ 0.66	$< 2.5 \times 10^{-5}$ after 600	1 M Na ₂ SO ₄ at pH 2.5	22%
	CoO_x/ PMPDI/ SnO ₂ ^h (6 μm)/ FTO [88]	\sim AM 1.5G ; $\lambda > 400$ nm	$\sim 2.0 \times 10^{-5}$ @ 1.41	-	0.1 M phosphate buffer at pH 7	31 \pm 7%
	Ru₄POM (1% Nafion)/ KuQ(O)₃OH/ SnO ₂ (3 μm)/ FTO [91]	AM 1.5G $\lambda > 400$ nm	$\sim 2.3 \times 10^{-5}$ @ 1.14	$\sim 3.0 \times 10^{-6}$ after 5400	0.1 M Na ₂ SiF ₆ -NaHCO ₃ buffer at pH 5.8	70 \pm 15%
^a OERC/dye refers to OERC bound to dye. OERC+dye refers to both co-sensitized on metal oxide. OERC-dye implies a binuclear bifunctional metal organic complex. ^b Multiple OERCs investigated. Best performing molecule is mentioned. ^c Thickness of mesoporous metal oxide not mentioned. ^d Pt was used as both reference and counter electrode. ^e J_{ph} here is photocurrent; the area of cell is not mentioned.			^f The polymer-OERC and polymeric Ru5 were deposited layer by layer 5 times over each other. ^g Multiple dyes investigated. Best performing molecule is mentioned. ^h Multiple metal oxides investigated. Best performing oxide is mentioned. ⁱ First 50 s of illumination cycle allows 1.25×10^{-2} C.cm ⁻² , the third cycle allows 7.50×10^{-2} C.cm ⁻² .			

1.7.2. TF-PECs: Literature Overview

DS-PECs in general suffer the same drawbacks as traditional DSSCs, such as charge recombination due to the high surface area of the metal oxide/dye interface.^[94–96] Moreover, the demonstrated stability of DS-PEC does not suggest that these photoanodes will be used in practical devices soon. These drawbacks warrant investigation into photoanodes with a different architecture to reduce charge recombination and improve the J_{ph} and stability. Thin film (TF) based OSC PEC cells can be considered as an improvement as they reduce the device complexity. Indeed, given the relatively high charge carrier mobility in many OSCs, a reasonably performing photoanode can be prepared by simply coating a thin film of an OSC on to a conductive substrate. However, while planar TFs of OSCs absorb light quite efficiently due to high absorption coefficients, they do not integrate a mechanism for charge carrier separation like the DS-PEC (via fast charge injection into the mesoporous metal oxide). In fact, given the different reorganization energies and dielectric constant of an OSC (compared to a typical inorganic semiconductor), coulombically-bound electron-hole pairs (excitons) are typically present at room temperature and these need to be separated to create free charge carriers. Different strategies to enhance charge separation in thin film OSCs, compared to a simple mono-layer TF-OSC multilayering of OSCs^[97–100] where different energy levels and intrinsic charge transport properties of the OSC layers can facilitate charge separation, and the blending of OSCs into BHJs^[101–104] which increase the interfacial area between electron donating (p-type) and electron accepting (n-type) OSC phases, which are shown schematically in Figure 1.7.5.

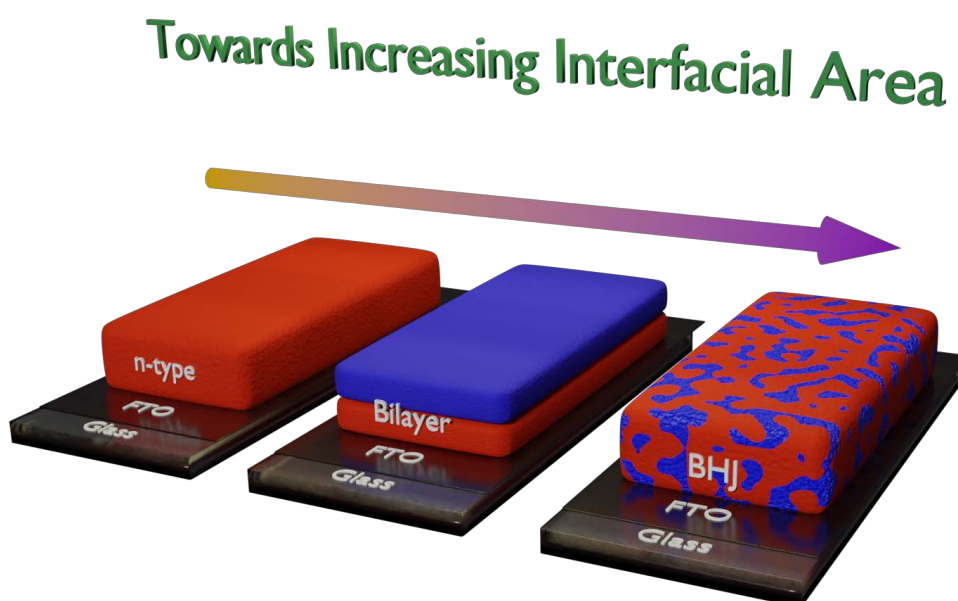


Figure 1.7.5: Schemes for increasing the interfacial area between n-type (Red) and p-type (Blue) OSCs in n-i-p architectures.

Both latter approaches create an internal photogenerated electric field which aids in exciton separation and transport of electrons and holes. In all cases, OERCs deposited on the surface or embedded in the OSC thin films accept the photogenerated holes and oxidize water under operational conditions.

The earliest reported TF-PECs were by Norimatsu and coworkers,^[105,106] where the relatively insoluble but electrochemically robust OSCs PTCBI (n-type) and CoPc (p-type), see structures in Figure 1.7.6, were successively vacuum deposited at high temperatures on ITO substrates forming a bilayer photoanode. The use of an OERC (Nafion covered IrO₂) resulted in J_{ph} of 10 $\mu\text{A cm}^{-2}$ at 1.23 V_{RHE} . After this, Swiegers and coworkers used a Mn-molecular catalyst embedded in polymers ((*TTh*)_n and (EDOT)_n), see structures in Figure 7, that were either electrochemically polymerized or vapor phase polymerized with the help of an oxidant on ITO or flexible ITO-Polyethylene terephthalate (PET) substrates,^[107,108] which could oxidize seawater and were stable for 1 hour, albeit with $J_{ph} \sim 30 \mu\text{A cm}^{-2}$ at potentials > 1.33 V_{RHE} .

Another class of TF-PECs focused on using traditional n-type OSCs as the photoabsorbers. For example, JinCai and co-workers used a hybrid trilayer photoanode of PC₆₁BM/PTCDA_{11.6}:PC₆₁BM₁/ PTCDA on ITO,^[109] achieving a J_{ph} of $\sim 17 \mu\text{A cm}^{-2}$ at 0.36 V_{RHE} in acidic conditions. TF-PECs by Finke and co-workers^[110] used water-processed PMPDI spin-coat on FTO (40-50 nm) with CoO_x as the OERC. A $J_{ph} \sim 0.28 \text{ mA cm}^{-2}$ at 1.81 V_{RHE} was achievable using this photoanode in neutral pH conditions. Another fullerene derivative (PC₇₁BM) of a smaller bandgap with ZnO passivated overlayer showed photoanodic properties without any OERC. These photoanodes operated in alkaline conditions and were stable for over 1400 seconds, albeit with $J_{ph} \sim 15 \mu\text{A cm}^{-2}$.

To improve the stability of TF-PEC anodes with OSC, at LIMNO, the researchers sought a robust organic semiconductor. BBL was known since the 1990s as a robust, semiconducting, stable n-type conjugated polymer. But due to poor solution processability, was not widely explored for photoelectrochemical applications. Bornoz et al.^[111] demonstrated an organic acid processed, spray-coated BBL film that was extremely stable as photoanode for water oxidation with Ni-Co OERC (where a thin, 1 nm, TiO₂ layer was used to help the adhesion between the OERC and the BBL). In addition, by tuning the deposition method this work established that increasing the surface area of the OSC/water interface helped to increase the rate of the solar-driven oxidation reaction. However, the

most stable TF-PEC photoanodes to date used reduced graphene oxide (rGO) as an overlayer, with nanoNi or NiOOH as water oxidation catalyst, as demonstrated by Swiegers and coworkers^[112] and Chan Lim and coworkers^[113] respectively.

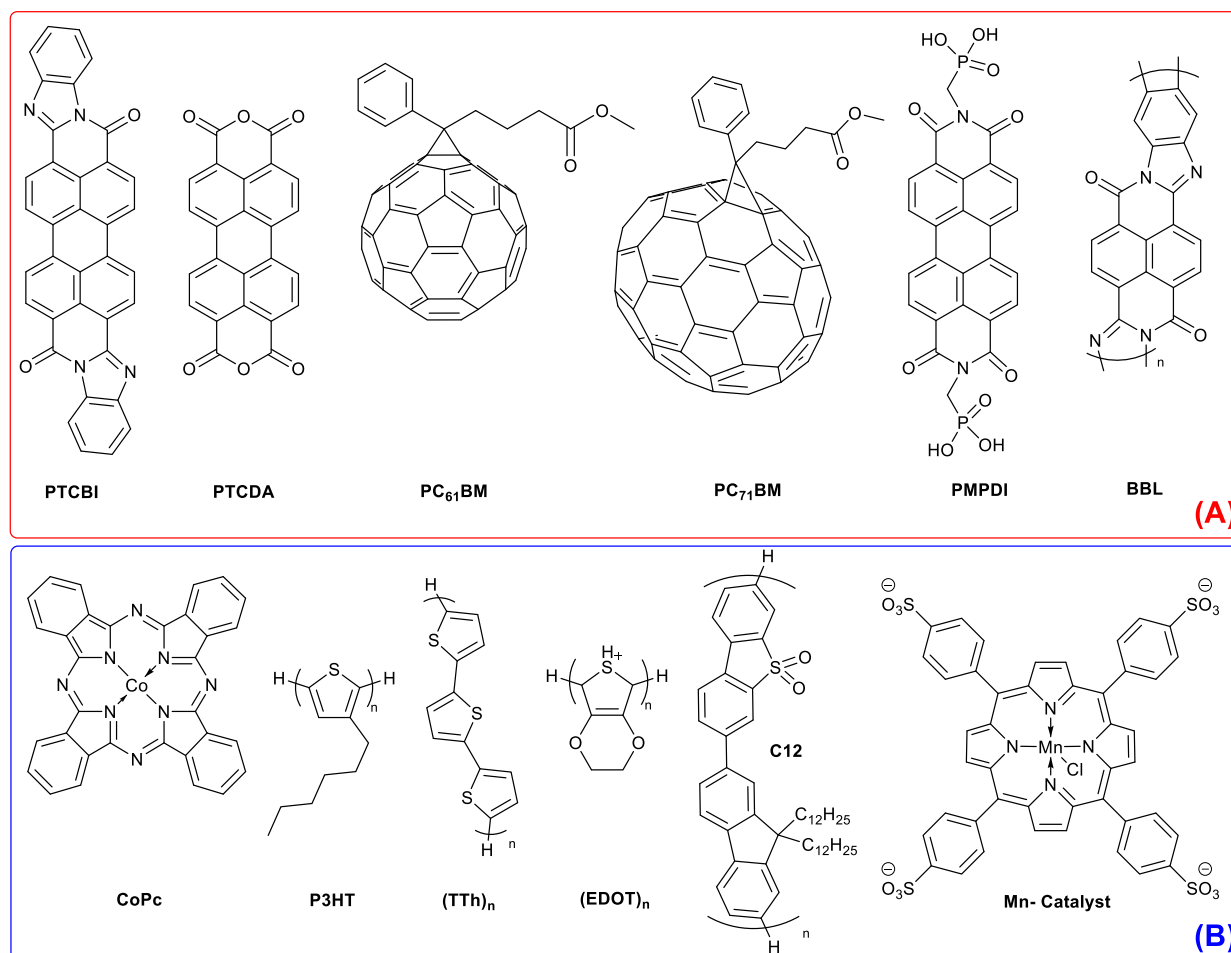


Figure 1.7.6: OSCs in TF-PECs: A) n-type (red box), B) p-type (blue box). Mn-catalyst is an OERC used.

While Chan Lim's photoanode consisted of an organic Bulk Heterojunction (BHJ) donor:acceptor (P3HT:PC₆₁BM) blend as the photoactive layer, the photoanode of Swiegers aided the intrinsic electrocatalytic ability of Pt by depositing an OSC, (EDOT)_n, over it. In alkaline pH, these photoanodes effectively oxidized water and were stable for hours, and in the case of Chan Lim's work, at $J_{ph} \sim 0.6 \text{ mA cm}^{-2}$ with only 0.25 Sun illumination intensity. TF-PEC photoanode results are summarized in Table 1.3.

At LIMNO, recent work indicates that using a BHJ approach easily facilitates charge separation and stable photoanode functionality, at least for a few hours. The first approach involved an organic-inorganic heterojunction, with the mesoporous SnO₂ acting as the n-type electron acceptor (and also the electron transport layer (ETL)) in the heterojunction, and the in-situ generated covalent polymer network as the p-type electron donor.^[114] In

this work, iodide was oxidized to iodine/triiodide as it has a lower redox potential than water oxidation and does not require catalysts (Figure 1.7.7).

Also, subsequently, a preliminary demonstration of tandem PEC electrodes, for H₂ splitting was shown. The stable BHJ photocathode from earlier demonstration was chosen and electronically connected to the hybrid photoanode. Due to high onset potentials, *j*-*V* curves of the two complementary electrodes only had poor overlapping regions, and hence led to $J_{ph} \sim \mu A$, but this is the first demonstration of an OSC based tandem PEC application.

The second demonstration is the use of an organic BHJ in n-i-p architecture form with sprayed Li⁺ doped IrO₂ nanoparticles as oxygen evolution catalyst.^[115] To improve stability, the contact area between ETL and BHJ, the former was made mesoporous, and the device could function in neutral-weakly alkaline pH where $J_{ph} \sim 2 \text{ mA}\cdot\text{cm}^{-2}$ (Figure 1.7.8).

Note that this table focuses on photoelectrodes and not “buried junction” devices where the active semiconductor layers are not in close contact with the aqueous interfaces. However, results from these buried junction devices can also be impressive. Indeed, Jang and coworkers^[116] used a BHJ donor:acceptor (D:A) blend in a fully functional OPV protected with overlayers and liquid metal eutectic interlayers, and demonstrated a stability for over 10 hours with about 10% loss in J_{ph} when using a Ni-Fe layered double hydroxide OERC. A few other noteworthy publications also try other variations using similar metal-based and metal free OSCs (ex. C12)^[117] but are not elaborated in this article due to poor stability, performance, oxygen evolution.^[75,81,118] Polyheptazine derivatives (g-C₃N₄) also show decent performance and stability as photoanodes for water oxidation,^[119-125] however these semiconductors are not solution processable.

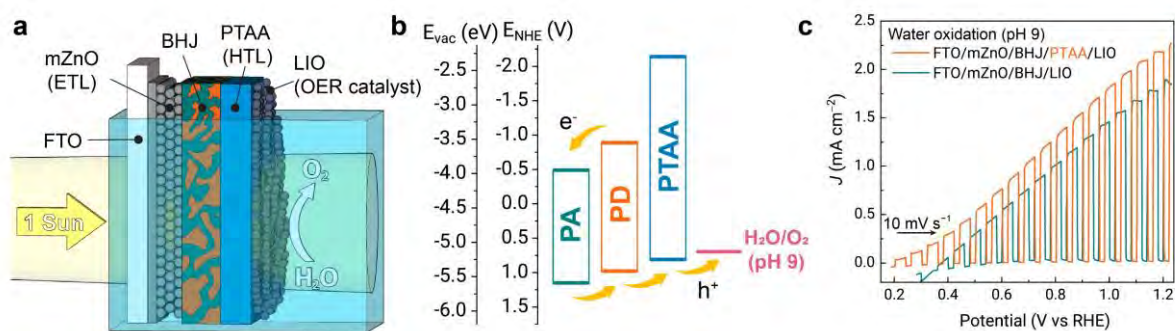
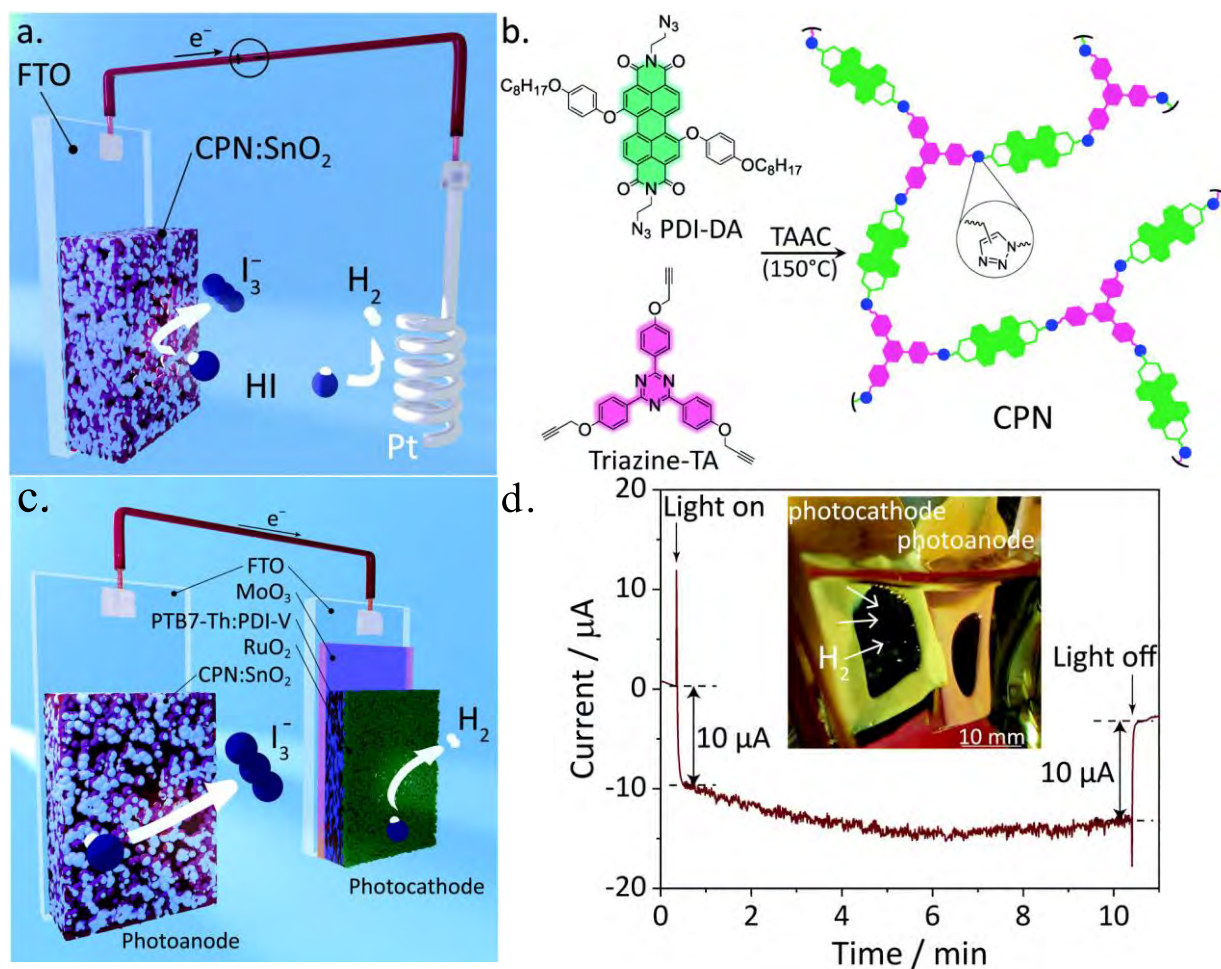


Table 1.3: TF-PECs and operating parameters, observed J_{ph} and stability with faradaic efficiencies.

Type	Overlayers (if any)/ OERC and Photo-absorber / Electron Transport Layer / Electrode	Illumination & Filters (λ : cutoff wavelength)	J_{ph} ($A.cm^{-2}$) @ Applied Potential (V_{RHE})	Stability (J_{ph} , in $A.cm^{-2}$ after time, in seconds)	Electrolyte	Faradaic Efficiency for O_2 generation (%)
TF-PECs	CoPc (0.19 μm)/ PTCBI (0.6 μm)/ ITO [105]	70 mW.cm ⁻²	$\sim 1.7 \times 10^{-5}$ @ 1.14	Stable at $\sim 5.0 \times 10^{-6}$ for ~ 3600	NaOH (aq.) at pH 11 ^{a,b}	-
	Nafion (30 nm)- IrO₂ / H₂Pc (0.16 μm)/ PTCBI (0.45 μm)/ ITO [106]	70 mW.cm ⁻²	$\sim 1.0 \times 10^{-5}$ @ 1.23	$\sim 5.0 \times 10^{-6}$ after 60	KOH (aq.) at pH 10 ^a	-
	(TTh) _{3n} -(Mn catalyst) _n / ITO [107]	50 W halogen lamp	$\sim 2.3 \times 10^{-5}$ @ 1.51	Stable over 24 hours	0.1 M Na ₂ SO ₄ at pH 7	> 99.2% in seawater ^c
	PC₆₁BM (3 nm)/ PTCDA_{11.6} : PC₆₁BM₁ (35 nm)/ PTCDA (20 nm)/ ITO [109]	110 mW.cm ⁻² ; $\lambda > 420$ nm	$\sim 1.7 \times 10^{-4}$ @ 0.36	$< 1.0 \times 10^{-4}$ after 1000	35 mM KNO ₃ at pH 2.0 (adjusted with 1 M H ₂ SO ₄)	$\sim 92\%$
	(EDOT) _{3n} -(Mn catalyst) _n / ITO [108]	3 sun intensity. $\lambda > 420$ nm	$\sim 3.0 \times 10^{-5}$ @ 1.33	$\sim 2.6 \times 10^{-5}$ after 3600	Seawater at pH 8.57	> 99.2% in seawater ^c
	CoO_x / PMPDI (40-50 nm)/ ITO [110]	100 mW.cm ⁻²	$\sim 2.8 \times 10^{-4}$ @ 1.81	$\sim 1.0 \times 10^{-4}$ after 300	0.1 M potassium phosphate buffer at pH 7	80 \pm 15%
	Ni-Co / TiO ₂ (1 nm)/ BBL (230 nm)/ FTO [111]	100 mW.cm ⁻²	$\sim 3.0 \times 10^{-5}$ @ 1.23	Stable at 1.03×10^{-5}	Phosphate buffer at pH 7 ^d	82 \pm 16%
	rGO/ NiO-OH / (EDOT) _n :PSS/ P3HT : PC₆₁BM (1:1; 100 nm)/ ZnO/ ITO [113]	100 mW.cm ⁻² ; AM 1.5G	$> 1.0 \times 10^{-4}$ @ 1.23	Stable at $\sim 6.0 \times 10^{-5}$ after 4 hr	0.1 M Na ₂ SO ₄ at pH ~ 13.0	-
	ZnO(<2 nm)/ PC₇₁BM (~ 60 nm)/ ITO [126]	100 mW.cm ⁻² ; AM 1.5G	$< 1.5 \times 10^{-5}$ @ 1.23	$< 6 \times 10^{-6}$ after 1400	M KOH at pH ~ 13	$\sim 33\%$
	rGO/ nano-Ni / (EDOT) _n / Pt/ FTO [112]	0.25 sun intensity	5.5×10^{-4} @ 1.7	6.0×10^{-4} after 50 hr	0.2 M Na ₂ SO ₄ at pH 12	>99.9%
	C12 / TiO ₂ nanorods (250 nm)/ FTO [117]	Xe lamp; $\lambda > 420$ nm	3.25×10^{-5} @ 1.21	$> 3.0 \times 10^{-5}$ after 200	0.5 M Na ₂ SO ₄ at pH ~ 7.0	-

^a Under Argon atmosphere
^b Sacrificial electron shuttle of 1 mM TEA was used.
^c Cl₂ detection in O₂ gas by Merckoquant® test strips.
^d 0.5 M Na₂SO₄ + 0.09 M KH₂PO₄ + 0.01 M K₂HPO₄

1.8. Thesis Goals

From the above sections and the results compiled in Table 1.2 and Table 1.3, it is understood that DS-PECs despite initial high performance, eventually are not long lasting and quickly degrade or deteriorate. Therefore, in this thesis, TF-PECs are explored. Most of the OSCs used in the photoelectrodes are derivatives of perylene imides, due to deep MO levels of the molecule. Taking cues from earlier works at LIMNO, extended conjugation was shown to result in stable photoanodes. Therefore, the initial goal is to work with an OSC combining the features of perylene di-imides and extended conjugation. And from 1.7.2.TF-PECs: Literature Overview, blending multiple OSCs resulting in multi-junctions should also be explored to enhance the charge separation to get higher J_{ph} . Eventually the obtained photoanode could be used in devices, in tandem with OSC based photocathodes to result in an unassisted all OSC based tandem PEC cell.

1.9. Conclusion and Thesis Overview

This chapter outlines the introduction and motivation to the relatively new field of OSC based photoanodes. The first few sections highlight the challenges and requirements to move towards a solar driven carbon free energy resource and provide theoretical background necessary to understand the upcoming chapters. The three different methods of generating solar fuels are discussed, and the focus towards PEC is stated. Then a brief recap into the literature of OSC based PECs is mentioned elaborating the different OSCs, catalysts, additional layers and their resulting performance parameters. Lastly, the goals of this thesis are mentioned.

The second chapter gives an idea about the methods used to measure the performance of the photoanodes. In the next chapters, a few OSC molecules which were tried and tested as candidates for potential high performance, stable photoanodes are described. The motivation, synthesis, material characterization, device optimization and outlook of the molecules chosen will be described in detail. Specifically, the third chapter deals with the use of quaterylene diimide as a photoanode material, the drawbacks of using a neat material etc. despite structural modifications. The fourth chapter transitions to BHJ photoanodes, and the donor molecule of choice. The fifth chapter deals with the acceptor molecule to complement the donors. The BHJ properties of thin films are elaborated in the sixth chapter, and how these thin films perform as photoanodes. Finally, the photoanode is tailored for use in tandem with a photocathode to drive a complete photoelectrochemical reaction in the seventh chapter. An outlook for the future and conclusion is provided in the last concluding chapter.

1.10. References

- [1] E. A. Wrigley, *Philos. Trans. R. Soc. Math. Phys. Eng. Sci.* **2013**, 371, 20110568, DOI: 10.1098/rsta.2011.0568.
- [2] R. Lee, *Science* **2011**, 333, 569, DOI: 10.1126/science.1208859.
- [3] Total world population - Our World in Data. The data for the period before 1900 are taken from the History Database of the Global Environment (HYDE). The data for the World Population between 1900 and 1940 is taken from the UN publication "The World at Six

Billion". The annual data for the World Population between 1950 and 2019 is taken from the UN's World Population Prospects: The 2019 Revision., <https://ourworldindata.org/grapher/world-population-1750-2015-and-un-projection-until-2100>.

[4] T. Ahmad, D. Zhang, *Energy Rep.* **2020**, 6, 1973, DOI: 10.1016/j.egyr.2020.07.020.

[5] Global Primary Energy Consumption by source - Our World in Data; Energy transitions: global and national perspectives, <https://ourworldindata.org/energy-production-consumption>; Praeger, An Imprint Of ABC-CLIO, LLC, Santa Barbara, California, 2017.

[6] BP Statistical Review of World Energy 2017, <https://www.bp.com/content/dam/bp/en/corporate/pdf/energy-economics/statistical-review-2017/bp-statistical-review-of-world-energy-2017-full-report.pdf>, accessed January 18, **2018**.

[7] Intergovernmental Panel on Climate Change, O. Edenhofer, Eds. , 'Climate change 2014: mitigation of climate change: Working Group III contribution to the Fifth Assessment Report of the Intergovernmental Panel on Climate Change', Cambridge University Press, New York, NY, **2014**.

[8] P. Friedlingstein, M. O'Sullivan, M. W. Jones, R. M. Andrew, J. Hauck, A. Olsen, G. P. Peters, W. Peters, J. Pongratz, S. Sitch, C. Le Quéré, J. G. Canadell, P. Ciais, R. B. Jackson, S. Alin, L. E. O. C. Aragão, A. Arneeth, V. Arora, N. R. Bates, M. Becker, A. Benoit-Cattin, H. C. Bittig, L. Bopp, S. Bultan, N. Chandra, F. Chevallier, L. P. Chini, W. Evans, L. Florentie, P. M. Forster, T. Gasser, M. Gehlen, D. Gilfillan, T. Gkritzalis, L. Gregor, N. Gruber, I. Harris, K. Hartung, V. Haverd, R. A. Houghton, T. Ilyina, A. K. Jain, E. Joetzjer, K. Kadono, E. Kato, V. Kitidis, J. I. Korsbakken, P. Landschützer, N. Lefèvre, A. Lenton, S. Lienert, Z. Liu, D. Lombardozzi, G. Marland, N. Metzl, D. R. Munro, J. E. M. S. Nabel, S.-I. Nakaoka, Y. Niwa, K. O'Brien, T. Ono, P. I. Palmer, D. Pierrot, B. Poulter, L. Resplandy, E. Robertson, C. Rödenbeck, J. Schwinger, R. Séférian, I. Skjelvan, A. J. P. Smith, A. J. Sutton, T. Tanhua, P. P. Tans, H. Tian, B. Tilbrook, G. van der Werf, N. Vuichard, A. P. Walker, R. Wanninkhof, A. J. Watson, D. Willis, A. J. Wiltshire, W. Yuan, X. Yue, S. Zaehle, *Earth Syst. Sci. Data* **2020**, 12, 3269, DOI: 10.5194/essd-12-3269-2020.

[9] Annual total CO2 emissions, by world region; Global, Regional, and National Fossil-Fuel CO2 Emissions (1751 - 2014) (V. 2017), <https://ourworldindata.org/grapher/annual-co-emissions-by-region>; 10.3334/CDIAC/00001_V2017, accessed July 20, **2021**.

[10] S. Manabe, *Tellus Dyn. Meteorol. Oceanogr.* **2019**, 71, 1620078, DOI: 10.1080/16000870.2019.1620078.

[11] Average temperature anomaly, Global - Our World in Data; Quantifying uncertainties in global and regional temperature change using an ensemble of observational estimates., <https://ourworldindata.org/co2-and-other-greenhouse-gas>

emissions;<https://onlinelibrary.wiley.com/doi/10.1029/2011JD017187>, accessed July 20, **2021**.

[12] R. Perez, M. Perez, 'A fundamental look at energy reserves for the planet', IEA/SHC Task Force 36, SOLAR UPDATE, **2009**.

[13] 'Key World Energy Statistics 2020', IEA, Paris, **2020**.

[14] P. Sreevani, *AIP Conf. Proc.* **2018**, 1992, 040007, DOI: 10.1063/1.5047972.

[15] G. Feulner, *Proc. Natl. Acad. Sci.* **2017**, 114, 11333, DOI: 10.1073/pnas.1712062114.

[16] The Proton-Proton Chain: Astronomy 162: Stars, Galaxies, and Cosmology., <https://web.archive.org/web/20160620155744/http://csep10.phys.utk.edu/astr162/lect/energy/ppchain.html>, accessed July 20, **2021**.

[17] S. M. Hanasoge, T. L. Duvall, K. R. Sreenivasan, *Proc. Natl. Acad. Sci.* **2012**, 109, 11928, DOI: 10.1073/pnas.1206570109.

[18] Reference Air Mass 1.5 Spectra, <https://www.nrel.gov/grid/solar-resource/spectra-am1.5.html>, accessed July 28, **2021**.

[19] Total Surface Area Required to Fuel the World With Solar, <https://landartgenerator.org/blagi/archives/127>, accessed July 26, **2021**.

[20] V. L. Martins, H. R. Neves, I. E. Monje, M. M. Leite, P. F. M. D. Oliveira, R. M. Antoniassi, S. Chauque, W. G. Morais, E. C. Melo, T. T. Obana, B. L. Souza, R. M. Torresi, *An. Acad. Bras. Ciênc.* **2020**, 92, DOI: 10.1590/0001-3765202020200796.

[21] K. N. Nwaigwe, P. Mutabilwa, E. Dintwa, *Mater. Sci. Energy Technol.* **2019**, 2, 629, DOI: 10.1016/j.mset.2019.07.002.

[22] O. Gröger, H. A. Gasteiger, J.-P. Suchsland, *J. Electrochem. Soc.* **2015**, 162, A2605, DOI: 10.1149/2.0211514jes.

[23] Z. P. Cano, D. Banham, S. Ye, A. Hintennach, J. Lu, M. Fowler, Z. Chen, *Nat. Energy* **2018**, 3, 279, DOI: 10.1038/s41560-018-0108-1.

[24] A. Z. AL Shaqsi, K. Sopian, A. Al-Hinai, *Energy Rep.* **2020**, 6, 288, DOI: 10.1016/j.egyr.2020.07.028.

[25] J. He, C. Janáky, *ACS Energy Lett.* **2020**, 5, 1996, DOI: 10.1021/acsenergylett.0c00645.

[26] S. O. Alsayegh, R. Varjian, Y. Alsalik, K. Katsiev, T. T. Isimjan, H. Idriss, *ACS Energy Lett.* **2020**, 5, 540, DOI: 10.1021/acsenergylett.9b02455.

[27] S. Esiner, J. Wang, R. A. J. Janssen, *Cell Rep. Phys. Sci.* **2020**, 1, 100058, DOI: 10.1016/j.xcrp.2020.100058.

-
- [28] T. Kunene, L. Xiong, J. Rosenthal, *Proc. Natl. Acad. Sci.* **2019**, *116*, 9693, DOI: 10.1073/pnas.1904856116.
- [29] Thermodynamic Properties of Selected Substances, <http://hyperphysics.phy-astr.gsu.edu/hbase/Tables/therprop.html#c1>, accessed July 28, **2021**.
- [30] H. H. G. Jellinek, H. Kachi, *Int. J. Hydrog. Energy* **1984**, *9*, 677, DOI: 10.1016/0360-3199(84)90265-9.
- [31] DLR scientists achieve solar hydrogen production in a 100-kilowatt pilot plant, https://www.dlr.de/content/en/downloads/news-archive/2008/20081125_dlr-scientists-achieve-solar-hydrogen-production-in-a-100-kilowatt-pilot-plant_14380.pdf?__blob=publicationFile&v=13.
- [32] S. Koumi Ngoh, D. Njomo, *Renew. Sustain. Energy Rev.* **2012**, *16*, 6782, DOI: 10.1016/j.rser.2012.07.027.
- [33] N. A. Kelly, T. L. Gibson, D. B. Ouwerkerk, *Int. J. Hydrog. Energy* **2008**, *33*, 2747, DOI: 10.1016/j.ijhydene.2008.03.036.
- [34] J. H. Kim, D. Hansora, P. Sharma, J.-W. Jang, J. S. Lee, *Chem. Soc. Rev.* **2019**, *48*, 1908, DOI: 10.1039/C8CS00699G.
- [35] W. J. Chang, K.-H. Lee, H. Ha, K. Jin, G. Kim, S.-T. Hwang, H. Lee, S.-W. Ahn, W. Yoon, H. Seo, J. S. Hong, Y. K. Go, J.-I. Ha, K. T. Nam, *ACS Omega* **2017**, *2*, 1009, DOI: 10.1021/acsomega.7b00012.
- [36] Q. Wang, K. Domen, *Chem. Rev.* **2020**, *120*, 919, DOI: 10.1021/acs.chemrev.9b00201.
- [37] A. Fujishima, K. Honda, *Nature* **1972**, *238*, 37, DOI: 10.1038/238037a0.
- [38] T. Watanabe, A. Fujishima, K. Honda, *Bull. Chem. Soc. Jpn.* **1976**, *49*, 355, DOI: 10.1246/bcsj.49.355.
- [39] I. E. Paulauskas, J. E. Katz, G. E. J. Jr, N. S. Lewis, L. A. Boatner, G. M. Brown, *J. Electrochem. Soc.* **2009**, *156*, B580, DOI: 10.1149/1.3089281.
- [40] L. Ji, M. D. McDaniel, S. Wang, A. B. Posadas, X. Li, H. Huang, J. C. Lee, A. A. Demkov, A. J. Bard, J. G. Ekerdt, E. T. Yu, *Nat. Nanotechnol.* **2015**, *10*, 84, DOI: 10.1038/nnano.2014.277.
- [41] W. Yang, J. H. Kim, O. S. Hutter, L. J. Phillips, J. Tan, J. Park, H. Lee, J. D. Major, J. S. Lee, J. Moon, *Nat. Commun.* **2020**, *11*, DOI: 10.1038/s41467-020-14704-3.
- [42] S. Akiyama, M. Nakabayashi, N. Shibata, T. Minegishi, Y. Asakura, M. Abdulla-Al-Mamun, T. Hisatomi, H. Nishiyama, M. Katayama, T. Yamada, K. Domen, *Small* **2016**, *12*, 5468, DOI: <https://doi.org/10.1002/sml.201601929>.
- [43] A. R. Bielinski, S. Lee, J. J. Brancho, S. L. Esarey, A. J. Gayle, E. Kazyak, K. Sun, B. M. Bartlett, N. P. Dasgupta, *Chem. Mater.* **2019**, *31*, 3221, DOI: 10.1021/acs.chemmater.9b00065.
-

-
- [44] Y. W. Chen, J. D. Prange, S. Dühnen, Y. Park, M. Gunji, C. E. D. Chidsey, P. C. McIntyre, *Nat. Mater.* **2011**, *10*, 539, DOI: 10.1038/nmat3047.
- [45] I. A. Cordova, Q. Peng, I. L. Ferrall, A. J. Rieth, P. G. Hoertz, J. T. Glass, *Nanoscale* **2015**, *7*, 8584, DOI: 10.1039/C4NR07377K.
- [46] M. F. Lichterman, A. I. Carim, M. T. McDowell, S. Hu, H. B. Gray, B. S. Brunschwig, N. S. Lewis, *Energy Environ. Sci.* **2014**, *7*, 3334, DOI: 10.1039/C4EE01914H.
- [47] H.-P. Jen, M.-H. Lin, L.-L. Li, H.-P. Wu, W.-K. Huang, P.-J. Cheng, E. W.-G. Diau, *ACS Appl. Mater. Interfaces* **2013**, *5*, 10098, DOI: 10.1021/am402687j.
- [48] A. Y. Al-Ahmad, F. Almayhi, M. F. Al-Mudhaffer, M. J. Griffith, W. Liu, S. Li, K. Sivunova, D. Elkington, N. A. Cooling, K. Feron, M. Shi, W. Belcher, H. Chen, P. Dastoor, T. R. Andersen, *Sustain. Energy Fuels* **2020**, *4*, 940, DOI: 10.1039/C9SE01149H.
- [49] K. Y. Mitra, A. Alalawe, S. Voigt, C. Boeffel, R. R. Baumann, *Micromachines* **2018**, *9*, DOI: 10.3390/mi9120642.
- [50] B. Fan, W. Zhong, L. Ying, D. Zhang, M. Li, Y. Lin, R. Xia, F. Liu, H.-L. Yip, N. Li, Y. Ma, C. J. Brabec, F. Huang, Y. Cao, *Nat. Commun.* **2019**, *10*, 4100, DOI: 10.1038/s41467-019-12132-6.
- [51] Y. Cui, H. Yao, L. Hong, T. Zhang, Y. Tang, B. Lin, K. Xian, B. Gao, C. An, P. Bi, W. Ma, J. Hou, *Natl. Sci. Rev.* **2020**, *7*, 1239, DOI: 10.1093/nsr/nwz200.
- [52] Y. Cui, H. Yao, J. Zhang, T. Zhang, Y. Wang, L. Hong, K. Xian, B. Xu, S. Zhang, J. Peng, Z. Wei, F. Gao, J. Hou, *Nat. Commun.* **2019**, *10*, 2515, DOI: 10.1038/s41467-019-10351-5.
- [53] Y. Lin, B. Adilbekova, Y. Firdaus, E. Yengel, H. Faber, M. Sajjad, X. Zheng, E. Yarali, A. Seïtkhan, O. M. Bakr, A. El-Labban, U. Schwingenschlöggl, V. Tung, I. McCulloch, F. Laquai, T. D. Anthopoulos, *Adv. Mater.* **2019**, *31*, 1902965, DOI: 10.1002/adma.201902965.
- [54] K. Kakiage, Y. Aoyama, T. Yano, K. Oya, J. Fujisawa, M. Hanaya, *Chem. Commun.* **2015**, *51*, 15894, DOI: 10.1039/C5CC06759F.
- [55] X. Elias, Q. Liu, C. Gimbert-Suriñach, R. Matheu, P. Mantilla-Perez, A. Martinez-Otero, X. Sala, J. Martorell, A. Llobet, *ACS Catal.* **2016**, *6*, 3310, DOI: 10.1021/acscatal.6b01036.
- [56] Y. Gao, V. M. L. Corre, A. Gaïtis, M. Neophytou, M. A. Hamid, K. Takanabe, P. M. Beaujuge, *Adv. Mater.* **2016**, *28*, 3366, DOI: <https://doi.org/10.1002/adma.201504633>.
- [57] S. Esiner, G. W. P. van Pruissen, M. M. Wienk, R. A. J. Janssen, *J. Mater. Chem. A* **2016**, *4*, 5107, DOI: 10.1039/C5TA10459A.
- [58] L. Yao, N. Guijarro, F. Boudoire, Y. Liu, A. Rahmanudin, R. A. Wells, A. Sekar, H.-H. Cho, J.-H. Yum, F. Le Formal, K. Sivula, *J. Am. Chem. Soc.* **2020**, *142*, 7795, DOI: 10.1021/jacs.0c00126.
-

-
- [59] F. Fumagalli, S. Bellani, M. Schreier, S. Leonardi, H. C. Rojas, A. Ghadirzadeh, G. Tullii, A. Savoini, G. Marra, L. Meda, M. Grätzel, G. Lanzani, M. T. Mayer, M. R. Antognazza, F. D. Fonzo, *J. Mater. Chem. A* **2016**, *4*, 2178, DOI: 10.1039/C5TA09330A.
- [60] L. Francàs, E. Burns, L. Steier, H. Cha, L. Solà-Hernández, X. Li, P. S. Tuladhar, R. Bofill, J. García-Antón, X. Sala, J. R. Durrant, *Chem. Commun.* **2018**, *54*, 5732, DOI: 10.1039/C8CC01736K.
- [61] A. Mezzetti, F. Fumagalli, A. Alfano, D. Iadicicco, M. R. Antognazza, F. di Fonzo, *Faraday Discuss.* **2017**, *198*, 433, DOI: 10.1039/c6fd00216a.
- [62] L. Steier, S. Bellani, H. C. Rojas, L. Pan, M. Laitinen, T. Sajavaara, F. D. Fonzo, M. Grätzel, M. R. Antognazza, M. T. Mayer, *Sustain. Energy Fuels* **2017**, *1*, 1915, DOI: 10.1039/C7SE00421D.
- [63] H. C. Rojas, S. Bellani, F. Fumagalli, G. Tullii, S. Leonardi, M. T. Mayer, M. Schreier, M. Grätzel, G. Lanzani, F. D. Fonzo, M. R. Antognazza, *Energy Environ. Sci.* **2016**, *9*, 3710, DOI: 10.1039/C6EE01655C.
- [64] B. M. Savoie, N. E. Jackson, L. X. Chen, T. J. Marks, M. A. Ratner, *Acc. Chem. Res.* **2014**, *47*, 3385, DOI: 10.1021/ar5000852.
- [65] A. Pallikkara, K. Ramakrishnan, *Int. J. Energy Res.* *n/a*, DOI: 10.1002/er.5941.
- [66] W. Cao, J. Xue, *Energy Environ. Sci.* **2014**, *7*, 2123, DOI: 10.1039/C4EE00260A.
- [67] I. M. Abdellah, A. El-Shafei, *RSC Adv.* **2020**, *10*, 27940, DOI: 10.1039/D0RA03916K.
- [68] P. Brogdon, H. Cheema, J. H. Delcamp, *ChemSusChem* **2018**, *11*, 86, DOI: <https://doi.org/10.1002/cssc.201701441>.
- [69] Y. Gao, X. Ding, J. Liu, L. Wang, Z. Lu, L. Li, L. Sun, *J. Am. Chem. Soc.* **2013**, *135*, 4219, DOI: 10.1021/ja400402d.
- [70] W. J. Youngblood, S.-H. A. Lee, Y. Kobayashi, E. A. Hernandez-Pagan, P. G. Hoertz, T. A. Moore, A. L. Moore, D. Gust, T. E. Mallouk, *J. Am. Chem. Soc.* **2009**, *131*, 926, DOI: 10.1021/ja809108y.
- [71] Y. Zhao, J. R. Swierk, J. D. Megiatto, B. Sherman, W. J. Youngblood, D. Qin, D. M. Lentz, A. L. Moore, T. A. Moore, D. Gust, T. E. Mallouk, *Proc. Natl. Acad. Sci.* **2012**, *109*, 15612, DOI: 10.1073/pnas.1118339109.
- [72] Zhang Linlin, Gao Yan, Ding Xin, Yu Ze, Sun Licheng, *ChemSusChem* **2014**, *7*, 2801, DOI: 10.1002/cssc.201402561.
- [73] L. Alibabaei, B. D. Sherman, M. R. Norris, M. K. Brennaman, T. J. Meyer, *Proc. Natl. Acad. Sci.* **2015**, *112*, 5899, DOI: 10.1073/pnas.1506111112.
-

-
- [74] K. E. Michaux, A. A. Gambardella, L. Alibabaei, D. L. Ashford, B. D. Sherman, R. A. Binstead, T. J. Meyer, R. W. Murray, *J. Phys. Chem. C* **2015**, *119*, 17023, DOI: 10.1021/acs.jpcc.5b05711.
- [75] P. Wei, B. Hu, L. Zhou, T. Su, Y. Na, *J. Energy Chem.* **2016**, *25*, 345, DOI: 10.1016/j.jechem.2016.03.020.
- [76] G. Leem, B. D. Sherman, A. J. Burnett, Z. A. Morseth, K.-R. Wee, J. M. Papanikolas, T. J. Meyer, K. S. Schanze, *ACS Energy Lett.* **2016**, *1*, 339, DOI: 10.1021/acsenergylett.6b00171.
- [77] G. F. Moore, J. D. Blakemore, R. L. Milot, J. F. Hull, H. Song, L. Cai, C. A. Schmuttenmaer, R. H. Crabtree, G. W. Brudvig, *Energy Environ. Sci.* **2011**, *4*, 2389, DOI: 10.1039/C1EE01037A.
- [78] J. R. Swierk, D. D. Méndez-Hernández, N. S. McCool, P. Liddell, Y. Terazono, I. Pakk, J. Tomlin, N. V. Oster, T. A. Moore, A. L. Moore, D. Gust, T. E. Mallouk, *Proc. Natl. Acad. Sci.* **2015**, *112*, 1681, DOI: 10.1073/pnas.1414901112.
- [79] M. Yamamoto, Y. Nishizawa, P. Chábera, F. Li, T. Pascher, V. Sundström, L. Sun, H. Imahori, *Chem. Commun.* **2016**, *52*, 13702, DOI: 10.1039/C6CC07877J.
- [80] A. Nayak, R. R. Knauf, K. Hanson, L. Alibabaei, J. J. Concepcion, D. L. Ashford, J. L. Dempsey, T. J. Meyer, *Chem. Sci.* **2014**, *5*, 3115, DOI: 10.1039/C4SC00875H.
- [81] A. Nayak, S. Roy, B. D. Sherman, L. Alibabaei, A. M. Lapides, M. K. Brennaman, K.-R. Wee, T. J. Meyer, *ACS Appl. Mater. Interfaces* **2016**, *8*, 3853, DOI: 10.1021/acsami.5b10587.
- [82] F. Ronconi, Z. Syrgiannis, A. Bonasera, M. Prato, R. Argazzi, S. Caramori, V. Cristino, C. A. Bignozzi, *J. Am. Chem. Soc.* **2015**, *137*, 4630, DOI: 10.1021/jacs.5b01519.
- [83] R. J. Lindquist, B. T. Phelan, A. Reynal, E. A. Margulies, L. E. Shoer, J. R. Durrant, M. R. Wasielewski, *J. Mater. Chem. A* **2016**, *4*, 2880, DOI: 10.1039/C5TA05790F.
- [84] F. Li, K. Fan, B. Xu, E. Gabrielsson, Q. Daniel, L. Li, L. Sun, *J. Am. Chem. Soc.* **2015**, *137*, 9153, DOI: 10.1021/jacs.5b04856.
- [85] K.-R. Wee, B. D. Sherman, M. K. Brennaman, M. V. Sheridan, A. Nayak, L. Alibabaei, T. J. Meyer, *J. Mater. Chem. A* **2016**, *4*, 2969, DOI: 10.1039/C5TA06678F.
- [86] P. K. Poddutoori, J. M. Thomsen, R. L. Milot, S. W. Sheehan, C. F. A. Negre, V. K. R. Garapati, C. A. Schmuttenmaer, V. S. Batista, G. W. Brudvig, A. van der Est, *J. Mater. Chem. A* **2015**, *3*, 3868, DOI: 10.1039/C4TA07018F.
- [87] R. J. Kamire, K. L. Materna, W. L. Hoffeditz, B. T. Phelan, J. M. Thomsen, O. K. Farha, J. T. Hupp, G. W. Brudvig, M. R. Wasielewski, *J. Phys. Chem. C* **2017**, *121*, 3752, DOI: 10.1021/acs.jpcc.6b11672.
- [88] J. T. Kirner, R. G. Finke, *ACS Appl. Mater. Interfaces* **2017**, *9*, 27625, DOI: 10.1021/acsami.7b05874.
-

-
- [89] D. L. Ashford, B. D. Sherman, R. A. Binstead, J. L. Templeton, T. J. Meyer, *Angew. Chem. Int. Ed.* **2015**, *54*, 4778, DOI: <https://doi.org/10.1002/anie.201410944>.
- [90] M. Yamamoto, L. Wang, F. Li, T. Fukushima, K. Tanaka, L. Sun, H. Imahori, *Chem. Sci.* **2016**, *7*, 1430, DOI: 10.1039/C5SC03669K.
- [91] G. A. Volpato, M. Marasi, T. Gobbato, F. Valentini, F. Sabuzi, V. Gagliardi, A. Bonetto, A. Marcomini, S. Berardi, V. Conte, M. Bonchio, S. Caramori, P. Galloni, A. Sartorel, *Chem. Commun.* **2020**, *56*, 2248, DOI: 10.1039/C9CC09805D.
- [92] H.-J. Son, C. Prasittichai, J. E. Mondloch, L. Luo, J. Wu, D. W. Kim, O. K. Farha, J. T. Hupp, *J. Am. Chem. Soc.* **2013**, *135*, 11529, DOI: 10.1021/ja406538a.
- [93] C. L. Gray, P. Xu, A. J. Rothenberger, S. J. Koehler, E. Elacqua, B. H. Milosavljevic, T. E. Mallouk, *J. Phys. Chem. C* **2020**, *124*, 3542, DOI: 10.1021/acs.jpcc.0c00493.
- [94] N. F. M. Sharif, M. Z. A. A. Kadir, S. Shafie, S. A. Rashid, W. Z. Wan Hasan, S. Shaban, *Results Phys.* **2019**, *13*, 102171, DOI: 10.1016/j.rinp.2019.102171.
- [95] S. A. Haque, E. Palomares, B. M. Cho, A. N. M. Green, N. Hirata, D. R. Klug, J. R. Durrant, *J. Am. Chem. Soc.* **2005**, *127*, 3456, DOI: 10.1021/ja0460357.
- [96] E. Palomares, J. N. Clifford, S. A. Haque, T. Lutz, J. R. Durrant, *Chem. Commun.* **2002**, 1464, DOI: 10.1039/B202515A.
- [97] S. Saleh Ardestani, R. Ajeian, M. Nakhaee Badrabadi, M. Tavakkoli, *Sol. Energy Mater. Sol. Cells* **2013**, *111*, 107, DOI: 10.1016/j.solmat.2012.12.039.
- [98] J. Lee, Y. K. Jung, D. Y. Lee, J.-W. Jang, S. Cho, S. Son, J. Jeong, S. H. Park, *Synth. Met.* **2015**, *199*, 408, DOI: 10.1016/j.synthmet.2014.12.013.
- [99] K. H. Lee, P. E. Schwenn, A. R. G. Smith, H. Cavaye, P. E. Shaw, M. James, K. B. Krueger, I. R. Gentle, P. Meredith, P. L. Burn, *Adv. Mater.* **2011**, *23*, 766, DOI: <https://doi.org/10.1002/adma.201003545>.
- [100] S. Dong, K. Zhang, B. Xie, J. Xiao, H.-L. Yip, H. Yan, F. Huang, Y. Cao, *Adv. Energy Mater.* **2019**, *9*, 1802832, DOI: <https://doi.org/10.1002/aenm.201802832>.
- [101] D. A. Vithanage, A. Devižis, V. Abramavičius, Y. Infahsaeng, D. Abramavičius, R. C. I. MacKenzie, P. E. Keivanidis, A. Yartsev, D. Hertel, J. Nelson, V. Sundström, V. Gulbinas, *Nat. Commun.* **2013**, *4*, 2334, DOI: 10.1038/ncomms3334.
- [102] R. Zhou, Z. Jiang, C. Yang, J. Yu, J. Feng, M. A. Adil, D. Deng, W. Zou, J. Zhang, K. Lu, W. Ma, F. Gao, Z. Wei, *Nat. Commun.* **2019**, *10*, 5393, DOI: 10.1038/s41467-019-13292-1.
- [103] M. C. Heiber, A. A. Herzing, L. J. Richter, D. M. DeLongchamp, *J. Mater. Chem. C* **2020**, *8*, 15339, DOI: 10.1039/D0TC03087B.
- [104] A. J. Mozer, N. S. Sariciftci, L. Lutsen, D. Vanderzande, R. Österbacka, M. Westerling, G. Juška, *Appl. Phys. Lett.* **2005**, *86*, 112104, DOI: 10.1063/1.1882753.
-

-
- [105] T. Abe, K. Nagai, S. Kabutomori, M. Kaneko, A. Tajiri, T. Norimatsu, *Angew. Chem. Int. Ed.* **2006**, *45*, 2778, DOI: 10.1002/anie.200504454.
- [106] T. Abe, K. Nagai, T. Ogiwara, S. Ogasawara, M. Kaneko, A. Tajiri, T. Norimatsu, *J. Electroanal. Chem.* **2006**, *587*, 127, DOI: 10.1016/j.jelechem.2005.11.001.
- [107] J. Chen, P. Wagner, L. Tong, G. G. Wallace, D. L. Officer, G. F. Swiegers, *Angew. Chem. Int. Ed.* **2012**, *51*, 1907, DOI: 10.1002/anie.201107355.
- [108] J. Chen, P. Wagner, L. Tong, D. Boskovic, W. Zhang, D. Officer, G. G. Wallace, G. F. Swiegers, *Chem. Sci.* **2013**, *4*, 2797, DOI: 10.1039/C3SC50812A.
- [109] G. Liu, C. Chen, H. Ji, W. Ma, J. Zhao, *Sci. China Chem.* **2012**, *55*, 1953, DOI: 10.1007/s11426-011-4469-6.
- [110] J. T. Kirner, J. J. Stracke, B. A. Gregg, R. G. Finke, *ACS Appl. Mater. Interfaces* **2014**, *6*, 13367, DOI: 10.1021/am405598w.
- [111] P. Borno, M. S. Prévot, X. Yu, N. Guijarro, K. Sivula, *J. Am. Chem. Soc.* **2015**, *137*, 15338, DOI: 10.1021/jacs.5b05724.
- [112] M. Alsultan, S. Balakrishnan, J. Choi, R. Jalili, P. Tiwari, P. Wagner, G. F. Swiegers, *ACS Appl. Energy Mater.* **2018**, *1*, 4235, DOI: 10.1021/acsaem.8b00728.
- [113] S.-Y. Park, M. Kim, J. Jung, J. Heo, E. M. Hong, S. M. Choi, J.-Y. Lee, S. Cho, K. Hong, D. C. Lim, *J. Power Sources* **2017**, *341*, 411, DOI: 10.1016/j.jpowsour.2016.12.017.
- [114] L. Yao, Y. Liu, H.-H. Cho, M. Xia, A. Sekar, B. Primera Darwich, R. A. Wells, J.-H. Yum, D. Ren, M. Grätzel, N. Guijarro, K. Sivula, *Energy Environ. Sci.* **2021**, DOI: 10.1039/D1EE00152C, DOI: 10.1039/D1EE00152C.
- [115] H.-H. Cho, L. Yao, J.-H. Yum, Y. Liu, F. Boudoire, R. A. Wells, N. Guijarro, A. Sekar, K. Sivula, *Nat. Catal.* **2021**, *4*, 431, DOI: 10.1038/s41929-021-00617-x.
- [116] J. M. Yu, J. Lee, Y. S. Kim, J. Song, J. Oh, S. M. Lee, M. Jeong, Y. Kim, J. H. Kwak, S. Cho, C. Yang, J.-W. Jang, *Nat. Commun.* **2020**, *11*, 5509, DOI: 10.1038/s41467-020-19329-0.
- [117] C. Dai, X. Gong, X. Zhu, C. Xue, B. Liu, *Mater. Chem. Front.* **2018**, *2*, 2021, DOI: 10.1039/C8QM00275D.
- [118] T. Abe, H. Ichinohe, S. Kakuta, K. Nagai, *Jpn. J. Appl. Phys.* **2010**, *49*, 015101, DOI: 10.1143/JJAP.49.015101.
- [119] X. Fan, T. Wang, B. Gao, H. Gong, H. Xue, H. Guo, L. Song, W. Xia, X. Huang, J. He, *Langmuir* **2016**, *32*, 13322, DOI: 10.1021/acs.langmuir.6b03107.
- [120] Y. Fang, X. Li, X. Wang, *ChemSusChem* **2019**, *12*, 2605, DOI: <https://doi.org/10.1002/cssc.201900291>.
-

-
- [121] Y. Fang, X. Li, Y. Wang, C. Giordano, X. Wang, *Appl. Catal. B Environ.* **2020**, 268, 118398, DOI: 10.1016/j.apcatb.2019.118398.
- [122] N. Karjule, J. Barrio, L. Xing, M. Volokh, M. Shalom, *Nano Lett.* **2020**, 20, 4618, DOI: 10.1021/acs.nanolett.0c01484.
- [123] J. Liu, H. Wang, Z. P. Chen, H. Moehwald, S. Fiechter, R. van de Krol, L. Wen, L. Jiang, M. Antonietti, *Adv. Mater.* **2015**, 27, 712, DOI: 10.1002/adma.201404543.
- [124] J. Qin, J. Barrio, G. Peng, J. Tzadikov, L. Abisdreis, M. Volokh, M. Shalom, *Nat. Commun.* **2020**, 11, 4701, DOI: 10.1038/s41467-020-18535-0.
- [125] Y. Yang, S. Wang, Y. Jiao, Z. Wang, M. Xiao, A. Du, Y. Li, J. Wang, L. Wang, *Adv. Funct. Mater.* **2018**, 28, 1805698, DOI: 10.1002/adfm.201805698.
- [126] L. Wang, D. Yan, D. W. Shaffer, X. Ye, B. H. Layne, J. J. Concepcion, M. Liu, C.-Y. Nam, *Chem. Mater.* **2018**, 30, 324, DOI: 10.1021/acs.chemmater.7b02889.

Chapter 2. Methods

A typical project involved the selection of semiconductor, its synthesis, separation, and purification, followed by physical and chemical characterization. The OSCs are then used in devices for PEC applications, and the device had to be fabricated and optimized as well. The various methods, techniques and instrumentation used in the entire process are explained in this chapter. The first section in this chapter deals with the general methods and instrumentation. The second section is a brief description of a typical organic synthesis reaction. Once the desired product is purified, it is characterized analytically, and the next sections explain the various characterization tools used. The first step is confirming the chemical nature of the product, and hence it is subject to NMR and mass spectroscopy. This is followed by optical, electronic, and electrochemical characterizations, all of which are explained briefly. From a device perspective, the experiments and methods are elaborated in the *PEC* subsection, and other tools to evaluate thin films visually and microscopically are also mentioned.

2.1. Overview

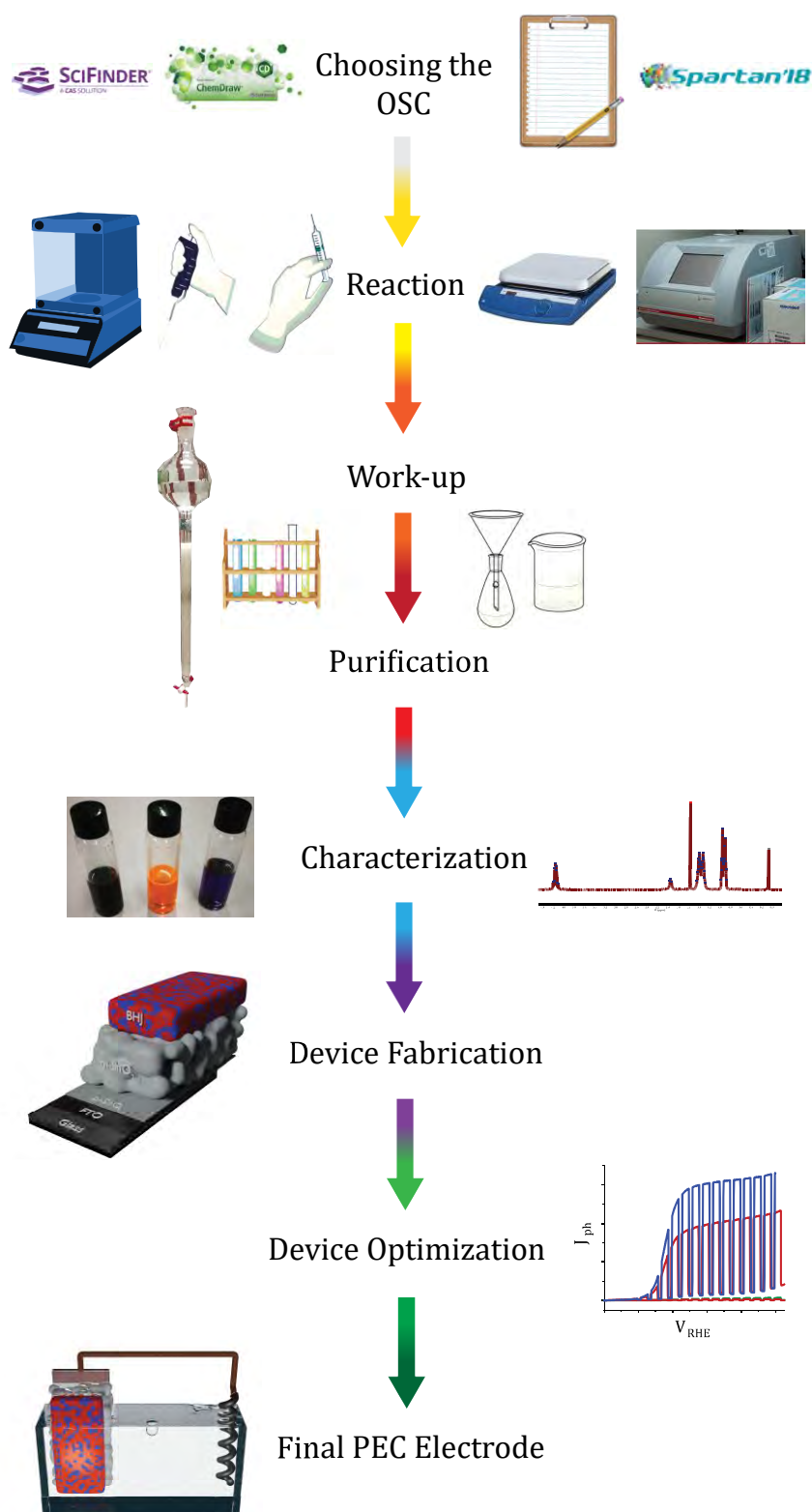


Figure 2.1.1: Stages involved in research – from synthesis to application.

Different stages of the process involved, from synthesis to the final device testing are illustrated in Figure 2.1.1 and elaborated in the following sections.

2.2. General Methods & Instrumentation

2.2.1. Synthetic methods

All reagents were of commercial reagent grade (*Sigma-Aldrich*, *Acros*, *TCI* & *Fluorochem*) & were used without further purification. Toluene, Chloroform, Tetrahydrofuran (*Fisher Chemical*, HPLC grade) & chlorobenzene (*Alfa Aesar*, HPLC grade) were purified & dried on a Pure Solv-MD Solvent Purification System (*Innovative Technology*, Amesbury, United States) apparatus. Dioxane, Ethanolamine and trifluoroacetic acid were purchased from *TCI*. Technical grade solvents for purification and workup were from *Thommen-Furler AG* and were used directly. Normal phase silica gel chromatography was performed with an *Acros Organic* silicon dioxide (pore size 60 Å, 40–50 µm technical grades).

2.2.2. Gel Permeation Chromatography

The polymers were analyzed using *Shimadzu Prominence LC-20AP* in CF at 40°C, armed with an analytic size exclusion PSS SDV linear M column (8mm x 250 mm, 40°C, CF, mobile phase 1 mL/min) with the UV-Vis detectors at 371 and 462 nm. For the reference calibration, commercially available fluorophore-tagged polystyrene was used.

2.2.3. Nuclear Magnetic Resonance characterization

The ^1H & ^{13}C NMR spectra were recorded at room temperature using per-deuterated solvents, usually CDCl_3 , as internal standards on a 400 MHz NMR Bruker AVANCE III-400 spectrometer (Bruker, Rheinstetten, Germany) unless explicitly mentioned. For heavier molecules and polymers, to get spectra with higher resolutions, a 600 MHz NMR Bruker AVANCEIIIHD-600 spectrometer (Bruker, Rheinstetten, Germany) and 800 MHz NMR Bruker AVANCEII-800 spectrometer (Bruker, Rheinstetten, Germany) were used, in which samples could be heated, hence here TCE-d₂ (CD_2Cl_4) was used as a solvent and spectra measured at 60°C. Chemical shifts are given in parts per million (ppm) referenced to residual ^1H or ^{13}C signals in CDCl_3 (^1H : 7.26, ^{13}C : 77.0).

2.2.4. Mass spectrum characterization

EI-MS spectrum was recorded on an EI/CI-1200L GC-MS (Varian) instrument & APPI-MS spectrum was recorded on an ESI/APCI LC-MS Autopurification System with a ZQ Mass detector (Waters, Milford, United States) instrument using a positive mode. However, these results are used at a purification stage and not reported in this thesis. Instead, the MALDI-TOF spectra are reported. The MALDI-TOF (see 2.3.1. Mass Spectroscopy for

details) AutoFlex speed can be operated in reflector and linear modes (up to 100 kDa for intact proteins and large molecules such as polymers), as well as TOF/TOF tandem mass spectrometry. Its SmartbeamTM-II 2 kHz laser and system electronics allow intensive and high throughput applications.

2.2.5. UV-Vis and Photoluminescence Spectroscopy

Shimadzu UV-3600 UV-Vis-NIR spectrophotometer for Absorbance and Transmission analysis is used. Armed with an integrating sphere, the film's reflection was also measured if needed. The photoluminescence spectra were measured using a *Fluorolog-3 Spectrofluorometer (Horiba)*, whose Xe lamp was aimed at an angle of 45° at the substrate. The excitation wavelength depended on the sample but varied from 450-600 nm.

2.2.6. (Photo)Electrochemical Studies

The electrochemical cyclic voltammetry data was recorded by a computer interfaced *SP-200* potentiostat (Biologic Technologies). This potentiostat also offered a vast variety of built-in options to execute other electrochemical studies, which were used for photo-electrochemical characterizations like linear sweep voltammetry, chronoamperometry, open circuit potential calculation, electrochemical impedance, chronopotentiometry etc. The techniques used, and components of the PEC cell are explained in 2.5.Photoelectrochemistry (PEC).

2.2.7. Miscellaneous Instrumentation

For Differential Scanning Calorimetry, the instrument used is a *PerkinElmer DSC 8000*, calibrated with the low melting Indium element.

The optical microscope images were captured by a NIKON Eclipse E600 microscope and processed digitally using a computer interface. These images shed light on the micrometer sized topography and overall roughness of the film formed. In certain cases, neat crystals of stacked or aggregated OSCs could be seen as well.

The surface topography/morphology of the blended OSCs were studied by Atomic Force Microscopy (AFM) using Asylum Research Cypher in alternate current tapping mode using the soft Pt-Ir Atomic Force AC240 tips, measuring the films in dark conditions.

2.2.8. Electrolyte Preparation

1 M stock solutions of H_3PO_4 , KH_2PO_4 , K_2HPO_4 and K_3PO_4 are prepared in water and stirred at room temperature. (Buffer) Solution of needed pH are prepared by mixing these solutions. For electrolytes with sacrificial reductant Na_2SO_3 , needed amount of sulfite salt is first weighed, so that the result is a 1.5 M sulfite solution, and then 1 M stock solutions of phosphate are added to it to get a (buffered) electrolyte with measured pH.

2.2.9. Substrate Preparation

Photoanodes

FTO/glass

TCO22-15 FTO/glass substrate was purchased from Solaronix. After cutting it in the required dimensions, the substrates are sonicated and cleaned with mild detergent solution and DI water for 15 minutes each. This is followed by sonication in acetone and IPA for 15 minutes each.

mSnO₂/FTO/glass (only for Chapter 3: Quaterylene Di-imide)

The SnO_2 precursor ($\text{SnCl}_4 \cdot 5\text{H}_2\text{O}$) is dissolved in terpeneol. Lauric acid was added as an additive and ethyl cellulose was a binder to increase viscosity of paste. This was doctor bladed onto the cleaned FTO/glass substrate mentioned previously and annealed at 450°C for 30 minutes. Average thickness of $1.5\mu\text{m}$ with average nanoparticle size of 18nm were obtained. The ETL and mesoporous structure can be visualized using SEM in Figure 2.2.1.

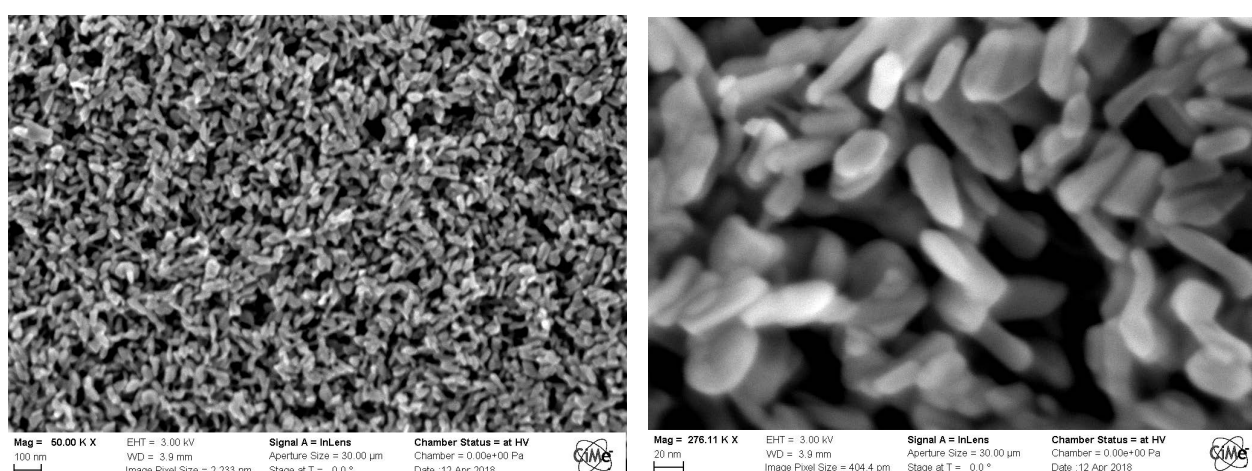


Figure 2.2.1: SEM images of doctor bladed mesoporous SnO_2 nanoparticles on FTO/glass (size $\sim 18\text{nm}$) at different magnification levels.

OSC/FTO/glass (only for Chapter 3: Quaterylene Di-imide)

A solution of the required OSC was prepared in dioxane of concentration 2mg/10mL. This solution was then sprayed onto the substrate of choice for the needed quantity and heated to 90°C for 10 minutes to remove the solvent completely.

pSnO₂/FTO/glass (Chapter 4:Donors[†]-Chapter 7:Applications)

The SnO₂ precursor (SnCl₄.5H₂O) is dissolved in EtOH/IPrOH (50 mM). On plasma cleaned FTO/glass, this solution is spun-coat at 3000 rpm for 45 seconds and heated on a hotplate at 500 °C for 30 minutes and allowed to gradually cool to room temperature.

mSnO₂/pSnO₂/FTO/glass

A solution of SnO₂ paste bought from ShareChem Co., LTD (South Korea) with ethanol is prepared in a 1:2 (w/w) ratio and stirred at room temperature till completely dispersed into a thick colloidal suspension. Spin-coat this suspension on the cooled *pSnO₂/FTO/glass* at 1500 rpm for 45 s and heat the substrate at 80°C for a few minutes to evaporate the ethanol. To form *mSnO₂*, subject this substrate to a heating cycle illustrated in Figure 2.2.2. The modified ETL and mesoporous structure using the commercial paste can be visualized using SEM in Figure 2.2.3.

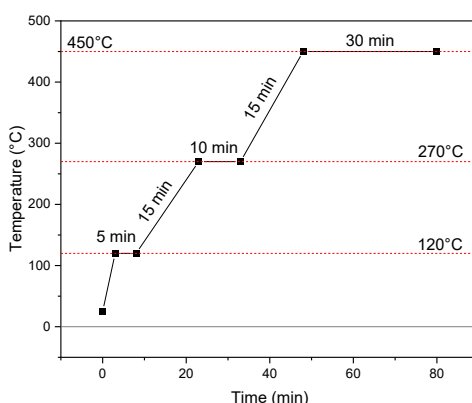


Figure 2.2.2: Annealing temperature profile for *mSnO₂*.

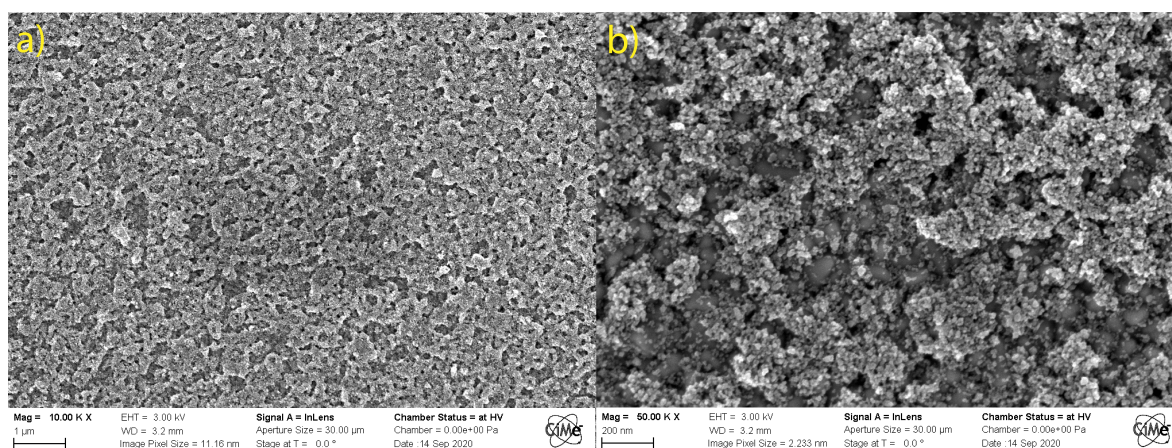


Figure 2.2.3: a) Mesoporous SnO₂ SEM images, b) zoomed in view.

SAM/mSnO₂/pSnO₂/FTO/glass

Plasma clean *mSnO₂/pSnO₂/FTO/glass* on cooling for 15 minutes and dip the substrate in an ethanolic solution of needed organic compound (1 mg·mL⁻¹) for 5 minutes. Rinse the substrate in acetone, ethanol and methanol to remove excess acid.

OSC/SAM/mSnO₂/pSnO₂/FTO/glass

For CB processed films:

Make a stock solution of the donor or acceptor or mixture in CB with a 20 mg·mL⁻¹ concentration. Let this stir overnight under argon in a glovebox at 90 °C. Prepare BHJ solution of needed ratio by mixing these solutions volumetrically and let it stir for a few hours on a hotplate as well. Spin-coat needed solution on *SAM/mSnO₂/pSnO₂/FTO/glass* at 800 rpm for 45 sec and anneal the substrate in argon on a hotplate if needed.

For CF processed films:

Make a stock solution of the donor or acceptor in CF with a 14 mg·mL⁻¹ concentration. Let this stir overnight under argon in a glovebox at 45 °C. Prepare BHJ solution of needed ratio by mixing these solutions volumetrically and let it stir for a few hours on a hotplate as well. Spin-coat needed solution on *SAM/mSnO₂/pSnO₂/FTO/glass* at 1000 rpm for 45 sec and anneal the substrate in argon on a hotplate if needed.

Catalysts

CrRuO_x and Li- doped IrO_x were synthesized according to previous literature^[7,8]. Organic catalysts like CoF₁₆Pc and Manganese porphyrins were also synthesized to evaluate the photoanodes. Concentrations of the catalyst drop cast or sprayed were 1-2 mg·mL⁻¹ in isopropyl alcohol.

Photocathodes

An 8 mg·mL⁻¹ stock solution of BHJ (D:A, 1:1) is prepared in chloroform and spun-coat at 1000 rpm on plasma cleaned FTO over which 2PAC-z (1 mg·mL⁻¹, 3000 rpm, 60 s, 100°C anneal for 10 minutes) was overlaid. The photocathode was annealed at 120°C for 10 minutes after which 1 mL of RuO_x (2 mg·mL⁻¹ in isopropyl alcohol) was sprayed at 80°C.

2.3. OSC Characterization

2.3.1. Mass Spectroscopy

Matrix assisted laser desorption/ionization coupled with a time-of-flight detector (MALDI-TOF) is a very soft method for detecting the molecular weight of the OSCs and precursors synthesized. This technique works best for molecules having relatively high molecular weights (>500 Da).

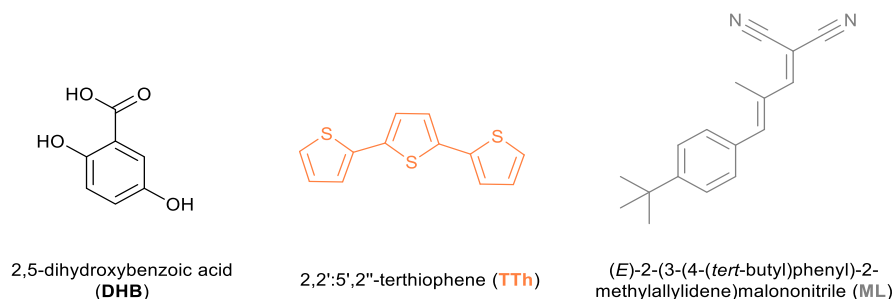


Figure 2.3.1: Matrices used in MALDI-TOF analyses.

Typically, commercially available matrices are used (structures in Figure 2.3.1). DHB matrix led to high signal-to-noise ratios and sharp peaks, but significantly low signal intensity, while TTh and ML had higher signal intensities for the OSCs measured. A dilute solution (0.25 mg. mL^{-1}) of the matrix in THF is used as the stock solution. In a few mLs of this solution, a small quantity ($<0.25 \text{ mg}$) of the organic product is dissolved. $100\text{-}200 \text{ }\mu\text{L}$ of this solution is drop cast onto the piranha solution cleaned stainless steel substrate holder plates and inserted into the machine for analysis.

Among the modes for detection, the reflective mode was often used as it led to lower noise with cleaner mass spectra detected, while the linear mode gave higher intensities without more noise. In the reflective mode, the ionized species had to travel twice the distance to the detector compared to the linear mode.

2.3.2. Cyclic Voltammetry

Cyclic voltammetry (CV) is an electrochemical experiment wherein the potential of the working electrode is ramped up linearly with time till a maximum (V_{max}) and is linearly reduced till a minimum (V_{min}) value. This process can be repeated multiple times (Figure 2.3.2a shows the chronal evolution of applied potential), and hence the name^[1].

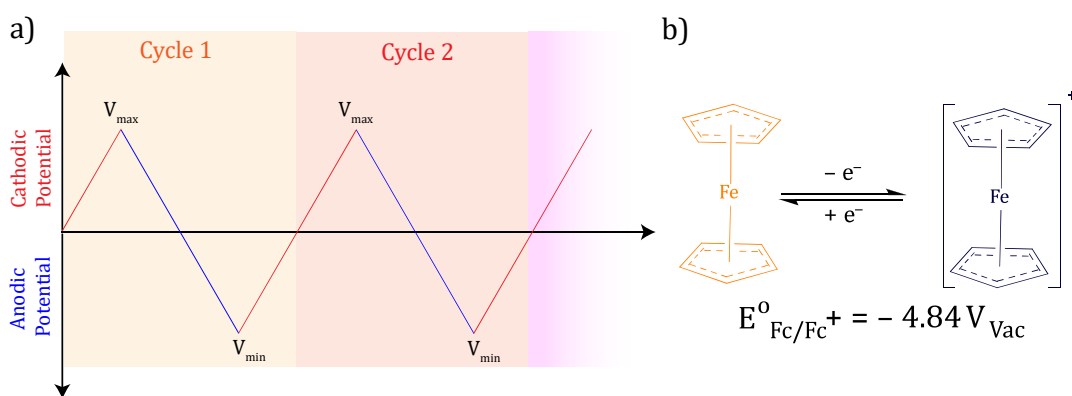


Figure 2.3.2: a) Potentiodynamic evolution of working electrode in CV, b) Ferrocene/Ferricinium reference redox reaction.

The two modes of measuring electrochemical energy levels of OSCs are either to dissolve them in an organic solvent or deposit their thin films onto a clean working electrode. When the applied potential allows for electronic transfer between molecular orbital levels of the OSC and platinum (working electrode), an oxidative or reductive current response is generated and measured. When the electronic transfer occurs from the working electrode to the LUMO levels, a reductive current is observed, while the transfer from the HOMO of the OSC to the working electrode results in oxidative current. Electrochemical current onset versus applied potential is then measured as molecular orbital energy level. These energy level orientations are illustrated in Figure 2.3.3.

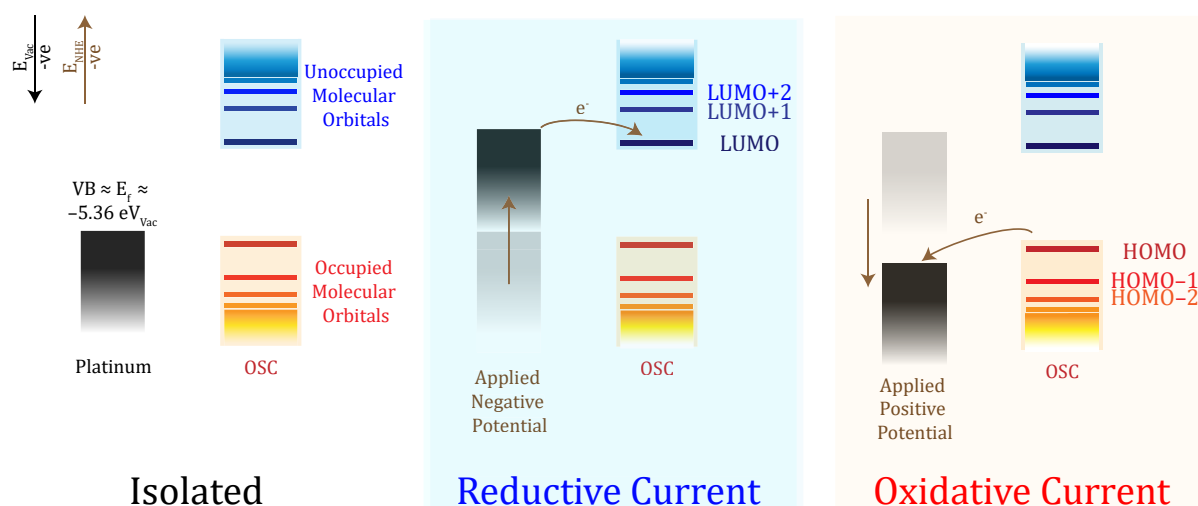


Figure 2.3.3: Energy level orientation at different applied potentials in CV.

The working components of a typical CV experiment involves 3 electrodes: a Platinum working electrode, a graphite/carbon rod counter electrode and Ag/Ag^+ reference electrode. The platinum working electrode is flame cleaned, and the OSC is drop cast on the film and dried. Usually, solvents with a high redox potential window of operation, like acetonitrile is chosen. Halogenated solvents like CH_2Cl_2 and CF could also

be used if the OSCs need to be dissolved in the electrolyte. Additionally, 0.1 M of organic salts like TBAPF₆ or TBAClO₄ are used to make the solvents conductive (Figure 2.3.4 shows the structures and an illustration of the 3-electrode setup).

While reversible electrochemical reactions exhibit both oxidative and reductive peaks on CV, OSCs tend to show irreversible reactions, and hence we observe only single peaks for either oxidation or reduction processes. Therefore, the onset of the irreversible peaks is considered for the sake of calculating the molecular energy levels.^[2]

Due to the sensitivity of the onset on the electrolyte, every CV measurement is calibrated with a (Ferrocene/Ferricenium) redox couple as the reference (redox reaction in Figure 2.3.2b)^[3], and the energy conversion equation for aqueous solutions used is:

$$E_{HOMO} = (-E_{ox.onset\ vs\ Fc/Fc^+} - 0.36 - 4.44) V_{Vac}$$

$$E_{LUMO} = (-E_{red.onset\ vs\ Fc/Fc^+} - 0.36 - 4.44) V_{Vac}$$

where E_i : Energy level of i orbital vs. vacuum energy level and $E_{j.onset\ vs\ Fc/Fc^+}$ is the potential “j”th onset vs. Fc/Fc⁺ redox energy potential.

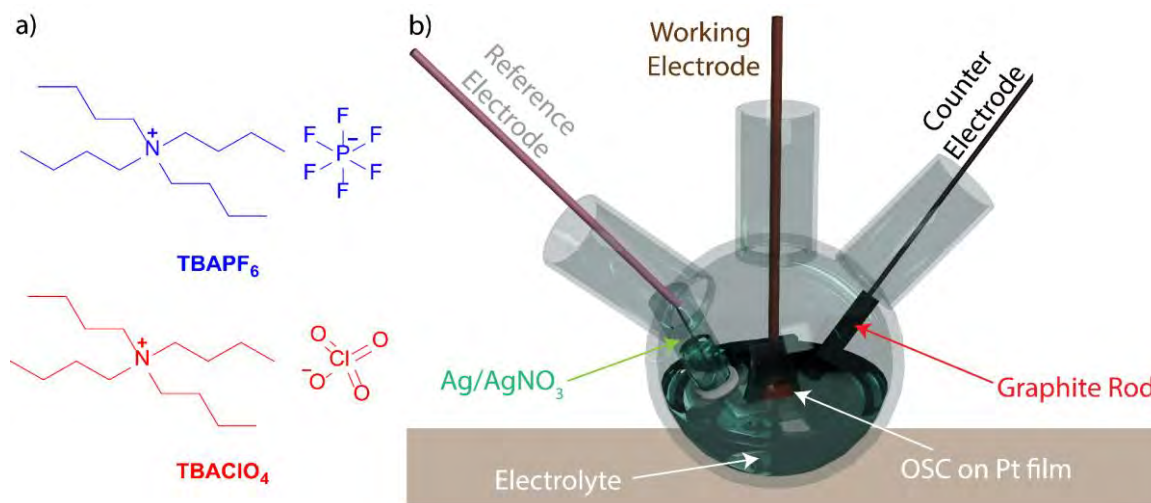


Figure 2.3.4: a) Electrolytic salts in CV, b) Scheme of CV experiment with electrodes & electrolyte.

2.3.3. Thin Film Transistors: Hole Mobility

Organic polymer and small molecule thin films show semiconducting properties, whose electron or hole mobilities can be measured. Towards this goal, the thin films need to be doped to increase their conductivity, and on doping with charges (electronic doping) when a positive or negative potential is applied, conductivity can be measured without changing the chemical properties of the OSCs.

Thin films of OSC were spun-coat on commercial pre-fabricated transistors, with multiple channel widths (Figure 2.3.5 shows the multiple layers in the prefabricated transistors).^[4] These bottom-gate-bottom-contact transistor substrates were purchased from *Fraunhofer Institute for Photonic Microsystems* and were composed of an n²⁺-doped silicon wafer as the bottom gate electrode, a 230 nm c-SiO₂ as dielectric layer, and a 30 nm Au layer as source and drain electrode. The channel lengths and width were 2.5 μm-20 μm and 10 mm, respectively.

Dilute (1 mg. mL⁻¹) solutions of neat polymers are prepared in CF and spun-coat under argon inside the glovebox on the transistors at 800 rpm for 45 s. If annealing was needed, samples were annealed under argon at 120°C for 10 minutes. When thin films are formed using concentrated solutions, shorting occurs, as higher Source-Drain potentials are needed to observe current flow. At certain gate voltages, the I-V curves showed saturated source-drain currents. This value was used to calculate the $\mu_{FET,h^+,sat}$, Hole Mobility. The formula used to calculate hole mobility from the saturated drain current is

$$\frac{2L}{I_{Drain,sat}C_{dielec}Width(V_{Gate-Source}-V_{Threshold})^2} = \mu_{FET,h^+,sat},$$

where,

$I_{Drain,sat}$: saturated source-drain current.

C_{dielec} : dielectric constant of c-SiO₂.

$Width$: channel width.

L : channel length.

$V_{Gate-Source}$: applied gate voltage.

$V_{Threshold}$: threshold voltage, above which current is observed.

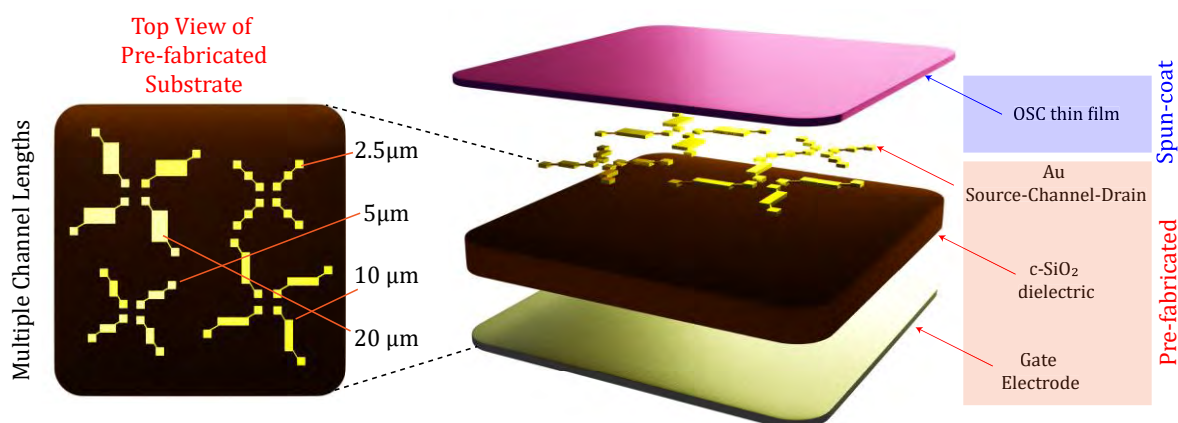


Figure 2.3.5: Layers in TFT analyzed for mobility calculations

2.3.4. Ultraviolet-Visible Absorption Spectroscopy

This spectroscopic technique measures the absorption or reflection of the radiation, as a function of the wavelength, in the full visible spectrum range, and part of Ultraviolet range.

The OSCs are conjugated semiconducting organic compounds, hence electrons present in their HOMO, on absorbing incoming photons, can be energetically promoted to the LUMO (transitions shown schematically in Figure 2.3.6). This statement is an extension of the molecular orbital theory, involving σ , σ^* , π , π^* and n orbital electrons, with possible transitions between $\sigma \rightarrow \sigma^*$, $n \rightarrow \sigma^*$, $\pi \rightarrow \pi^*$ and $n \rightarrow \pi^*$ orbitals.^[5] The difference in LUMO-HOMO energy level corresponds to the optical bandgap (E_g) of the OSC, which is one of its characteristic opto-electronic property.

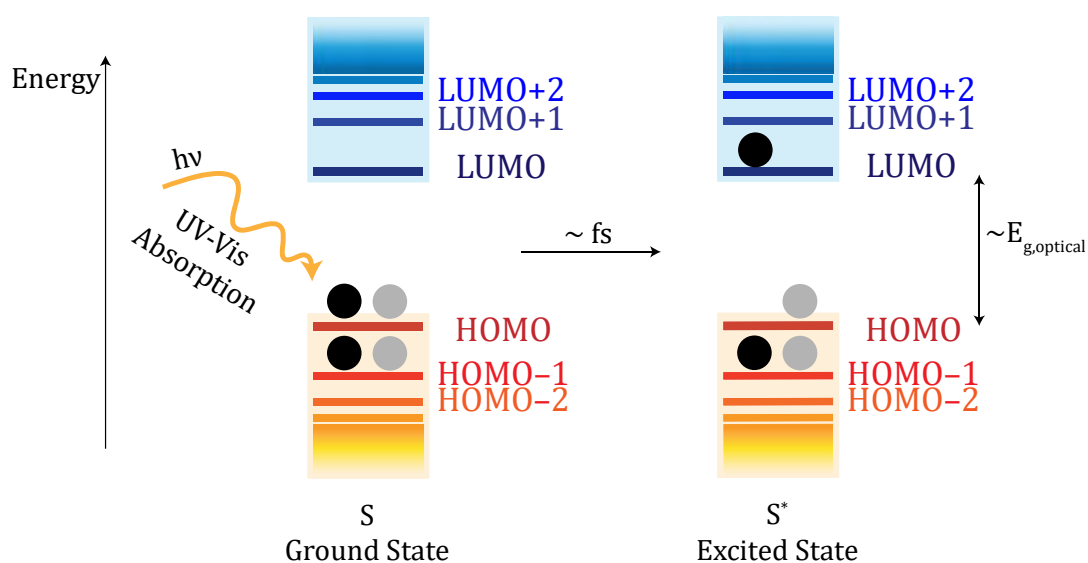


Figure 2.3.6: Electrons absorbing light in the UV-Vis range resulting in excited state formation.

For solution-based measurements, the OSCs are dissolved in needed organic solvents (usually CF or THF, in μM concentration) and subjected to illumination in the spectrometer. Higher concentrations lead to aggregations, saturation of the detector and deviation from assumptions of the physical parameters of the Beer-Lambert law elaborated below. For reference, usually blank/ neat solvents are first measured and calibrated as the “zero” value.

For Absorbance measurements of thin film solid state OSCs, which are usually for Incident Photon to Converted Electron (IPCE) and E_g calculations, the needed translucent substrate was first calibrated as the reference, onto which the thin film OSC was spun-coat, and the absorbance was measured.

The equations used for Absorbance (A_λ), Extinction Coefficient (ϵ_λ), Transmittance (T_λ) are:

$$T_\lambda = \frac{I_{transmitted}(= I_\lambda)}{I_{received}(= I_{\lambda,0})}$$

$$A_\lambda = -\log_{10}(T_\lambda)$$

$$A_\lambda = \epsilon_\lambda c l \text{ (Beer-Lambert Law)}$$

where c: concentration of the solution, l: optical length of the sample, $I_{transmitted}$ is the intensity of light transmitted by the sample and $I_{received}$ is the intensity of light received by the sample.

E_g is calculated for the OSC thin films from Absorbance, using the *Tauc* relation. Plotting the photonic energy ($h\nu$) as the abscissa (x-axis coordinates) and $(A * h\nu)^{1/2}$ as the ordinate (y-axis coordinates) of thin film OSCs, a linear region close to the onset of absorbance is observed, whose extrapolation onto the abscissa gives the optical bandgap. Here, ν : frequency of light, h : Planck’s constant. This optical bandgap closely matches the bandgap obtained from the extrapolation of the absorption onset from the solution state spectra.

2.3.5. Differential Scanning Calorimetry

In Differential Scanning Calorimetry (DSC), the difference in heat absorbed/released to increase/decrease the temperature of the sample is measured as a function of time or temperature, when the sample is subjected to a uniform, slow rate of heating or cooling ($10^\circ\text{C min}^{-1}$). A few mg (<2 mg) of OSC weighed on a microbalance is

loaded onto an aluminum pan and sealed with its lid using the sample encapsulation press. The sample and its reference (empty pan sealed with lid) are loaded onto the DSC and the heating and cooling regime is loaded. The first heating cycle is usually faster and shorter (up to 150°C) and is not considered as it releases residual solvents or water stuck to the sample. The second heating cycle is used.

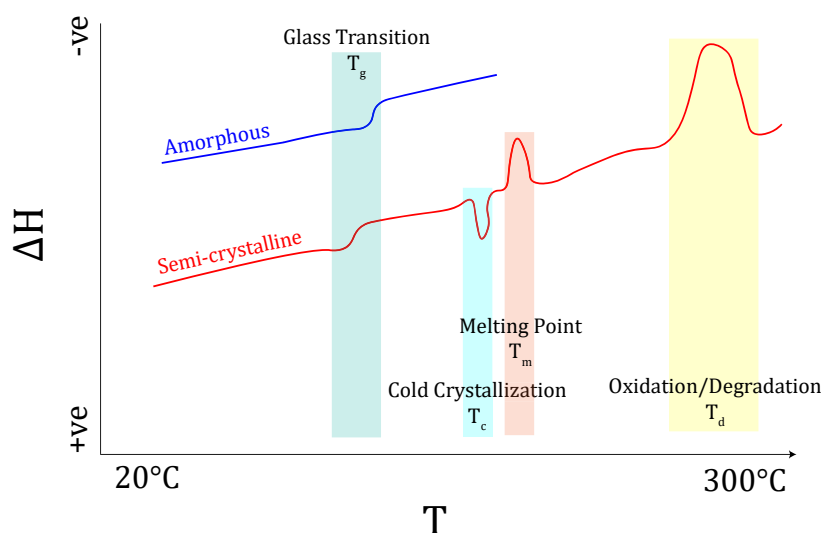


Figure 2.3.7: Typical heating curves for amorphous and semi-crystalline OSCs.

Figure 2.3.7 shows typical DSC curves. The glass transition temperature (T_g) is a second order phase transition observed in a few OSCs where the involved phases are still solids, but the higher energy state is based on a quenched disorder phase. The cold crystallization and melting points (T_c and T_m) involve latent heats and are observed reversible peaks on cooling as well. Above T_m , the OSC is in its liquid state, and at higher temperatures the OSC gets oxidized (T_d) and this is an irreversible change, which won't be seen in the cooling curve.

2.4. Thin Film: Binary Mixtures Characterization

2.4.1. Photoluminescence Spectroscopy

Photoluminescence (PL) is a physical phenomenon that occurs after absorption of light by the material. After photoexcitation, OSCs in the excited state lose their energy radiatively and emit light of a longer wavelength than their absorption; this effect is known as fluorescence.

In case of binary mixtures of two semiconductors which form a donor-acceptor BHJ, the fluorescence intensities do not add up cumulatively on absorbing light (PL phenomena shown in Figure 2.4.1). This is because the photogenerated charges transfer energy or electrons between the species (either by Förster or Dexter mechanisms),^[6,7] thereby forbidding the traditional fluorescence de-excitation, resulting in reduction of the fluorescence intensity. Consequently, the more a BHJ film shows quenching, the extent of charge separation is better.

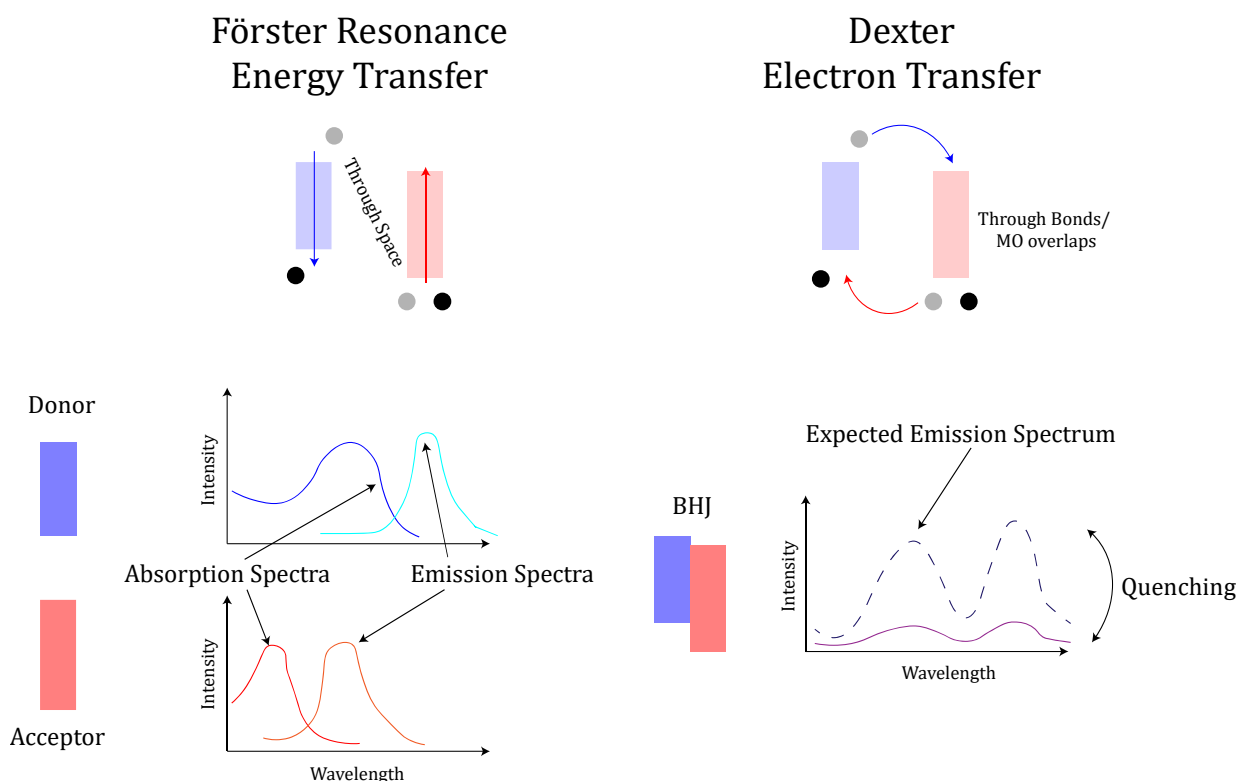


Figure 2.4.1: PL quenching in BHJs.

In this thesis, PL is used to analyze the extent of quenching in BHJs, and is supplementing the photoanode performance results on annealing. Well intermixed BHJ on excitation, have low PL intensities as the charges are extracted by complementary species, and the excited state eventually loses energy by other non-radiative means.

2.4.2. Atomic Force Microscopy

The surface topography/morphology of the blended OSCs were studied by Atomic Force Microscopy (AFM) using Asylum Research Cypher in alternate current tapping mode using the soft Pt-Ir Atomic Force AC240 tips, measuring the films in dark conditions.

With topography and phase images, the morphology, roughness factor and the domains or aggregates of OSCs can be observed in the sub-micrometer scale.

2.5. Photoelectrochemistry (PEC)

2.5.1. PEC instrumentation

A custom built “Cappuccino” cell, which is a 3-electrode setup (Figure 2.5.1 and Figure 2.5.2 illustrate the setup) with available transparent areas for front and back illumination (exposed area: 0.238-0.245 cm²). An Ag/AgCl electrode is used as a reference electrode ($E_{Ag/AgCl}^0 = 0.197 V_{NHE}$) and Pt wire or graphite rod is used as a counter electrode. In almost all the electrochemical experiments, the substrate was illuminated from the back, which ensures light is not attenuated through the electrolyte.

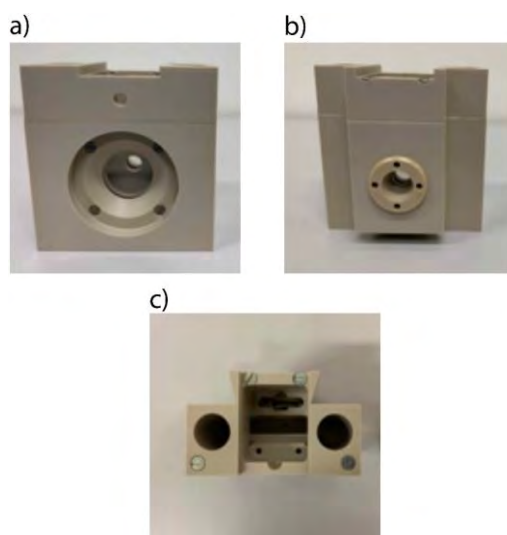


Figure 2.5.1: Photograph of the cappuccino cell used for PEC analysis, a) Front View, b) Back view, c) Top View.

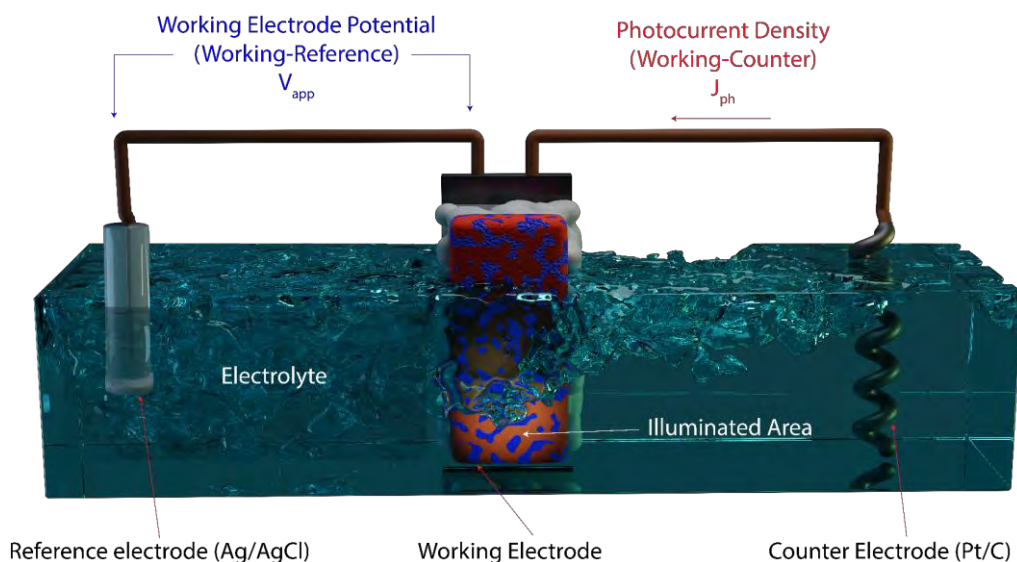


Figure 2.5.2: A typical PEC experiment setup for testing photoanodes.

The Xe lamp is switched on and stabilized over a period of 30 minutes. A fully loaded cell with the substrate, electrodes and electrolyte is then placed on the sample holder (scheme shown in Figure 2.5.3) and fixed at the needed position (Refer 2.5.2.Xenon Lamp Calibration). The required electrochemical studies are performed under light illumination with a chopper which regulates the on/off period of the light.

2.5.2. Xenon Lamp Calibration

The Solar simulator to evaluate device performance consists of a Xe arc lamp (*Newport 66921*, 450 W), optical focusing lens, filters, automatic chopper, and a substrate holder mounted on a rail, illustrated below in Figure 2.5.3.

The converging lens converts the near point source of light into parallel beams which passes through a *Schott KG3* grade filter (*Edmund Optics*) effectively only allowing the 300-900 nm illumination range to fall on the sample.

Substrate holder lies on a metallic rail, and the displacement between the lamp and the holder can be changed along its axis, corresponding to the required intensity or current reading on the photodiode. For point sources of light,

$$I_r \propto \frac{1}{r^2}$$

where r : the distance from the point source and I_r is the intensity.

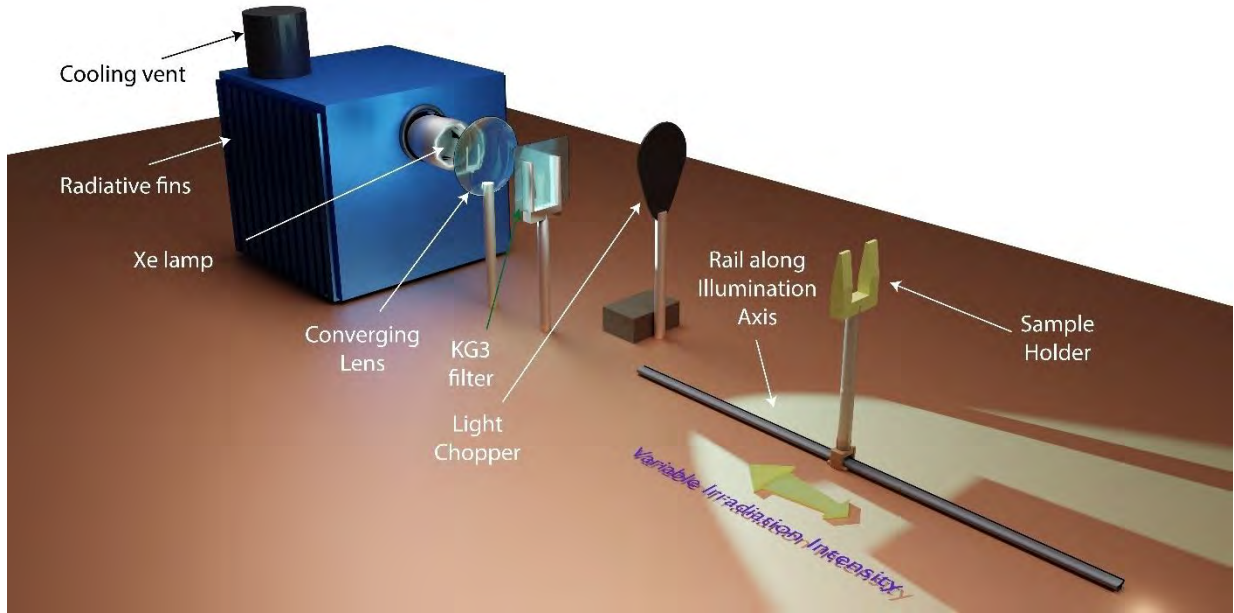


Figure 2.5.3: Scheme of PEC device testing area with solar simulator.

Photocurrent reading on the photodiode is indicative of the photon density, and by moving the sample holder towards or away from the source, a position where the lamp irradiation matches the AM1.5G in the wavelength range of the photoelectrode absorption is attained. When it comes to matching the lamp spectrum to the solar spectrum, the substrate holder is fixed where the Power of the spectra match, or the Photonic Density, as indicated by example spectra in Figure 2.5.4. This matching in simple terms corresponds to matching the area under the curves for solar irradiation with the Xe lamp (equations in Table 2.1). In all the experiments mentioned in this thesis, it is the photon density of the lamp that corresponds to AM1.5G.

Table 2.1: Formulae for matching spectra of Xe lamp with AM1.5G

Energy equivalence (between λ_1 and λ_2)	Photon density equivalence (between λ_1 and λ_2)
$\int_{\lambda_1}^{\lambda_2} \left(\frac{hc}{\lambda}\right) N_{photons}^{AM\ 1.5G}(\lambda) d\lambda = \int_{\lambda_1}^{\lambda_2} \left(\frac{hc}{\lambda}\right) N_{photons}^{lamp}(\lambda) d\lambda$	$\int_{\lambda_1}^{\lambda_2} N_{photons}^{AM\ 1.5G}(\lambda) d\lambda = \int_{\lambda_1}^{\lambda_2} N_{photons}^{lamp}(\lambda) d\lambda$

The normalized spectrum of the lamp was recorded by a spectrometer (*Ocean Optics USB2000+XR1-ES*) with a cosine corrector (*Ocean Optics CC-3-UV-S*) and the solar spectrum was obtained from a simple model of radiative transfer of sunshine through the atmosphere. A long pass filter (allows $>590\text{nm}$) is also used when needed.

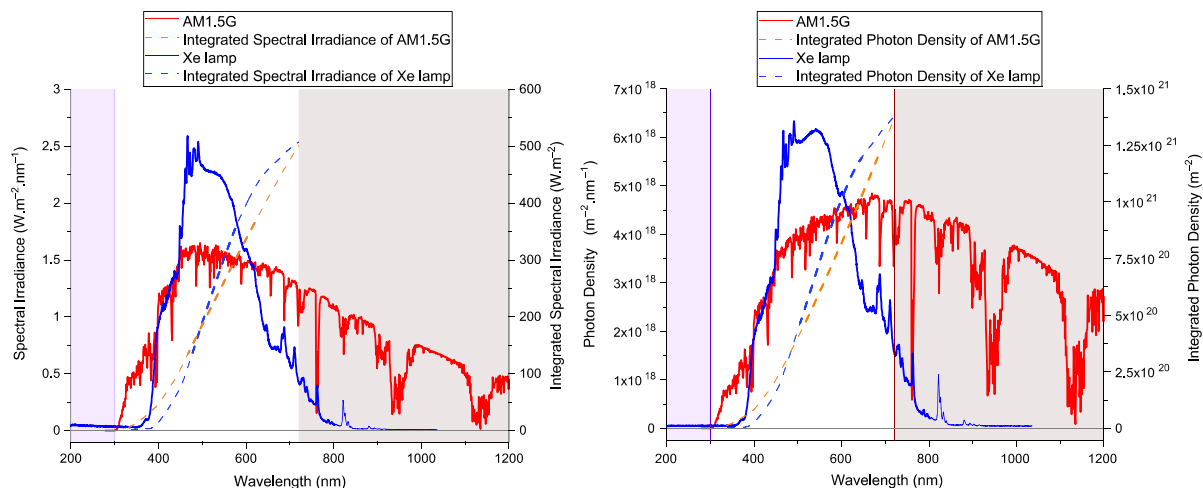


Figure 2.5.4: Matching the Xe lamp light source with AM1.5G by Photon Density (right) or Spectral Irradiance (left) in 300-720 nm range.

2.5.3. PEC experiments

Linear Sweep Voltammetry

In linear sweep voltammetry (LSV), the applied potential is swept linearly from an initial to a final potential, in a series of small staircase intervals. The sweep rate is kept to 5 mV.s^{-1} to avoid capacitive currents in all the experiments, which are usually indicative of excitons dissociated into a charge separated state at the metal oxide/OSC interface, instead of electron injection. If needed, the experiment is run under chopped light illumination, in which the behavior of the LSV curves contains information about limitations like mass transport deficiencies, etc. In general, after a certain positive applied potential, electron injection occurs from the OSCs/electron transport layer (ETL) to the conducting glass (fluorine doped tin oxide, or FTO) which is recorded as photocurrent. This value is normalized with respect to the area of illumination and is reported as photocurrent density or J_{ph} .

Chronoamperometry

Chronoamperometry (CA) is used for testing the stability of photoelectrodes, and how the J_{ph} evolves over time. A fixed potential is applied to the electrode, and under illumination, J_{ph} evolution is observed. With regular bubbling of argon in the electrolyte near the illumination area, mass transport limitations are avoided by forced convection transfers.

Figure 2.5.5 shows the control potential vs time curves for the two PEC experiments.

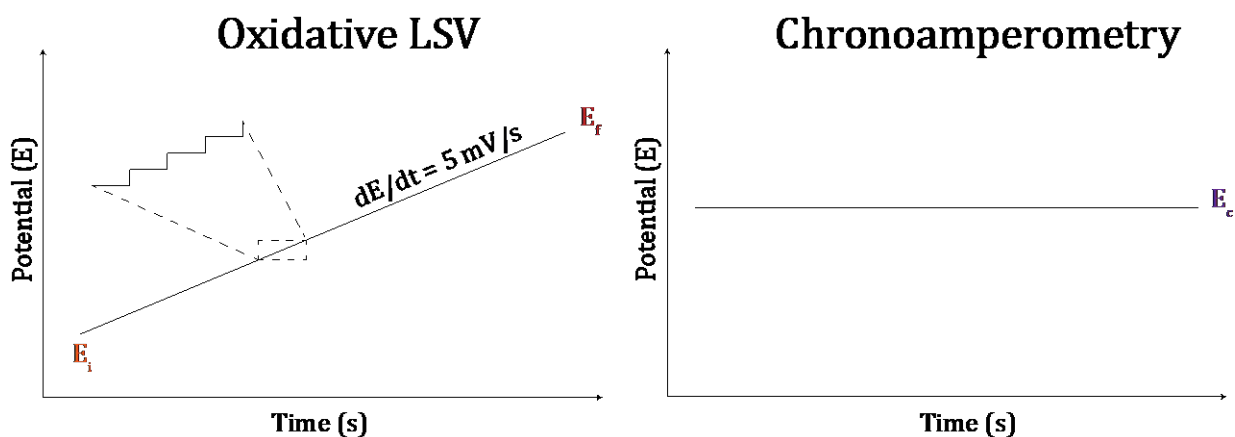


Figure 2.5.5: Applied potential vs time for different PEC experiments.

2.5.4. Incident Photon to Converted Electron (IPCE) studies

The IPCE (Internal Quantum Efficiency) experiments are carried out to study the electrochemical J_{ph} as a function of the wavelength of incident light. This helps to identify the contribution of different OSCs to the J_{ph} , and if normalized with the absorption spectrum, can represent the Absorbed Photons to Converted Electrons (External Quantum Efficiency), and can determine the overall efficiency of the photoabsorber. The hardware involved in this experiment, however, combines two separate parts: the potentiostat and the monochromator (Figure 2.5.6 shows the chroral evolution of observed J_{ph} generated as a function of wavelength of a photoanode from this thesis).

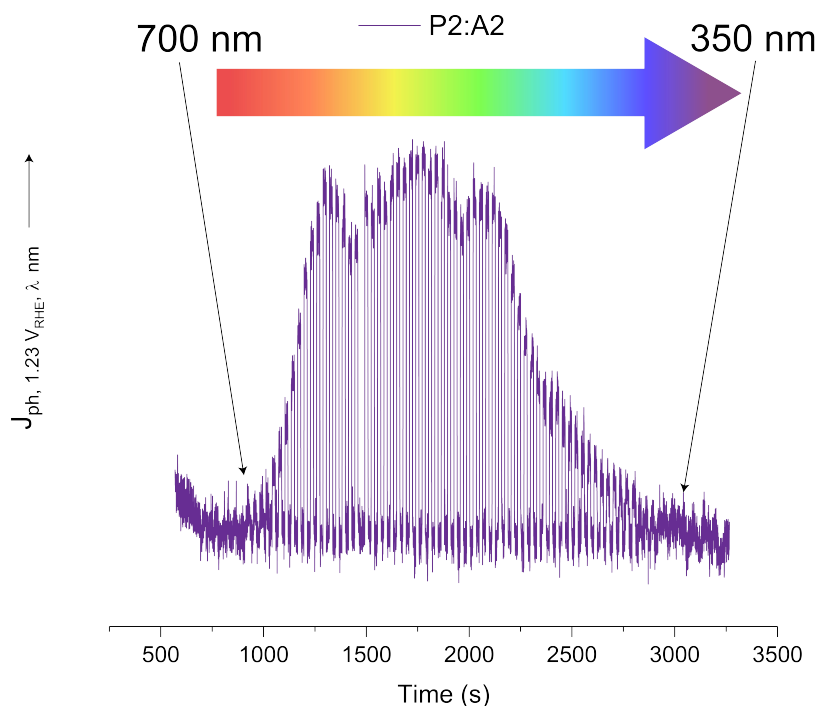


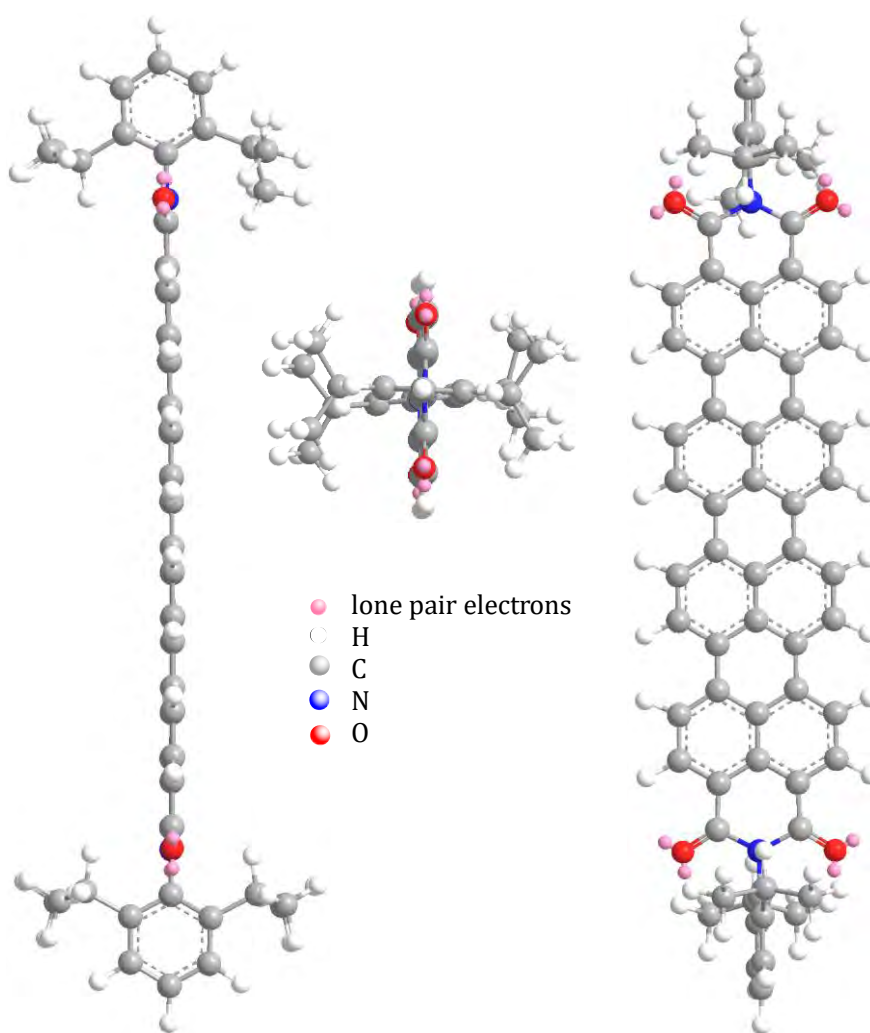
Figure 2.5.6: Measured J_{ph} vs time, as a function of wavelength for a sample photoanode used in this thesis

2.6. References

- [1] R. S. Nicholson, Irving. Shain, *Anal. Chem.* **1964**, *36*, 706, DOI: 10.1021/ac60210a007.
- [2] C. Sandford, M. A. Edwards, K. J. Klunder, D. P. Hickey, M. Li, K. Barman, M. S. Sigman, H. S. White, S. D. Minteer, *Chem. Sci.* **2019**, *10*, 6404, DOI: 10.1039/C9SC01545K.
- [3] L. M. Mukherjee, *J. Phys. Chem.* **1972**, *76*, 243, DOI: 10.1021/j100646a017.
- [4] J.-H. Yum, S.-J. Moon, L. Yao, M. Caretti, S. Nicolay, D.-H. Kim, K. Sivula, *ACS Appl. Energy Mater.* **2019**, *2*, 6616, DOI: 10.1021/acsaem.9b01154.
- [5] Y. Liu, P. Kilby, T. J. Frankcombe, T. W. Schmidt, *Chem. Sci.* **2019**, *10*, 6809, DOI: 10.1039/c9sc02534k.
- [6] O. V. Mikhnenko, P. W. M. Blom, T.-Q. Nguyen, *Energy Environ. Sci.* **2015**, *8*, 1867, DOI: 10.1039/C5EE00925A.
- [7] C. B. Murphy, Y. Zhang, T. Troxler, V. Ferry, J. J. Martin, W. E. Jones, *J. Phys. Chem. B* **2004**, *108*, 1537, DOI: 10.1021/jp0301406.

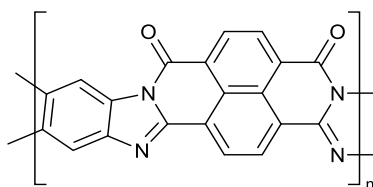
Chapter 3. Quaterrylene Di-imide

An extension of conjugation in the previously researched n-type organic semiconductor for photoanodes was thought to improve its PEC performance. Hence, a previously unexplored rylene di-imide (RDI) with suitable energy levels as a photoanode for water oxidation is synthesized. This compound is then characterized spectroscopically and electrochemically. Thin films are made using this molecule on different substrates using a spray coating technique. Their PEC performance is then evaluated in the presence of a sacrificial reductant dissolved in aqueous solutions under different conditions. The reason for loss in photocurrent measured over time is then investigated. Chemical modifications to this molecule are also investigated, hoping to mitigate the drawbacks of solubility and aggregation.



3.1. Motivation

As previously mentioned, a work by Borno, P. et al.^[1] demonstrated the use of a standalone ladder-type conjugated polymer as a photoanode for water oxidation. The stable, robust OSC chosen for this was the BBL polymer (Figure 3.1.1 shows the chemical structure), which was purchased commercially.



poly-(benzimidazobenzophenanthroline) (**BBL**)

Figure 3.1.1: BBL polymer.

While the BBL has high electron mobilities of up to $0.1 \text{ cm}^2\text{V}^{-1}\text{s}^{-1}$,^[2] making good transistor devices, it has poor solution processability. It requires harsh solvents like nitric acid or methanesulfonic acid to spin-process or spray-coated into films. Not surprisingly, the various morphologies in the photoanodes processed differently resulted in different PEC performances while oxidizing sulfite sacrificial electrolytes.

Encouraged by BBL, which was one of the early examples which oxidize water, albeit temporarily, other different OSCs were tried as photoanodes to emulate BBL. The result suggests that an extended conjugation in a robust ladder-like structure is helpful for water oxidation as the photogenerated holes would be delocalized over an extended area within the molecule, hence being stabilized.

Also, examples suggest the n-type OSCs based on perylene-imides were tried as photoelectrodes with a few limited successes.^[3-6] These perylene imides also had other inherent drawbacks, like the use of alkaline sensitive anchoring groups, limited absorption in the visible range (<550 nm) etc.

To combine the chemical properties of robustness, n-type OSC energy levels, solution processability and extended conjugation, the initial idea was to expand the rylene imide. In a study by Zhao, X. et al.,^[7] a comparison of computationally calculated energy levels of RDIs was performed. Since it is the HOMO which hosts the photogenerated holes to oxidize water, there should be sufficient driving force for hole extraction by the catalyst/electrolyte. From the HOMO levels and the water oxidation potentials (energy

levels illustrated in Figure 3.1.2), there is a scope for RDIs other than perylene di-imides to be viable candidates for photoanodes.

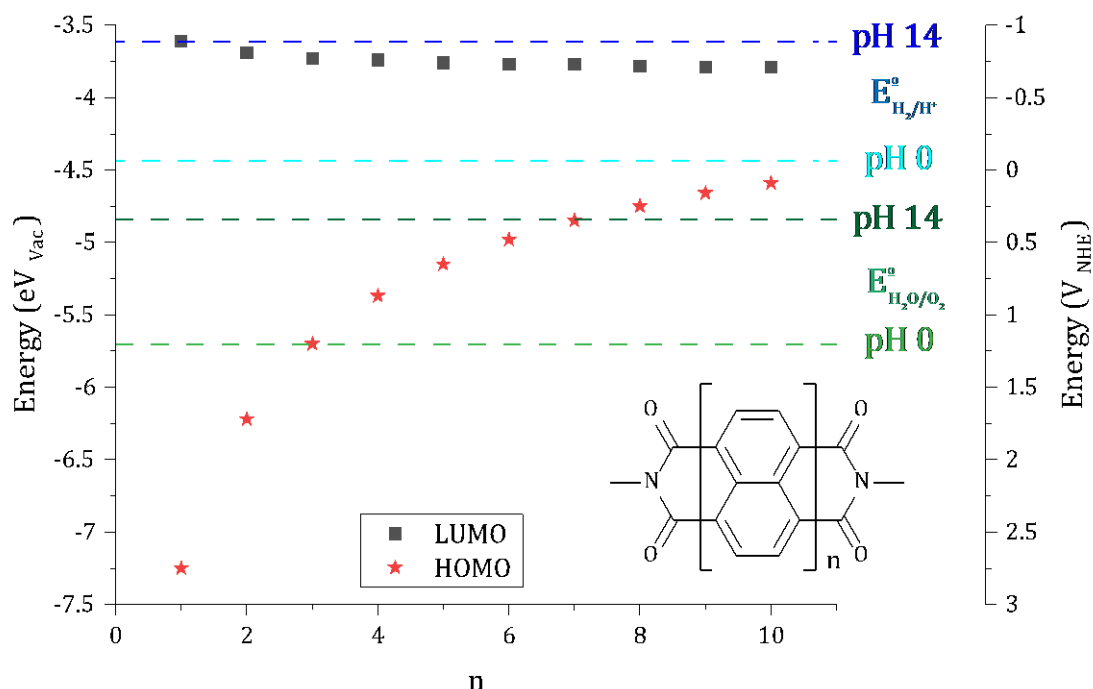


Figure 3.1.2: Representation of HOMO and LUMO computed energy levels (B3LYP, 6311g basis set)^[6]. For comparison, the redox potentials of water oxidation and reduction potentials are also shown at the extreme pH levels

Quaterylene di-imide (**QDI**, $n=4$) was chosen to be evaluated for its use as in photoanodes due to favorable HOMO energy level, which at certain pH levels could potentially drive water oxidation.

QDI molecule has not been extensively used in different applications unlike the naphthalene di-imide (NDI) or the perylene di-imide (PDI) species, which are n-type acceptors and whose variants find use in OPVs, transistors and other devices.^[8,9]

Previous literature on the **QDI** molecule suggest that, compared to the perylene analogue, the bandgap is smaller and hence absorption is red-shifted.^[10]

3.2. Synthesis

Commercially available perylene-3,4,9,10-tetracarboxylic dianhydride (**PDA**) is first converted to arylated perylene-3,4-dicarboximide (**PMI**) by a high temperature (190°C) autoclave reaction in the presence of excess imidazole and water mixture, catalyzed by $\text{Zn}(\text{OAc})_2 \cdot 2\text{H}_2\text{O}$ with 0.5 equivalent of 2,6-diisopropylaniline (A-I).^[11] **PMI** was then selectively mono-brominated in the peri position with excess K_2CO_3 and limiting equivalence of liquid bromine to get **PMI-Br** (A-II).^[12] A modified, step wise one pot

stannylation-stille coupling was set up to obtain a PMI dimer: **PMI₂** in decent yields (A-III) from **PMI-Br**, as opposed to the traditional Suzuki coupling.^[13] **PMI₂** is then subjected base promoted ring closing oxidative cyclization with excess K₂CO₃ in ethanolamine (A-IV) to get **QDI**.^[13]

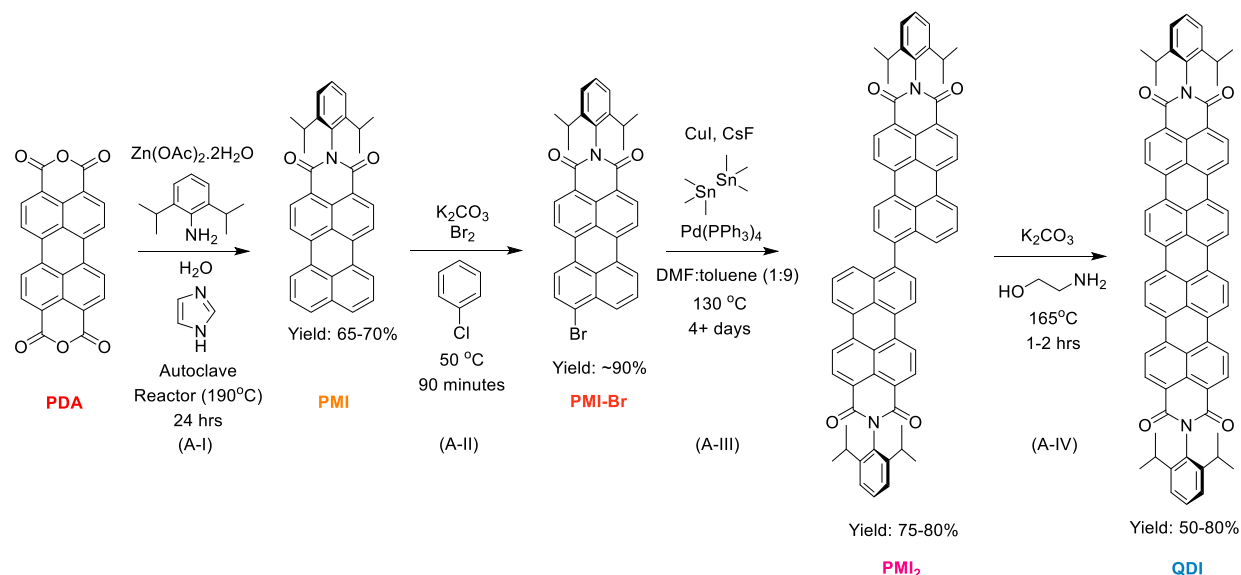


Figure 3.2.1: Overall scheme of **QDI** synthesis

The major advantage of this route is that only step (A-I) requires the use of column chromatography for purification and steps (A-II), (A-III) and (A-IV) can be purified by solvent washing/precipitation alone to get product **QDI** in decent yields of ¹H NMR spectrum verified purity.

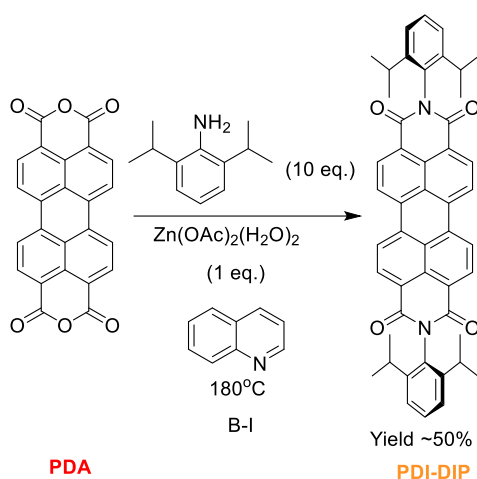


Figure 3.2.2: Scheme of **PDI-DIP** synthesis.

For more detailed explanation, refer Figure 3.2.1 and 3.7.1.Methods. As a reference molecule, the corresponding n=2 RDI , **PDI-DIP** was also synthesized.^[14] Commercially available **PDA** is converted to arylated perylene-3,4,9,10-dicarboximide (**PDI-DIP**) by a high temperature (180°C) autoclave reaction in the presence of excess quinoline, 1 eq. of

Zn(OAc)₂·2H₂O with 10 equivalents of 2,6-diisopropylaniline (B-I). For more detailed explanation, refer Figure 3.2.2 and 3.7.1.Methods.

3.3. Characterization

3.3.1. NMR

The ¹H NMR and 2D NMR (COSY) were used to determine the chemical structure of the **QDI** and **PDI-DIP**. The following spectra illustrate the various ¹H protons present in the synthesized product molecules. The ¹H spectra of the intermediate molecules are attached in 3.7.2.Miscellaneous NMR.

Figure 3.3.1 is the ¹H NMR spectrum of the **QDI** molecule. This molecule has an extremely planar structure and is solubilized by the hindered aromatic groups inhabiting the di-imide positions and is hence only sparingly soluble in most solvents. The compound tends to aggregate quickly in the NMR tube, and this is the reason for significant noise observed in the spectrum signal.

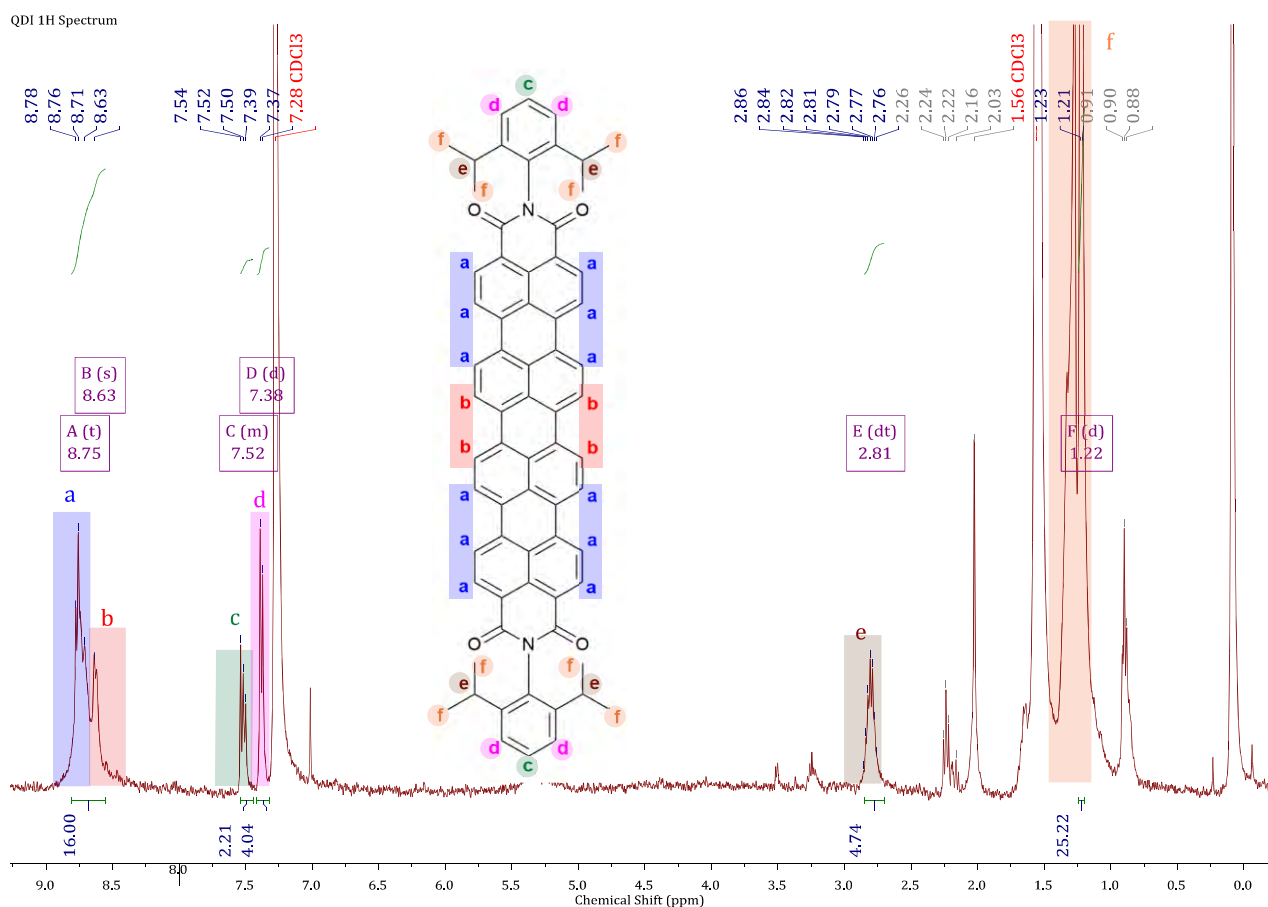


Figure 3.3.1: ¹H NMR (400 MHz) in CDCl₃ at 25°C of **QDI**.

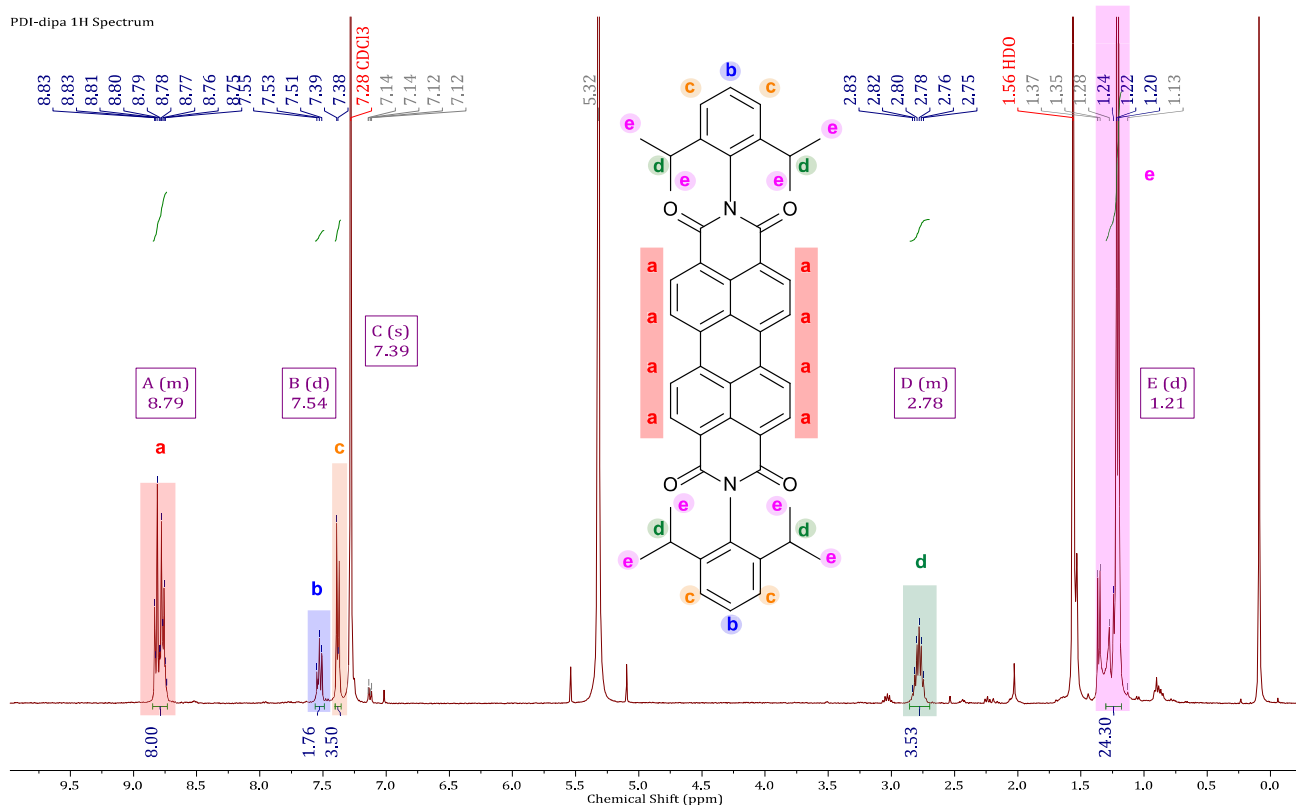


Figure 3.3.2: ^1H NMR (400 MHz) in CDCl_3 at 25°C of **PDI-DIP**.

Broadly, the peaks present in 8.6-8.8 ppm range are the protons covalently bound to the quaterylene core and those in 7.3-7.6 ppm range are the protons found in the imide substituents. Figure 3.3.2 is the NMR spectrum of the **PDI-DIP** molecule. The peaks present in 8.7-8.85 ppm range are the protons covalently bound to the perylene core and those in 7.3-7.6 ppm range are the protons found in the imide substituents.

3.3.2. UV-Vis Absorption

UV-Vis absorption spectroscopy studies on the synthesized **QDI** and **PDI-DIP** dissolved in chloroform and as thin films were conducted. The extinction coefficients of these molecules in solution are tabulated in Table 3.1. The absorption of **QDI** is significantly red-shifted (by ~ 300 nm) compared to the **PDI-DIP**. The normalized UV-Vis spectra of the synthesized compounds are illustrated in Figure 3.3.3. The cyclization of dimers (**PMI₂**) results in a significant increase in extinction coefficient of the OSCs, thereby indicating another advantage of extended RDIs. Moreover, from the Tauc plots, the optical bandgap ($E_{g,opt}$) is calculated. **QDI** has an E_g of ~ 1.4 eV whereas **PDI-DIP**'s is 2.2 eV. Further information can be found in 3.7.4. Miscellaneous UV-Vis Absorption Spectra.

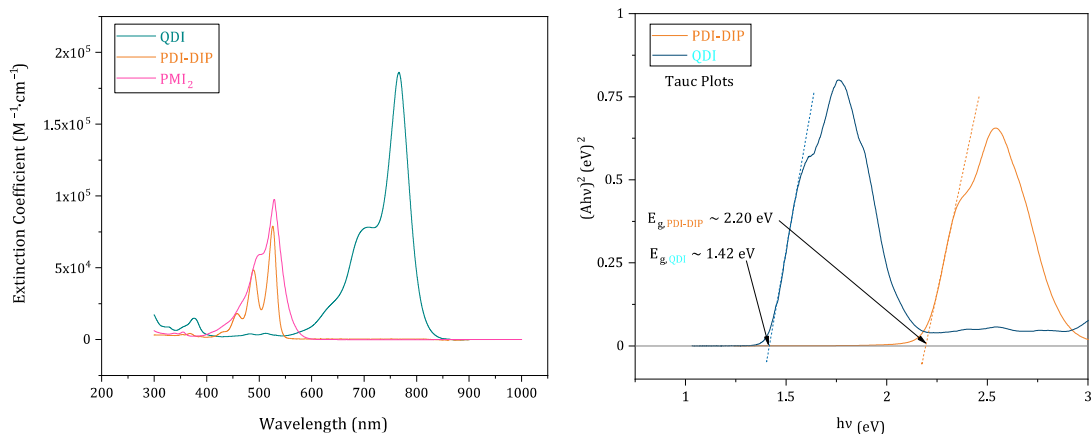
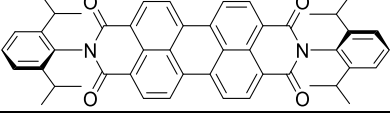
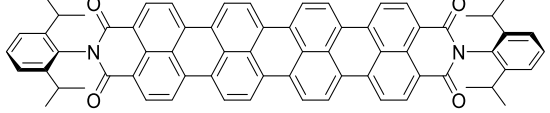


Figure 3.3.3: (Left) Normalized Absorption Spectra of the OSCs in solution, (Right) Tauc Plots of Thin Films.

Table 3.1: Summary of Absorption spectra of OSCs

Molecules	λ_{\max} (nm)	Extinction Coefficient	Optical Bandgap; $E_{g,opt}$
		($M^{-1}\cdot cm^{-1}$)	(eV)
	526	77758 \pm 0.15%	2.2 eV
	765	188750 \pm 3%	1.42 eV

3.3.3. Cyclic Voltammetry

Probing the MO levels is easily done by electrochemistry. **QDI** and **PDI-DIP** thin films are drop-cast on flame cleaned Pt foils and subjected to cyclic voltammetry (Figure 3.3.4).

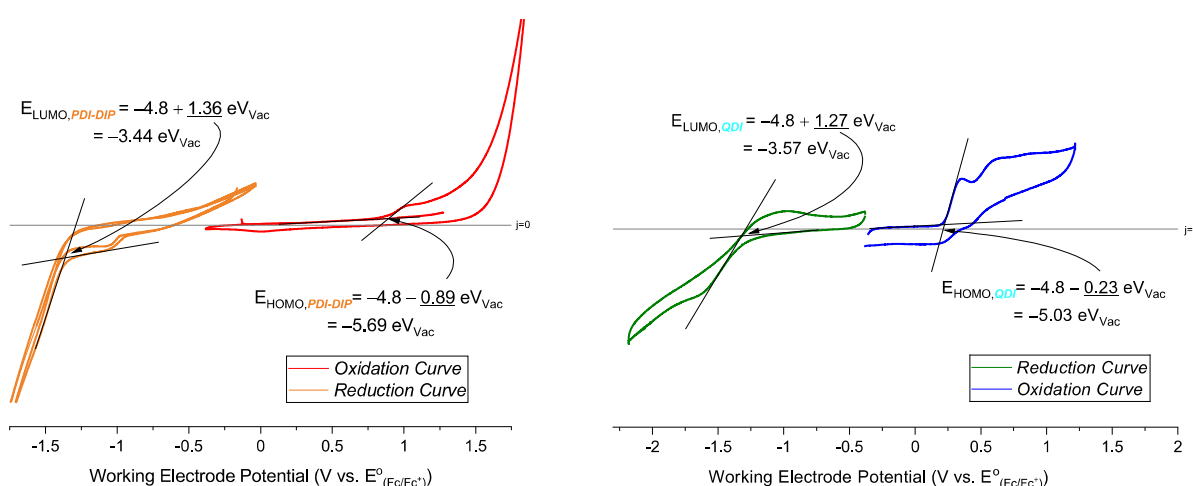


Figure 3.3.4: The CV spectra of **PDI-DIP** and **QDI**.

The electrochemical bandgap ($E_{g,elec}$) of **QDI** is 1.56 eV, which is considerably smaller than the 2.25 eV for **PDI-DIP**; these values correspond well with the measured

$E_{g,opt}$. However, the effect of extended conjugation is reflected more on the HOMO levels, with **QDI** having destabilized HOMO of -5.03 eV_{Vac} compared to a more stable -5.69 eV_{Vac} for **PDI-DIP**.

3.4. PEC Characterization

Films of the OSCs synthesized were deposited on FTO/glass and mSnO_2 (doctor bladed)/FTO/glass substrates. The primary deposition technique used was spray coating. The synthesized **QDI** has a poor solubility in most solvents, hence spin-coating was not used as it requires a concentrated solution. The effect of post-processing conditions, electrolytes and operation parameters are explored in this section. As co-catalysts engineering and optimization is beyond the scope of this study, only the electron injection properties are studied from the J_{ph} measured from sulfite oxidation, as opposed to water oxidation. Besides offering a kinetic advantage ($2e^-$ for sulfite vs. $4e^-$ for water oxidation), the thermodynamic redox potential is also much lower ($+0.7 \text{ V}_{RHE}$ vs. $+1.23 \text{ V}_{RHE}$).^[15]

3.4.1. Effect of pH

Three different phosphate buffered solutions containing a sacrificial hole accepting agent of $1 \text{ M Na}_2\text{SO}_3$ (aq.) were prepared (pH~6,9,12). These solutions were used as electrolytes for the **QDI** sprayed photoanodes. Linear Sweep Voltammetry (LSV) under chopped light intensity was performed under a lamp calibrated to mimic solar spectrum photon density in the 300-950 nm range.

The highest photocurrent was obtained in the pH 6 electrolyte. The more alkaline electrolytes result in smaller J_{ph} , suggesting that the presence of OH^- ions is detrimental to the performance of this photoanode (LSV curves in Figure 3.4.1). The subsequent PEC characterizations were carried out in electrolytes of pH 6. This effect could perhaps be due to the affinity of hydroxyl ions to the acidic ETL which prevent efficient electron injection and adhesion of **QDI** to the ETL. This is despite considering the pH dependence of fermi level ETLs, as there exists sufficient driving force for electron injection in more alkaline pH, especially with the destabilized MO levels of **QDI**.

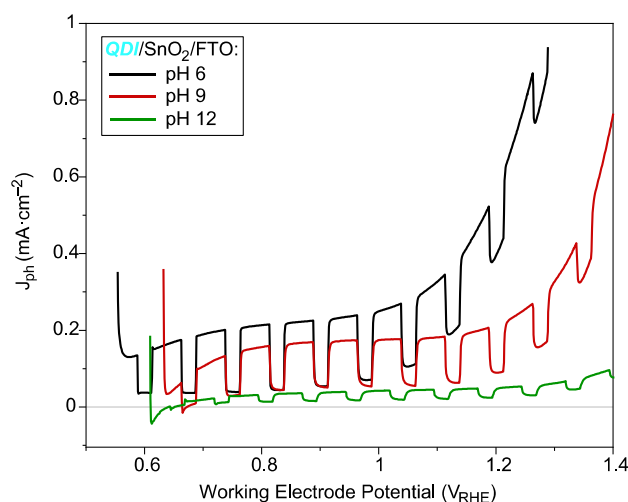


Figure 3.4.1: Effect of pH on J_{ph} .

3.4.2. Amount of QDI sprayed

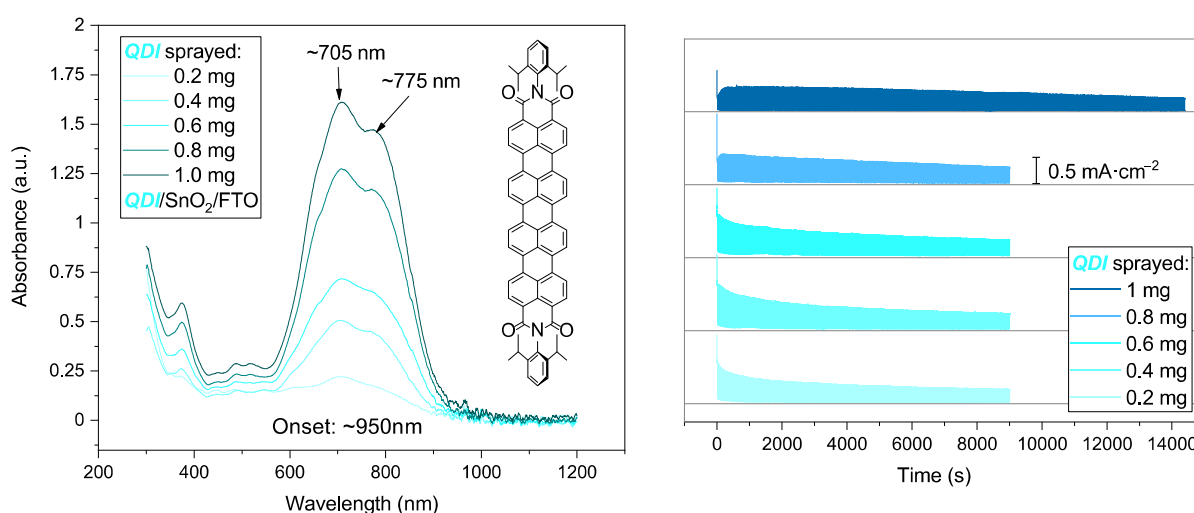


Figure 3.4.2: (Left) Absorbance of QDI/mSnO₂/FTO substrates, (Right) J_{ph} evolution with time on operation.

The amount of QDI sprayed can be tracked by absorption studies (Figure 3.4.2, Left) where the absorbance corresponds to quantity sprayed, and the effect of this quantity on the performance can be seen in chronoamperometry (CA) experiments (Figure 3.4.2, Right). The stability of the devices, as can be inferred by loss in J_{ph} , increases with more QDI sprayed, but all the devices show loss under operation at 0.95 V_{RHE} . The initial J_{ph} (at $t=0$) reaches a maximum for 0.8 mg of QDI sprayed, then reduces for 1 mg sprayed devices.

3.4.3. Effect of mSnO₂ underlayer

Not surprisingly, the use of mSnO₂ underlayer greatly enhanced (~ 250 - 300 times) the J_{ph} obtained due to extraction of photogenerated electrons, effectively forming a p-n hybrid organic-inorganic junction (bi-layer's scheme shown in Figure 3.4.3).

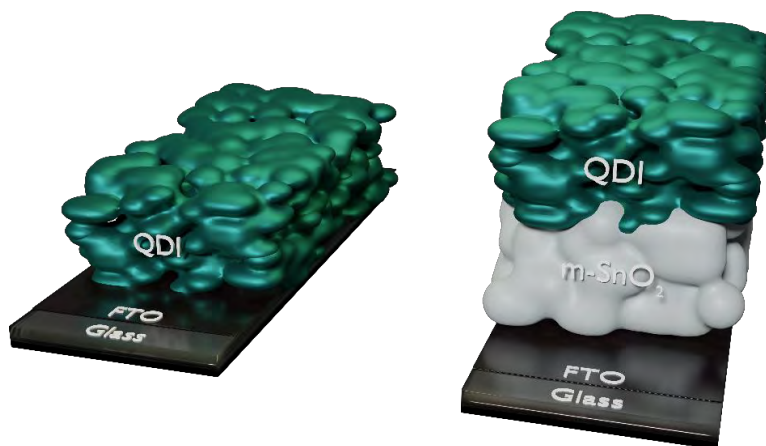


Figure 3.4.3: Photoanode without (left) and with (right) ETL, $m\text{SnO}_2$.

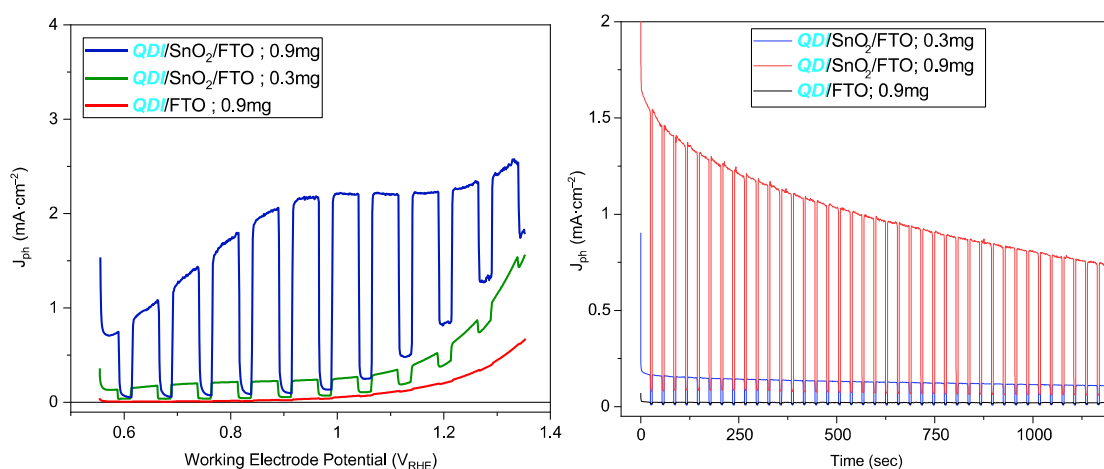


Figure 3.4.4: (Left) LSV curves with and without underlayer, (Right) Corresponding CA curves.

As seen before, the J_{ph} measured does not persist for a long time, i.e., the PEC stability is very poor (Figure 3.4.4, Right). J_{ph} in the CA experiment under chopped light illumination drops rapidly over time while operating at 0.95 V_{RHE} . However, the presence of an underlayer is indeed beneficial to J_{ph} , as seen in the LSV curves (Figure 3.4.4, Left).

3.4.4. Effect of Annealing

To identify the factors behind the loss in J_{ph} seen in CA experiments, possible parameters are explored. It is known that thermal annealing leads to thermodynamically favored reorganization in OSCs due to better crystalline π - π stacking configuration.^[16] Here, on annealing higher J_{ph} is indeed observed, but there is a slight effect on stability: for substrates annealed at 240°C and 300°C the linear (with time) loss in J_{ph} has a smaller slope than the others (Figure 3.4.5). All substrates were annealed in air for 1 hour.

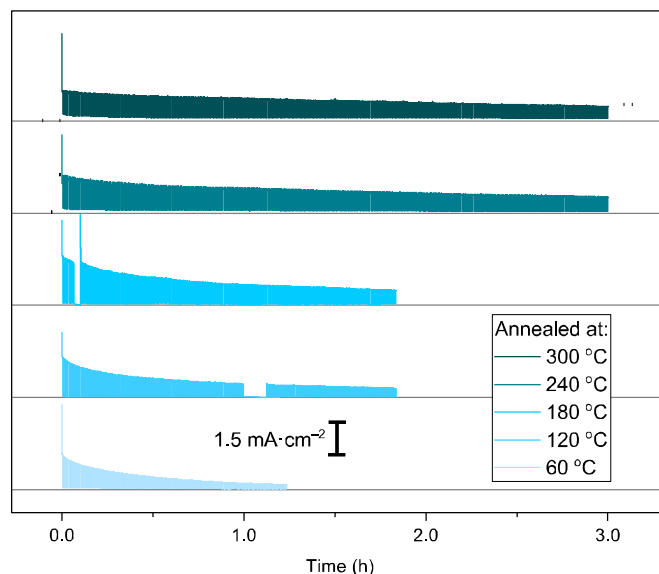


Figure 3.4.5: Effect of annealing the **QDI**/SnO₂/FTO/glass photoanode at specified temperature for 1 hour on CA.

3.4.5. Effect of Applied Potential

QDI/mSnO₂/FTO photoanodes were prepared at the previously optimized conditions: spray coating 0.8 mg of **QDI**, and then annealed at 240 °C for 1 hour. From Figure 3.4.6, the reduction in photocurrent is dependent on the applied potential. Higher applied potentials lead to rapid decline in J_{ph} , while low potentials are more stable. This can be correlated with the HOMO levels of **QDI**: at 0.95 V_{RHE}, the applied potential is highly oxidative and < -5.03 eV_{Vac} hence the OSC is oxidized over time.

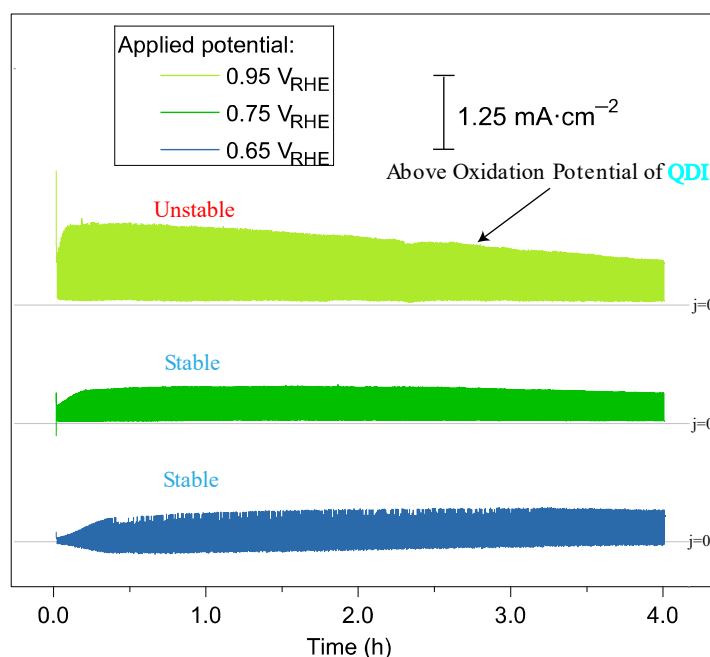


Figure 3.4.6: Effect of applied potential on stability.

3.5. Modifications to QDI

3.5.1. Drawbacks of QDI

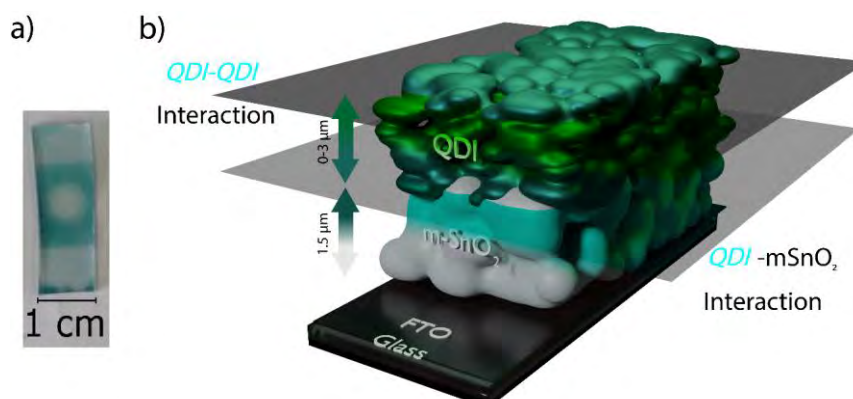


Figure 3.5.1: a) Photograph of substrate after 1000s operation, b) Scheme of QDI sprayed on mSnO₂.

As seen from the chronoamperometric evolution of QDI films, the loss in J_{ph} occurs rapidly in the first few seconds, followed by a slower, gradual depletion in J_{ph} . After chronoamperometry of a few thousand seconds, QDI completely dissolves/degrades from the mSnO₂ (Figure 3.5.1a), exposing the ETL underlayer.

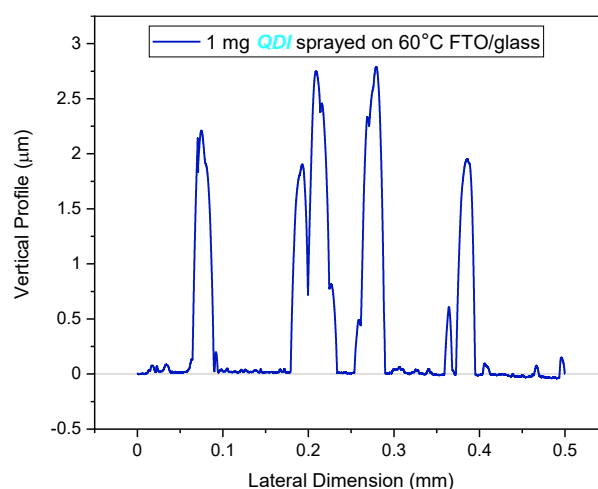


Figure 3.5.2: Surface topography of sprayed QDI measured using profilometer.

The surface topographic profile of the sprayed photoanode (Figure 3.5.2) is looked at. Due to aggregative nature of QDI, discrete chunks of the OSC are crystallized onto the underlayer. Using this information, it can be deduced that the initial loss of J_{ph} could be due to the erosion of the OSCs away from the ETL (as shown in Figure 3.5.1b), which are held together by a weaker π - π stacking, whereas the molecules closer to the ETL which are well annealed onto the mesoporous substrates are physically trapped in, hence are dissolved only gradually on operation at higher applied potentials. Moreover, the effect of the p-n

junction is greater experienced by the molecules close to the ETL interface which ensures efficient charge separation, compared to the molecules closer to the electrolyte.

3.5.2. Structural Changes

All these drawbacks of **QDI** could be modified synthetically. Just by retaining the core extended conjugation, other properties of the OSC are altered. The first change is to improve solubility, as the OSCs could be spun-coat and incorporated into BHJs. The second change is to energetically prevent degradation/dissolution at higher working potentials. Both these were possible by attaching substituents to the bay positions of **QDI** (Figure 3.5.3).^[17]

The first step to modify **QDI** is to halogenate the molecule. Unlike smaller RDI where selective mono-bromination is possible,^[18,19] with **QDI** due to the presence of multiple bay positions, only the final hexabrominated product, **QDI**Br₆, can be easily recovered during purification (NMR shown in Figure 3.5.4). The integration factors of the aromatic and alkylated protons perfectly correspond to the structure and clearly show hexabromination and the structural isomeric ratio for the bay positions (ratio of 10:7). The partially brominated **QDI**Br_{x=1-5} have many structural isomers and cannot be selectively isolated.

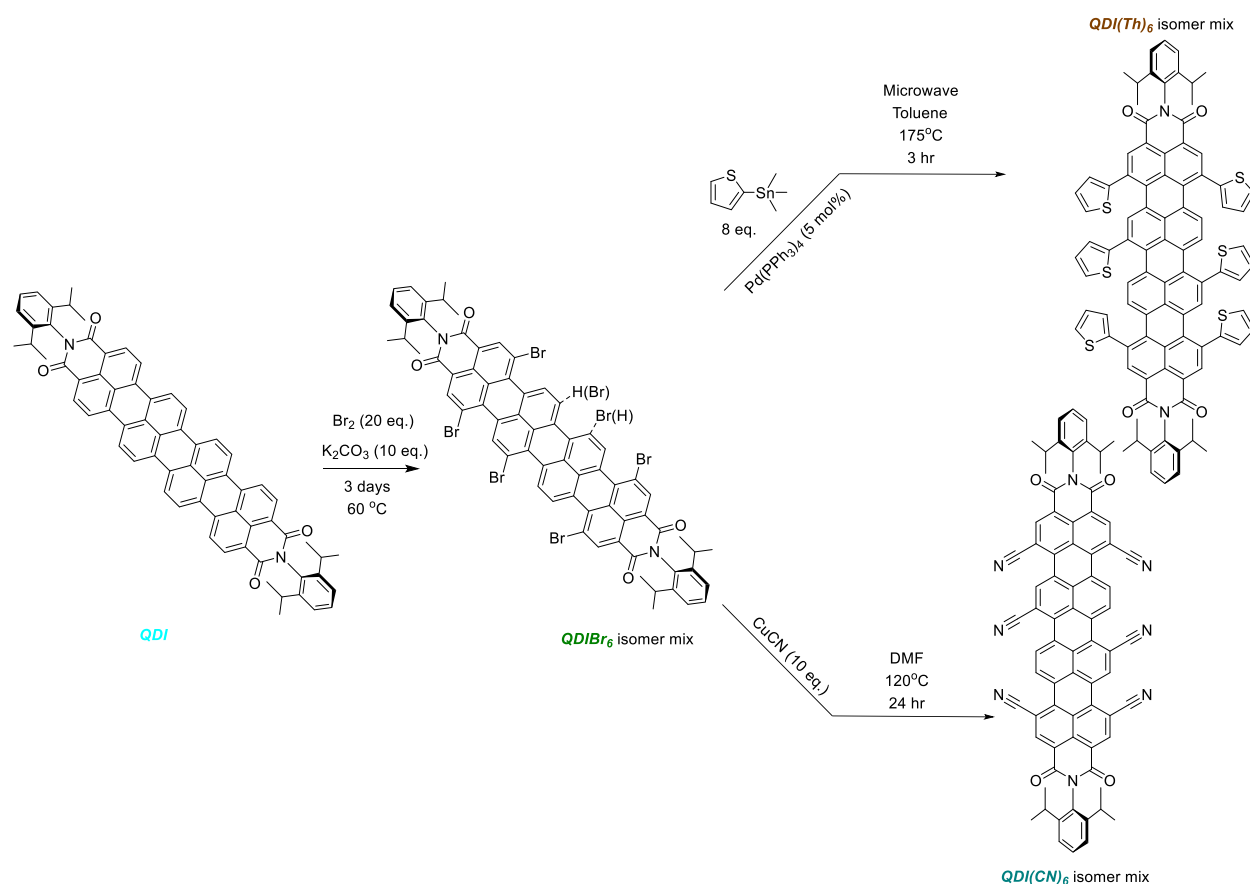


Figure 3.5.3: Reaction scheme for *QDI* modification

Towards lowering the HOMO-LUMO levels, so that the molecule can sustain at higher oxidative applied potentials, substituent moieties which are electronegative were attached to the bay positions. In this case, the groups were attached by a simple nucleophilic aromatic substitution mechanism, resulting in *QDI(CN)*₆ (¹H NMR shown in Figure 3.5.5).^[20] The NMR spectrum corresponds well to the structure with the integration factors of the protons, and the isomeric ratio of 10:7 is still maintained in this product.

This, however, resulted in a molecule with highly negative energy levels. While the HOMO is sufficiently positive to drive oxidative reactions, the LUMO (~ -4.5 eV_{Vac}; CV spectra in Figure 3.5.7) is lower than E_{H^+/H_2O}^0 , which is not desired. These would make good n-type transistors due to low energy levels, that would impart them air and moisture stability, but cannot be used for PEC applications. Also, while the cyano groups increase solubility in solvents like CF and Chlorobenzene, the OSC still forms smaller aggregates on spin-coating, which could be disadvantageous for smooth BHJ formation (Optical Microscope Images in Figure 3.5.9 showing aggregate formation under different processing conditions), albeit a marked improvement from neat *QDI*. So, an alternative substituent had to be explored.

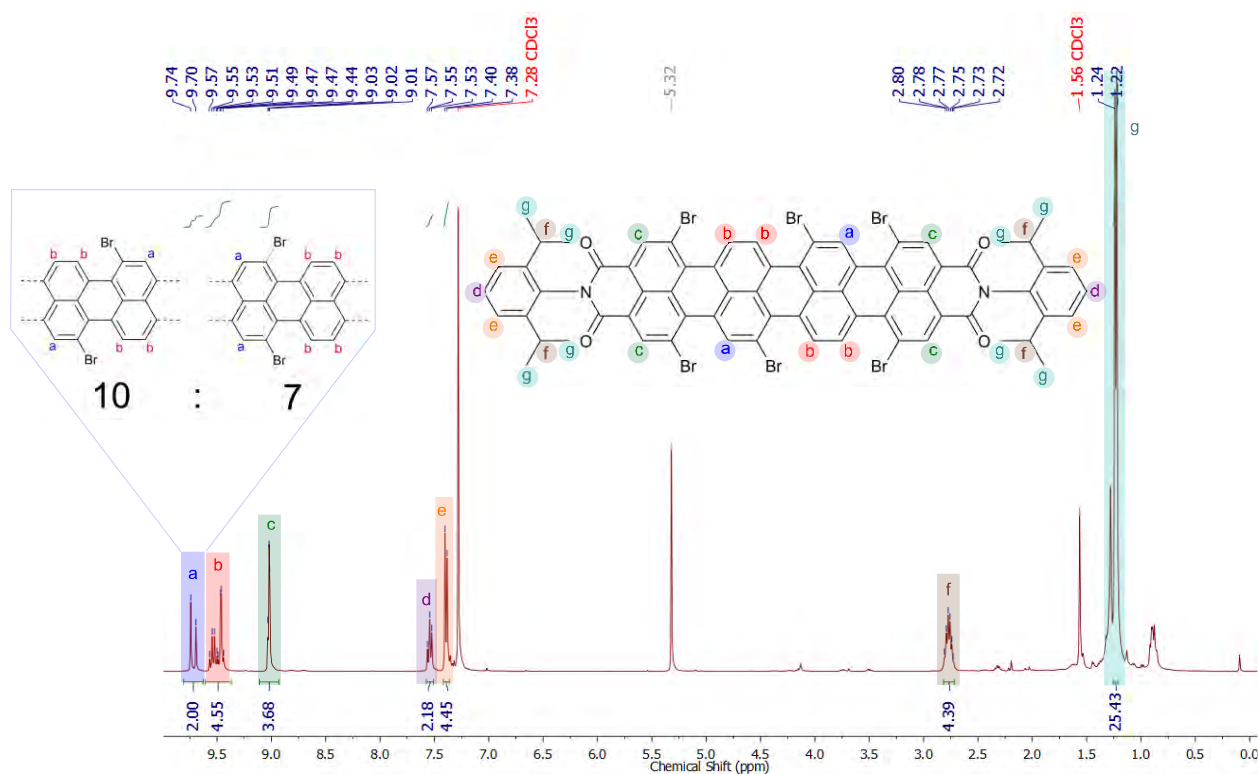


Figure 3.5.4: ¹H NMR of *QDI*₆Br₆ showing structural isomer distribution.

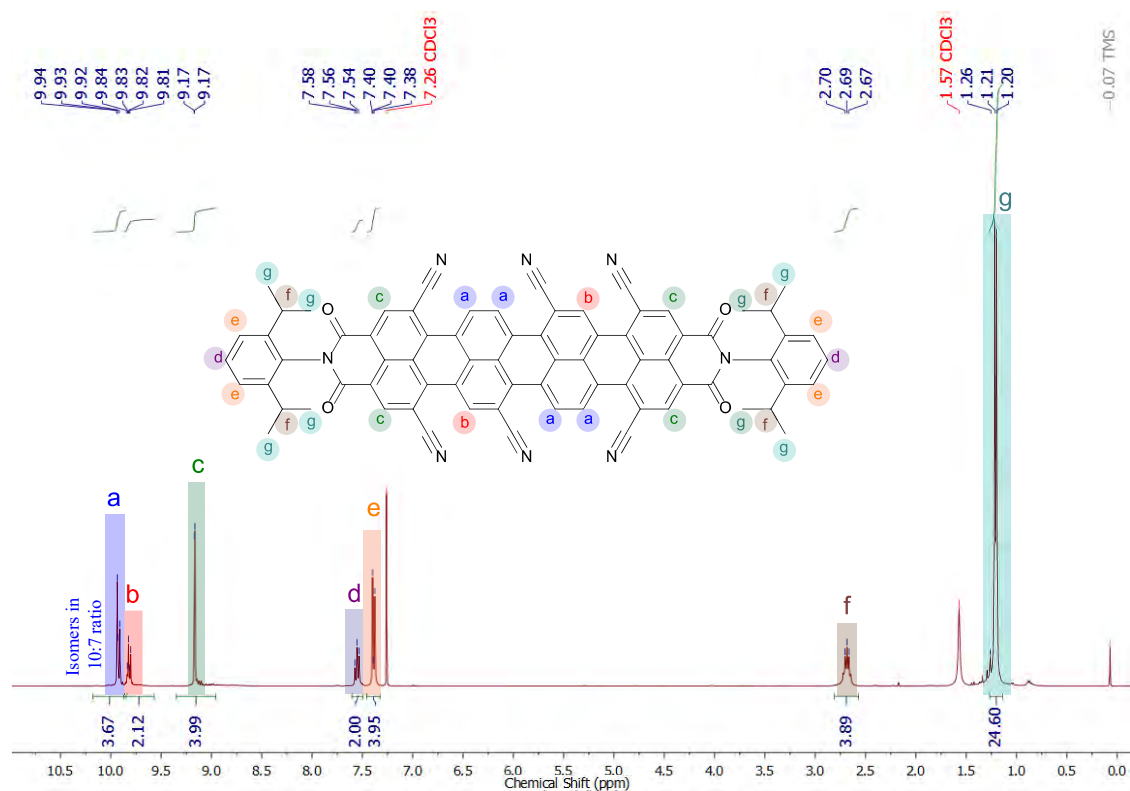


Figure 3.5.5: ^1H NMR of $\text{QDI}(\text{CN})_6$ showing structural isomer distribution.

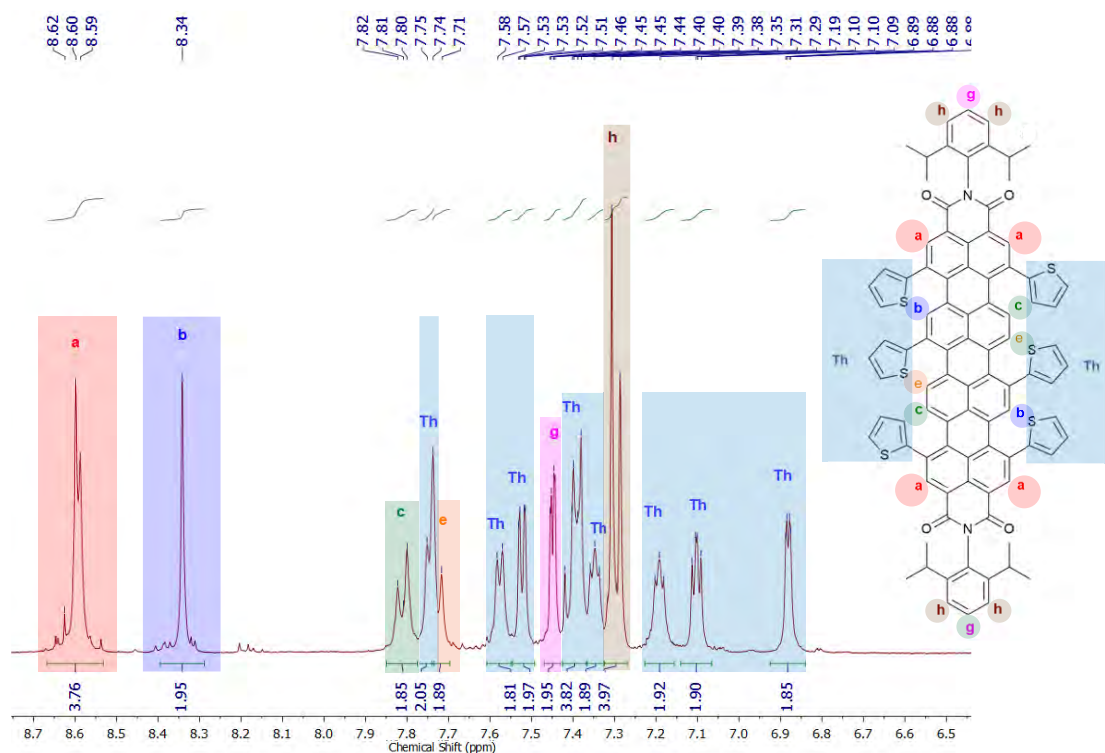


Figure 3.5.6: ^1H NMR of $\text{QDI}(\text{Th})_6$ showing the aromatic regions.

The second **QDI** modification is to attach thiophene units to the bay positions by *Stille* coupling. The product **QDI(Th)₆** (NMR of the aromatic protons in Figure 3.5.6, whole spectrum in Figure 3.7.5, and the structure corresponds with the integration factors of the aromatic and alkyl protons) is a highly red-shifted n-type OSC (UV-Vis Absorption Spectra and Tauc Plots showing optical bandgaps in Figure 3.5.8).^[21] The absorption onset is close to 955 nm, and this corresponds to an ultra-narrow bandgap of 1.29 eV. This compound also showed interesting properties in oxidative environments (Refer Cyclized Hexathiopheno-quaterylene di-imide (**PC-QDI(Th)₆**) for more information on synthesis).

Synthesized by a Pd-catalyzed *Stille* coupling reaction, this **QDI(Th)₆** has lower energy levels than **QDI**. However, on incorporating with PTB7-Th polymer donor as an electron acceptor in a photoanode, the performance is not impressive with negligible J_{ph} , possibly due to high HOMO levels, and an overall non-viability as an electron acceptor (as it has many electron- rich thiophene units, and only a weak electron-poor rylene core). Thus both the synthetic modifications which result in fully characterized pure OSCs, are unfortunately not useful from the perspective of an organic photoanode. For a stable organic photoanode, other strategies or molecules need investigation.

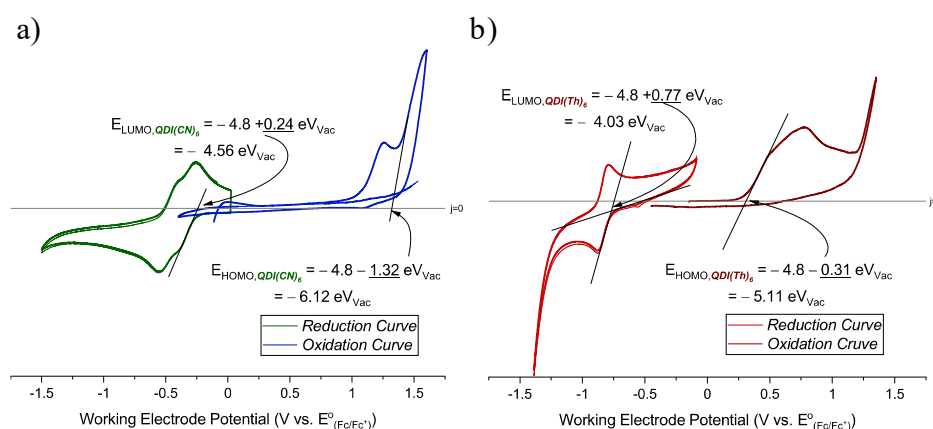


Figure 3.5.7: Cyclic Voltammetry of a) **QDI(CN)₆** and b) **QDI(Th)₆**.

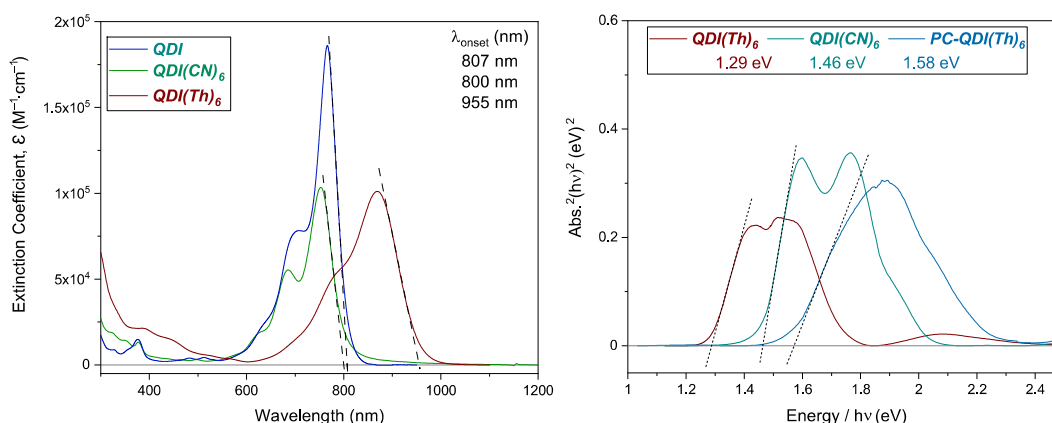


Figure 3.5.8: (Left) UV-Vis Absorbance of modified **QDI**, (Right) Tauc Plots of modified **QDI**.

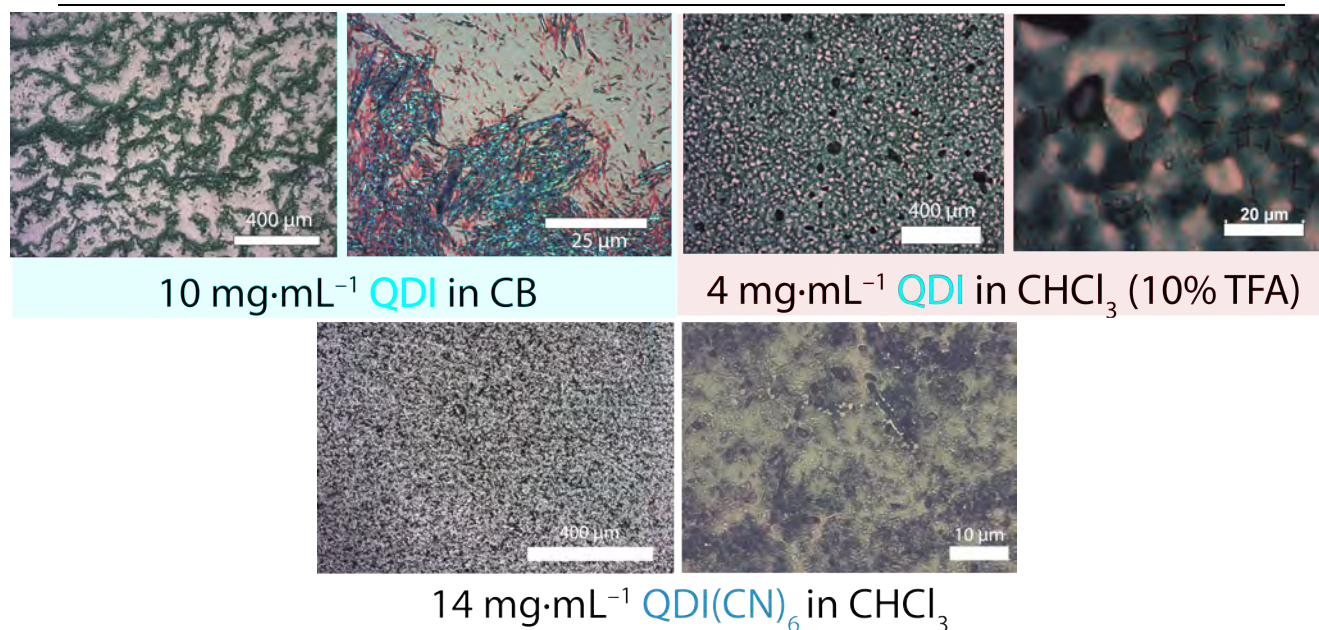


Figure 3.5.9: Optical Microscope images of spun-coat (Top) **QDI**, (Bottom) **QDI(CN)₆**.

3.6. Conclusion

Inspired by previous literature on rylene imide based photoanodes and the earlier work based on the BBL polymer, it was decided that a vertically extended RDI could be an interesting target molecule for PEC applications. In this chapter, the synthesis, analytical and PEC characterization are elaborated. A few workarounds were tried to improve the drawbacks of **QDI**: different operating parameters, alternate synthetic modifications etc. While the idea of using **QDI** and its derivatives were initially appealing, the PEC studies and practical feasibility issues prevents the usage of these OSCs in photoanodes for high performance and stability. So, instead of using single component OSCs which exhibit quick degradation, perhaps other techniques to enhance charge separation to prevent accumulation need attention.

3.7. Supporting Information

3.7.1. Methods

All the synthesis steps were improvisations of previously published/patented results,^[22–24] whose details are elaborated below.

Perylene-3,4-dicarboximide (**PMI**)

Perylene-3,4,9,10-tetracarboxylic dianhydride (**PDA**, 1.75 g, 4.46 mmol, 1 eq.), 2,6-Diisopropylaniline (395 mg, 48.5 mmol, 0.5 eq.), zinc acetate dihydrate (617 mg, 2.81 mmol, 0.63 eq.), imidazole (8.5 g, 125 mmol, 28 eq.), and water (3.7 mL, 205.2 mmol, 46 eq.) were combined in an autoclave reactor and heated to 190 °C for 24 hours. After cooling the reaction mixture to room temperature, the crude was suspended in 1 M HCl: EtOH (9:1) mixture. The mixture was filtered through a celite plug; the filtered solids were washed once with 100 mL water: EtOH (9:1) mixture. Crude **PMI** was extracted from the filter cake by soxhlet extraction chloroform over 72 hours. The crude reaction mixture was purified via column chromatography using dichloromethane as the eluent, yielding 760 mg **PMI** (1.58 mmol, 70.8% yield). ¹H NMR (400 MHz, Chloroform-d) δ 8.70 (d, J = 8.0 Hz, 2H), 8.53 (t, J = 7.4 Hz, 2H), 7.97 (d, J = 8.1 Hz, 2H), 7.70 (t, J = 7.9 Hz, 2H), 7.50 (d, J = 7.7 Hz, 2H), 7.37 (d, J = 7.8 Hz, 2H), 2.80 (p, J = 6.9 Hz, 2H), 1.21 (d, J = 6.8 Hz, 12H). ¹³C NMR (101 MHz, Chloroform-d) δ 24.15, 29.28, 76.85, 77.16, 77.48, 120.44, 121.22, 124.05, 124.16, 127.31, 129.46, 129.58, 131.16, 131.23, 132.23, 134.56, 137.77, 145.89.

8-bromo perylene-3,4-dicarboximide (**PMI-Br**)

A mixture of **PMI** (3.3 gm, 6.85 mmol, 1 eq.) and K₂CO₃ (4.74 gm, 34.26 mmol, 5 eq.) in chlorobenzene (50 mL) was heated to 40 °C. Liquid Br₂ (457 μL, 8.91 mmol, 1.3 eq.) in chlorobenzene (10 mL) was added to this solution dropwise. The bright orange color of the solution turns dark maroon-red over time and was stirred for 2 hours at 50 °C. The solution was then cooled and Na₂S₂O₃ solution was added to quench the excess bromine. Chloroform was added in excess and the organic fraction was separated out and dried by adding MgSO₄ powder. On removing the solvents, the crude was used directly without purification in the next step. The resulting **PMI-Br** weighed 3.5 gm (6.24 mmol, 91% yield). ¹H NMR (400 MHz, Chloroform-d) δ 8.68 (dd, J = 8.1, 6.1 Hz, 2H), 8.55 – 8.43 (m, 3H), 8.34 (d, J = 8.4 Hz, 1H), 8.28 (d, J = 8.3 Hz, 1H), 7.94 (d, J = 8.1 Hz, 1H), 7.76 (s, 1H), 7.50 (s, 1H), 7.36 (d, J = 7.7 Hz, 1H), 2.84 – 2.70 (m, 2H), 1.20 (d, J = 6.8 Hz, 12H).

Dimer of perylene-3,4-dicarboximide (**PMI₂**)

PMI-Br (600 mg, 1.07 mmol, 1 eq.) was taken in a 250mL *Schlenk* and was evacuated and argon back filled. After transferring the *Schlenk* into an argon filled glovebox, room temperature warmed hexamethylditin (245 μL, 1.18 mmol, 1.1 eq.) and 0.5 mol% of Pd(PPh₃)₄ were added and dry, degassed toluene was used to solubilize the contents in the *Schlenk* flask. This flask is then heated under argon at 130 °C for 2 days. An overall color

change is observed as the solution turns dark red over 2 days and black particles settle at the bottom of the flask (which could be oxidized Pd catalyst). The second part of this one pot reaction involves cooling the flask to room temperature under argon and taking it into the glovebox again. Another 1 eq. of PMI-Br is added along with CsF (325 mg, 2.14 mmol, 2 eq.), CuI (20.4 mg, 107.4 μ mol, 0.1 eq.) and DMF resulting in an overall solution mixture of Toluene: DMF (9:1, v/v). Additional catalyst of 5 mol% is also added. This reactant mixture is then again heated under argon at 130 °C for 2+ days. For the workup, cool down the reaction mixture and transfer contents to a separating funnel containing brine. Add needed quantities of chloroform and brine and extract selectively the organic layer and dispose aqueous solution carefully as it contains toxic tin byproducts. The organic layer is dehydrated by adding MgSO₄ powder and is passed through a celite plug to remove suspended catalysts and inorganic residues. On evaporating the solvents, a dark red solid is obtained (**PMI₂**, a bright pink solution in chloroform) which shows a single spot on a TLC plate after vigorous hexane and petroleum ether washing to remove unreacted starting materials and directly used without further purification or characterization.

Quaterrylene di-imide (**QDI**)

PMI₂ (550 mg, 572 μ mol, 1 eq.) is taken in a round bottom flask and excess K₂CO₃ (2gm, 14.3 mmol, 25 eq.) is added. Ethanolamine is used as the solvent (>500 eq.) and a few mLs of dioxane are added to facilitate refluxing and to help dissolve the product in the solution. The solution is refluxed at a high temperature of 165 °C for 1-2 hours or more. A drastic color change of the solution from an initially insoluble red suspension to green and finally dark blue solution is observed during the refluxing process. This solution is cooled to room temperature and added to a solution of 1 M HCl: EtOH (9:1) mixture. The resulting suspension is transferred to a separating funnel containing chloroform and the organic content is extracted through the chloroform fraction. Adding MgSO₄ dehydrates the organic but also makes it very difficult to wash and extract **QDI** which aggregates easily on the MgSO₄ powders. Hence the resulting MgSO₄ and organic solid is washed continuously with chloroform: trifluoroacetic acid (24:1, v/v) or dioxane by means of a soxhlet extractor for over 6 hours. On evaporating the solvents, a purple blue solid (**QDI**) weighing 420mg (76.5% yield) is obtained which is precipitated in hexane and dried. ¹H NMR (400 MHz, Chloroform-d) δ 8.80 – 8.61 (m, 16H), 7.56 – 7.48 (m, 2H), 7.38 (d, J = 7.8 Hz, 4H), 2.80 (dt, J = 19.5, 6.4 Hz, 4H), 1.22 (d, J = 6.7 Hz, 24H).

Hexabromo-quaterrylene di-imide (*QDI*Br₆)

Adapted from an earlier procedure^[16]. *QDI* (1 gm; 1.04 mmol) is dissolved in 40mL Chlorobenzene with K₂CO₃ (10 eq.; 1.5 gm; 10.5 mmol). To this solution, on stirring, add dropwise Br₂ (20 eq.; more if needed, track by TLC; ~1200μL). Heat solution at 60 °C for 2-3 days, till product is seen as a dark green spot on the TLC during elution with CH₂Cl₂. Quench reaction on cooling with saturated sodium thiosulfate solution to neutralize the bromine. Extract organic fraction selectively using a separating funnel while extracting it with CF. Evaporate the solvents. Subject crude to column chromatography in CH₂Cl₂ to extract isomeric mixture of *QDI*Br₆ products, weighing 1.1 gm (Yield: 74%). ¹H NMR (400 MHz, Chloroform-d) δ 9.72 (d, J = 18.8 Hz, 2H(59%)), 9.54 (q, J = 8.6 Hz, 2H (41%)), 9.47 (d, J = 2.6 Hz, 4H), 9.02 (t, J = 3.2 Hz, 4H), 7.55 (t, J = 7.8 Hz, 2H), 7.39 (d, J = 7.8 Hz, 4H), 2.76 (dq, J = 11.3, 5.7, 4.6 Hz, 4H), 1.23 (d, J = 6.9 Hz, 24H).

Hexacyano-quaterrylene di-imide (*QDI(CN)₆*)

QDIBr₆ (750 mg; 0.53 mmol) is dissolved in dehydrated 50 mL DMF, to which CuCN (10 eq.; 470 mg, 5.24 mmol) is added. Under an argon atmosphere, the solution is heated at 100°C for over 24 hours (track the product using TLC, DCM elution). Quench solution after cooling in FeCl₃ aqueous solution and filter over celite bed. Elute dry solids with CH₂Cl₂ and concentrate the crude. Perform column chromatography in CH₂Cl₂ to obtain the green fraction, which is a mixture of isomers. Yield: 510 mg (88 %). ¹H NMR (400 MHz, Chloroform-*d*) δ 9.93 (d, *J* = 10.1 Hz, 2H), 9.83 (dd, *J* = 8.8, 4.5 Hz, 4H), 9.17 (d, *J* = 1.4 Hz, 4H), 7.56 (t, *J* = 7.8 Hz, 2H), 7.39 (d, *J* = 7.9 Hz, 4H), 2.87 – 2.50 (m, 4H), 1.20 (d, *J* = 6.8 Hz, 24H).

Hexathiopheno-quaterrylene di-imide (*QDI(Th)₆*)

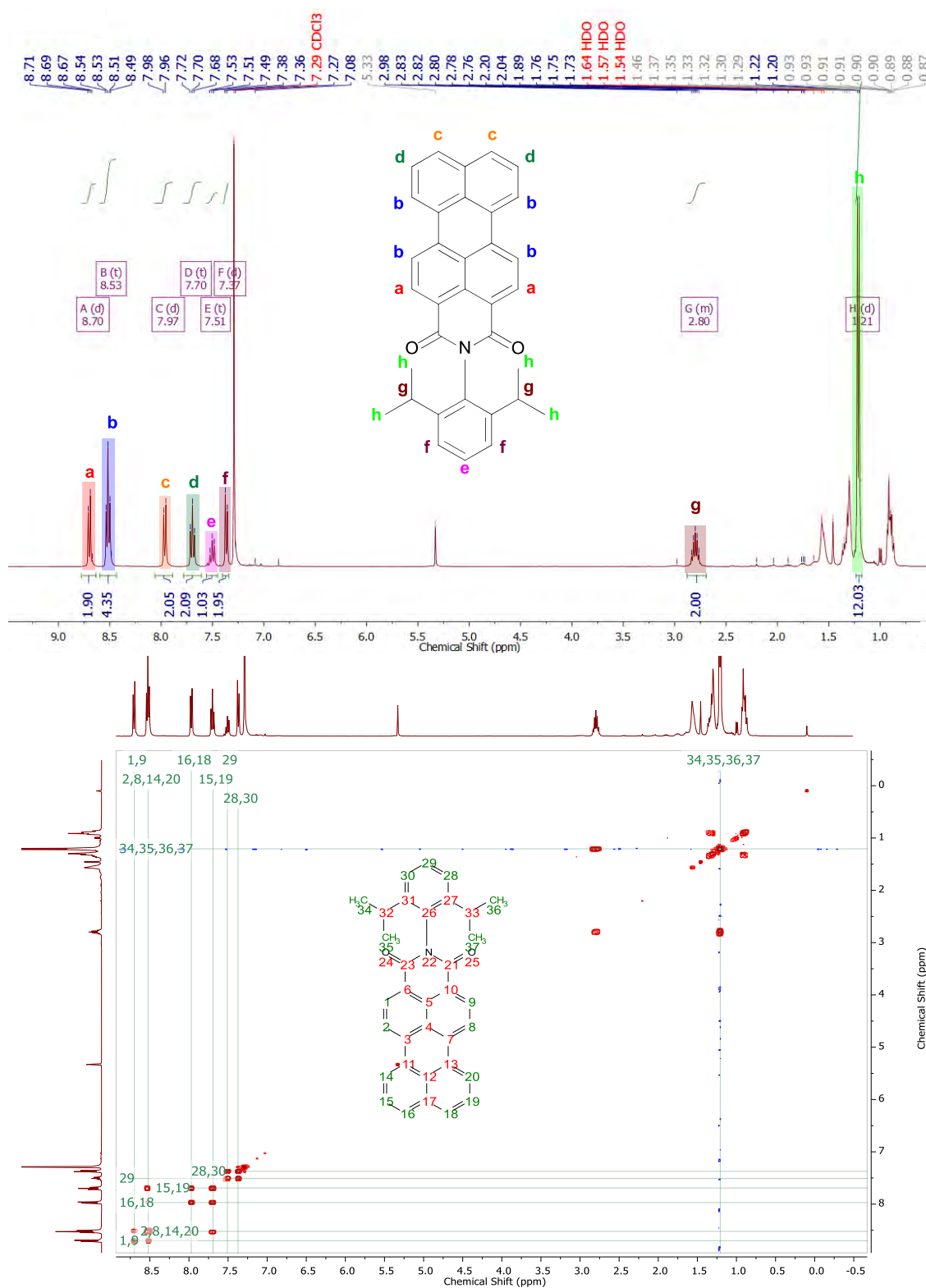
QDIBr₆ (400 mg; 0.28 mmol) and tributyl(thiophen-2-yl)stannane (730 μL; 2.23 mmol, 8 eq.) is loaded in a *Schlenk* vessel under argon atmosphere. To this, Pd(PPh₃)₄ (5 mol%; 16.2 mg, 14 μmol) is added and 10mL toluene is added to dissolve the reactants. Heat the vessel under argon at 175°C for 3 hrs in a microwave oven. After cooling, quench solution in 0.1 M HCl. Extract organic solution using a separating funnel with CF. Evaporate solvents and dry the crude solids. Perform column chromatography in SiO₂ column with DCM: Hexane (1:2) solvent mixture, to obtain brown *QDI(Th)₆* product isomer mixture. Yield: 374 mg (92%). ¹H NMR (400 MHz, Chloroform-*d*) δ 8.74 – 8.58 (m, 4H), 8.28 (d, *J* = 10.9 Hz, 2H), 7.78 (t, *J* = 9.2 Hz, 6H), 7.64 – 7.44 (m, 6H), 7.40 – 7.23 (m, 10H), 7.09 (ddd, *J* = 24.4, 5.2, 3.6 Hz, 4H), 6.83 (dd, *J* = 3.6, 1.2 Hz, 2H), 2.91 – 2.53 (m, 4H), 1.18 (d, *J* = 6.9 Hz, 24H).

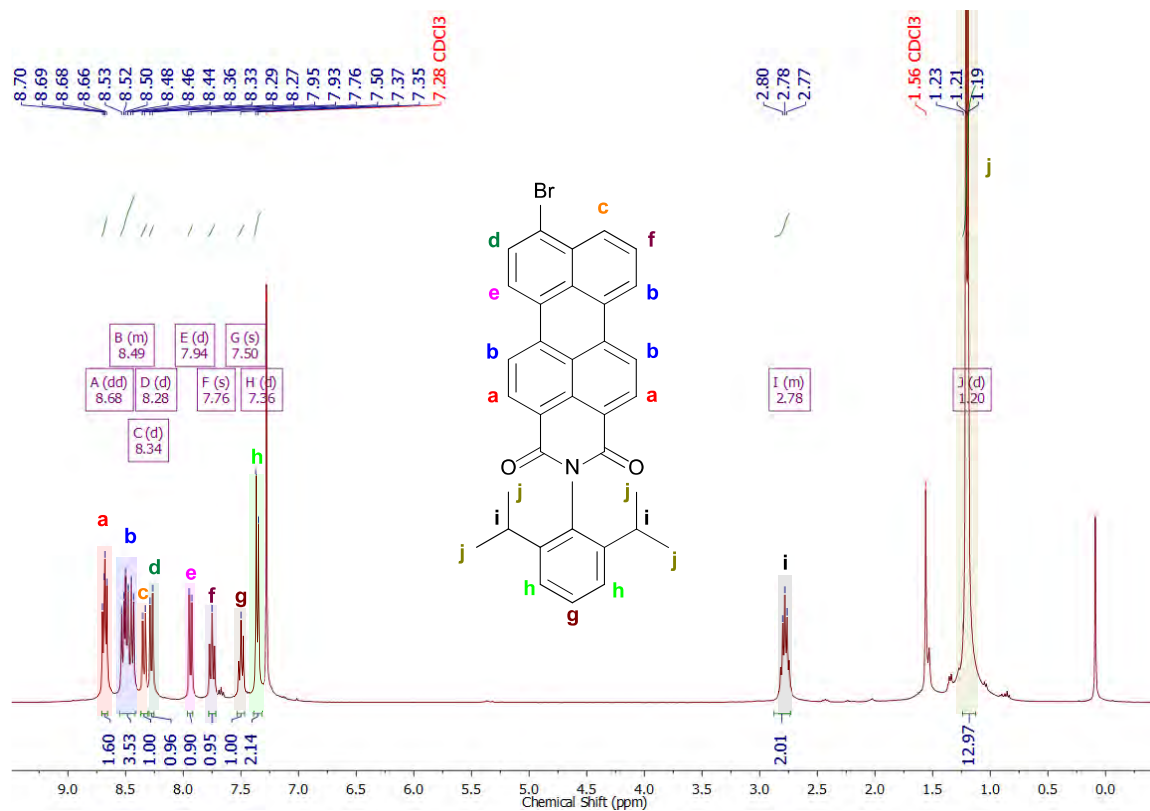
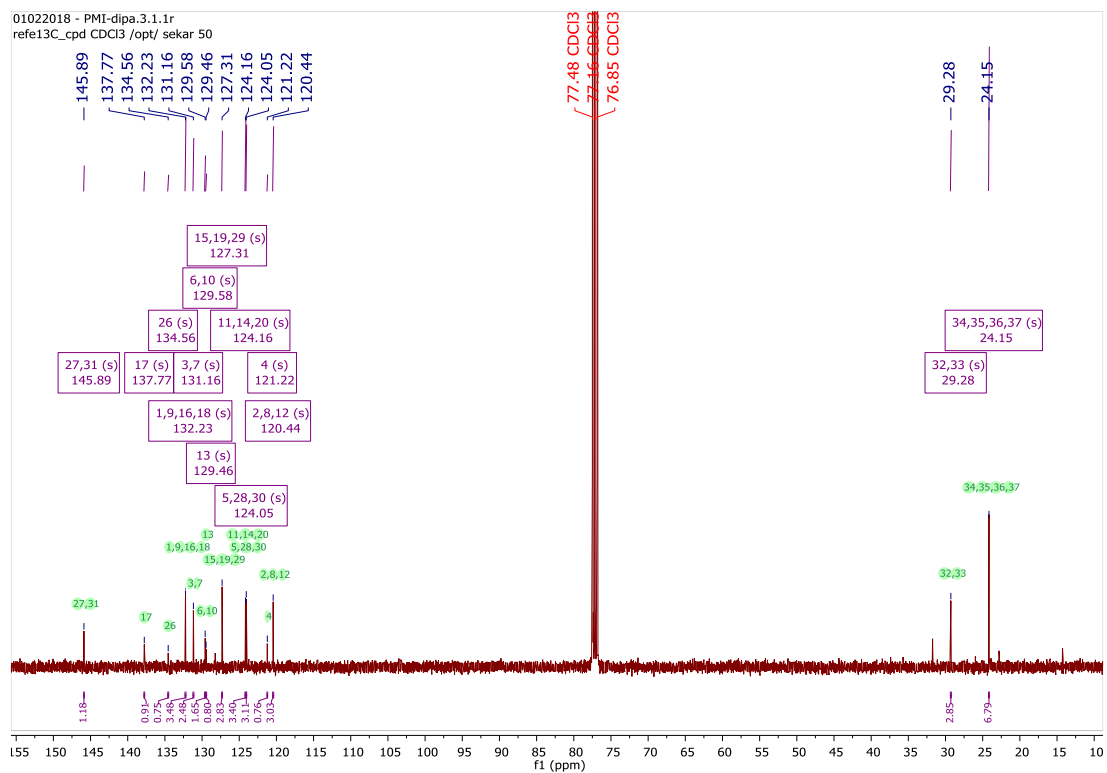
Cyclized Hexathiopheno-quaterrylene di-imide (*PC-QDI(Th)₆*)

A film of *QDI(Th)₆* spun-coat on FTO glass is subject to vapor phase iodine treatment. The substrate is taped to the walls of an air-tight vessel and a few mg of iodine pellets are added to the vessel. Seal the vessel and heat it in an oven at 120°C for 2 hours. After cooling, wash away the excess iodine carefully by soaking the substrate in methanol and drying. The different optical bandgaps can be visualized from their thin films on FTO, pictured below.



3.7.2. Miscellaneous NMR





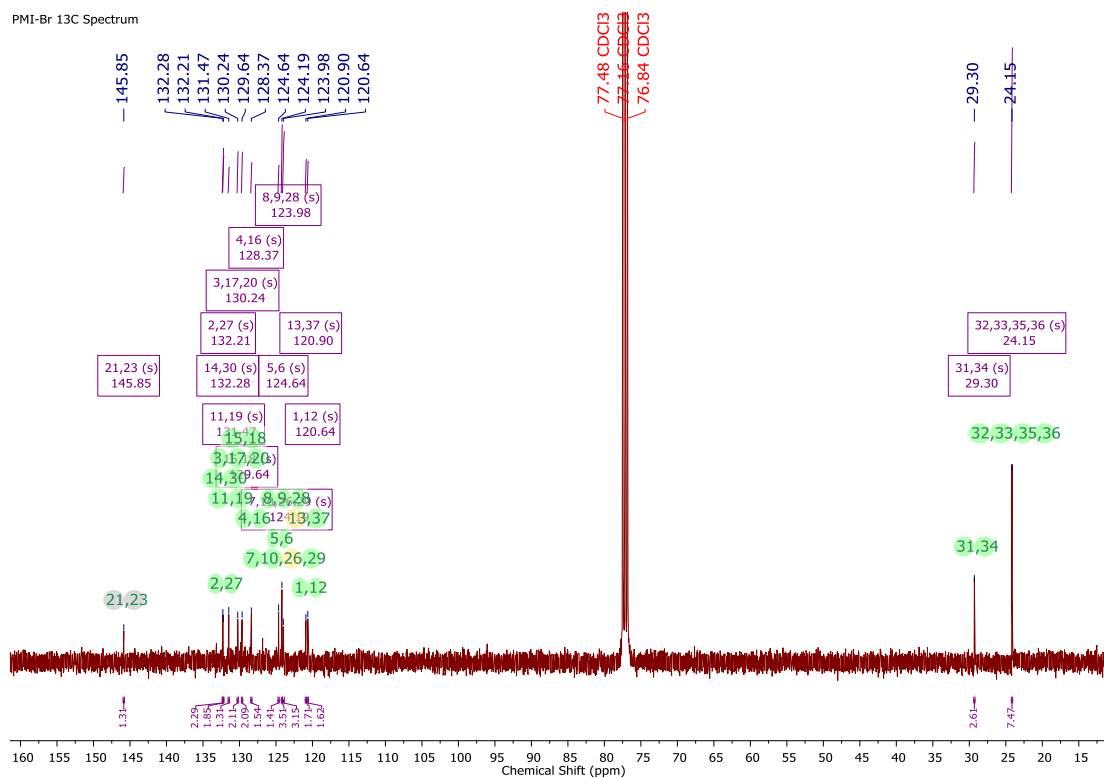
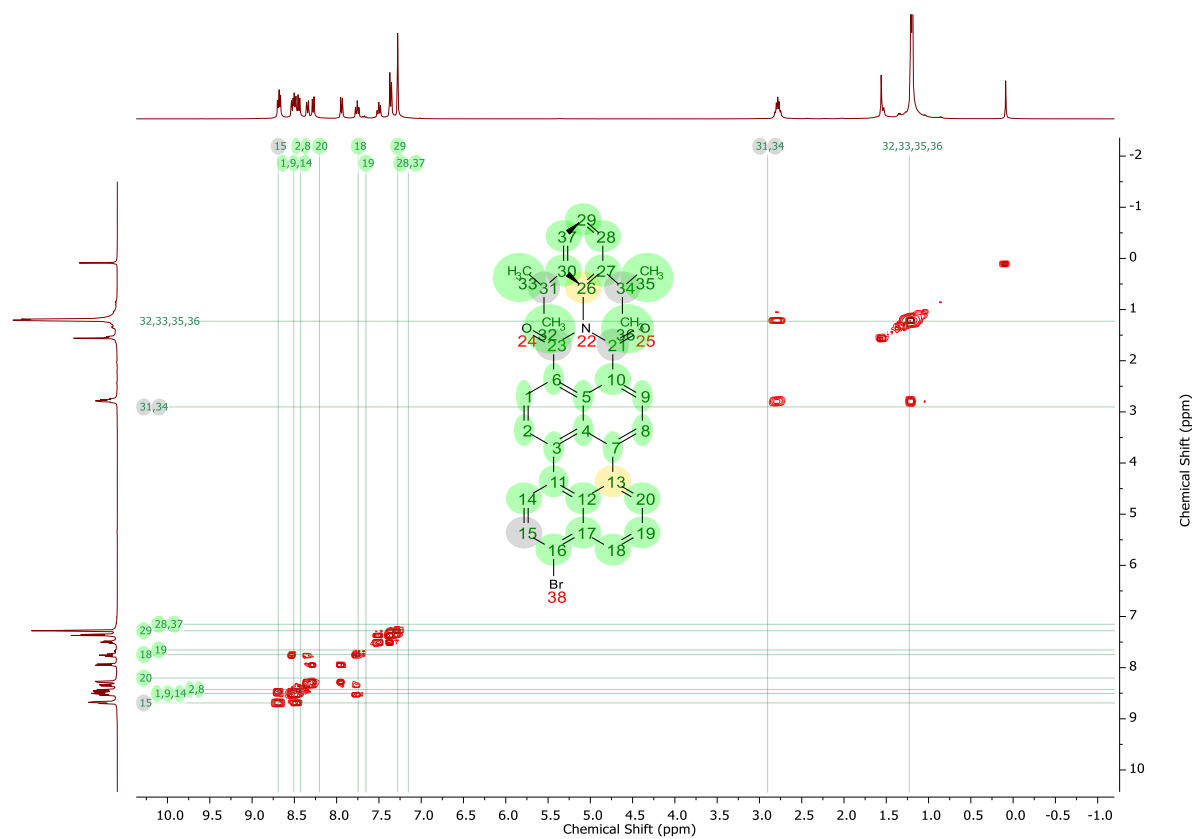


Figure 3.7.2: Complete ^1H , COSY and ^{13}C spectrum of PMI-Br

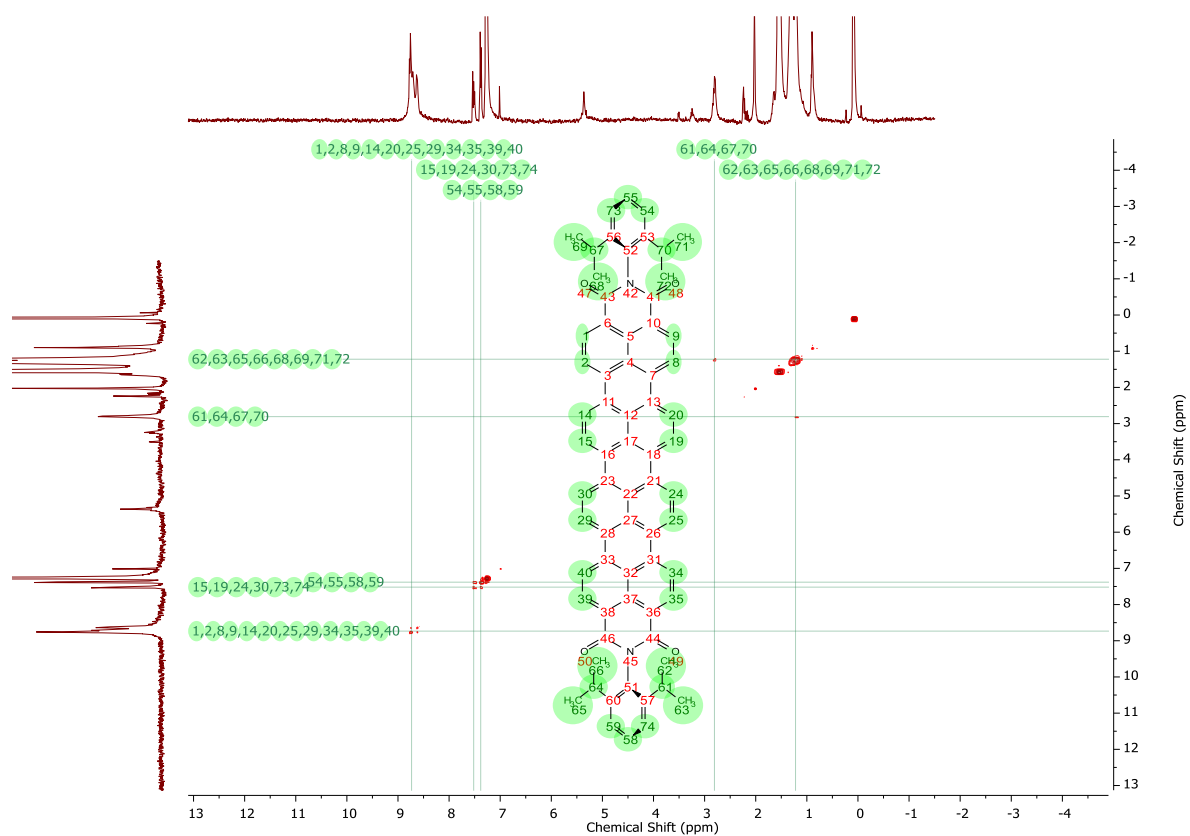


Figure 3.7.3: ^1H - ^1H COSY of **QDI** in CDCl_3 .

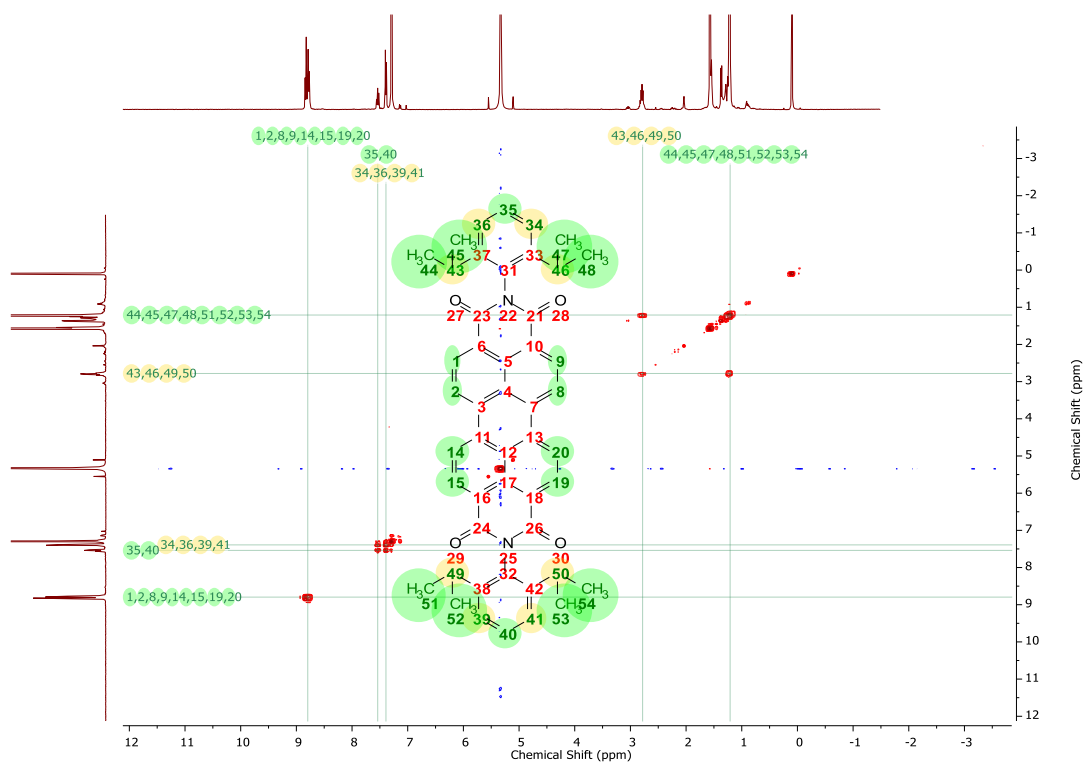


Figure 3.7.4: ^1H - ^1H COSY of **PDI-DIP** in CDCl_3 .

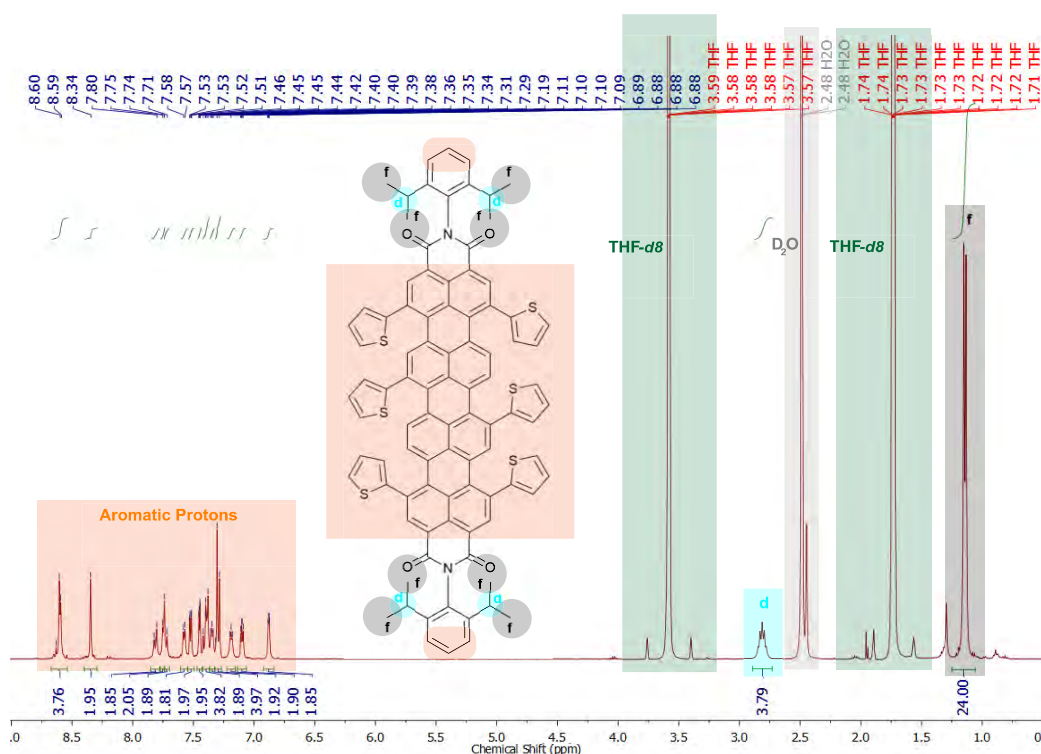


Figure 3.7.5: The whole ^1H NMR spectrum of $\text{QDI}(\text{Th})_6$.

The other relevant ^1H , ^{13}C and 2D COSY spectra of the RDIs and their derivatives are shown in Figure 3.7.1, Figure 3.7.2, Figure 3.7.3 and Figure 3.7.4. The integration factors of the protons match well with the structure, while the 2D COSY spectra helps locate neighboring protons and confirm the structure as well.

3.7.3. MALDI-TOF

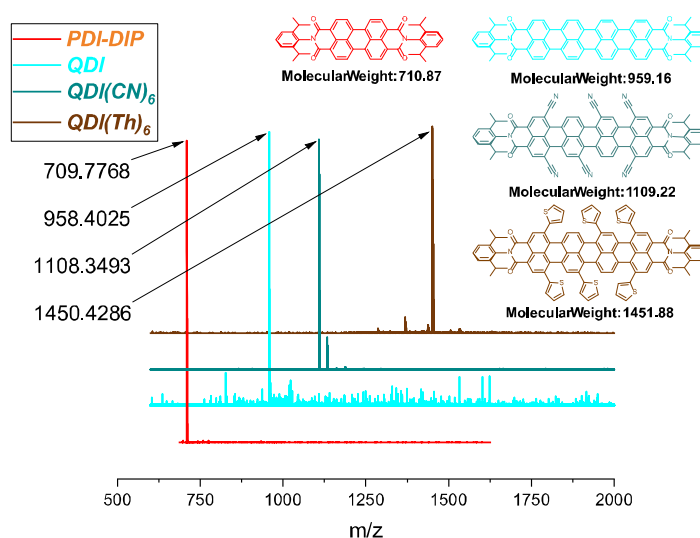


Figure 3.7.6: MALDI-TOF spectra of the synthesized OSCs.

Using a *TTh* matrix, MALDI-TOF analysis of the OSCs showed the required product peaks, hence satisfy qualitatively the presence of the products with $< \pm 2$ Da certainty (Figure 3.7.6 shows the MALDI-TOF spectra with the structures and theoretical molecular masses).

3.7.4. Miscellaneous UV-Vis Absorption Spectra

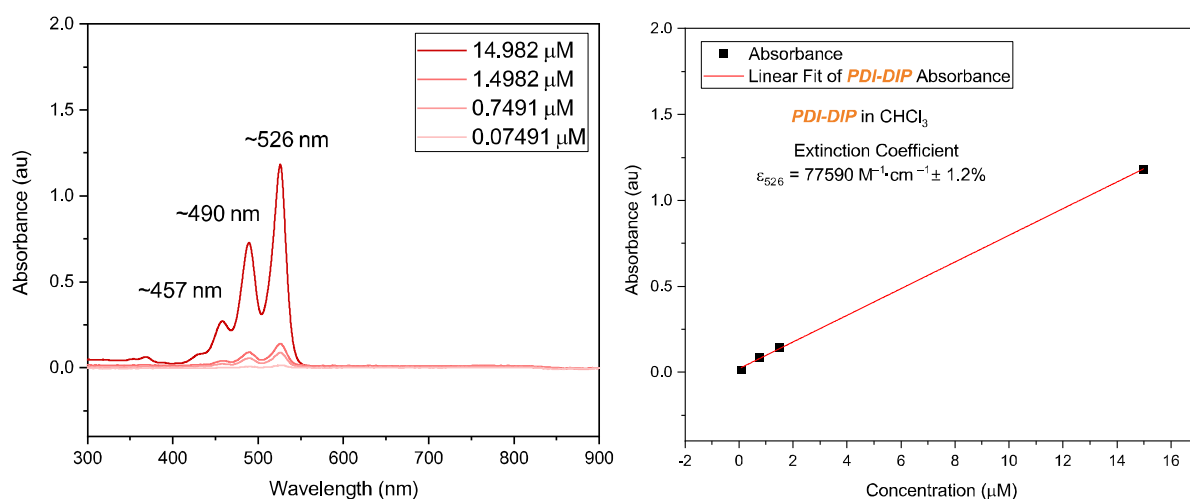


Figure 3.7.7: Solution state absorption spectra of *PDI-DIP*

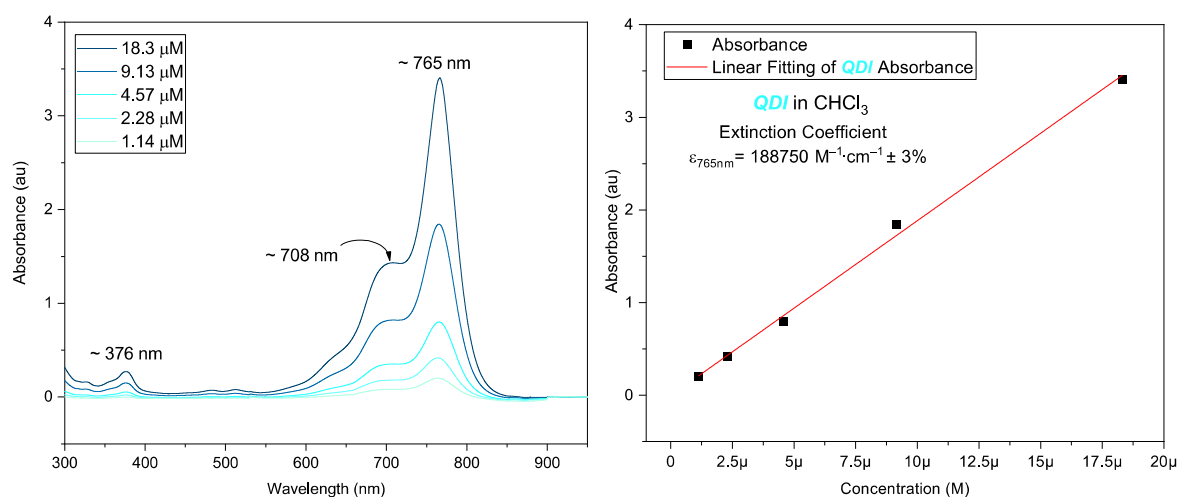


Figure 3.7.8: Solution state absorption spectra of *QDI*

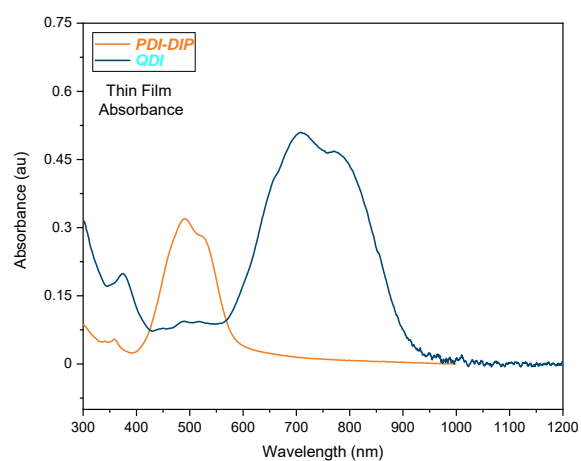


Figure 3.7.9: Solid State Absorbance of OSCs.

The Beer-Lambert plots of the RDIs dissolved in CF are in Figure 3.7.7 and Figure 3.7.8, while their solid state thin film absorption spectra is Figure 3.7.9.

3.8. References

- [1] P. Borno, M. S. Prévot, X. Yu, N. Guijarro, K. Sivula, *J. Am. Chem. Soc.* **2015**, *137*, 15338, DOI: 10.1021/jacs.5b05724.
- [2] C.-Y. Yang, M.-A. Stoeckel, T.-P. Ruoko, H.-Y. Wu, X. Liu, N. B. Kolhe, Z. Wu, Y. Puttison, C. Musumeci, M. Massetti, H. Sun, K. Xu, D. Tu, W. M. Chen, H. Y. Woo, M. Fahlman, S. A. Jenekhe, M. Berggren, S. Fabiano, *Nat. Commun.* **2021**, *12*, 2354, DOI: 10.1038/s41467-021-22528-y.
- [3] J. T. Kirner, J. J. Stracke, B. A. Gregg, R. G. Finke, *ACS Appl. Mater. Interfaces* **2014**, *6*, 13367, DOI: 10.1021/am405598w.
- [4] J. T. Kirner, R. G. Finke, *ACS Appl. Mater. Interfaces* **2017**, *9*, 27625, DOI: 10.1021/acsami.7b05874.
- [5] R. J. Kamire, K. L. Materna, W. L. Hoffeditz, B. T. Phelan, J. M. Thomsen, O. K. Farha, J. T. Hupp, G. W. Brudvig, M. R. Wasielewski, *J. Phys. Chem. C* **2017**, *121*, 3752, DOI: 10.1021/acs.jpcc.6b11672.
- [6] R. J. Kamire, M. B. Majewski, W. L. Hoffeditz, B. T. Phelan, O. K. Farha, J. T. Hupp, M. R. Wasielewski, *Chem. Sci.* **2016**, *8*, 541, DOI: 10.1039/C6SC02477G.
- [7] X. Zhao, Y. Xiong, J. Ma, Z. Yuan, *J. Phys. Chem. A* **2016**, *120*, 7554, DOI: 10.1021/acs.jpca.6b07552.
- [8] Z. Chen, Y. Zheng, H. Yan, A. Facchetti, *J. Am. Chem. Soc.* **2009**, *131*, 8, DOI: 10.1021/ja805407g.
- [9] C. Huang, S. Barlow, S. R. Marder, *J. Org. Chem.* **2011**, *76*, 2386, DOI: 10.1021/jo2001963.
- [10] S. K. Lee, Y. Zu, A. Herrmann, Y. Geerts, K. Müllen, A. J. Bard, *J. Am. Chem. Soc.* **1999**, *121*, 3513, DOI: 10.1021/ja984188m.
- [11] X. Chen, Y.-N. Wang, R.-X. Rong, C.-M. Zhao, X.-L. Li, K.-R. Wang, *Dyes Pigments* **2019**, *160*, 779, DOI: 10.1016/j.dyepig.2018.09.011.
- [12] S. Stappert, C. Li, K. Müllen, T. Basché, *Chem. Mater.* **2016**, *28*, 906, DOI: 10.1021/acs.chemmater.5b04602.
- [13] C. Liu, S. Zhang, J. Li, J. Wei, K. Müllen, M. Yin, *Angew. Chem. Int. Ed.* **2019**, *58*, 1638, DOI: 10.1002/anie.201810541.
- [14] M. Kremer, M. Kersten, S. Höger, *Org. Chem. Front.* **2018**, *5*, 1825, DOI: 10.1039/C8QO00222C.
- [15] T. N. Das, R. E. Huie, P. Neta, *J. Phys. Chem. A* **1999**, *103*, 3581, DOI: 10.1021/jp9900234.
- [16] M. Chowdhury, M. T. Sajjad, V. Savikhin, N. Hergué, K. B. Sutija, S. D. Oosterhout, M. F. Toney, P. Dubois, A. Ruseckas, I. D. W. Samuel, *Phys. Chem. Chem. Phys.* **2017**, *19*, 12441, DOI: 10.1039/C7CP00877E.

-
- [17] Y. Avlasevich, S. Müller, P. Erk, K. Müllen, *Chem. – Eur. J.* **2007**, *13*, 6555, DOI: 10.1002/chem.200700523.
- [18] P. Rajasingh, R. Cohen, E. Shirman, L. J. W. Shimon, B. Rybtchinski, *J. Org. Chem.* **2007**, *72*, 5973, DOI: 10.1021/jo070367n.
- [19] M. Takahashi, K. Asaba, T. T. Lua, T. Inuzuka, N. Uemura, M. Sakamoto, T. Sengoku, H. Yoda, *J. Org. Chem.* **2018**, *83*, 624, DOI: 10.1021/acs.joc.7b02540.
- [20] L. Perrin, P. Hudhomme, *Eur. J. Org. Chem.* **2011**, *2011*, 5427, DOI: 10.1002/ejoc.201100513.
- [21] Y. Li, W. Xu, S. D. Motta, F. Negri, D. Zhu, Z. Wang, *Chem. Commun.* **2012**, *48*, 8204, DOI: 10.1039/C2CC33529H.
- [22] S. M. Dyar, E. A. Margulies, N. E. Horwitz, K. E. Brown, M. D. Krzyaniak, M. R. Wasielewski, *J. Phys. Chem. B* **2015**, *119*, 13560, DOI: 10.1021/acs.jpcc.5b02378.
- [23] W.-L. Gong, Z.-J. Xiong, C. Li, M.-Q. Zhu, *RSC Adv.* **2014**, *4*, 64371, DOI: 10.1039/C4RA10451J.
- [24] F. O. Holtrup, G. R. J. Müller, H. Quante, S. De Feyter, F. C. De Schryver, K. Müllen, *Chem. – Eur. J.* **1997**, *3*, 219, DOI: 10.1002/chem.19970030209.

Chapter 4. Donors[†]

Using neat OSCs did not make robust and stable high performance photoanodes. In this chapter, there is a transition to a multicomponent OSC based photoanode, as suggested by the reports in 1.7.2.TF-PECs: Literature Overview. But for such BHJ type photoanodes, donors and acceptors were required. Since the donors transfer holes to the electrolyte to drive the oxidation reaction, energetically their HOMO levels need to be deep enough. Based on various donors used in OPVs, thiophene dicarboximide (TPD) based donors were chosen as possible candidates. This chapter focuses on the synthesis and characterization of donor polymers for photoanodes and the PEC investigation of neat donors on ETL.



[†]Part of this chapter is used in a manuscript submitted to *ACS Applied Materials & Interfaces* (Under Review).

4.1. Motivation

The options for donors and acceptors should be looked at, from an energetic perspective. The commonly used donors do not possess deep energy levels as is shown in Figure 4.1.1,^[1] thereby leading to smaller or negligible thermodynamic driving force for water oxidation.

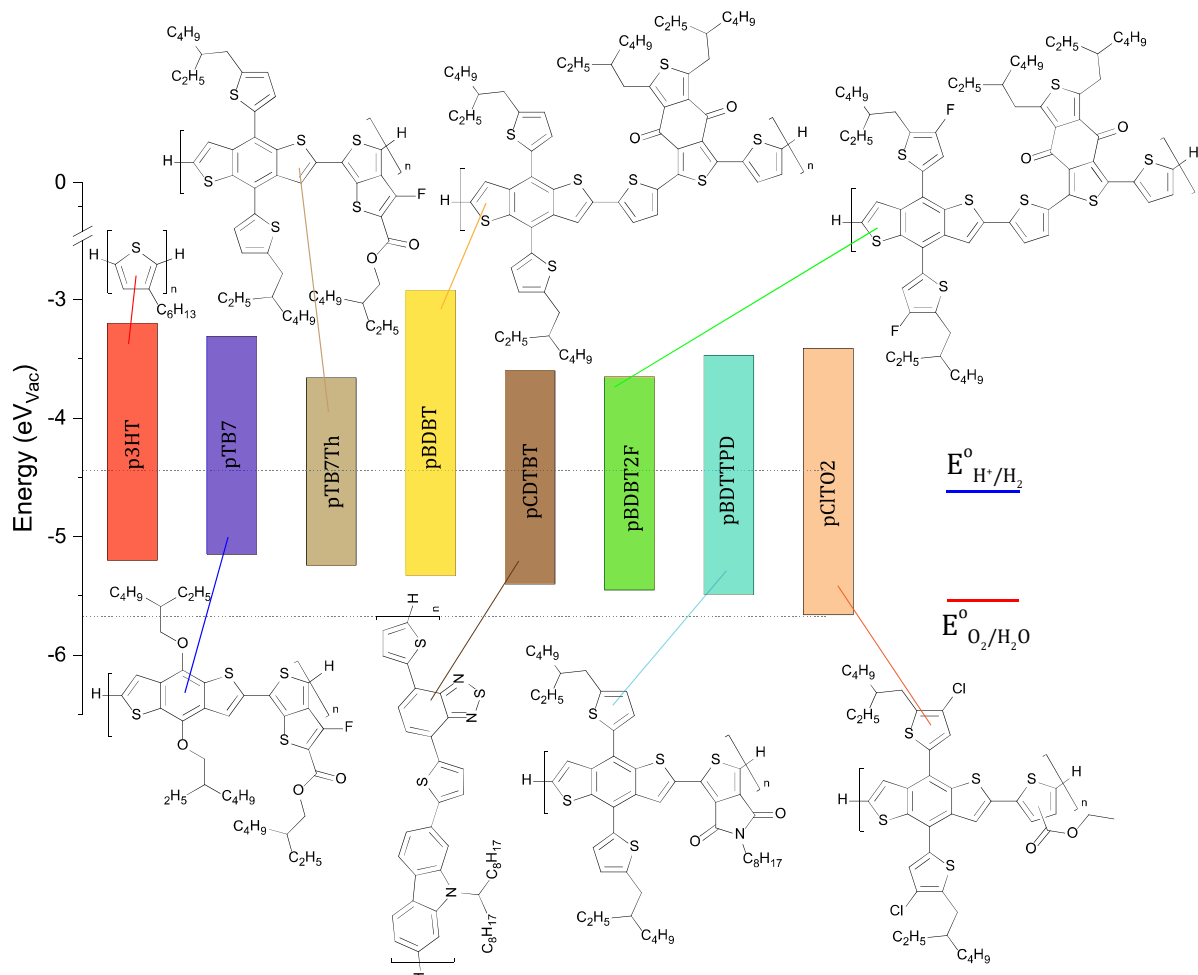


Figure 4.1.1: Various p-type donor OSCs with their energy levels matched vs. water oxidation and reduction potentials.

From previous work,^[2] the pBDTTTPD donor polymer was shown to oxidize water. The goal is to show that other donor candidates, with similar or deeper HOMO levels too, show photoanodic capabilities, compared to donors with shallower HOMO levels. A few recent publications in the OPV field show the use of the benzodithiophene (BDT) core modified polymers,^[3-5] resulting in wide bandgap p-type donors with device PCE~14-15%. Similarly, the traditionally used PTB7-Th polymer was also modified with a chlorinated BDT core,^[6] resulting in a polymer homologue with similar bandgap, but with HOMO levels deepened by ~200meV.

So, by combining the core of the donor from pBDTTTPD (hereby named **P1**), a homologue with BDT-2Cl was synthesized (pBDTTCITPD, hereby named **P2**), and its opto-electronic and photoanodic properties was compared with **P1**.

4.2. Synthesis

The goal is to synthesize a series of p-type low HOMO donor polymers containing TPD monomeric units.

For both the polymers, a Pd-catalyzed *Stille* polycondensation reaction was carried out in a microwave vial, initially in small batches of ~100mg reactants similar to the previously published work, but finally in larger quantities during scale-up (Reaction Scheme in Figure 4.2.1).^[2] Negligible differences in yield and polymer molecular weights were observed between batches of the same polymers.

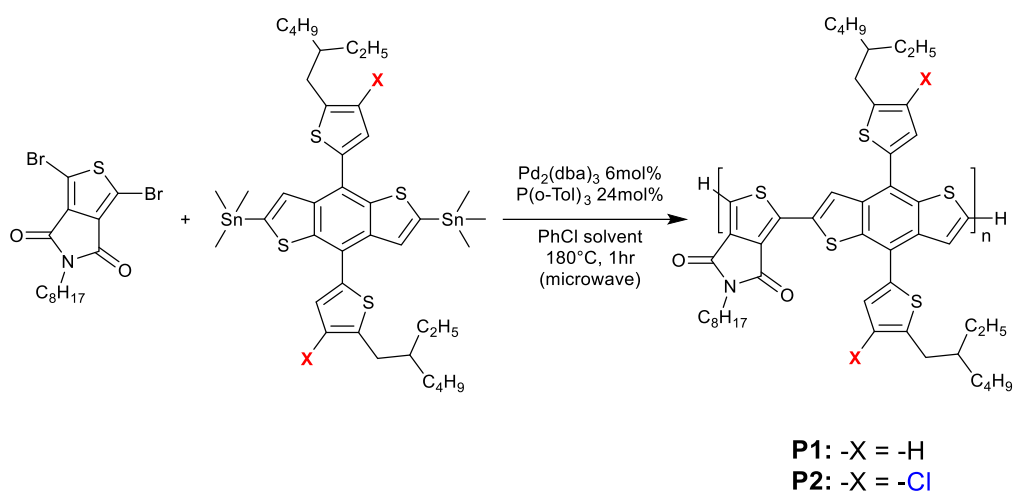


Figure 4.2.1: Stille Polycondensation reaction for **P1** and **P2**.

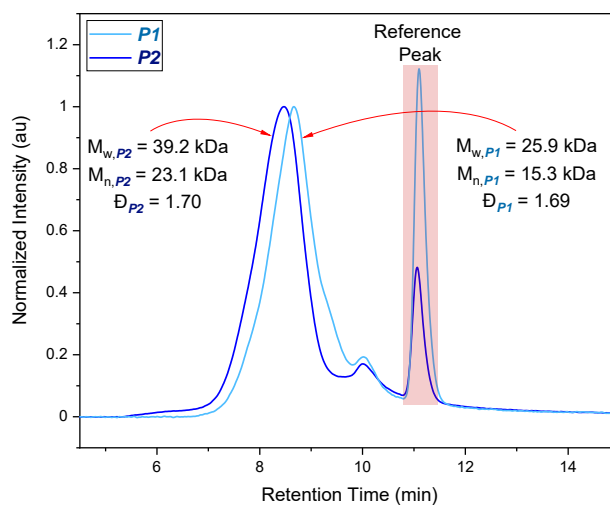


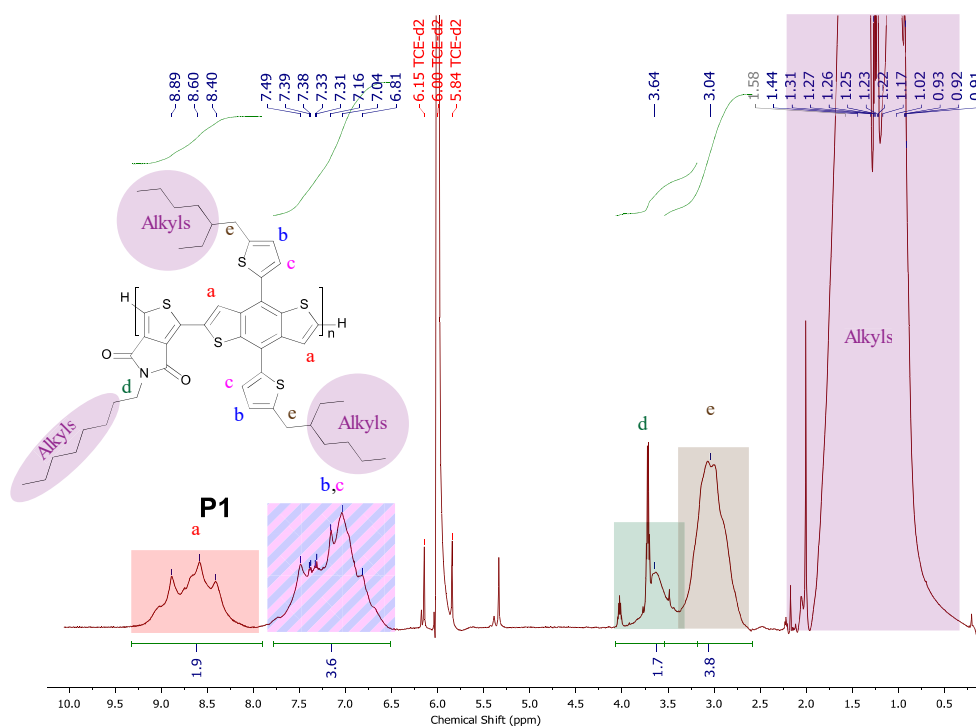
Figure 4.2.2: Gel Permeation Chromatogram of **P1** and **P2** polymerized under identical reaction conditions.

An overall observation was the increase in molecular weights of **P2** compared to **P1** in the same reaction conditions (Gel Permeation Chromatogram spectra in Figure 4.2.2). This is possibly a direct effect of the increased solubility of **P2** (due to side chains consisting of the bulky Cl- substituents, which increases the twist due to the breaking of symmetry and the presence of an additional dipole moment within the molecule).^[7]

This effect of increased solubility firstly helps increase the overall extent of polymerization during the reaction due to the dissolution of all the oligomeric species, as typical step-growth polymerization proceeds. In the case of **P1**, it is possible that due to the saturation of chlorobenzene with oligomers, after a certain point the species involved in polymerization precipitate out, and the homogeneous catalyst loses reactive species. During the soxhlet extraction, even poor solvents like hexane and EtOAc, elute out purple colored species (indicating extended conjugation) in **P2**, as opposed to pale yellowish elution from **P1** (indicating only monomers and oligomers being washed away). All these factors are reflected in the qualitative Gel Permeation Chromatogram of the polymers, which show a 1.5x increase in both M_n and M_w for **P2** with respect to **P1**.

4.3. Characterization

4.3.1. NMR



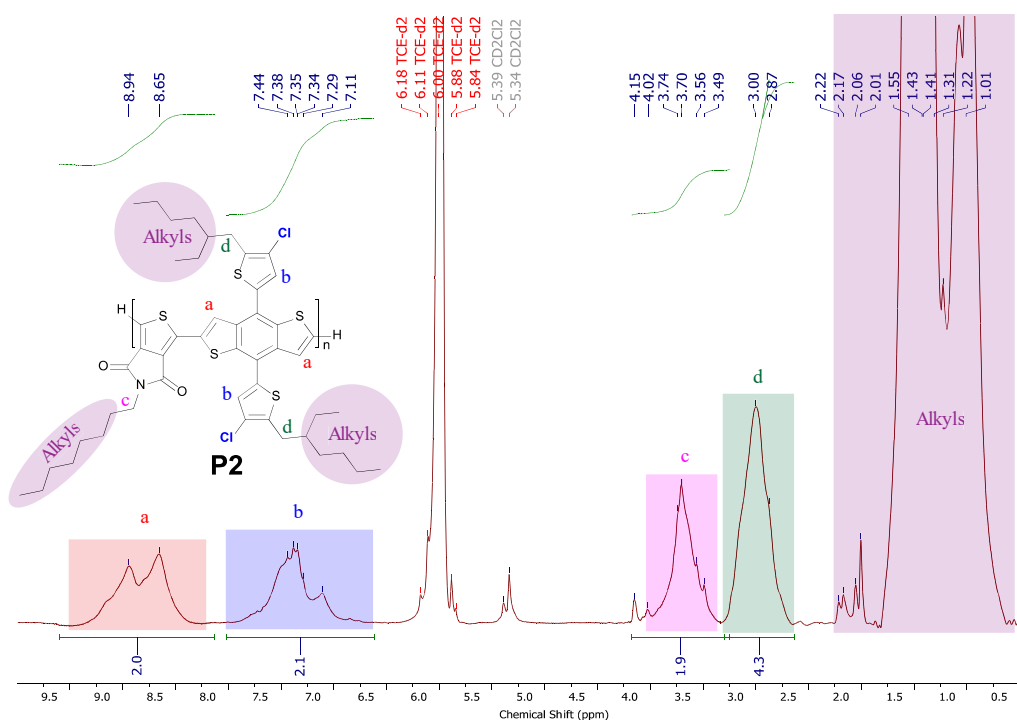


Figure 4.3.1: High Field (600 MHz) ^1H NMR spectra of (Top) **P1** and (Bottom) **P2** in CD_2Cl_4 at 60°C .

High field (600 MHz) ^1H NMR was used to characterize the two polymers in CD_2Cl_4 at 60°C to reduce aggregation of the polymer chains in the NMR tube.

The peaks in the aromatic region of **P1** integrate well in 1:2 ratio and of **P2** in 1:1 ratio, indicating a good match with the theoretical structure (without and with $-\text{Cl}$ units in the thiophene side chains of BDT core; ^1H NMR spectra in Figure 4.3.1).

4.3.2. UV-Vis Absorption

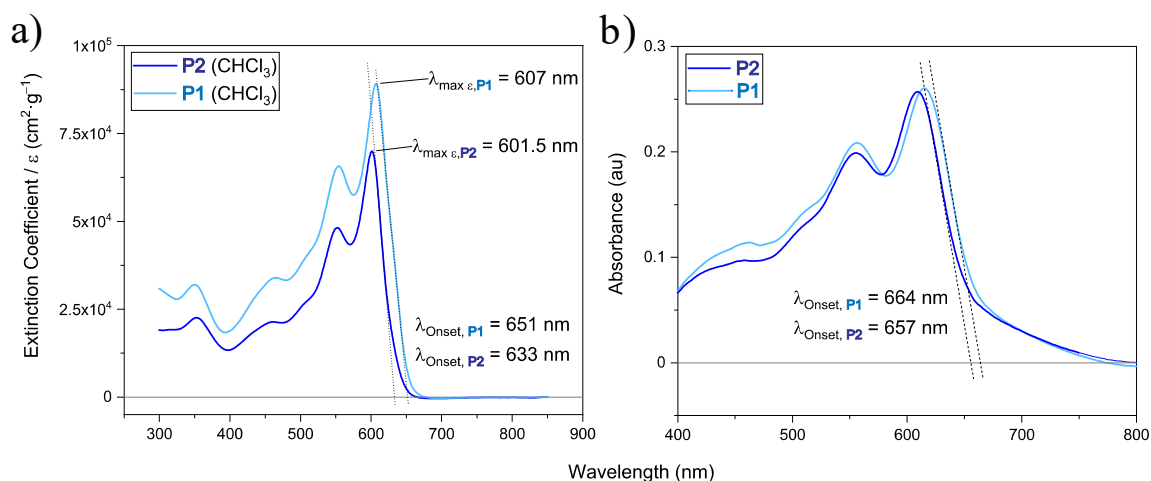


Figure 4.3.2: a) Solution state absorption spectra, b) Solid state absorption spectra of **P1** and **P2**.

The optical properties of **P1** are only slightly affected due to the chlorine group substituents. From the solution state UV-Vis absorption spectra (Figure 4.3.2a) in CF, **P1**

has a higher extinction coefficient due to its higher number of symmetry modes. It is slightly more red-shifted than **P2**, with an onset shift ~ 20 nm.

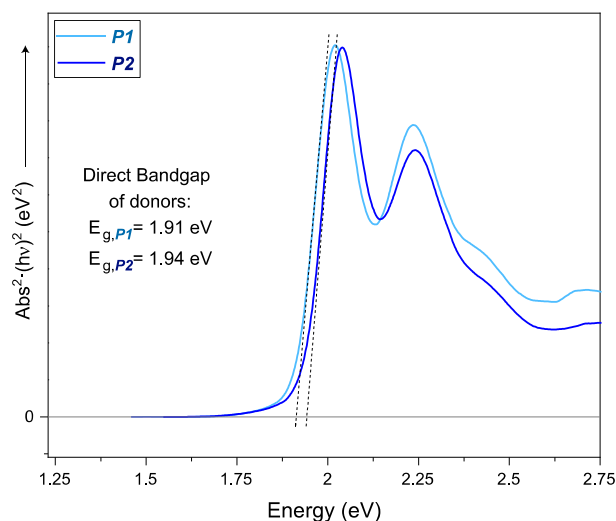


Figure 4.3.3: Tauc relation in the solid-state thin films of **P1** and **P2**.

In the solid state (Figure 4.3.2b), this onset difference reduces to 7nm, indicating almost similar optical properties in the donor polymers. Converting the absorption spectra into units for calculating the $E_{g,opt}$ using the Tauc relation (Figure 4.3.3), the $E_{g,opt,P1} = 1.91$ eV and $E_{g,opt,P2} = 1.94$ eV by extrapolation.

4.3.3. Cyclic Voltammetry

Scanning through a wide window of applied potentials, the oxidation and reduction curves of the donors were observed (electrochemical CV spectra in Figure 4.3.4). By locating the onset of the peaks, the corresponding HOMO and LUMO levels can be determined electrochemically.

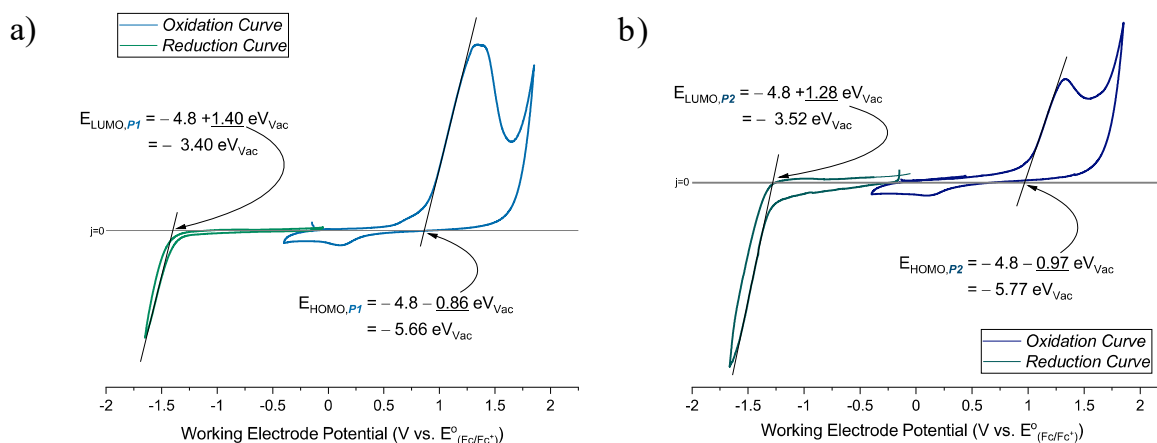


Figure 4.3.4: Redox curves in conductive acetonitrile with potentials vs. Ferrocene redox for a) **P1** and b) **P2** donors.

P2 has its HOMO about 110 meV lower than **P1**, due to electronegative chlorine units and higher molecular weights. Indeed, of most reported p-type donor polymers, this value is one of the deepest. $E_{g,elec}$ given by the HOMO-LUMO difference is 2.26 eV for **P1** and 2.25 eV for **P2**, which is about 300 meV higher than their $E_{g,opt}$, due to additional interfacial barrier for charge insertion.

4.3.4. TFT: Mobility

In general, the trend observed is that **P1** has lower hole mobilities than **P2**, both with and without thermal annealing (hole mobilities summarized in Figure 4.3.5, also showing a sample I-V curve), and the numerical values are mentioned below. Each case is an average of 4 transistors with channel width of 20 μm .

$$\mu_{FET,h^+,\mathbf{P1},As\ Cast} = 4.10 \times 10^{-5} \text{ cm}^2 \text{ V}^{-1} \text{ s}^{-1} \pm 33\%$$

$$\mu_{FET,h^+,\mathbf{P1},Annealed} = 1.02 \times 10^{-4} \text{ cm}^2 \text{ V}^{-1} \text{ s}^{-1} \pm 11\%$$

$$\mu_{FET,h^+,\mathbf{P2},As\ Cast} = 3.18 \times 10^{-4} \text{ cm}^2 \text{ V}^{-1} \text{ s}^{-1} \pm 11\%$$

$$\mu_{FET,h^+,\mathbf{P2},Annealed} = 9.23 \times 10^{-4} \text{ cm}^2 \text{ V}^{-1} \text{ s}^{-1} \pm 8\%$$

On an average, **P2** results in 7.8x increase in hole mobilities in as cast conditions, and approximately 9x increase when annealed thermally, compared to **P1**.

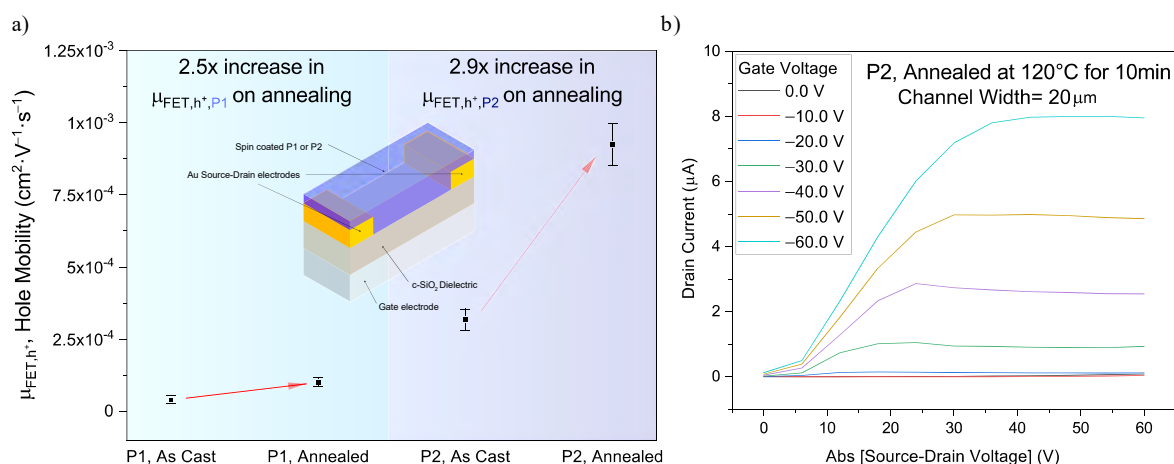


Figure 4.3.5: a) Summary of hole mobilities in the polymers, b) an example j-V curve showing saturated source-drain currents.

4.4. PEC performance

As a prologue to BHJ, the neat polymers were spin-coat onto $\text{mSnO}_2/\text{pSnO}_2/\text{FTO}$ substrates, which were treated with a SAM consisting of benzoic acid (more details in later

chapters). The electrolyte was 1 M KPi buffered at pH 6.8 containing 1.5 M sodium sulfite sacrificial reductant. The graphs in Figure 4.4.1 show LSV and CA under 1-sun chopped light illumination.

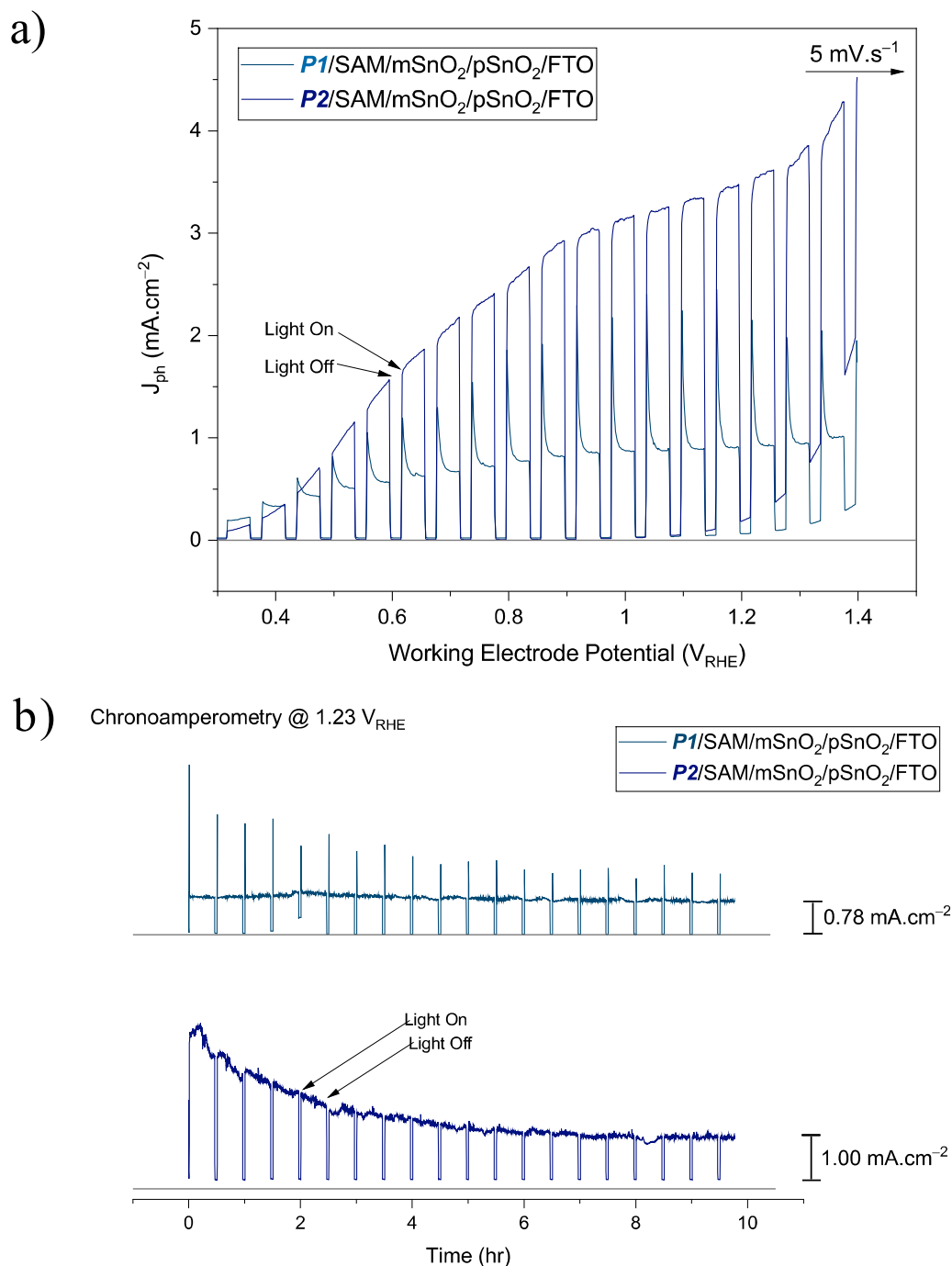


Figure 4.4.1: a) LSV curves b) CA curves (@1.23V_{RHE}) of **P1** and **P2**, in a pH 6.8 KPi buffer with 1.5 M sulfite.

P2 has a higher initial and final J_{ph} under similar conditions as **P1**, showing a potential overall improvement in the PEC performance. Additionally, from Figure 4.4.2, the reduction in J_{ph} does not correspond to polymer degradation under operation, as the

reduction in the absorption spectra of the films does not completely correspond to the larger loss in J_{ph} . This reduction in J_{ph} on operation is distinctly dissimilar to the loss in J_{ph} seen with the **QDI** molecules, which lose a major percentage of J_{ph} within a few seconds.

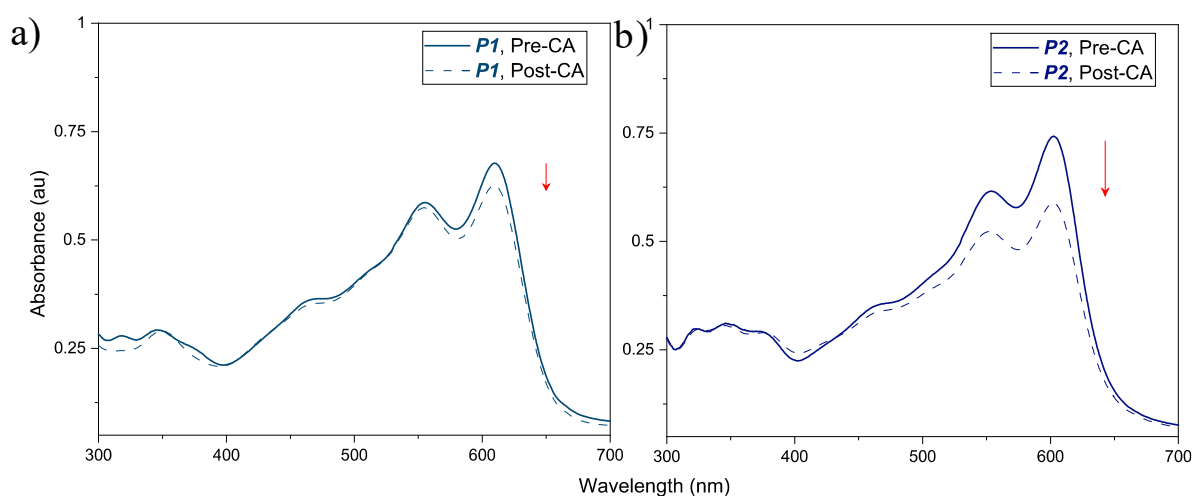


Figure 4.4.2: Absorption spectra of the a) **P1** and b) **P2** based photoanodes before and after CA operation at 1.23 V_{RHE}

4.5. Conclusion

Two donor polymers **P1** and **P2** which are structural homologues belonging to the TPD family were synthesized. Their synthesis, optical and electrochemical characterization are discussed in this chapter. Owing to electronegative groups, their HOMO levels are quite stabilized and positive to thermodynamically transfer holes to the electrolyte and drive oxidation reactions. Additionally, the novel polymer **P2** is shown superior to the **P1** polymer in terms of molecular weights, hole mobilities and J_{ph} . In the later chapters, BHJ photoanodes using these polymers will be discussed.

4.6. Supporting Information

4.6.1. Synthesis

P1 (pBDTTTPD)

4,8-bis(5-(2-ethylhexyl)thiophen-2-yl) benzo[1,2-b:4,5-b'] dithiophene-2,6-diyl) bis(trimethylstannane) (64 mg, 1 equiv.) and 1,3-dibromo-5-octyl-4H-thieno[3,4-c] pyrrole-4,6(5H)-dione (30 mg, 1 equiv.) were placed in a vial for microwave reactor and degassed with argon. Then, the vial was transferred to an Argon glove box to add $Pd_2(dba)_3$ (3.84 mg, 6 mol%), $P(o-tol)_3$ (5.12 mg, 24 mol%) and dry chlorobenzene (2.8 mL to have a concentration of reactants at 0.05M). The vial was sealed with a cap and placed in the

microwave reactor. The mixture vigorously stirred at 180 °C for 1 hr. After cooling to room temperature, the resulting mixture was precipitated into methanol (50 mL). Multiple runs of this reaction in the same scale were repeated. After 6 runs, the precipitated polymer was placed in Soxhlet filter and was purified by extraction with methanol, hexane, acetone, and chloroform. The final chloroform fraction was re-precipitated into methanol, isolated by the filtration, and dried under vacuum for 24 h.

P2 (pBDTTCITPD)

Follows the exact procedure as for **P1**, but instead with (4,8-Bis(4-chloro-5-(2-ethylhexyl) thiophen-2-yl) benzo[1,2-b:4,5-b'] dithiophene-2,6-diyl) bis (trimethyl stannane) monomer. After 3 runs and soxhlet extraction, the chloroform eluted fraction on drying yielded 150mg, 79%.

4.7. References

- [1] Data taken from Ossila website: Donor Polymers like P3HT, PCE10 etc., <https://www.ossila.com/products/pce10>, accessed August 17, **2021**.
- [2] H.-H. Cho, L. Yao, J.-H. Yum, Y. Liu, F. Boudoire, R. A. Wells, N. Guijarro, A. Sekar, K. Sivula, *Nat. Catal.* **2021**, 4, 431, DOI: 10.1038/s41929-021-00617-x.
- [3] Y. Cui, H. Yao, L. Hong, T. Zhang, Y. Xu, K. Xian, B. Gao, J. Qin, J. Zhang, Z. Wei, J. Hou, *Adv. Mater.* **2019**, 31, 1808356, DOI: 10.1002/adma.201808356.
- [4] K. He, P. Kumar, Y. Yuan, Y. Li, *Mater. Adv.* **2021**, 2, 115, DOI: 10.1039/D0MA00790K.
- [5] H. Yao, Y. Cui, D. Qian, C. S. Ponseca, A. Honarfar, Y. Xu, J. Xin, Z. Chen, L. Hong, B. Gao, R. Yu, Y. Zu, W. Ma, P. Chabera, T. Pullerits, A. Yartsev, F. Gao, J. Hou, *J. Am. Chem. Soc.* **2019**, 141, 7743, DOI: 10.1021/jacs.8b12937.
- [6] P. Chao, Z. Mu, H. Wang, D. Mo, H. Chen, H. Meng, W. Chen, F. He, *ACS Appl. Energy Mater.* **2018**, 1, 2365, DOI: 10.1021/acsaem.8b00506.
- [7] T. Zheng, A. M. Schneider, L. Yu, in 'Synthetic Methods for Conjugated Polymers and Carbon Materials', John Wiley & Sons, Ltd, **2017**, pp. 1, DOI: 10.1002/9783527695959.ch1.

Chapter 5. Acceptors[†]

From Chapter 3, the conclusion is that probably using neat OSCs does not make robust and stable high performance photoanodes. Hence, the transition to a multicomponent OSC based photoanode. In addition to donors, acceptors need examination. This chapter deals with a series of acceptors which can energetically complement the low HOMO donors from Chapter 4. This series of NFA molecules have stabilized MO levels due to electronegative groups and complement **P1** and **P2** thermodynamically and optically. Their synthesis, optical and electrochemical characterization is discussed here. In the subsequent chapters, these acceptors would be coupled with the polymer donors to form BHJ photoanodes.



[†]Part of this chapter is used in a manuscript submitted to *ACS Applied Materials & Interfaces* (Under Review).

5.1. Motivation

To form a BHJ, in addition to the donor polymers, there exists a requirement for electron poor n-type acceptors to complement the donors electronically. In the OPV field, there exists a large library on n-type acceptors, ranging from the traditionally used fullerene based molecules (PC₆₁BM,^[1,2] PC₇₁BM^[3]) to the recent small molecule acceptors with indacenodithiopheno-(ITIC derivatives^[4–6]) or thienothienopyrrolo-(Y6,Y7^[7,8] etc.) derivatives as non-fullerene acceptors (NFAs).

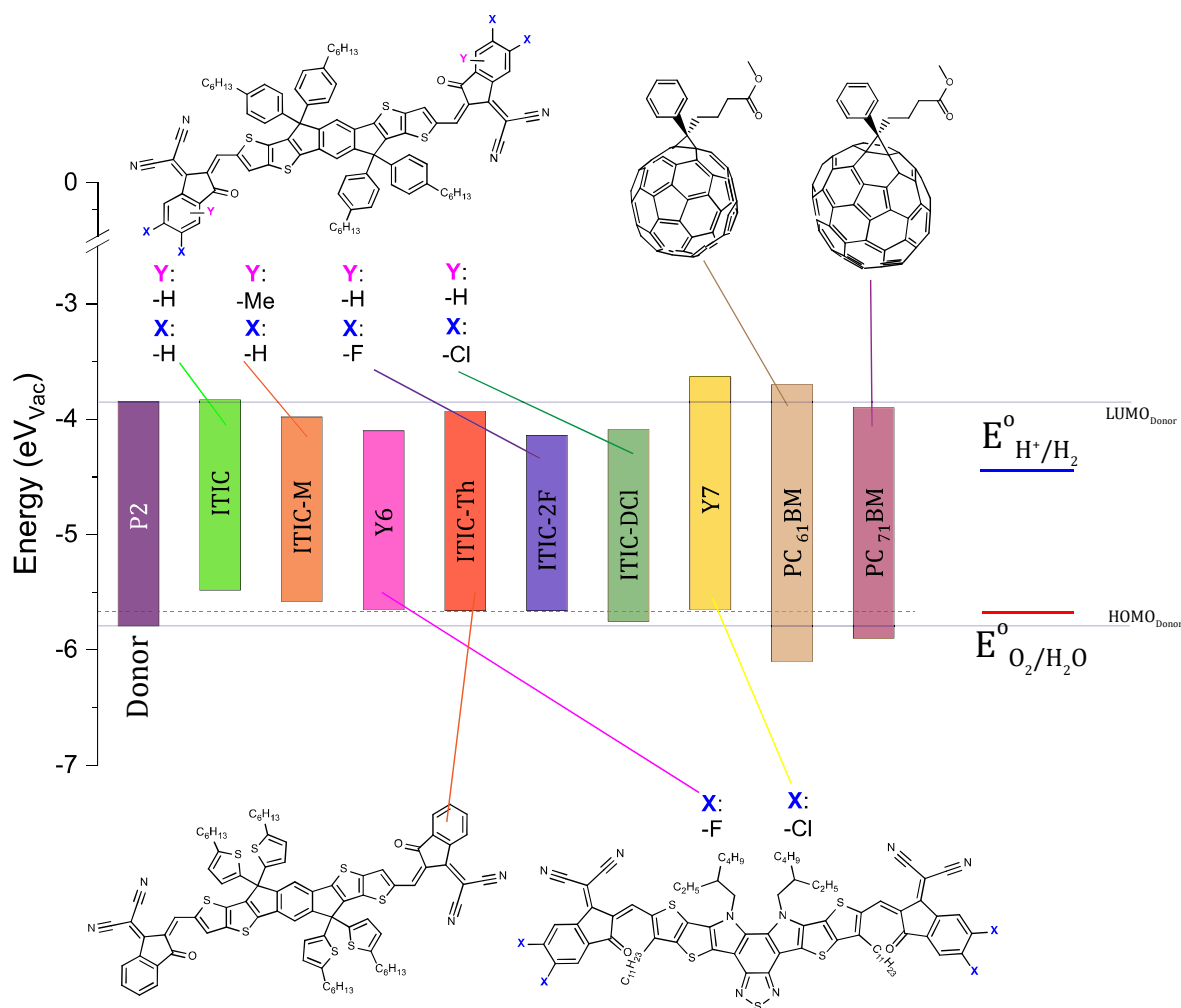


Figure 5.1.1: n-type acceptors with their energy levels matched vs. water oxidation, reduction potentials and **P2** donor.

While NFAs offer significant advantages in terms of operational stability,^[9] extended absorption up to the near-infrared region and overall increase in PCE%,^[10] such high performance NFAs cannot be used with **P2** to make D:A pairs, due to energy level mismatch, as shown in Figure 5.1.1.^[11] Besides, these OSCs are also quite expensive. Thus, there is a need for novel acceptors with deeper energy levels for photoanodes.

From the previous attempts at an OSC based photoanode, neat n-type RDI-based molecules were used both in DS-PECs and TF-PECs (1.7.Organic Semiconductors for PEC Water Oxidation[†]). These molecules, have longer bandgaps and deeper band-edges, and hence could be used as acceptors with **P2**. For extended conjugation and smaller bandgap vertically expanding the conjugated core (**QDI**, Chapter 3) was tried, but due to issues of solubility and destabilized MO levels, the **QDI** was not a viable candidate, despite modifications (ex. **QDI(CN)₆** etc.).

Instead of vertical extension, there have been earlier reports of laterally extending the core of RDIs. This is more common with n-type polymers like N2200,^[12] PDI-V^[13] etc. which are prominent in OPVs and even OSC based photocathodes. But typically, all polymer solar cells have always shown smaller J_{ph} and PCE% than polymer(donor)- small molecule(acceptor) BHJ systems.^[14] Thus, an alternate way of laterally expanding the conjugation in RDIs, i.e., by oligomerization with itself, is proposed.

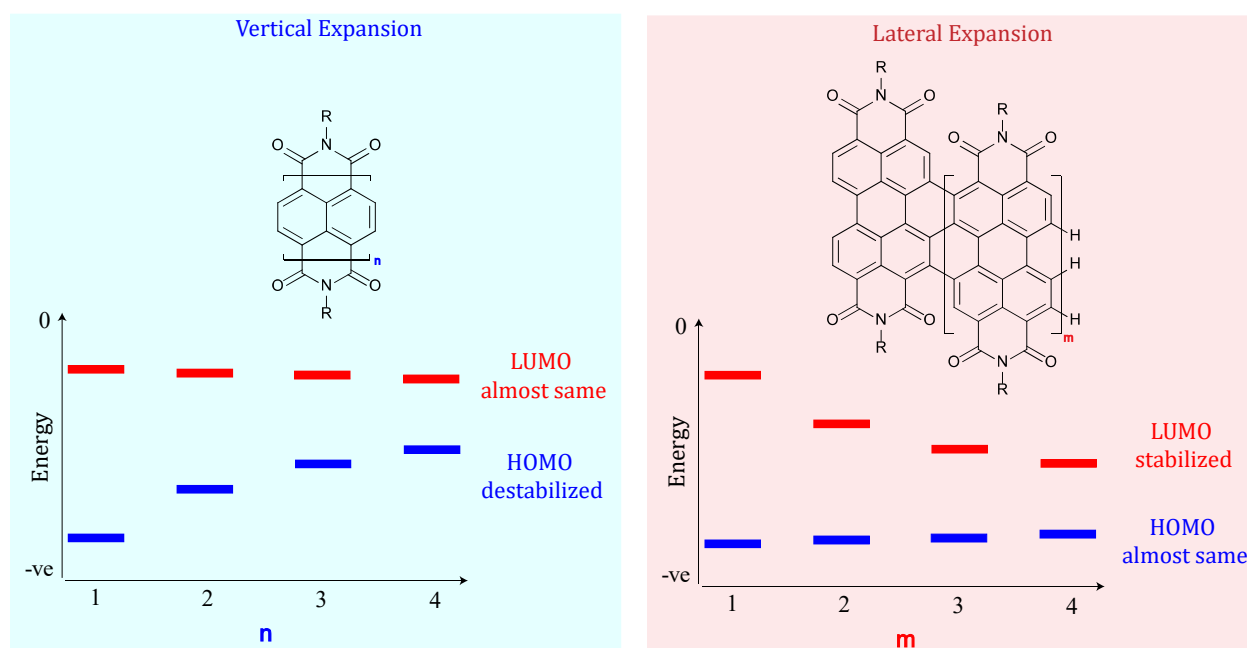


Figure 5.1.2: Scheme showing extended conjugation of RDIs and effect on HOMO-LUMO levels.

When *more than one covalent bond* is present between two RDI molecules, the structure has extended conjugation like a ladder polymer (BBL, **QDI** etc.). While extended conjugation leads to smaller bandgaps in the OSCs, the effect on specific MO levels is different depending on the method of extension. Schematically, the effect of “ladderizing” RDI with itself on the MO levels is shown in Figure 5.1.2, as opposed to vertically elongating RDIs.

This has indeed been done previously, and the resulting OSCs have been used in n-type OFETs,^[15–17] and in OPVs^[18,19] with limited success, mostly due to issues of aggregation. If bulky groups in the bay positions of the OSC are introduced, the aggregation can be broken apart, as in the case of an OFET,^[16] and this idea is implemented in the next section to synthesize acceptors.

5.2. Synthesis

The goal is to synthesize a series of n-type laterally expanded perylene diimide acceptors.

5.2.1. Optimizing oligomerization pathway

From previously demonstrated works,^[19,20] the method to obtain laterally expanded, triply linked perylene di-imide is primarily Cu- promoted *Ullmann* coupling. The main drawback of this reaction is the sensitivity to reaction temperature and poor yields. The active species on the n-type core needed to expand are the halide groups: -Cl, -Br or -I. At high temperature, the species simply dehalogenates instead of coupling, in the presence of copper. Therefore, the yields reported are often low. Here, in addition to the usual reactants, promoter, ligand and base, an excess of tetra-n-butyl ammonium iodide, which acts as a source for iodide ions, and increases the yield of the product to ~30% was also used. Refer Figure 5.2.1 for reaction scheme and 5.6.1.Synthesis for details.

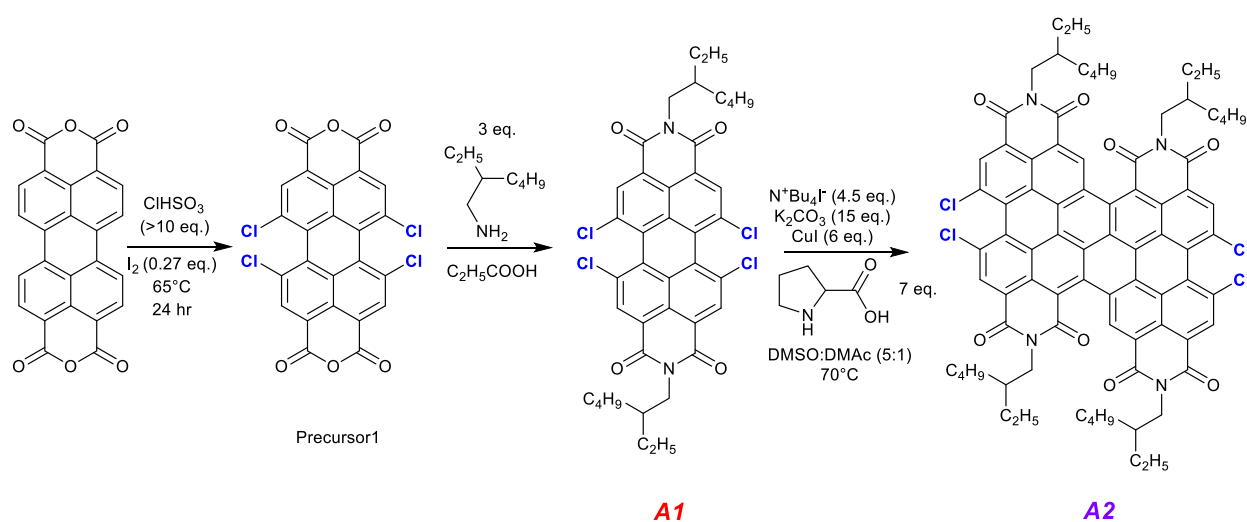


Figure 5.2.1: Reaction scheme for **A1** and **A2**, used as acceptors with **P1** and **P2**.

5.2.2. Cu- promoted vs Pd- catalyzed coupling reactions

While n-type **A1** and **A2** have been synthesized before, longer RDIs are rare for two reasons: poor yields and purification difficulties. Despite these, there have been a couple of

published works depicting the same. One achieves trimerization using the more reactive tetra-bromo perylene di-imide,^[21] while the other uses a synergic approach combining Cu-promoted Ullmann coupling with a Pd catalyst.^[22] Both these works suffer from low yields (~15% and 8% respectively) and are only demonstrative publications showing no possible application for the structures.

Coupling also occurs with a catalytic amount of Pd, albeit only a single C-C homocoupling bond is formed. This reaction is also interesting from a synthetic point of view, since the yields are higher than the traditional Cu-promoted Ullmann couplings. So, the possibility of dimerizing **A2** into longer n-type OSCs was investigated.

Copper promoted dimerization

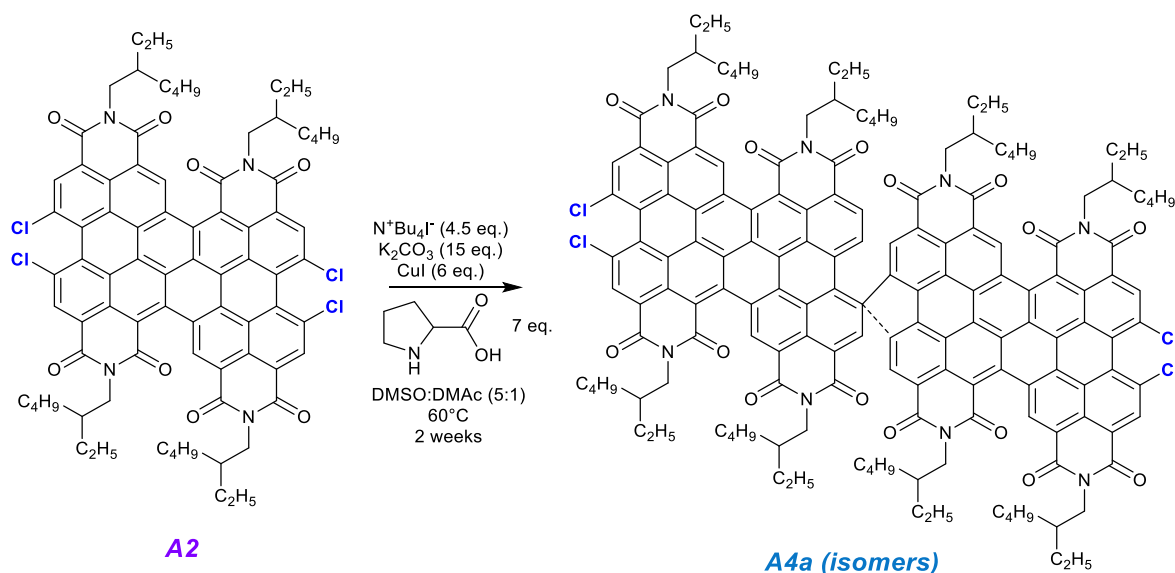


Figure 5.2.2: A possible/proposed reaction scheme for Cu promoted dimerization of **A2**, **A4a** is expected product.

Trying to reproduce the traditional dimerization of tetra-haloperylene di-imides, **A2** was dimerized in a similar fashion, albeit at a lower temperature of 60°C to ensure limited dehalogenation in the presence of copper. This causes long reaction times, and the reaction was left to run for 2 weeks under argon flow. Even after two weeks, it is seen that the expected triply linked product doesn't form (color of the product is blue and not green as reported before^[22]), but *possibly* only a single covalent C-C bond linked tetra-erylene di-imide with 4 Cl- groups intact is the major product, that too with modest yields. In fact, most of the starting reactant **A2** was recovered, with some dehalogenated versions of **A2** being side products. The bulky chlorine groups indeed aid in solubility and elution in the column chromatography, as CH_2Cl_2 is sufficient to elute the product. Let the product be called **A4a**, whose *theorized* structure is shown in the Figure 5.2.2.

Palladium catalyzed coupling reactions

This pathway was only discovered accidentally, when dehalogenation of **A2** was tried, based on previously published reactions.^[23,24] But instead of obtaining dehalogenated products, a coupled, red-shifted, dark blue product was obtained. This reaction was faster as it was a Pd- catalyzed reaction run in the microwave reactor at 150°C for 2 hours. And the reaction almost proceeds to completion as none of the starting material or its dehalogenated versions were observed among the products.

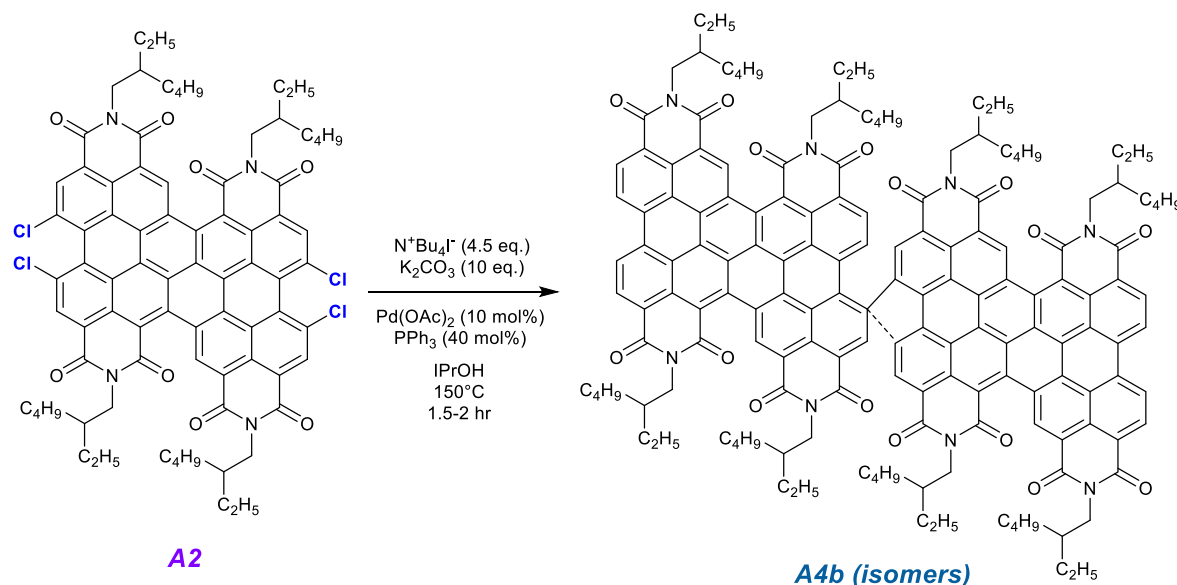


Figure 5.2.3: Reaction Scheme for Pd catalyzed dimerization of **A2**, where **A4b** is expected product.

The R_f values (Retention Factor in *Thin Layer Chromatography*, *TLC*) of the theorized product (called **A4b** henceforth) is significantly lesser than **A4a** with CH_2Cl_2 elution. In fact, **A4b** is almost stuck to the baseline with CH_2Cl_2 as the mobile phase during column chromatography and required more polar solvents like CF or CH_2Cl_2 enriched with EtOAc for elution (reaction scheme in Figure 5.2.3). Both **A4a** and **A4b** show the same color indicating similar conjugated core structures, but this needs further verification, and is elaborated in the next subsections.

Subsequently, **A1** was also dimerized in similar conditions. However, in this case a lower temperature of 120°C was sufficient to dimerize (higher temperatures led to many fractions; difficult to isolate). The product is soluble readily in all known organic solvents and cannot be precipitated. It is hence dried in a vial until it solidifies and is called **A2b** (refer 5.6.1.Synthesis-**A2b**) henceforth.

Due to energetics, **A1**, **A2** and **A4b** are in focus, rather than the other molecules, so these OSCs will be elaborated on the following sections and upcoming chapters.

5.3. Characterization

5.3.1. NMR

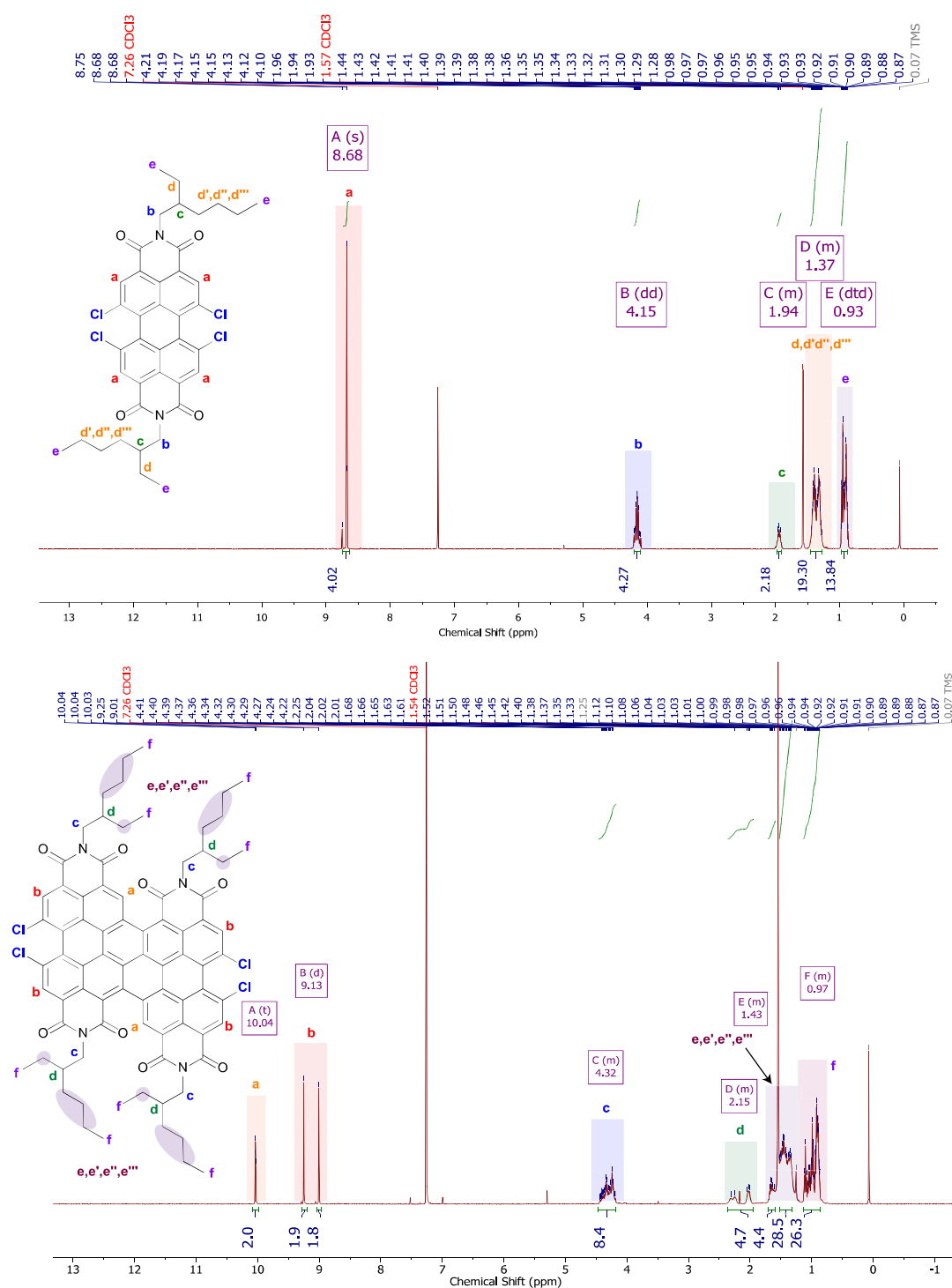


Figure 5.3.1: (Top) 400 MHz ^1H NMR (CDCl_3) of **A1**, (Bottom) ^1H NMR (CDCl_3) of **A2** at 25°C.

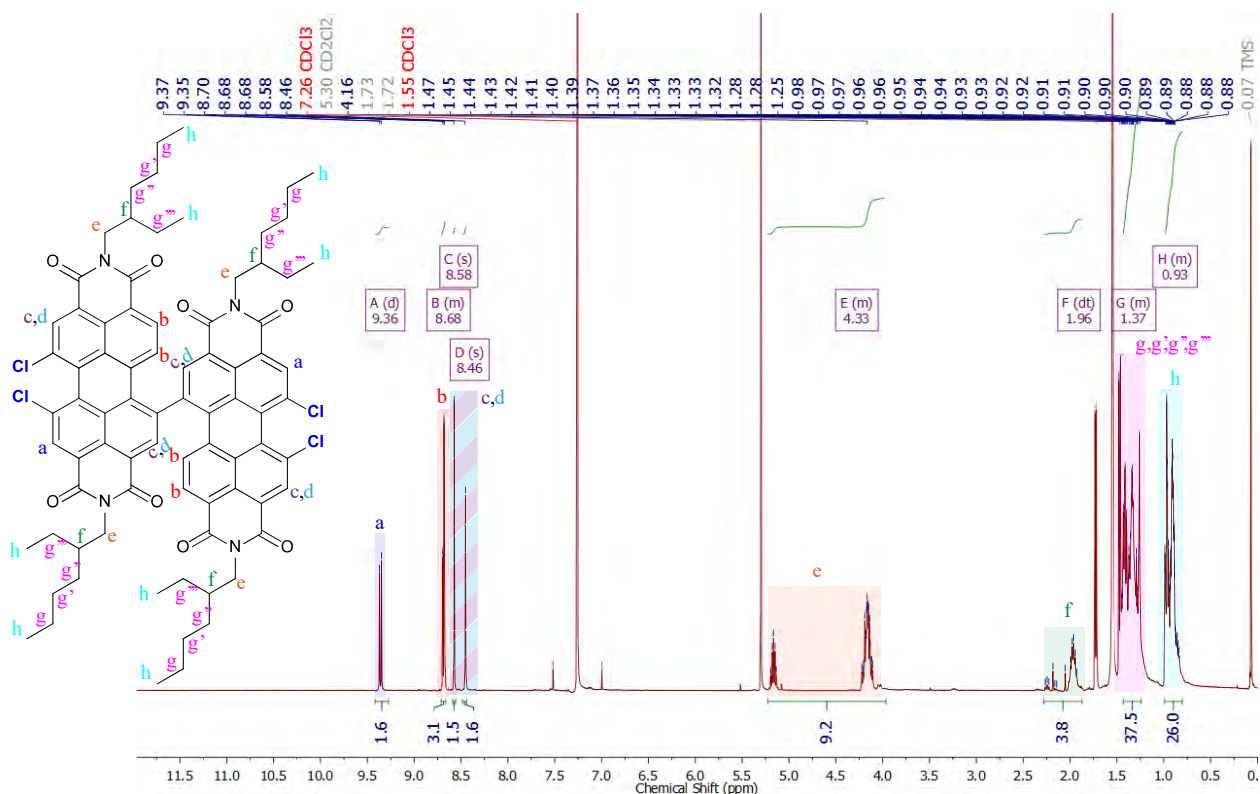


Figure 5.3.2: 400 MHz ^1H NMR (CDCl_3) of **A2b** at 25°C.

The aromatic region of **A1**'s ^1H NMR spectrum (Figure 5.3.1) shows only one singlet peak at 8.68 ppm indicating the ^1H proton at the ortho positions of **A1**, while the upfield protons at 4.15 ppm is a double doublet indicating the ^1H protons close to the nitrogen imides and the other peaks represent the protons of the 2-ethyl hexyl alkyl chains.

Similarly, the downfield protons peaks in **A2** (Figure 5.3.1) from 9.01-10.04 ppm are peaks showing the ortho protons, while the upfield protons at 4.15-4.49 ppm are multiplets indicating the ^1H protons close to the nitrogen imides and the other peaks represent the protons of the 2-ethyl hexyl alkyl chains.

While **A1** and **A2** are synthesized from known reactions, the subsequent products are unknown, and hence these structures based on the NMR spectrum are proposed and further verified with 5.3.2.MALDI-TOF. For **A2b** (Figure 5.3.2), the integration factor of downfield protons indicates not only the ortho protons, but also the protons at the bay positions, as this is probably a single covalent bond linked dimer of **A1**. The other upfield protons and alkyl chain protons match well with the structure too.

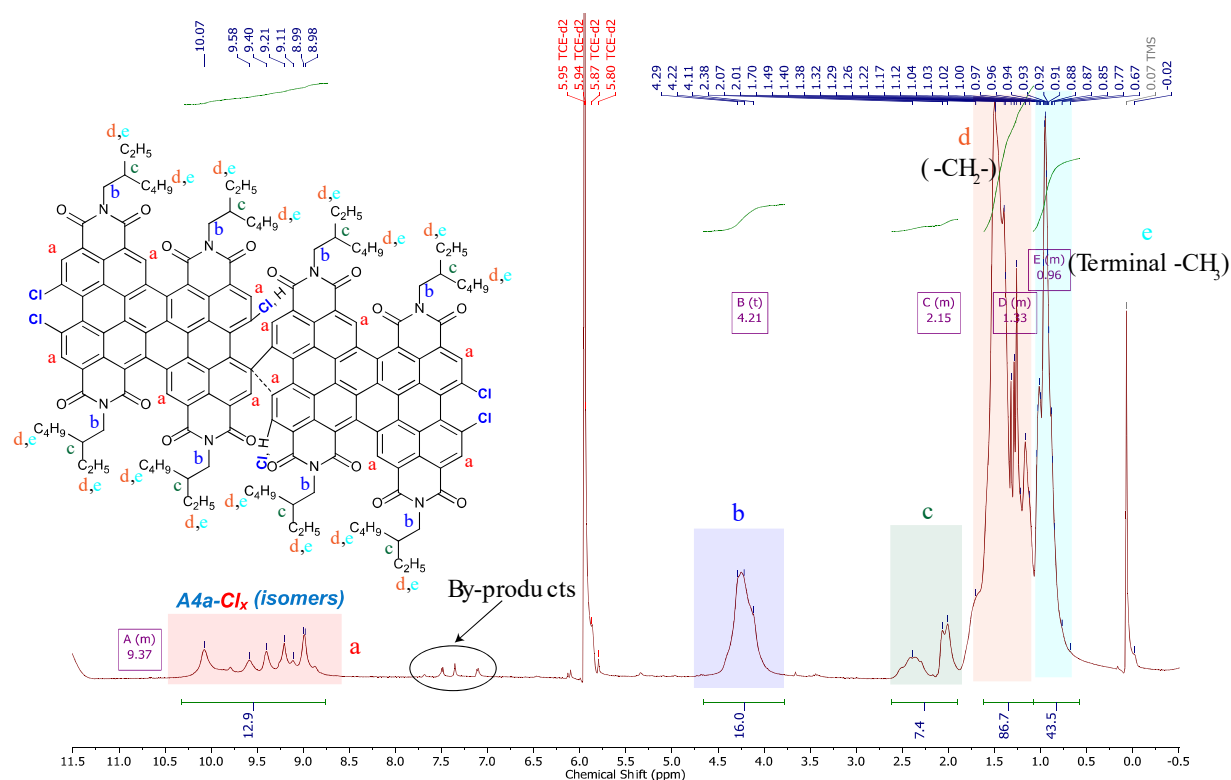


Figure 5.3.3: High field ^1H NMR (600 MHz, 70°C , $\text{C}_2\text{D}_2\text{Cl}_4$) of **A4a** purified product with proposed structure.

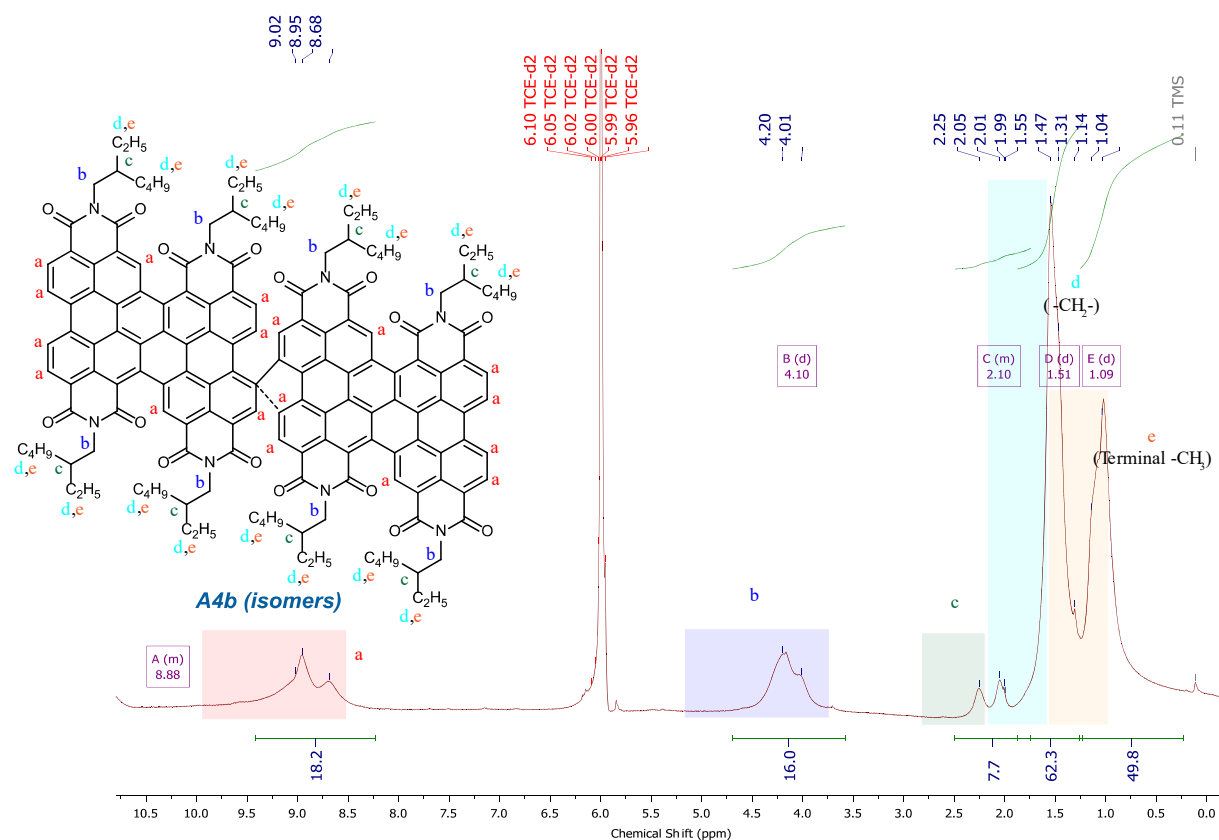


Figure 5.3.4: High field ^1H NMR (600 MHz, 70°C , $\text{C}_2\text{D}_2\text{Cl}_4$) of **A4b** purified product with proposed structure.

For **A4a** product, since the OSC is a large molecule, to get cleaner signals, high field 600 MHz ^1H NMR is used for higher resolutions, at a higher temperature of 70°C with CD_2Cl_4 solvent. The ^1H NMR spectrum (Figure 5.3.3) does not match the *theorized* product

proposed earlier. The integration factors of the protons in the aromatic region instead adds up to result in additional chlorine groups around the new covalent C-C bond. This probably occurs as the temperature of the reaction is very low, resulting in limited dehalogenation. Moreover, the NMR shows peaks for byproducts, possibly other isomers with greater or lesser number of chlorine groups, which could not be separated post-column chromatography. The exact mixture could be characterized using mass spectroscopy. Hereby, the product **A4a** is called **A4a-Cl_x**.

The **A4b** ¹H NMR spectrum (Figure 5.3.4) in similar high field NMR spectroscopy fortunately matches with the *theorized* product. The integration factors add up correctly. For both **A4a-Cl_x** and **A4b**, the aromatic peaks are not easily resolvable nor assignable to specific locations on the molecule, hence labelled in general cumulatively.

5.3.2. MALDI-TOF

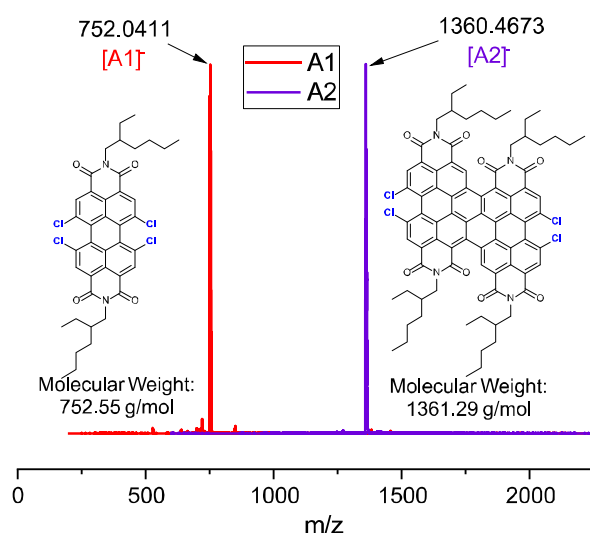


Figure 5.3.5: MALDI-TOF spectra of **A1** and **A2**.

Both **A1** and **A2** were dissolved in *TTh* matrix and subjected to reflective mode with negative ionization and resulted in clean spectra (Figure 5.3.5) showing the products with reasonable accuracy ($< \pm 1$ Da).

From Figure 5.3.6, while **A4b** clearly shows a single product peak corresponding to the theorized structure, **A4a-Cl_x** is a mixture of the isomers and byproducts containing one or two additional chlorine groups. However, this mixture could not be further purified by traditional column chromatography and would require HPLC or other techniques. From the MALDI-TOF and NMR spectrum, **A4a-Cl_x** is primarily **A4a-Cl₂**, with additional byproducts which are **A4a** and **A4a-Cl**.

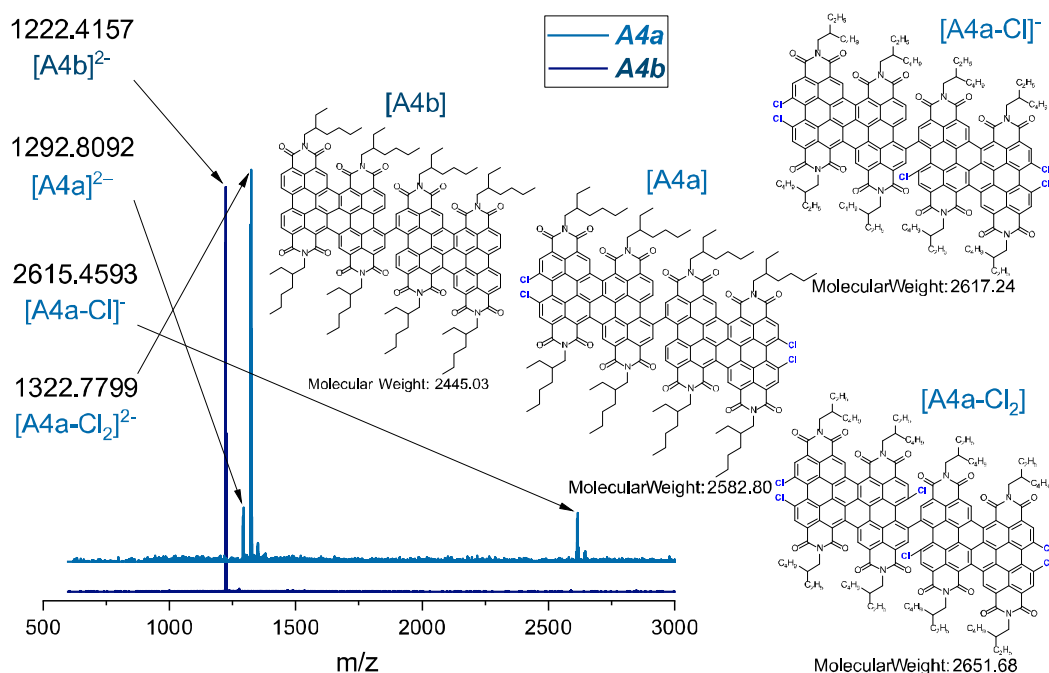


Figure 5.3.6: MALDI-TOF spectra of **A4a-Cl_x** and **A4b**.

5.3.3. UV-Vis Absorption

Clearly **A2** is red-shifted compared to **A1** due to extended conjugation (Figure 5.3.7a). The solution state onset wavelengths are blue-shifted compared to the corresponding solid state absorbances. The onset wavelengths of **A2** in the solid state was about 150 nm higher than that of **A1**, at 704 nm, resulting in an $E_{g,opt}$ of 2.26 and 1.79 eV for **A1** and **A2** (Figure 5.3.7b). For the single covalent bond linked RDIs, evidently due to extended conjugation, the molar extinction coefficient is much higher than the smaller molecules: **A4b** showing a peak extinction coefficient of $\sim 92000 \text{ M}^{-1}\text{cm}^{-1}$ at 412 nm and $\sim 44000 \text{ M}^{-1}\text{cm}^{-1}$ at 678.5 nm in CF, contrasting against extinction coefficients for **A1** ($\sim 35000 \text{ M}^{-1}\text{cm}^{-1}$ at 513.5 nm) and **A2** ($\sim 24000 \text{ M}^{-1}\text{cm}^{-1}$ at 403 nm & $\sim 18000 \text{ M}^{-1}\text{cm}^{-1}$ at 648.5 nm).

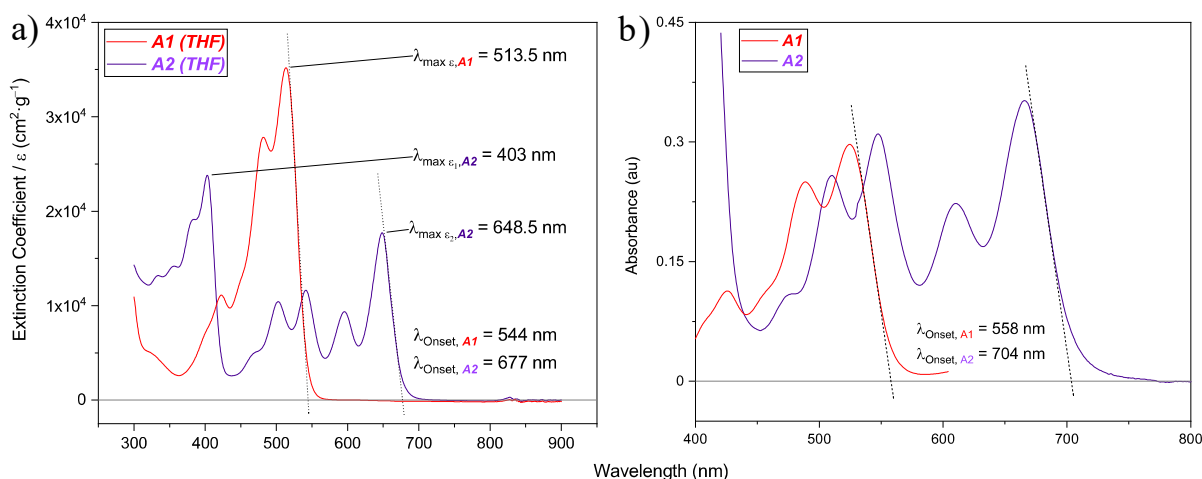


Figure 5.3.7: a) Solution state, b) Solid state Absorption Spectra of **A1** and **A2**.

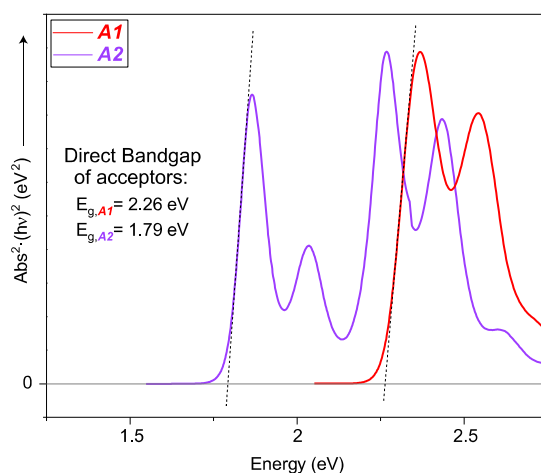


Figure 5.3.8: Tauc Plot of solid-state absorbance of **A1** and **A2**.

Also, **A4b** has a red-shifted onset tail wavelength, extending up to 800 nm in the solution state, and 875 nm in the solid state. Indeed, from the Tauc plots of the absorbances in solid state, (Figure 5.3.8 and Figure 5.3.9), the $E_{g,opt}$ of the bigger molecules reduces to about 1.6-1.7 eV.

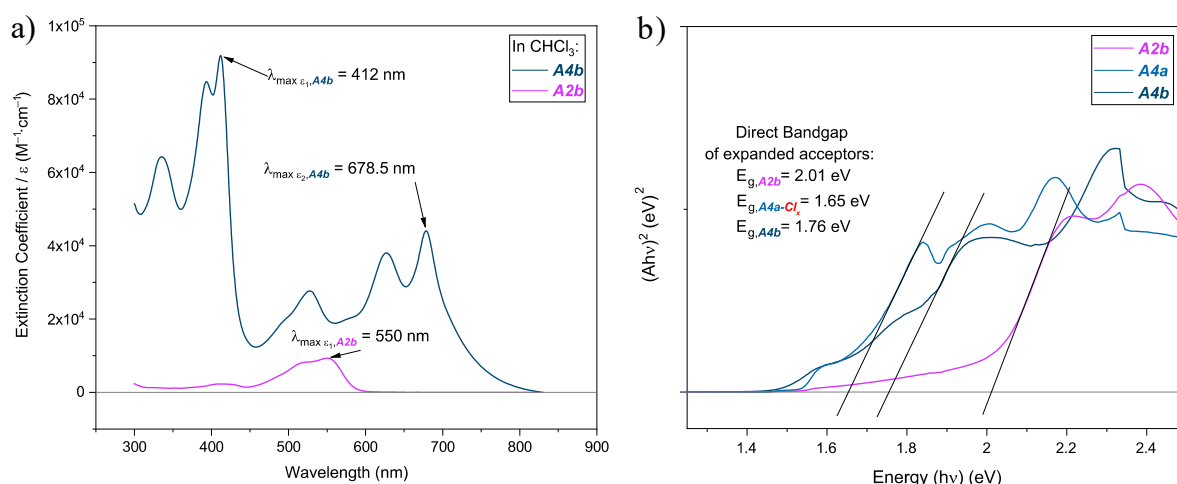


Figure 5.3.9: a) Solution state absorption spectra of, b) Solid state Tauc plots of **A2b**, **A4a-Cl_x** & **A4b**.

The solid-state CV experiments on thin films of **A2**, **A4a-Cl_x** and **A4b** (Figure 5.3.10) give an idea of how the MO levels change upon extended conjugation with copper promoted or palladium catalyzed reaction routes.

A2 shows the lowest LUMO levels, as the effect of two pairs of di-imide groups are linked by a three sigma covalent bonds with 4 chloro groups further stabilizing the MO levels. **A4a-Cl_x** shows a lower LUMO level of $-4.02 \text{ eV}_{\text{vac}}$ compared to **A4b**, whose LUMO level of $-3.96 \text{ eV}_{\text{vac}}$ is closer to that of **A1**.

While the chlorinated OSCs, have deepened HOMO levels (-6.10 to $-6.20 \text{ eV}_{\text{vac}}$), **A4b** shows a higher HOMO of $-5.8 \text{ eV}_{\text{vac}}$.

5.3.4. Cyclic Voltammetry

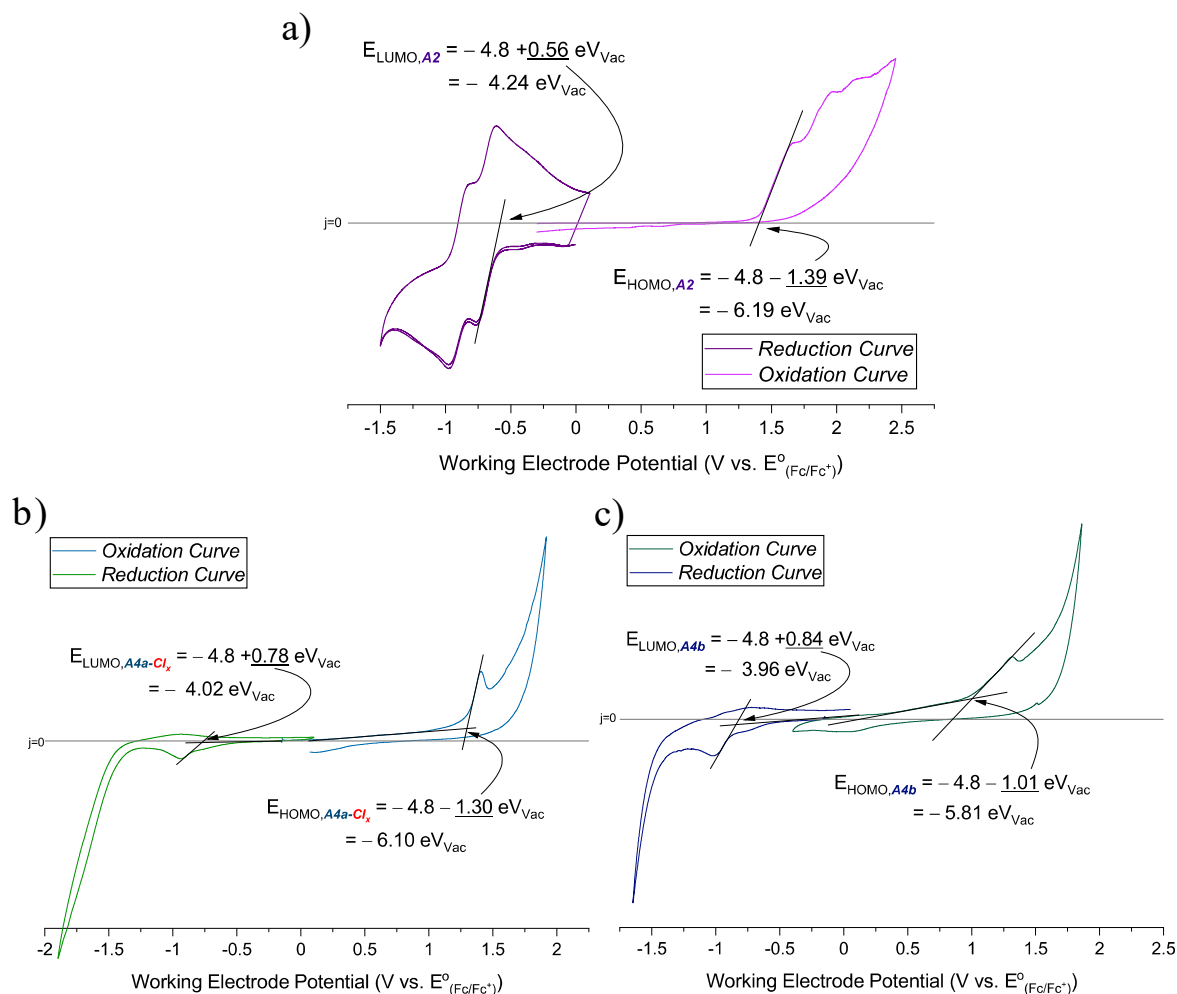


Figure 5.3.10: The CV spectra of a) **A2**, b) **A4a-Cl_x** and c) **A4b**.

5.3.5. Effect of Cl- substitution

With **A1** and a reference molecule (**PDI-EH**), which is its dehalogenated version, the effect of chloro- groups on the chemical properties is understood. The first is the reduction in extinction coefficient, making **PDI-EH** more absorptive than **A1**, as can be seen from the absorption spectra in Figure 5.3.11. This is due to reduction in number of symmetry modes, as this affects the various overlap integrals of electromagnetic incoming irradiation with the molecular orbitals of the molecule itself. With lesser symmetry modes, there are more forbidden transition dipole moments for absorption, hence a lower quantity of light is absorbed.^[25]

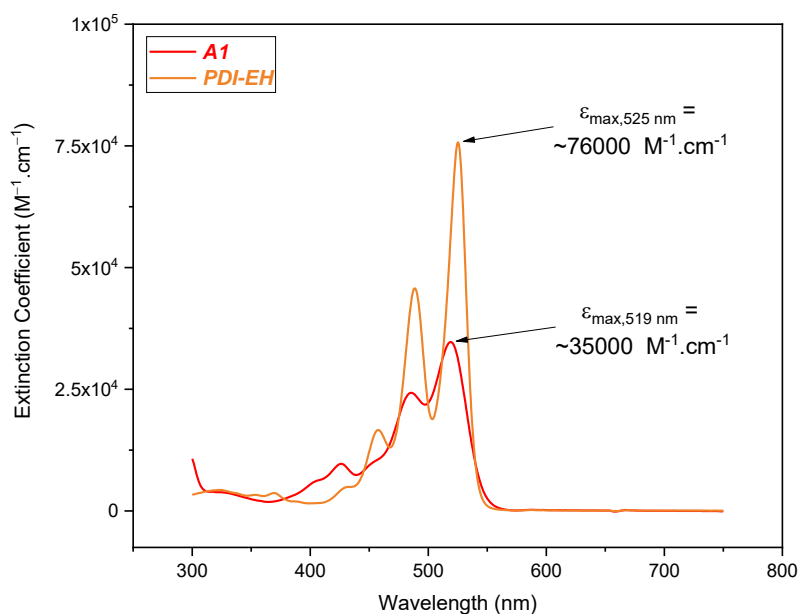


Figure 5.3.11: Effect of Cl- substituent on the extinction coefficient.

With respect to the energetics, the chloro- groups tend to stabilize the LUMO level, while the HOMO level remains slightly destabilized (Figure 5.3.12). The chloro- groups effectively reduce $E_{g,elec}$ from ~ 2.94 eV to ~ 2.58 eV.

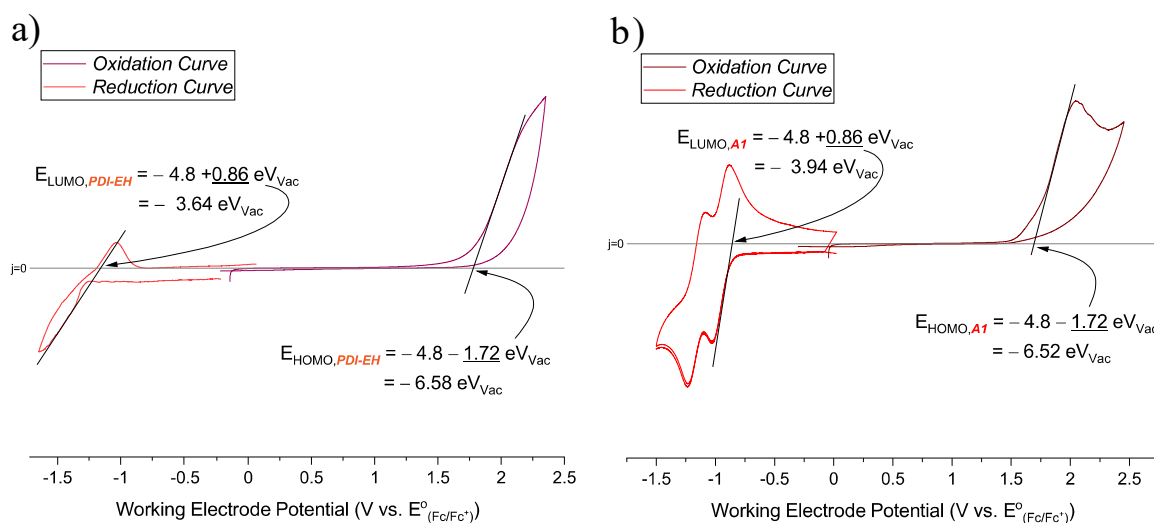


Figure 5.3.12: The CV spectra of a) **PDI-EH** and b) **A1**.

These effects also similarly correspond to the differences between **A4a-Cl_x** and **A4b**.

5.4. PEC characterization

Like the donors, the neat acceptors were spun-coat onto $\text{mSnO}_2/\text{pSnO}_2/\text{FTO}$ substrates, which were treated with a SAM of benzoic acid (more details in later chapters). The electrolyte was 1 M KPi buffered at pH 6.8 containing 1.5 M sodium sulfite sacrificial reductant. The graphs in Figure 5.4.1 show LSV and CA under chopped light illumination.

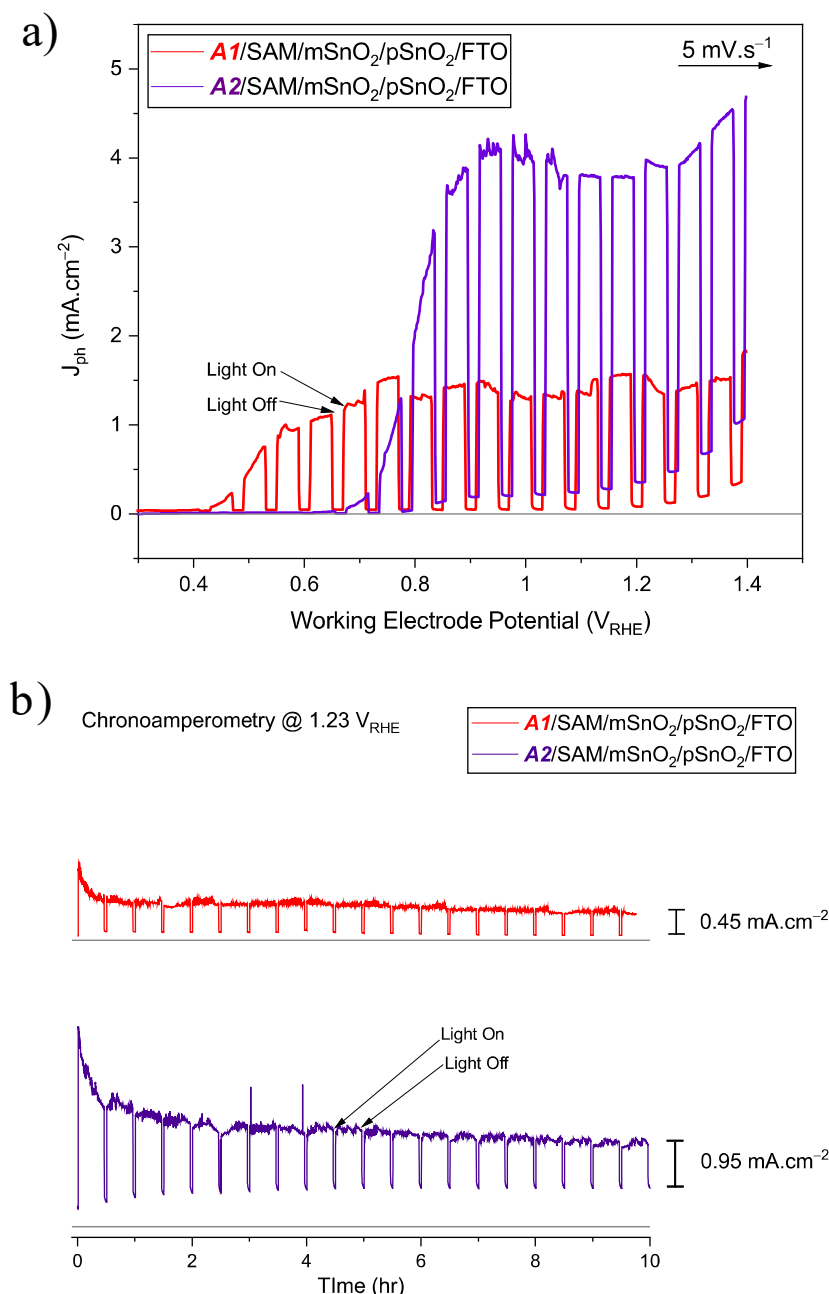


Figure 5.4.1: a) LSV curves b) CA curves (@ $1.23V_{RHE}$) of **A1** and **A2**, in a pH 6.8 KPi buffer with 1.5 M sulfite.

A2 has a higher initial and final J_{ph} under similar conditions as **A1**, showing a possible overall improvement in the PEC performance. The difference in onset potential is directly

related to the LUMO level difference in the OSCs, as there exists a need for higher applied potential with **A2** for a positive driving force for electron injection into the ETL.

From the UV-Vis absorption spectra of the photoanodes in Figure 5.4.2, the reduction in J_{ph} does not correspond to the OSC degradation under operation, as the reduction in the absorption spectra of the films does not completely correspond to the larger loss in J_{ph} . This reduction in J_{ph} on operation is distinctly dissimilar to the loss in J_{ph} seen with the **QDI** molecules, which lose a major percentage of J_{ph} within a few seconds.

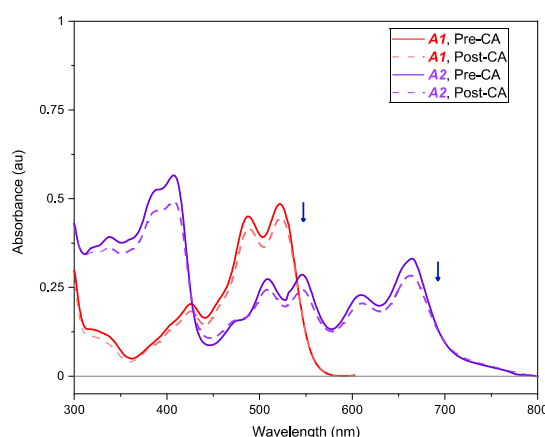


Figure 5.4.2: Absorption spectra of the a) **A1** and b) **A2** based photoanodes before and after CA operation at 1.23 V_{RHE} .

5.5. Conclusion

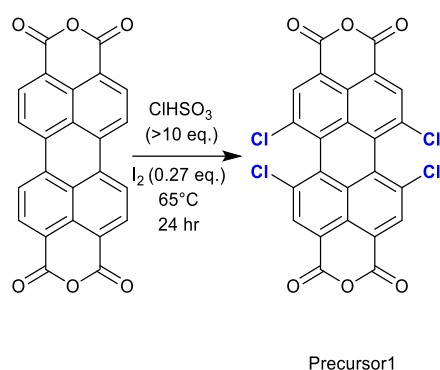
NFAs with MO levels to complement the donor polymer **P2** are not commonly available in the OPV field. Instead of modifying high-performance acceptors like ITIC and similar derivatives which are expensive to synthesize, a series of acceptors based on lateral elongation of perylene di-imide molecule was chosen as target molecules to be studied. The acceptors (**A1**, **A2** and **A4b**) were synthesized, optically and electrochemically characterized. The PEC performance of a couple of acceptors were also analyzed, which showed that the more red-shifted, elongated molecule showed a better performance while oxidizing a sacrificial reductant in water. In the coming chapters, these will be used as BHJ photoanodes in conjunction with the donor polymers.

5.6. Supporting Information

5.6.1. Synthesis

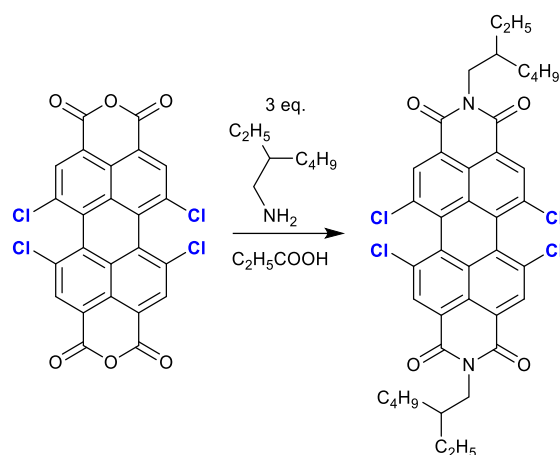
Precursor

Procedure adapted from previous work.^[26] 10.42 g of perylenetetracarboxy-3,4:9,10-dianhydride (26.6 mmol) was dissolved in chlorosulfuric acid (20mL, >10 eq.) and iodine (1.8 g, 0.27 eq.) was used to catalyse the bay substitution. The initial, viscous suspension was heated to 65°C for 24 hr. Later, on cooling back to room temperature, the highly concentrated acidic suspension was quenched by adding it in a drop-by-drop manner to a large beaker filled with ice. Handle the quenching process carefully due to HCl and H₂SO₃ evolved. The solids appear as bright orange in the cold-water suspension. Filter and dry in vacuum, use Precursor1 as it is, without further purification. Yield: 12.9 g, 91%.



A1

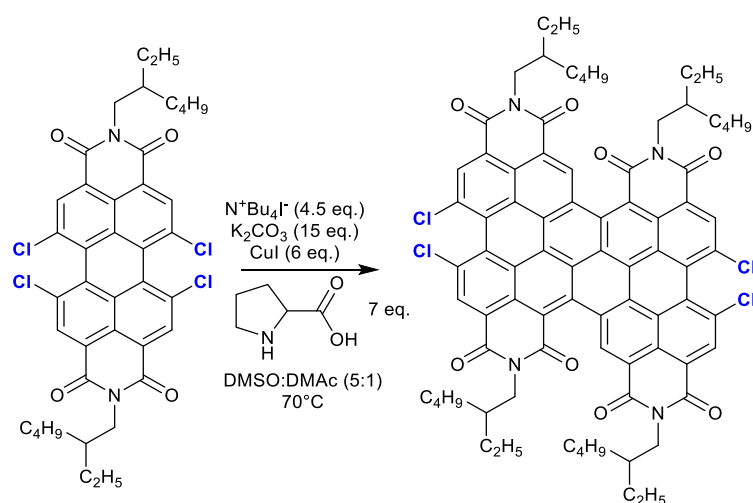
Under Argon atmosphere, add 2-ethyl-1-hexylamine (1.75 mL, 4 eq.) to 1.38 g of Precursor1. Dissolve the reactants in 10mL propionic acid and reflux the solution overnight. The reaction progress can be tracked by TLC to observe complete disappearance of Precursor1 spot in dichloromethane elution. After cooling, quench reaction mixture in Water: EtOH (10:1) and filter over a bed of celite. Wash the solids with MeOH to remove unreacted amine and finally with dichloromethane or chloroform to extract A1. Subject this orange-red crude to column chromatography with dichloromethane: hexane (4:1) elution to obtain pure A1. Other minor fractions are trichloro or dichloro analogues which can be disposed. Yield: 1.8 g, 92%. ¹H NMR (400 MHz, Chloroform-d) δ 8.68 (s, 4H), 4.15 (dd, J = 9.2, 7.3 Hz, 4H), 2.09 – 1.77 (m, 2H), 1.50 – 1.18 (m, 16H), 0.93 (dtd, J = 19.3, 7.2, 2.3 Hz, 12H).



A1

A2

Procedure adapted from previous work^[18,19]. Purge Ar into a *Schlenk* vessel with 3.3 g **A1** (4.4 mmol), 5.01 g CuI (6 eq.), 9.09 g K₂CO₃ (15 eq.), 7.29 g Tetra n-Butyl Ammonium Iodide (4.5 eq.) and 3.53 g L-Proline (7 eq.). Add 30 mL of DMSO: DMAc (5:1) mixture and heat at 70°C for 24 hr under Ar. Neutralize with 1 M HCl on cooling and filter solids over a bed of celite.



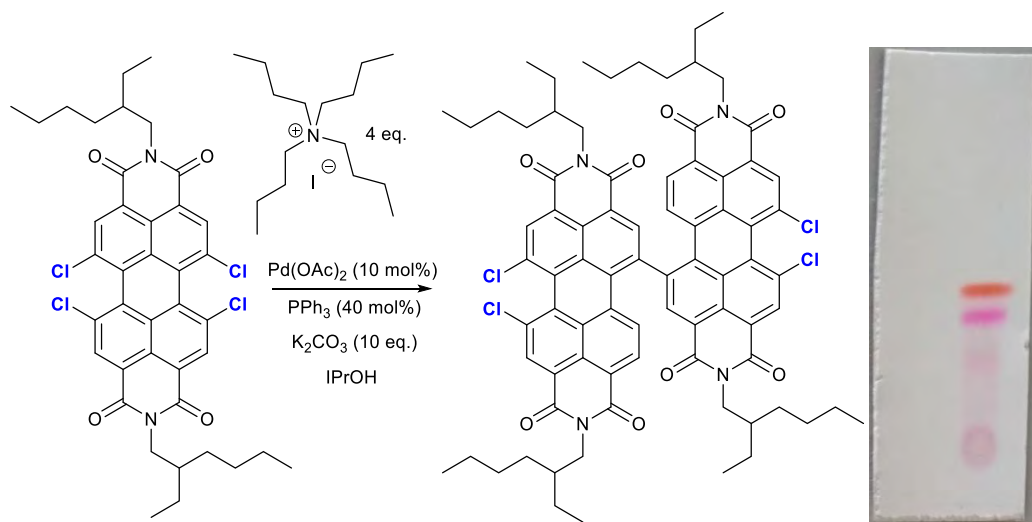
A1

A2

Extract crude with dichloromethane or chloroform and perform column chromatography in dichloromethane: hexane (1:1) mixture to get purple-blue fraction. If contaminated with another red colored product, repeatedly precipitate in hot acetonitrile to obtain pure **A2**. Yield: 1.1 g, 29%. ¹H NMR (400 MHz, Chloroform-d) δ 10.04 (t, *J* = 1.7 Hz, 2H), 9.25 (s, 2H), 9.01 (s, 2H), 4.49 – 4.15 (m, 8H), 2.28 (d, *J* = 23.9 Hz, 3H), 2.03 (d, *J* = 8.6 Hz, 1H), 1.65 (dt, *J* = 15.0, 7.5 Hz, 4H), 1.54 – 1.24 (m, 28H), 1.15 – 0.85 (m, 24H).

A2b

Load **A1** (1 gm; 1.41 mmol), Pd(OAc)₂ catalyst (31.75 mg; 10 mol%, 0.14 mmol), tetra-n-butyl ammonium iodide (2.36 gm; 4.5 eq, 6.37 mmol), PPh₃ ligand (149 mg; 40mol %, 0.57 mmol) and 10 eq. of K₂CO₃ (2 gm) to the dry microwave vial with a stir bar and seal it with the septum. Subject the vial to vacuum for 10 minutes under stirring, and then add isopropyl alcohol (10mL) to the vial. Purge argon through the suspension for 15 minutes, and then start the microwave reaction. The reaction is ramped to 120°C within 3 minutes and run for 90 minutes. On cooling, quench reaction by pouring contents in water. Stir for a few minutes and neutralize solution with 10% HCl till no more effervescence is observed. Filter solids over a celite bed and wash with water and dry. Elute solids with CH₂Cl₂ and remove organic solvent by rotavapor. Perform column chromatography in hexane (4% EtOAc) to isolate the pink fraction.

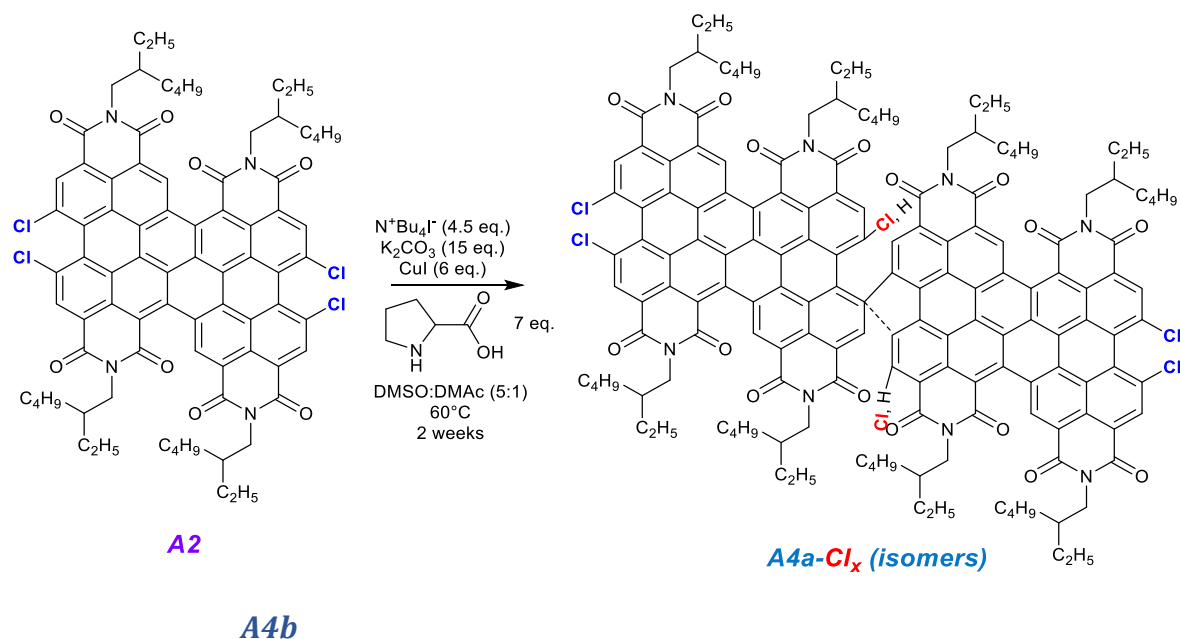


While the yield is relatively low (320 mg, 33%), there is significant recovery of the starting reactant **A1**, the orange fraction which elutes in the column before the product.¹H NMR (400 MHz, Chloroform-d) δ 9.36 (d, J = 8.2 Hz, 2H), 8.80 – 8.64 (m, 4H), 8.58 (s, 2H), 8.46 (s, 2H), 5.25 – 4.02 (m, 8H), 1.96 (dt, J = 13.5, 6.7 Hz, 4H), 1.49 – 1.20 (m, 32H), 1.01 – 0.74 (m, 12H).

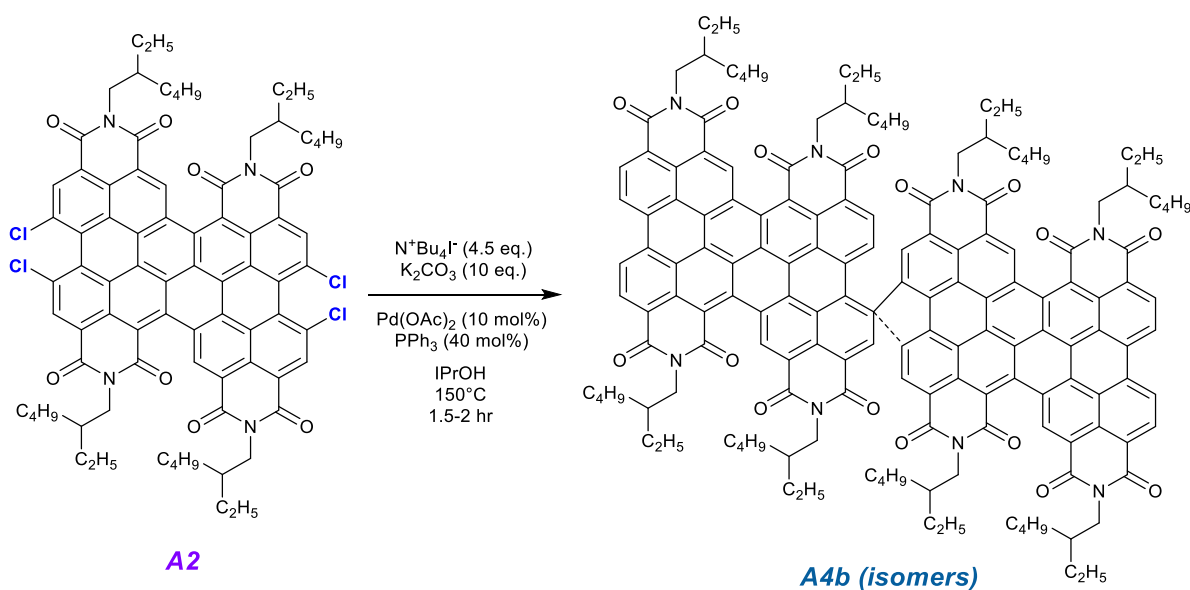
A4a-Cl_x

Purge Ar into a *Schlenk* vessel with 0.4 g **A2** (0.3 mmol), 336 mg CuI (6 eq.), 0.61 g K₂CO₃ (15 eq.), 0.49 g Tetra n-Butyl Ammonium Iodide (4.5 eq.) and 237 mg L-Proline (7 eq.). Add 30 mL of DMSO: DMAc (5:1) mixture and heat at 60°C for 2 weeks under Ar. Neutralize with 1 M HCl on cooling and filter solids over a bed of celite. Extract crude with

dichloromethane or chloroform and perform column chromatography in dichloromethane: hexane (3:1) mixture to get blue fraction. Most of the recovered fractions are **A2** and its dehalogenated byproducts, though. Yield: 62 mg, 16.2%. ^1H NMR (600 MHz,) δ 10.20 – 8.79 (m, 13H), 4.21 (t, J = 51.2 Hz, 16H), 2.61 – 1.87 (m, 8H), 1.88 – 1.07 (m, 64H), 1.08 – 0.58 (m, 48H).



Load **A2** (0.8 gm; 0.59 mmol), Pd(OAc)₂ catalyst (13.2 mg; 10 mol%, 0.06 mmol), tetra-*n*-butyl ammonium iodide (0.98 gm; 4.5 eq, 2.64 mmol), PPh₃ ligand (62 mg; 40mol %, 0.24 mmol) and 10 eq. of K₂CO₃ (0.82 gm) to the dry microwave vial with a stir bar and seal it with the septum.



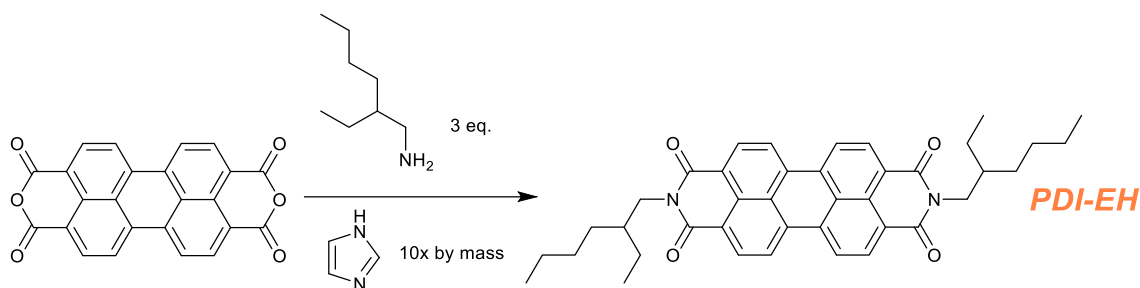
Subject the vial to vacuum for 10 minutes under stirring, and then add isopropyl alcohol (10mL) to the vial. Purge argon through the suspension for 15 minutes, and then start the microwave reaction. The reaction is ramped to 150°C within 3 minutes and run for 90 minutes.

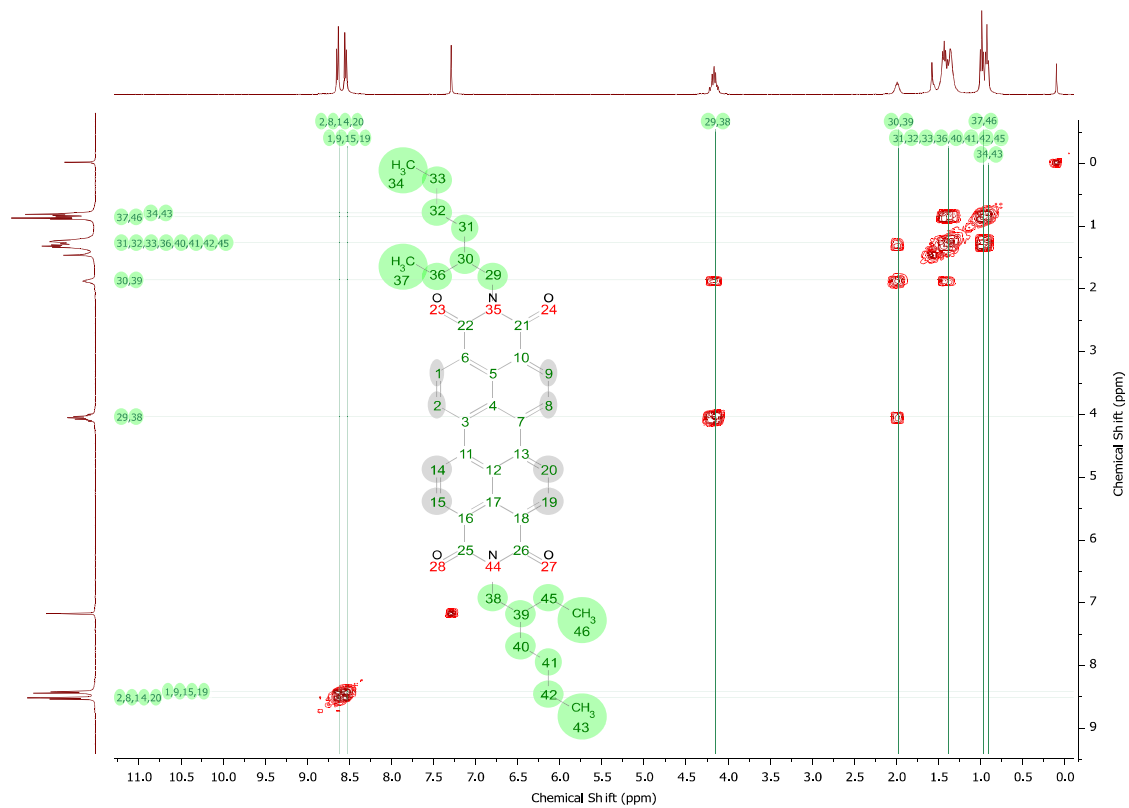
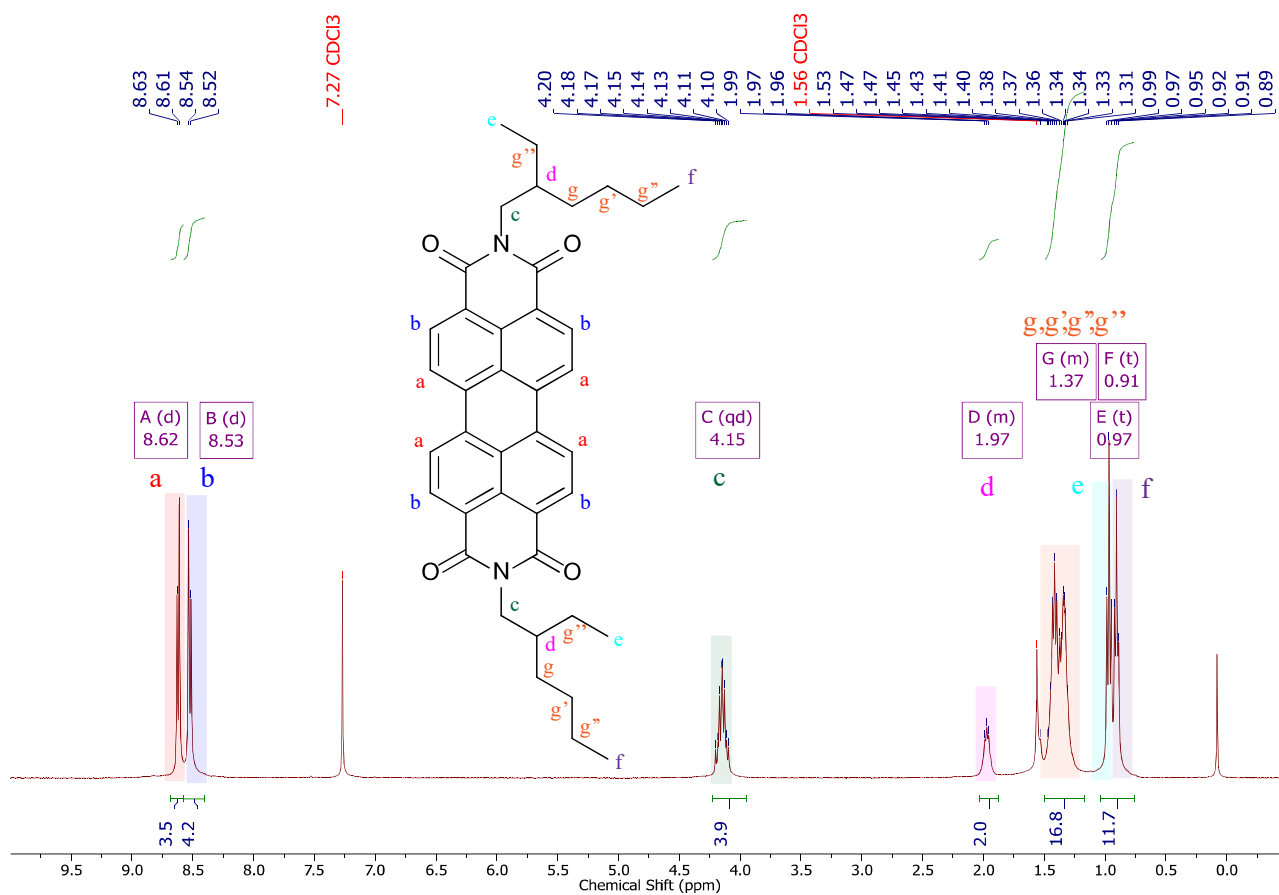
On cooling, quench reaction by pouring contents in water. Stir for a few minutes and neutralize solution with 10% HCl till no more effervescence is observed. Filter solids over a celite bed and wash with water and dry. Elute solids with CF and remove organic solvent by rotavapor. Perform column chromatography in CH₂Cl₂ (ramp up to 8% EtOAc) to isolate the dark blue fractions. Additionally, a prep TLC can also be performed to remove the byproducts before column chromatography.

¹H NMR (600 MHz, C₂D₂Cl₄) δ 9.50 – 8.16 (m, 18H), 4.10 (d, J = 112.4 Hz, 16H), 2.40 – 1.89 (m, 8H), 1.51 (d, J = 48.7 Hz, 64H), 1.09 (d, J = 63.6 Hz, 48H).

PDI-EH

Procedure adapted from previously published work.^[27] Almost quantitative yields. ¹H NMR (400 MHz, Chloroform-d) δ 8.62 (d, J = 7.9 Hz, 1H), 8.53 (d, J = 8.0 Hz, 4H), 4.15 (qd, J = 13.0, 7.2 Hz, 4H), 2.02 – 1.89 (m, 2H), 1.48 – 1.28 (m, 16H), 0.97 (t, J = 7.4 Hz, 6H), 0.91 (t, J = 6.8 Hz, 6H). ¹³C NMR (101 MHz, CDCl₃) δ 163.85, 134.59, 131.52, 129.48, 126.47, 123.44, 123.16, 77.48, 77.17, 77.16, 76.84, 44.51, 38.13, 30.94, 28.87, 24.25, 23.23, 14.26, 10.80. (Figure 5.6.1 shows all the relevant NMR spectra).





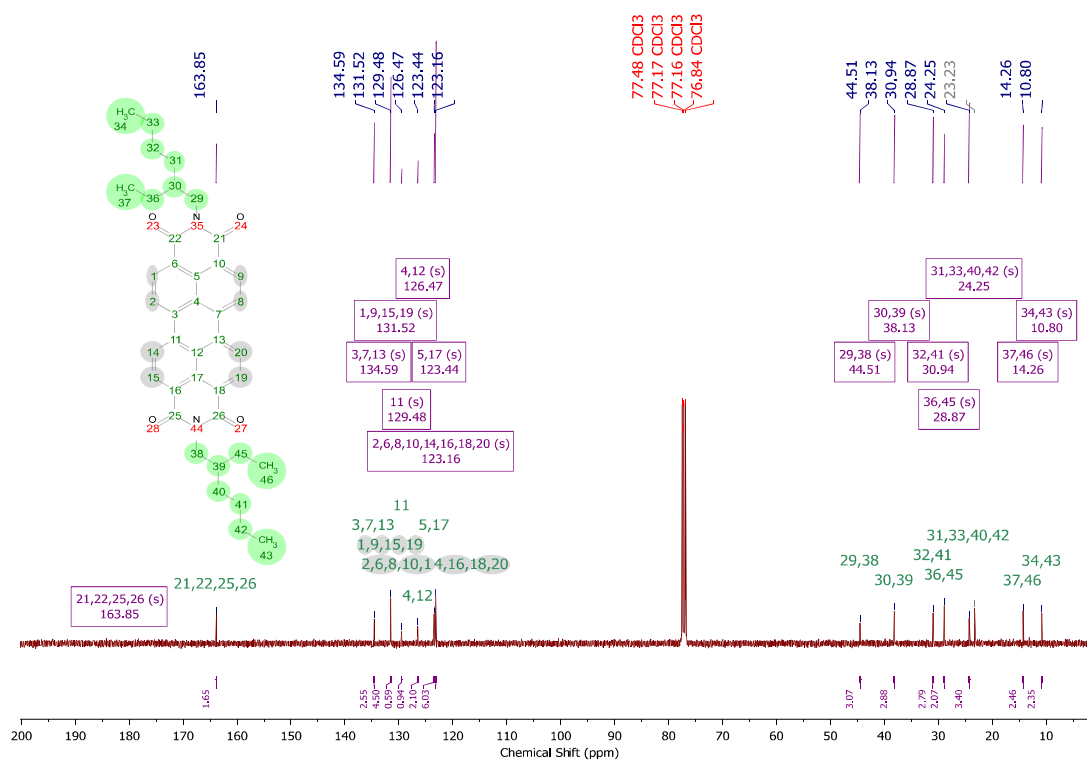


Figure 5.6.1: (Top) ^1H 400 MHz NMR spectrum, (Middle) 2D ^1H - ^1H COSY & (Bottom) ^{13}C NMR of **PDI-EH**.

5.7. References

- [1] N. S. Sariciftci, L. Smilowitz, A. J. Heeger, F. Wudl, *Science* **1992**, 258, 1474, DOI: 10.1126/science.258.5087.1474.
- [2] E. von Hauff, V. Dyakonov, J. Parisi, *Sol. Energy Mater. Sol. Cells* **2005**, 87, 149, DOI: 10.1016/j.solmat.2004.06.014.
- [3] F. Zhang, Z. Zhuo, J. Zhang, X. Wang, X. Xu, Z. Wang, Y. Xin, J. Wang, J. Wang, W. Tang, Z. Xu, Y. Wang, *Sol. Energy Mater. Sol. Cells* **2012**, 97, 71, DOI: 10.1016/j.solmat.2011.09.006.
- [4] H. Bin, Z.-G. Zhang, L. Gao, S. Chen, L. Zhong, L. Xue, C. Yang, Y. Li, *J. Am. Chem. Soc.* **2016**, 138, 4657, DOI: 10.1021/jacs.6b01744.
- [5] S. Li, L. Ye, W. Zhao, S. Zhang, S. Mukherjee, H. Ade, J. Hou, *Adv. Mater.* **2016**, 28, 9423, DOI: 10.1002/adma.201602776.
- [6] Y. Yang, Z.-G. Zhang, H. Bin, S. Chen, L. Gao, L. Xue, C. Yang, Y. Li, *J. Am. Chem. Soc.* **2016**, 138, 15011, DOI: 10.1021/jacs.6b09110.
- [7] J. Yuan, Y. Zhang, L. Zhou, G. Zhang, H.-L. Yip, T.-K. Lau, X. Lu, C. Zhu, H. Peng, P. A. Johnson, M. Leclerc, Y. Cao, J. Ulanski, Y. Li, Y. Zou, *Joule* **2019**, 3, 1140, DOI: 10.1016/j.joule.2019.01.004.
- [8] Y. Cui, H. Yao, J. Zhang, T. Zhang, Y. Wang, L. Hong, K. Xian, B. Xu, S. Zhang, J. Peng, Z. Wei, F. Gao, J. Hou, *Nat. Commun.* **2019**, 10, 2515, DOI: 10.1038/s41467-019-10351-5.

-
- [9] N. Y. Doumon, M. V. Dryzhov, F. V. Houard, V. M. Le Corre, A. Rahimi Chatri, P. Christodoulis, L. J. A. Koster, *ACS Appl. Mater. Interfaces* **2019**, *11*, 8310, DOI: 10.1021/acsami.8b20493.
- [10] P. Cheng, G. Li, X. Zhan, Y. Yang, *Nat. Photonics* **2018**, *12*, 131, DOI: 10.1038/s41566-018-0104-9.
- [11] PCBM / PC61BM / PC60BM for Perovskite Solar Cells & OPVs, <https://www.ossila.com/products/pcbm>, accessed August 19, **2021**.
- [12] L. Gao, Z.-G. Zhang, L. Xue, J. Min, J. Zhang, Z. Wei, Y. Li, *Adv. Mater.* **2016**, *28*, 1884, DOI: 10.1002/adma.201504629.
- [13] L. Yao, N. Guijarro, F. Boudoire, Y. Liu, A. Rahmanudin, R. A. Wells, A. Sekar, H.-H. Cho, J.-H. Yum, F. Le Formal, K. Sivula, *J. Am. Chem. Soc.* **2020**, *142*, 7795, DOI: 10.1021/jacs.0c00126.
- [14] C. Lee, S. Lee, G.-U. Kim, W. Lee, B. J. Kim, *Chem. Rev.* **2019**, *119*, 8028, DOI: 10.1021/acs.chemrev.9b00044.
- [15] X. Li, C. Xiao, W. Jiang, Z. Wang, *J. Mater. Chem. C* **2013**, *1*, 7513, DOI: 10.1039/C3TC31644K.
- [16] J. Zhang, L. Tan, W. Jiang, W. Hu, Z. Wang, *J. Mater. Chem. C* **2013**, *1*, 3200, DOI: 10.1039/C3TC30156G.
- [17] H. Liu, Y. Wu, Z. Wang, H. Fu, *Org. Electron.* **2013**, *14*, 2610, DOI: 10.1016/j.orgel.2013.05.021.
- [18] W. Jiang, L. Ye, X. Li, C. Xiao, F. Tan, W. Zhao, J. Hou, Z. Wang, *Chem. Commun.* **2013**, *50*, 1024, DOI: 10.1039/C3CC47204C.
- [19] L. M. J. Moore, M. B. Norman, A. R. Benasco, J. M. Richardson, S. E. Morgan, *Synth. Met.* **2018**, *237*, 56, DOI: 10.1016/j.synthmet.2018.02.005.
- [20] H. Qian, Z. Wang, W. Yue, D. Zhu, *J. Am. Chem. Soc.* **2007**, *129*, 10664, DOI: 10.1021/ja0740972.
- [21] H. Qian, F. Negri, C. Wang, Z. Wang, *J. Am. Chem. Soc.* **2008**, *130*, 17970, DOI: 10.1021/ja807803j.
- [22] Y. Zhen, C. Wang, Z. Wang, *Chem. Commun.* **2010**, *46*, 1926, DOI: 10.1039/B926618F.
- [23] J. Moon, S. Lee, *J. Organomet. Chem.* **2009**, *694*, 473, DOI: 10.1016/j.jorganchem.2008.10.052.
- [24] J. Chen, Y. Zhang, L. Yang, X. Zhang, J. Liu, L. Li, H. Zhang, *Tetrahedron* **2007**, *63*, 4266, DOI: 10.1016/j.tet.2007.03.061.
- [25] Electronic Spectroscopy - Interpretation, [https://chem.libretexts.org/Bookshelves/Physical_and_Theoretical_Chemistry_Textbook_Maps/Supplemental_Modules_\(Physical_and_Theoretical_Chemistry\)/Spectroscopy/Electronic_Spectroscopy/Electronic_Spectroscopy_-_Interpretation](https://chem.libretexts.org/Bookshelves/Physical_and_Theoretical_Chemistry_Textbook_Maps/Supplemental_Modules_(Physical_and_Theoretical_Chemistry)/Spectroscopy/Electronic_Spectroscopy/Electronic_Spectroscopy_-_Interpretation), accessed August 31, **2021**.
-

-
- [26] M. Queste, C. Cadiou, B. Pagoaga, L. Giraudet, N. Hoffmann, *New J. Chem.* **2010**, 34, 2537, DOI: 10.1039/C0NJ00240B.
- [27] J. Yi, Y. Ma, J. Dou, Y. Lin, Y. Wang, C.-Q. Ma, H. Wang, *Dyes Pigments* **2016**, 126, 86, DOI: 10.1016/j.dyepig.2015.11.013.

Chapter 6. BHJ Blends[†]

In Chapter 3, a neat n-type OSC was evaluated as a candidate for stable high-performing photoanodes. However, due to various factors, it was evident that charge separation had to be enhanced to prolong the stability of the devices. Using the donors and acceptors discussed in Chapter 4 and Chapter 5, BHJs are investigated in this chapter. In the BHJs, due to improved donor-acceptor interfacial area compared to bilayers or neat films, the performance of the PEC photoanodes is shown to considerably improve. The device optimizations, thin film and PEC characterization are reported in the following sections. Briefly, the novel donor polymer **P2** in conjunction with the red-shifted acceptor **A2** results in the highest J_{ph} while oxidizing sacrificial reductants in water photoelectrochemically.



[†]Part of this chapter is used in a manuscript submitted to *ACS Applied Materials & Interfaces* (Under Review).

6.1. Introduction

As mentioned in Chapter 1, to improve TF-PEC photoanodes, the interfacial area between the p-type and n-type OSCs need to be increased to an optimum to allow for balance between charge separation and transport, which is the basis of using a BHJ architecture. From previous chapters, donor and acceptor homologues, with deep HOMO-LUMO levels and other optoelectronic properties were obtained. The use of such low HOMO donors coupled with low LUMO NFAs which are based on laterally expanded RDIs have not been explored before even in OPVs, this chapter explores the very possibility as OSC based photoanodes.

For an initial study, **P1** and **P2** as donors with **A1** and **A2** as acceptors were chosen. The summary of their physical and chemical properties is listed in Table 6.1.

Table 6.1: Summary of optoelectronic and electrochemical properties of **P1**, **P2**, **A1** and **A2**.

OSC	Solution State ^[a]			Solid State ^[b]		Measured Electrochemistry		$\mu_{FET,h^+,sat.}$ Hole Mobility ^[c] ($10^{-5} \text{ cm}^2 \text{ V}^{-1} \text{ s}^{-1}$)	
	λ_{Onset}^{Abs} (nm)	λ_{Max}^{Abs} (nm)	$\epsilon_{\lambda_{Max}^{Abs}}^{[d]}$ ($10^3 \text{ cm}^2 \text{ g}^{-1}$)	$E_{g,opt}$ (eV)	λ_{Onset}^{Abs} (nm)	HOMO (eV _{Vac})	LUMO (eV _{Vac})	As Cast	Annealed
P1	651	607	89.14	1.91	664	-5.66	-3.40	4.1	10.2
P2	633	601.5	69.94	1.94	657	-5.77	-3.52	31.8	92.3
A1	544	513.5	3.52	2.26	558	-6.52	-3.94	-	-
A2	677	648.5 403	1.77 2.38	1.79	704	-6.19	-4.24	-	-

[a] **P1** and **P2** were measured in CF, while **A1** and **A2** were measured in tetrahydrofuran. [b] Solutions were spun-coat on glass. [c] OTFT measurements. [d] Mass extinction coefficient considered here due to polymers. **A2** showed an intense, secondary absorption peak.

6.2. Architecture Optimization

In photoanodes, the BHJ needs to supply holes to the electrolyte for oxidative reactions, while the electron requires extraction through the electronic contacts for the counter half-reaction. This configuration necessitates an n-i-p configuration so that the electrolyte can extract holes from the donor polymers in the BHJ. This however requires an electron transport layer or ETL to extract electrons for the acceptor.

All experiments in this chapter would be for sulfite oxidation, as water oxidation would require co-catalyst optimization which is beyond the scope of this initial work. Co-catalysts are usually transition metal oxides which accept holes from the BHJ and catalyse water oxidation, like IrO_x, Ru- coordination complexes etc.^[1,2]

From earlier demonstration^[3], for pH stability in acidic-neutral conditions to complement the photocathodes for tandem use, SnO₂ as the ETL was chosen. The other possible ETL candidates are: WO₃ which is only stable in pH<4; ZnO which is stable in pH>7 and Fe₂O₃ which is stable in pH>10, from *Pourbaix* diagrams for operational stability so that the ETL does not dissociate into ions.^[4–6] Figure 6.2.1 maps out the components involved into an energy diagram, which gives an idea of how the BHJ would look like electronically.

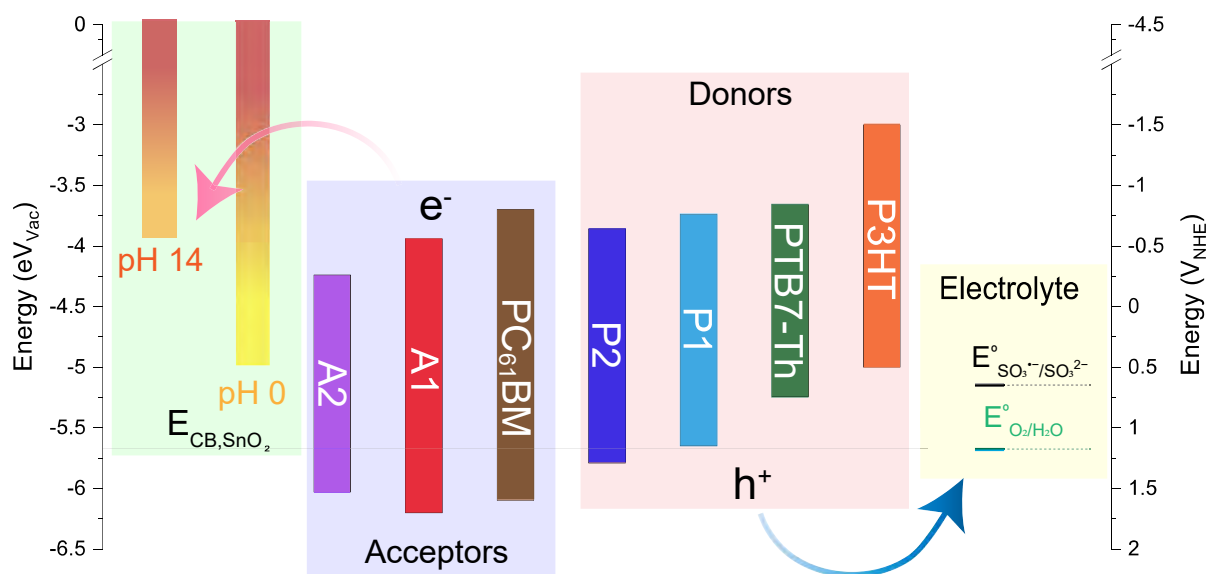


Figure 6.2.1: Energy diagram of ETL at different pH; **P1**, **P2**, **A1** and **A2** as atypical OSC materials for photoanodes and traditional OSCs used in OPVs.

So, with the new OSCs, 4 combinations of BHJs are explored in the upcoming subsections. There are a series of experiments to be performed to optimize the device to get the highest J_{ph} . The first optimization, however, is the device architecture in terms of ETL engineering. The ETL can be used in both mesoporous and planar forms, with the former resulting in a high contact area with the BHJ. Initially **P2**: **A2** in 2:3 weight ratio in a 12 mg·mL⁻¹ chlorobenzene solution as a starting stock solution (which, at this stage is unoptimized for devices) was used and the underlayers were engineered. Since TiO₂ is also a viable pH stable ETL which has higher/destabilized *Fermi* levels than SnO₂, it was also included in this optimization experiment (Figure 6.2.2a). Additionally, to aid smooth film formation, the metal oxides were also treated with functionalized silanes in specific cases.

The first series of LSVs (Figure 6.2.2a) shows that the use of mSnO₂ over pSnO₂ results in the higher J_{ph} for the BHJ. In the second run (Figure 6.2.2b), the stock solution is a more concentrated (20 mg·mL⁻¹) solution in a 1:1 weight ratio. Instead of a silane ether treated ETL, a more traditional self-assembled mono-layer (SAM) from benzoic acid, which

also energetically affects the SnO_2 ^[7] was experimented on. In both series of experiments, the photoanode was annealed at 120°C for 10 minutes after spin-coating in argon.

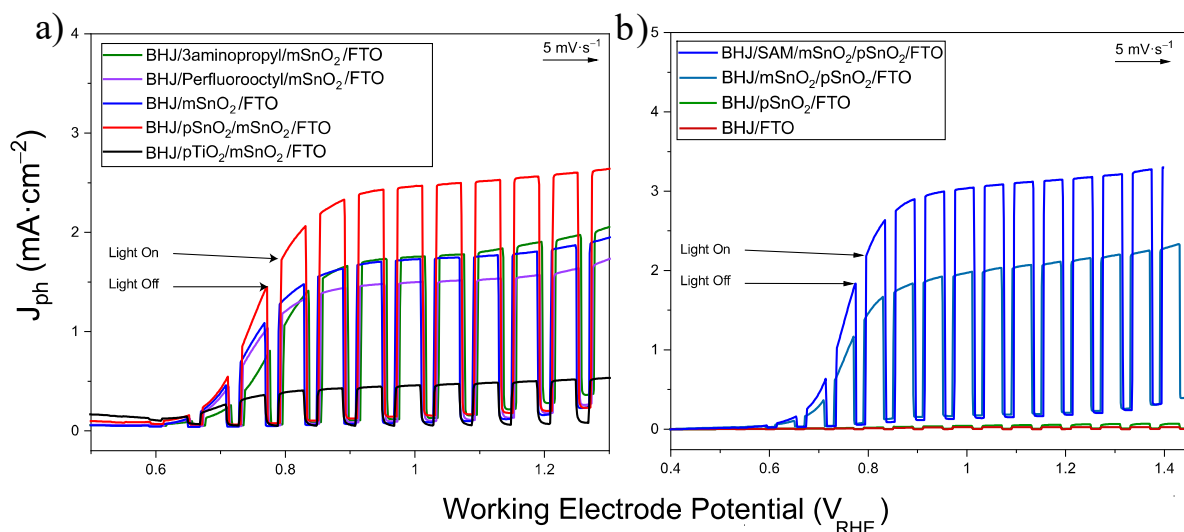


Figure 6.2.2: Optimization LSVs for ETL and underlayers with **P2: A2** in chlorobenzene a) 12 (2:3) $\text{mg}\cdot\text{mL}^{-1}$, b) 20 (1:1) $\text{mg}\cdot\text{mL}^{-1}$.

From these studies, we infer that the presence of mSnO_2 is a necessity, with a pSnO_2 possibly acting as a hole blocking underlayer; neat BHJ over planar metal oxides does not result in good devices. Surface modification with organic molecules is needed to aid in good film formation, as **A2** tends to aggregate easily (Figure 6.2.3 shows the molecules modifying the ETL and images of drop cast acceptor on the modified ETL).

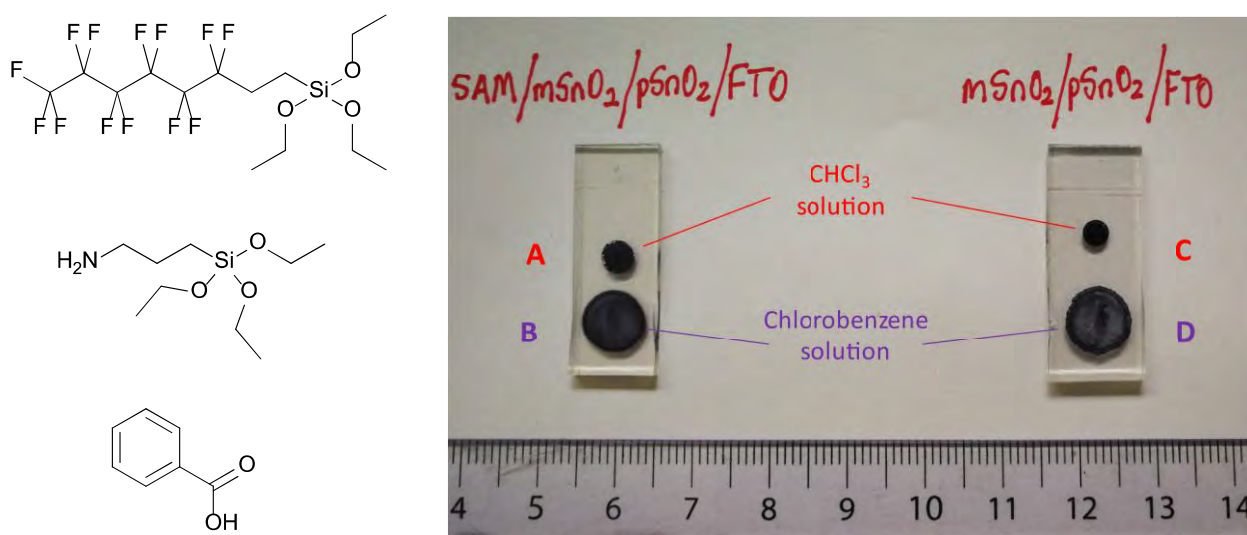


Figure 6.2.3: (Left) molecules modifying ETLs, (Right) with and without benzoic acid modification for **A2** solution.

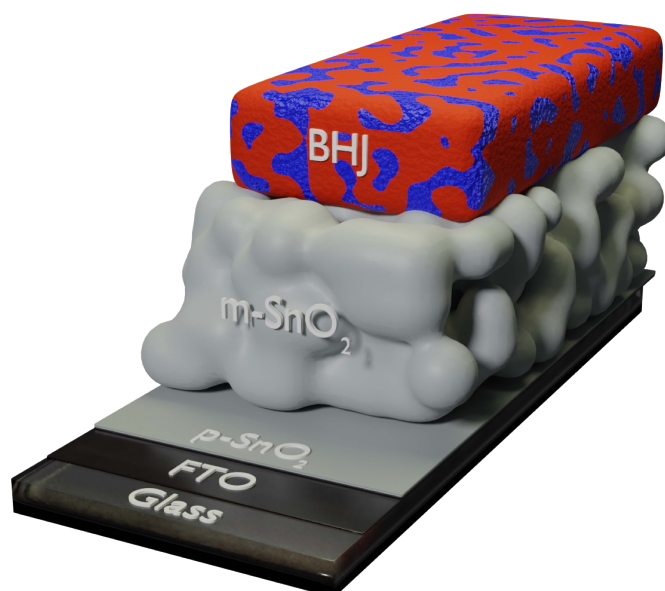


Figure 6.2.4: Rendered image of BHJ photoanode showing different layers involved.

In all subsequent experiments, the OSCs are dissolved in chlorobenzene to result in a $20 \text{ mg}\cdot\text{mL}^{-1}$ solution which is then spun-coat into BHJs over a benzoic acid treated plasma cleaned $\text{mSnO}_2/\text{pSnO}_2/\text{FTO}$ substrate (Figure 6.2.4 shows the multiple layers of a typical photoanode).

6.3. Donor:Acceptor Weight Ratio Optimization

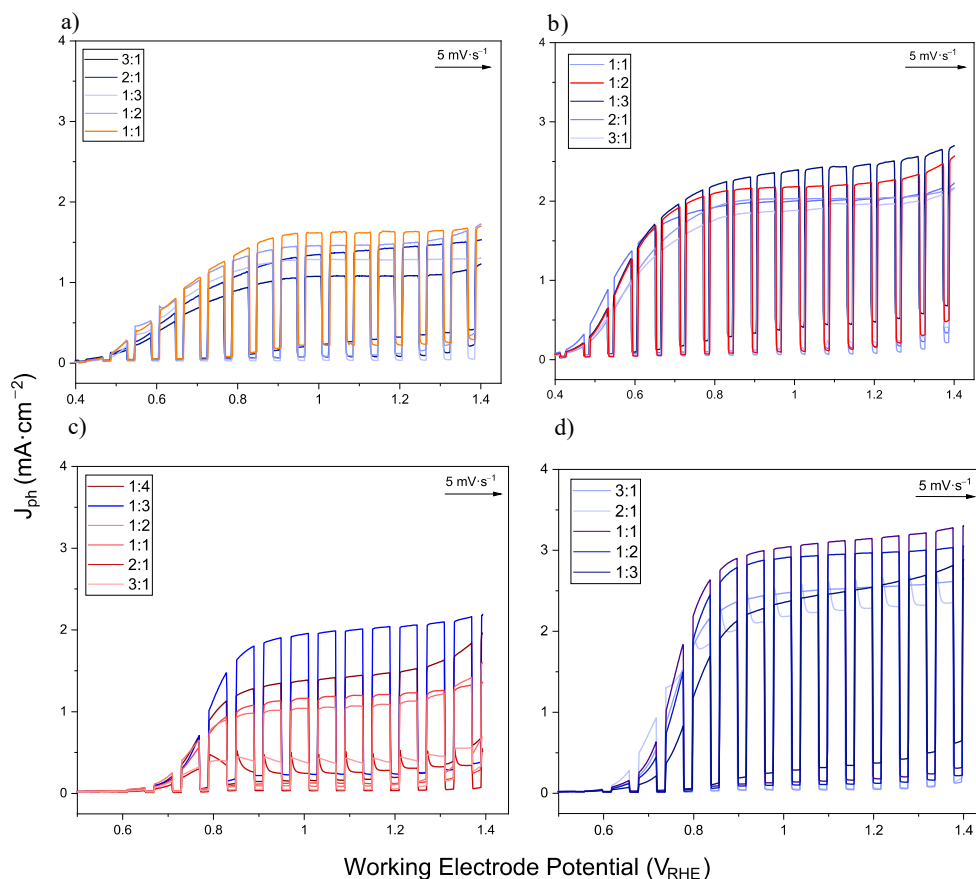


Figure 6.3.1: LSVs of BHJ with different D:A weight ratios for a) **P1: A1**, b) **P2: A1**, c) **P1: A2** and d) **P2: A2**.

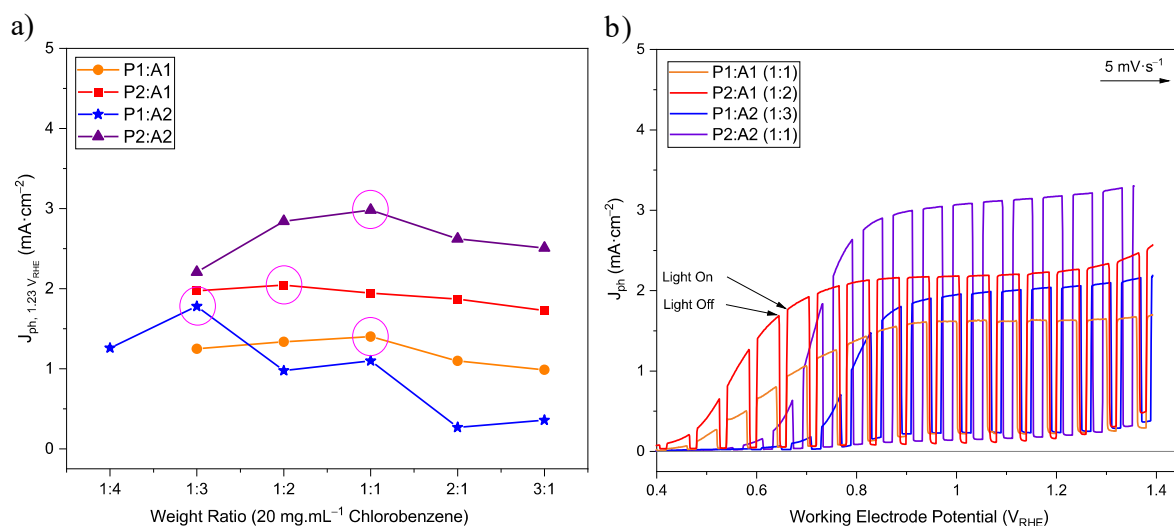


Figure 6.3.2: a) J_{ph} at 1.23 V_{RHE} for different photoanodes, b) LSVs for the highest J_{ph} cases summarized.

Like OPVs, the device optimization requires the right balance of donors and acceptors to allow for charge separation and transport. This weight ratio of donor and acceptor is expected to be different between the two acceptors as they have completely different physical properties. Also, due to the aggregative nature of **A2** while spin-coating, the ratio of the stock solution need not be reflected in the actual molar ratio in the films, thus adding to another uncertainty factor.

LSVs in near neutral pH electrolyte with sulfite (Figure 6.3.1) and plots of the J_{ph} at the water oxidation potential, ie. 1.23 V_{RHE} for the four different photoanodes annealed at 120°C for 10 minutes (Figure 6.3.2) are shown here. The weight ratio resulting in highest J_{ph} for each BHJ is chosen as the optimum and will be reproduced in the subsequent experiments.

6.4. Annealing Optimization

The second most crucial factor which affects the performance is the thermal annealing. For the previous experiments, 120°C for 10 minutes was chosen as the ideal annealing time, with the help of atomic force microscopy images and roughness factor calculations.

6.4.1. AFM images of BHJ

From the AFM images of **A1** based BHJs (Figure 6.4.1), the R_q (roughness factor) is <10 nm, with small phase angles of <3°. The “domains” are in the order of 100-200 nm, which is a high value, as charge recombination is predominant in this range. Comparison of these images with those of **A2** based BHJs (Figure 6.4.2) shows clear differences. One is the shape of the “domain” formed. The former has sphere-like components, whereas the

latter has needle-like “domains,” which are aggregates of **A2** in the BHJ. Another feature is the higher R_q (< 45 nm) and phase angles (<27°) in these BHJs.

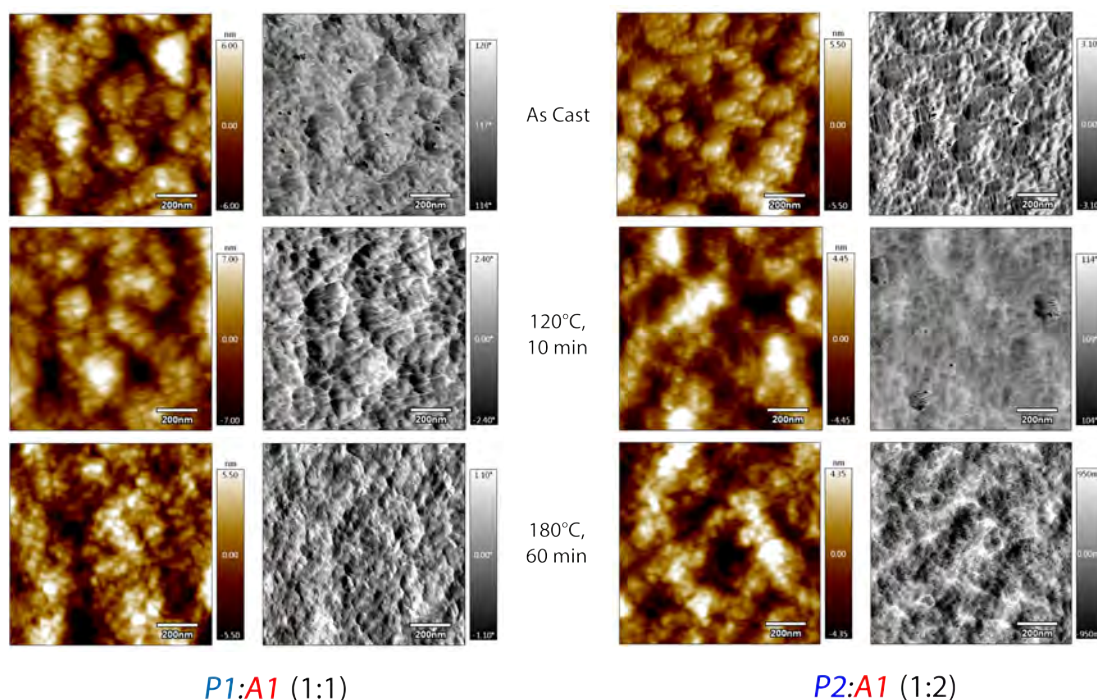


Figure 6.4.1: AFM images of topography with phase images for **P1,P2** and **A1** based BHJs with different annealing conditions.

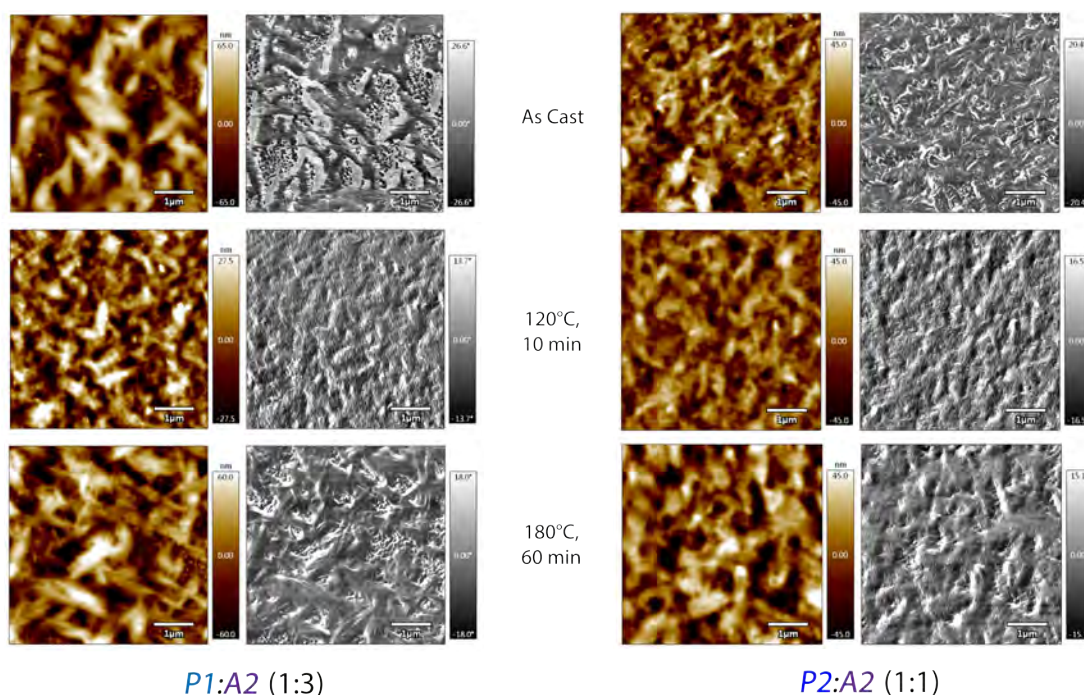


Figure 6.4.2: AFM images of topography with phase images for **P1,P2** and **A2** based BHJs with different annealing conditions.

The initial working assumption is that low R_q leads to better device performance (Figure 6.4.3), hence 120°C for 10 minutes was chosen as the default annealing condition. a series of LSVs on different photoanodes annealed at specific conditions to validate/refute this assumption were run.

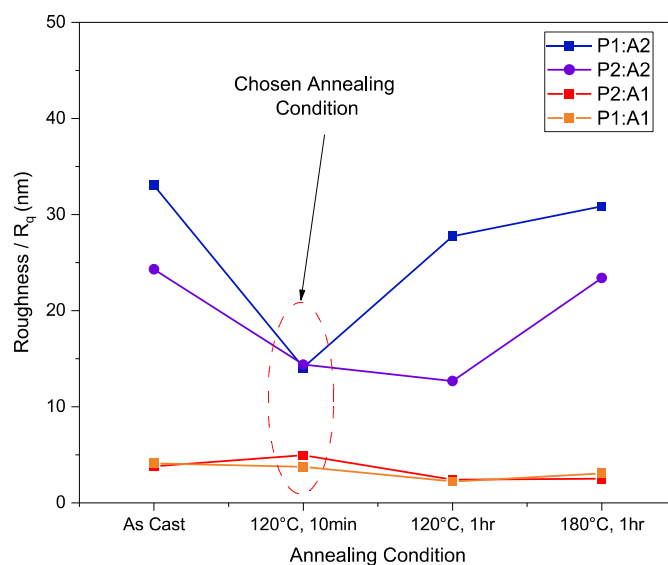


Figure 6.4.3: Roughness factors summarized for BHJs.

6.4.2. PEC validation

Annealing Temperature

A1 based BHJs show high J_{ph} when annealed at a lower temperature of 120°C, whereas the **A2** based films work well when annealed at 180°C (Figure 6.4.4). This observation already casts doubt on the earlier assumption.

Annealing Time

When the optimized films are annealed for a longer duration of 1 hour, the J_{ph} reduces compared to the films annealed for a shorter period. So, the quick annealing which dries out the remaining chlorobenzene solvent and thermally anneals the films is preferred. Longer annealing times do not drastically reduce the performance in **A2** based films as these are still better than the as cast films but do for the **A1** based BHJs (Figure 6.4.5). This could be attributed to the lower thermal melting point (DSC curves in Figure 6.4.7) of **A1**.

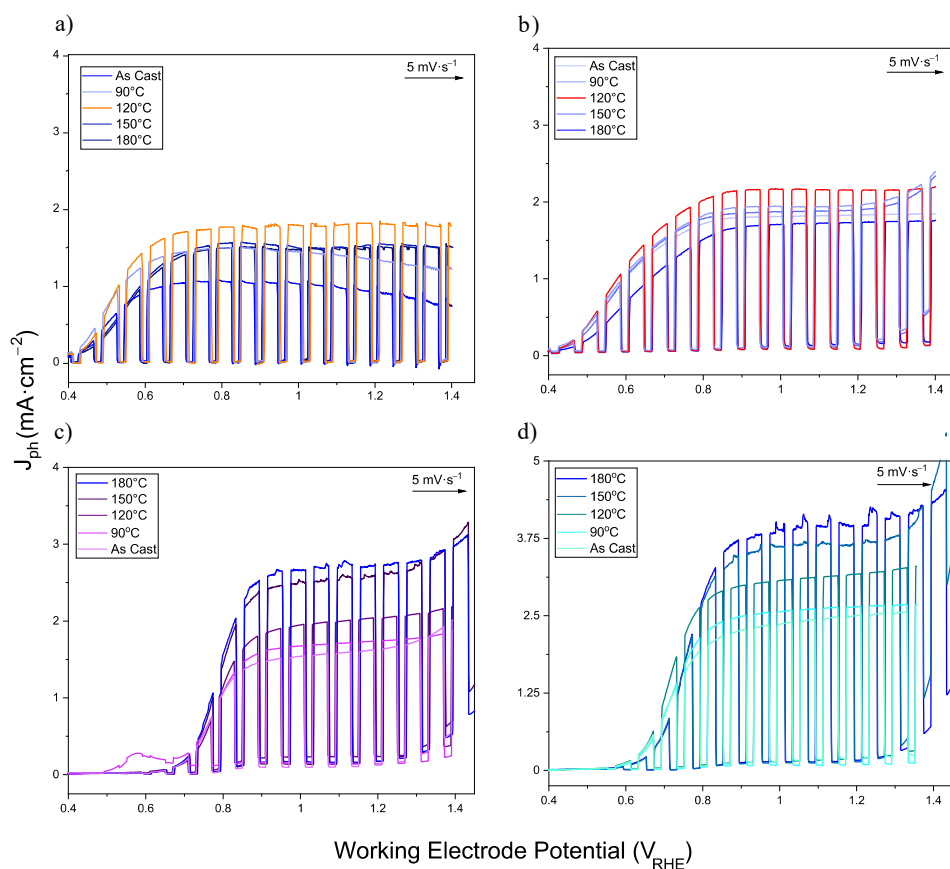


Figure 6.4.4: LSV curves of a) **P1: A1**, b) **P2: A1**, c) **P1: A2** and d) **P2: A2** BHJs annealed for 10 minutes.

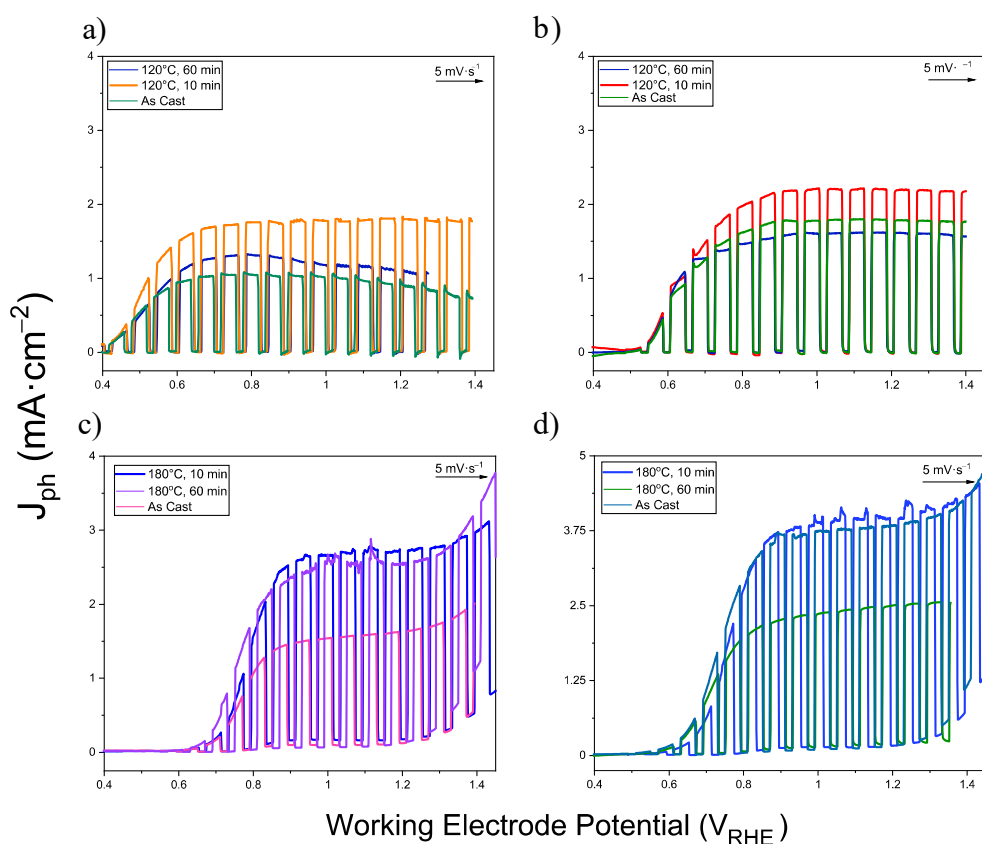


Figure 6.4.5: LSV curves of a) **P1: A1**, b) **P2: A1**, c) **P1: A2** and d) **P2: A2** BHJs annealed at the optimized temperatures.

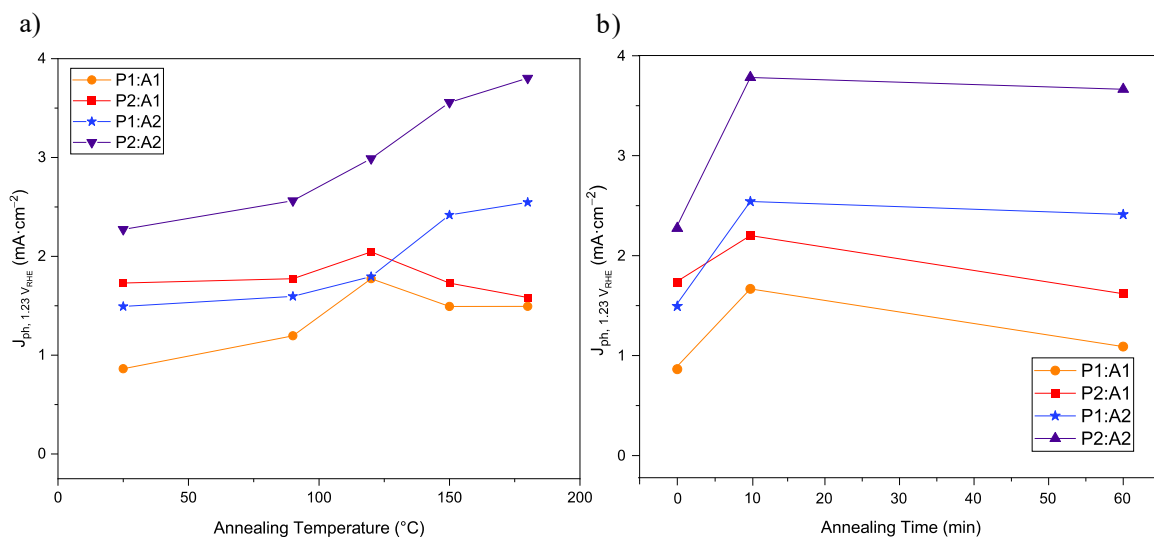


Figure 6.4.6: J_{ph} at $1.23 V_{RHE}$ for different photoanodes when annealed at a) different temperatures, b) different times.

The summarized versions of these figures are presented in the form of plotted J_{ph} at the water oxidation potential, i.e. $1.23 V_{RHE}$ for the four different photoanodes annealed at different conditions (Figure 6.4.6).

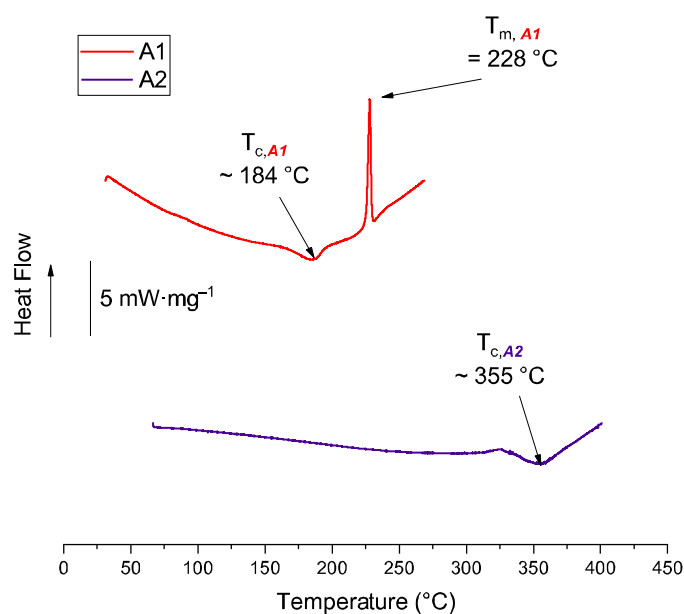


Figure 6.4.7: DSC curves of **A1** and **A2**.

6.4.3. Photoluminescence Studies

From the earlier subsection, the effect of R_q is not a major factor in device performance. To analyze what the exact effect of annealing is, the films using steady state photoluminescence (PL) were probed. Light of certain wavelength is irradiated on the BHJ so that both the donor and acceptor absorb the light, and the fluorescence emitted is recorded. The extent of quenching of the PL determines the charge separation efficiency of the BHJ.

From the PL spectra (Figure 6.4.8: the region under the red box is the emission due to acceptors, while those under the blue box is the emission due to donors), for the **A1** based films there is a minimum for the PL, after a certain extent of annealing. Annealing for longer or higher temperatures than 120°C leads to increase in the PL thereby indicating poorer charge separation. For the **A2** based films, the PL minimum occurs when heated to 180°C for 10 minutes instead. It is also at these conditions that we obtain the highest J_{ph} in the photoanodes. Hence, there is a direct correlation between annealing and the PL compared to its effect on the film topography and morphology.

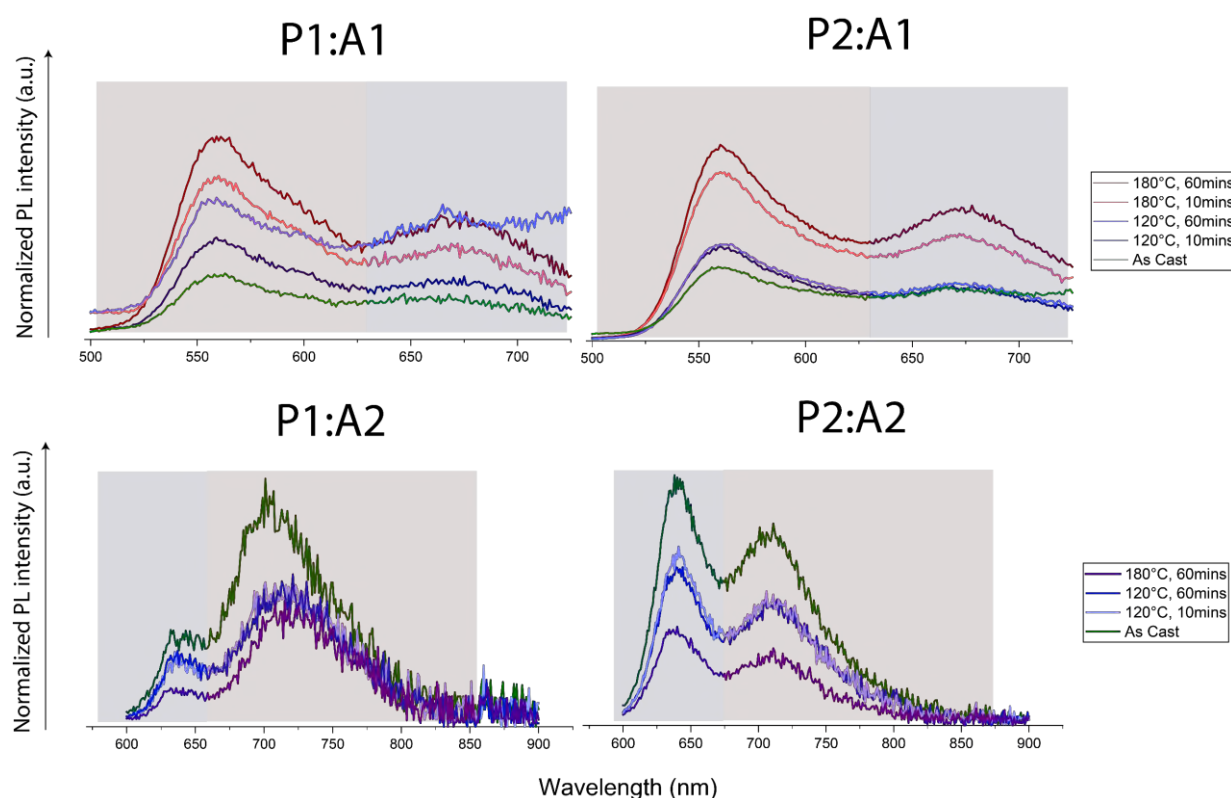


Figure 6.4.8: PL spectra of a) **P1: A1**, b) **P2: A1**, c) **P1: A2** and d) **P2: A2** on irradiation.

6.5. IPCE

Extended conjugation of the molecules leads to red-shifted absorption of the OSCs, and affects the J_{ph} of the photoanode. The IPCE studies on the photoanode (Figure 6.5.1) shed light on the features of the OSCs involved. In **A2** based photoanodes, the extended conjugation in the 670-720 nm region does not cause a significant increase in photogeneration of electrons, but it is the secondary peaks observed in the near 400 nm and 550-650 nm which result in higher J_{ph} . Additionally, **P1** based BHJ have an overall

smaller IPCE/APCE values than **P2** based BHJs, demonstrating the effectiveness of **P2** as a donor polymer over **P1**.

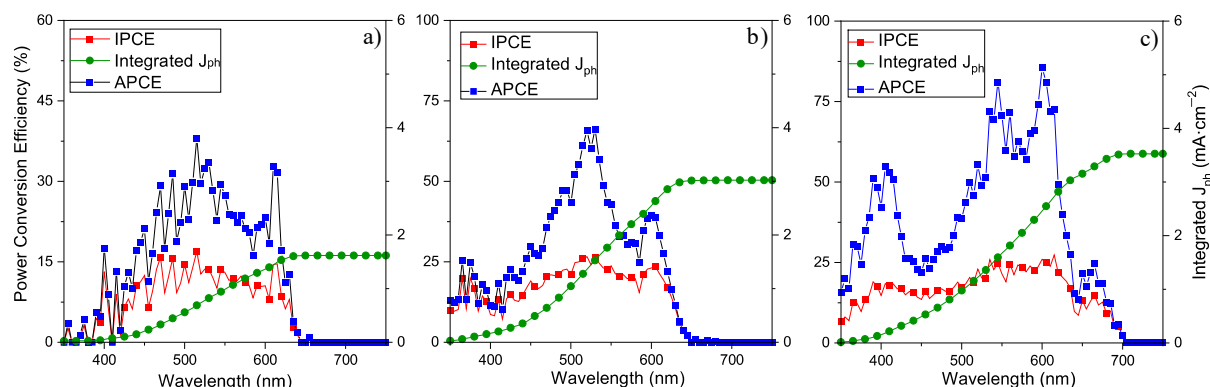


Figure 6.5.1 IPCE and APCE spectra of a) **P1**: **A1**, b) **P2**: **A1**, c) **P2**: **A2** BHJs.

6.6. Effect of Electrolytic pH

6.6.1. Electrochemical Impedance Spectroscopy

The pH dependence of bare ETL's and benzoic acid treated ETL's *Fermi* levels, is observed. Towards this goal, EIS on the substrates in contact with electrolytes of different pH and sacrificial reductant were performed.

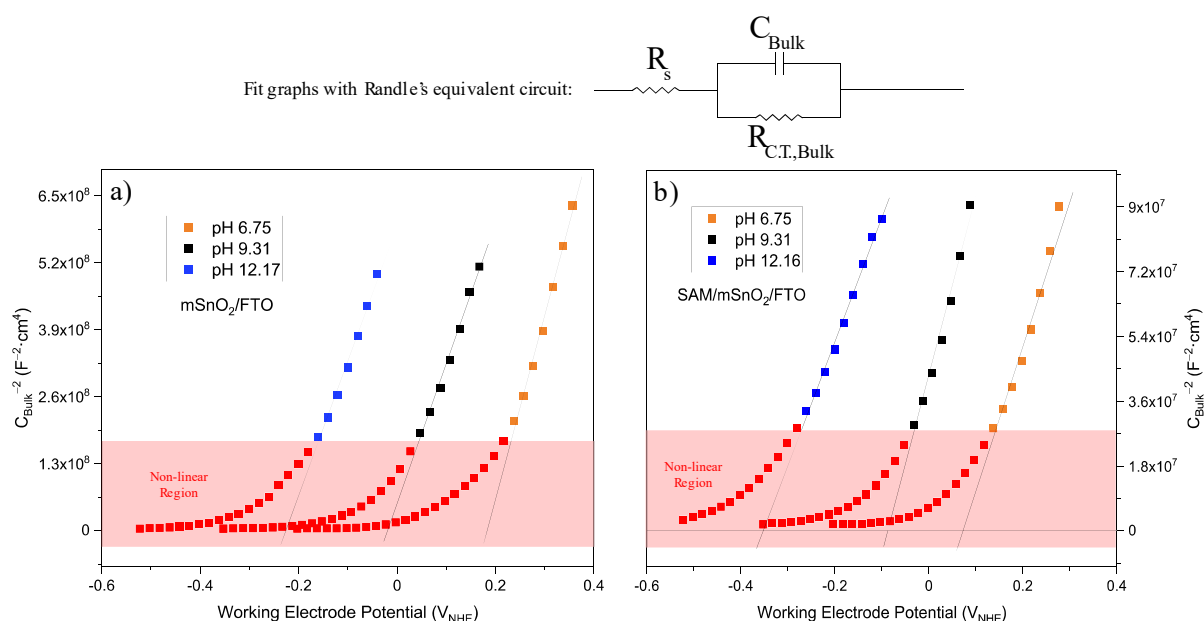


Figure 6.6.1: Mott-Schottky plots extracted from Electrochemical Impedance data taken under dark conditions (without illumination in 1.5 M sulfite and 1 M KPi electrolytes at various pH) of: a) $m\text{SnO}_2/\text{FTO}$ and b) $\text{SAM}/m\text{SnO}_2/\text{FTO}$

With the data extracted from EIS experiments, Mott-Schottky information is plotted for the two substrates (Figure 6.6.1), a distinct effect of pH on the flat band potential of the

metal oxide underlayer, which resembles a linear relationship vs pH (Figure 6.6.2) was noticed. Besides offering a solvophilic advantage, the benzoic acid SAM also p- dopes the metal oxide and increases its flat band potential by 100 meV.

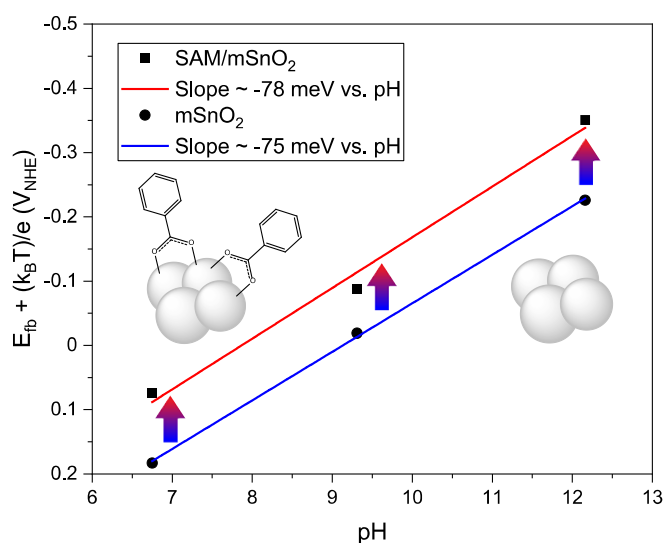


Figure 6.6.2: Effect of pH on the flat band potential of the ETL.

6.6.2. Dynamic Potential pH Diagram

From earlier works,^[8] despite complete coverage of mSnO₂ with an OSC, the pH dependence of the metal oxide fermi level persists, possibly due to channels in the OSC which facilitate contact with the electrolyte. Additionally, the OSCs do not show any change in HOMO-LUMO levels depending on pH, unless extreme pH damages the OSCs, which would probably result in the dissolution of the film.

LSV curves under constant illumination in electrolytes with a wide range of pH were performed to plot a dynamic potential-pH diagram (DPPD, Figure 6.6.3), where the x-axes indicate the pH of the electrolyte and the y-axes, the working electrode potential and the color indicates J_{ph} . The BHJs with **A1** operate in a wide range of pH before deactivation in highly alkaline conditions (pH >10), whereas the BHJs with **A2** are only active in the acidic-neutral conditions (pH <7). This observation can be explained easily. **A2** has a highly negative LUMO level and after a certain pH there is no positive driving force for electron injection into the conduction band of the ETL.

Whereas **A1**, whose LUMO level is about 300 meV higher than **A2**, can afford to function in a wider range of pH. Unfortunately, this also reinforces the fact that despite a hydrophobic layer of BHJ protecting mSnO₂ from the electrolyte, there exist channels within the chlorobenzene processed film exposing mSnO₂ to the electrolyte. Thereby, back

electron reactions leading to drop in J_{ph} are possible, which would be detrimental to water oxidation reaction with co-catalysts, since there would be an additional kinetic factor for hole extraction from BHJ and is not present in electrolytes with highly concentrated sacrificial reductant. This warrants further studies in film formation and interaction of BHJ with electrolyte to reduce the strain on co-catalyst engineering.

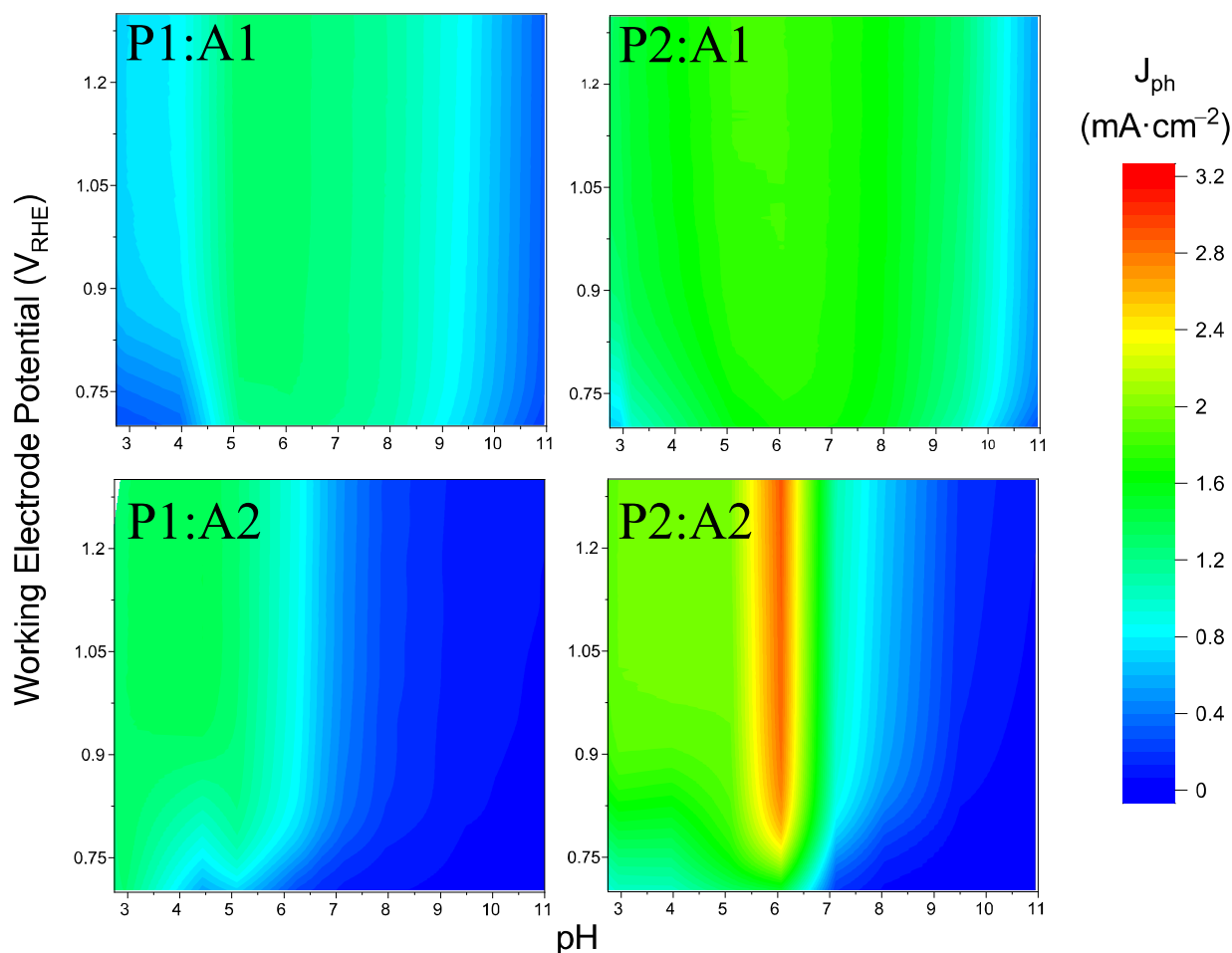


Figure 6.6.3: DPPD plots of BHJs, a) **P1: A1**, b) **P2: A1**, c) **P1: A2** and d) **P2: A2**

6.7. Solvent Choice: Chloroform or Chlorobenzene?

6.7.1. Morphology

As mentioned before, **A2** tends to aggregate, and this effect is more evident in chlorobenzene (CB) at lower temperatures. This proves a disadvantage during spin-coating, as many aggregates were formed in-situ on the film, which may not be desirable for device fabrication on a large scale. These do not seem to negatively affect the LSV of the photoanodes, as high J_{ph} were observed despite the micrometer-sized aggregates. The high boiling CB was also replaced with chloroform (CF), and any changes in the physical

appearance and performance of the devices, specifically those of the high performance BHJ **P2:A2** are described below.

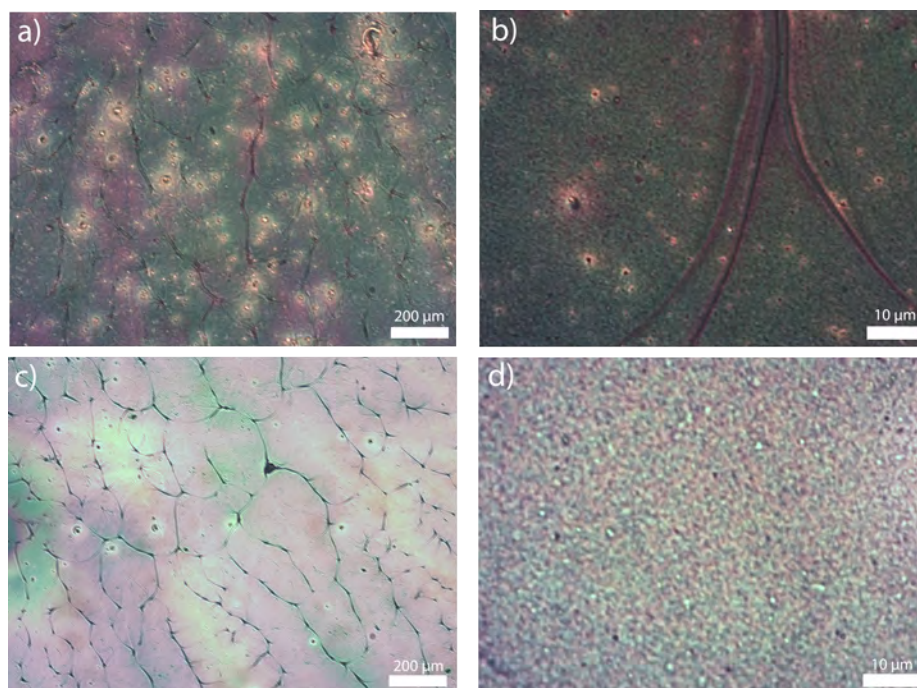


Figure 6.7.1: Optical Microscope images of a,b) CB processed, c,d) CF processed **P2:A2**.

From the optical microscope images in Figure 6.7.1, the number of aggregates is significantly reduced and the resulting films are smoother, with low R_q s for CF processed films (Figure 6.7.2). While among the CB processed films, the use of **A2** results in R_q of 30-45 nm, the CF processed films, irrespective of the acceptor, show $R_q < 5$ nm.

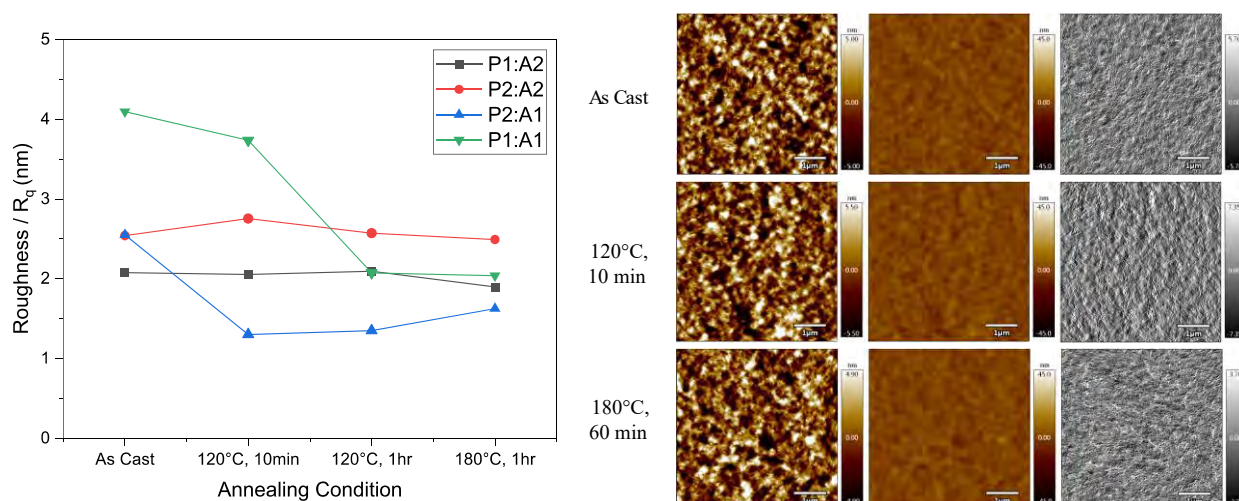


Figure 6.7.2: (Left) Summary of roughness factors for CF processed films, (Right) Topography and phase images of CF processed **P2:A2**.

6.7.2. PEC Performance

When subjected to long term chronoamperometry (CA) at the water oxidation potential (1.23 V_{RHE}), CF and CB processed films show a slight difference in the final stable $J_{ph,1.23V_{RHE}}$ (Figure 6.7.3). The CF processed photoanode attains a maximum J_{ph} after an hour of operation and ends with a stable $J_{ph,1.23V_{RHE}}$ of 2.5 mA·cm⁻², whereas for the CB processed photoanode, J_{ph} reduces over time to attain a stable $J_{ph,1.23V_{RHE}}$ of 1.6 mA·cm⁻².

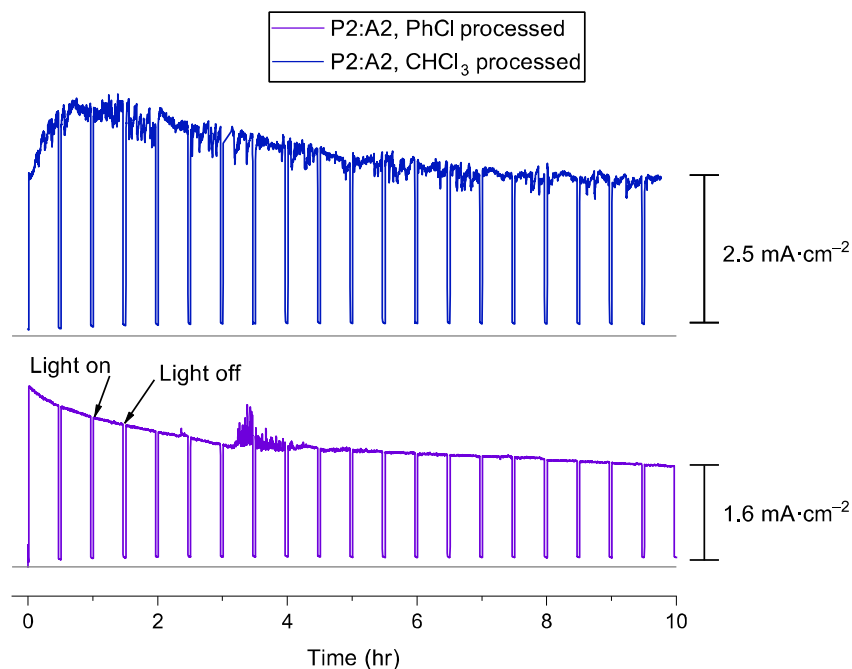


Figure 6.7.3: Long term CA of CF and CB processed **P2:A2** photoanodes.

6.8. Advantage over Traditional OSCs

The overall aim of using the new BHJ combinations was to show their advantages of traditional OSCs, which usually have shallow HOMO levels. While this might not be an issue for OPVs, due to a redox reaction extracting the holes from the photoanode, the energy levels come into play in photoanodes. This “advantage” is demonstrated by comparing the LSV/CA of the devices made with other traditionally used BHJ combinations. The chosen donors are P3HT and PTB7-Th, which have HOMO levels of -5.0 eV_{vac} and -5.24 eV_{vac} respectively. These are coupled with PC₆₁BM and **A2**, and the 4 BHJs are spun-coat on similar underlayers as in the previous sections.

From Figure 6.8.1b, it is evident that only donors with a deep HOMO can drive PEC oxidation of the electrolyte over extended time periods with high J_{ph} . The traditional BHJs

exhibit merely a <5% J_{ph} compared to **P2:A2**. Moreover, due to destabilized HOMO levels, even at low applied potentials, P3HT and PTB7-Th based BHJs show dark currents, indicating BHJ oxidation instead of electrolyte oxidation (the DPPD spectra of these BHJs are shown in Figure 6.8.1a, with darkened regions indicating dark currents).

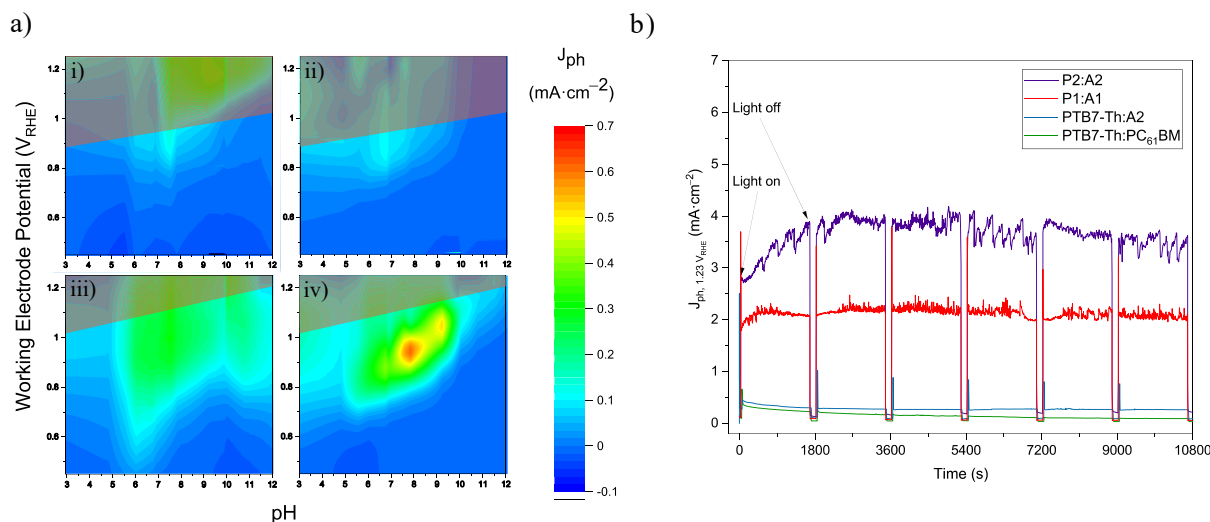


Figure 6.8.1: a) DPPD plots of i) P3HT:PC₆₁BM, ii) P3HT:**A2**, iii) PTB7-Th:PC₆₁BM, iv) PTB7-Th:**A2**, b) Long term CA of various BHJ photoanodes.

6.9. Supporting Information

6.9.1. Electron Microscopy

Typically, electron microscopy was used to look at SnO₂ underlayers and cross sections of the BHJ photoanodes to estimate thickness, film formation etc. On an average, the mSnO₂ underlayers are 300-350 nm thick while the CB processed BHJs are 130-150 nm thick (SEM images of the top and cross-section views in Figure 6.9.1).

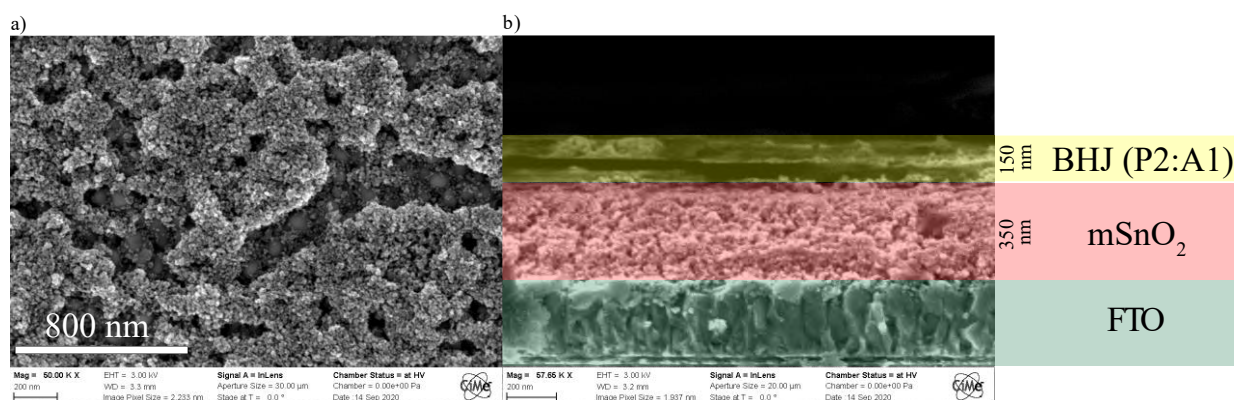


Figure 6.9.1: a) SnO₂ underlayer, shows a mesoporous structure, b) cross section SEM with BHJ.

SEM can also be used to visualize the domains formed. From the AFM, chunks or aggregates of OSCs are visible, but it cannot confirm the chemical nature of these species.

Using the Scanning Auger Microscopy techniques, the sulfur rich polymer donor domains can be visualized to a high resolution as 100-200 nm sized regions (Figure 6.9.2).

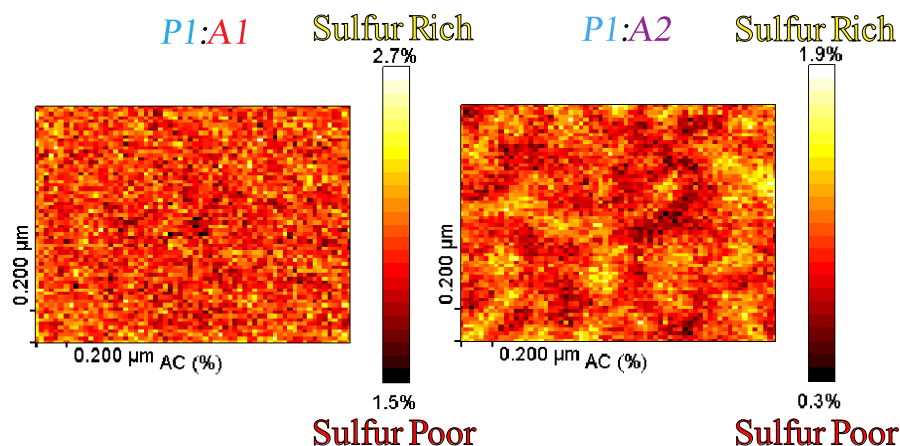


Figure 6.9.2: Scanning Auger Microscopy images of (left) **P1:A1** and (Right) **P1:A2**.

6.9.2. Miscellaneous PEC data

Figure 6.9.3 and Figure 6.9.4 show typical LSV curves of traditional BHJs in different pH electrolytes.

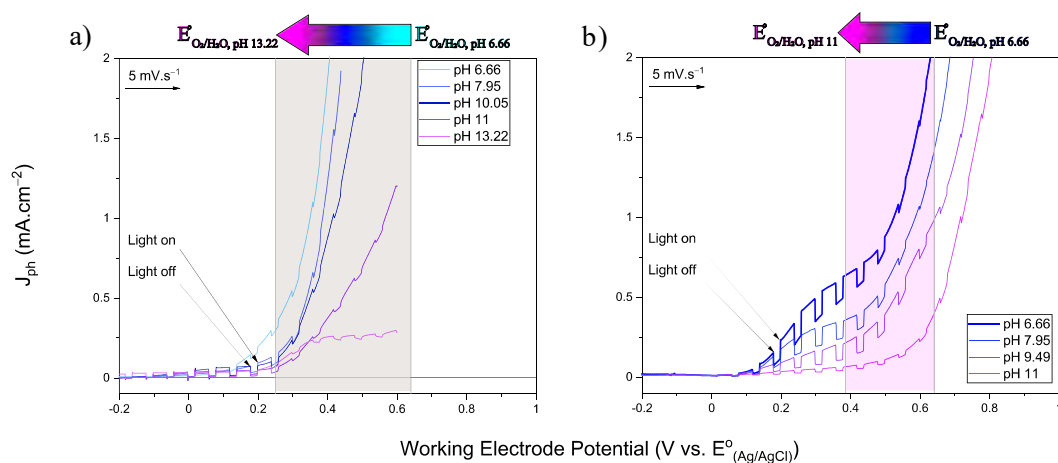


Figure 6.9.3: LSV curves at different pH of a) **P3HT:PC₆₁BM** and b) **P3HT:A2**.

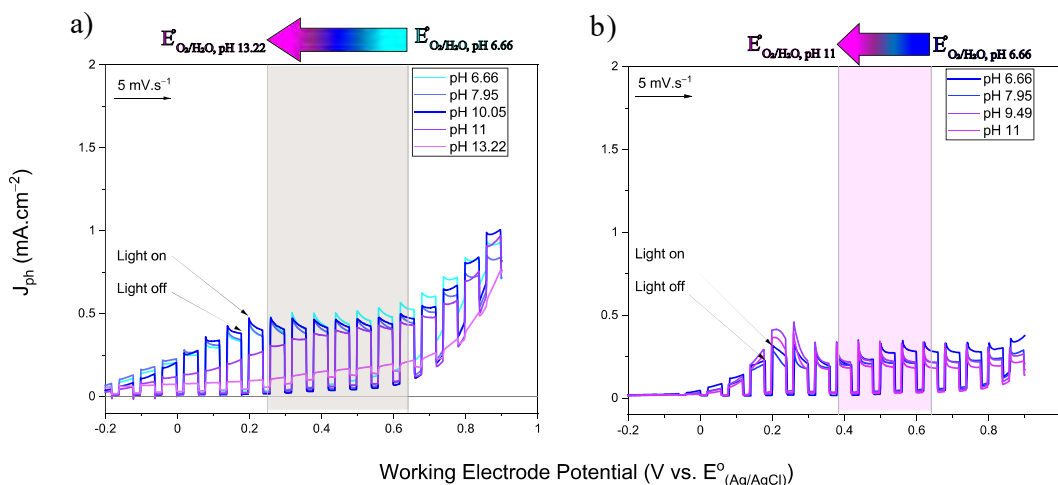


Figure 6.9.4: LSV curves at different pH of a) **PTB7-Th:PC₆₁BM** and b) **PTB7-Th:A2**.

6.10. Conclusion

BHJs were formed using donor polymers from Chapter 4 and acceptor RDIs from Chapter 5. These novel D:A combinations were never studied before in OPVs, however their energetics proved them to be valuable as OSCs for photoanodes. Optimizations to obtain high performance were performed: D:A weight ratios, annealing time and temperatures. The BHJ photoanode with **P2:A2** showed the highest J_{ph} and works well in acidic-neutral electrolytes. Overall, **P2** based BHJs worked better than **P1**. The onset potentials were also shown to be a function of the LUMO levels of the acceptors. An alternate processing solvent, chloroform proved to improve the overall stability of the photoanodes. Finally, these novel BHJ combinations trumped overall traditional OSCs like P3HT, PTB7-Th and PC₆₁BM while oxidizing the electrolyte with sacrificial reductant. In the next chapter, these optimized electrodes are used for applications in tandem devices.

6.11. References

- [1] J. Gao, C.-Q. Xu, S.-F. Hung, W. Liu, W. Cai, Z. Zeng, C. Jia, H. M. Chen, H. Xiao, J. Li, Y. Huang, B. Liu, *J. Am. Chem. Soc.* **2019**, *141*, 3014, DOI: 10.1021/jacs.8b11456.
- [2] L.-X. Xue, T.-T. Meng, W. Yang, K.-Z. Wang, *J. Photochem. Photobiol. B* **2015**, *152*, 95, DOI: 10.1016/j.jphotobiol.2015.07.005.
- [3] H.-H. Cho, L. Yao, J.-H. Yum, Y. Liu, F. Boudoire, R. A. Wells, N. Guijarro, A. Sekar, K. Sivula, *Nat. Catal.* **2021**, *4*, 431, DOI: 10.1038/s41929-021-00617-x.
- [4] P. A. Shinde, S. C. Jun, *ChemSusChem* **2020**, *13*, 11, DOI: 10.1002/cssc.201902071.
- [5] A. Khor, P. Leung, M. R. Mohamed, C. Flox, Q. Xu, L. An, R. G. A. Wills, J. R. Morante, A. A. Shah, *Mater. Today Energy* **2018**, *8*, 80, DOI: 10.1016/j.mtener.2017.12.012.
- [6] J. Ning, Y. Zheng, B. Brown, D. Young, S. Nešić, *Corrosion* **2015**, *71*, 945, DOI: 10.5006/1566.
- [7] L. Macaraig, T. Sagaw, S. Yoshikawa, *Energy Procedia* **2011**, *9*, 283, DOI: 10.1016/j.egypro.2011.09.030.
- [8] L. Yao, Y. Liu, H.-H. Cho, M. Xia, A. Sekar, B. Primera Darwich, R. A. Wells, J.-H. Yum, D. Ren, M. Grätzel, N. Guijarro, K. Sivula, *Energy Environ. Sci.* **2021**, 10.1039.D1EE00152C, DOI: 10.1039/D1EE00152C.

Chapter 7. Applications

Chapter 4-Chapter 6 dealt with donors, acceptors and thin film BHJ photoanodes which can be constructed from them. For evaluating the PEC performance, sulfite sacrificial reductant was used. This chapter deals with the applications of the photoanode devices. Due to the inherent drawbacks of using [A2](#), and alternate acceptor is explored in BHJ devices. Tandem applications where the photoanode is coupled with an OSC photocathode to perform hydrohalic acid splitting, initial forays into water splitting, and other concepts are introduced. Briefly, this is one of the first demonstrations of BHJ photoanodes capable of oxidizing iodides and bromides at acidic and near-neutral pH without the aid of any additional catalysts, with hour scale stabilities. Tandem, unassisted, solar-to-hydrogen and solar-to-chemical conversion is eventually demonstrated in the hour-scale.

7.1. Motivation

With optimized BHJ photoanodes now, applications can be explored: for example, PEC oxidation of iodide to iodine,^[1] with tandem architecture for a complete PEC reaction, etc. Tandem photoanodes with photocathodes to allow for complete unassisted photoelectrochemical reactions could also work. All experiments have been conducted with the working photoelectrode (BHJ photoanode), a reference electrode (Ag/AgCl) and a counter electrode (graphite rod). This single photoelectrode, however, does not have sufficient photovoltage to power any PEC reaction without external applied potentials, hence two photoelectrodes, one which performs the oxidation half reaction, and the other, the reduction, are combined and schematically shown in Figure 7.1.1.

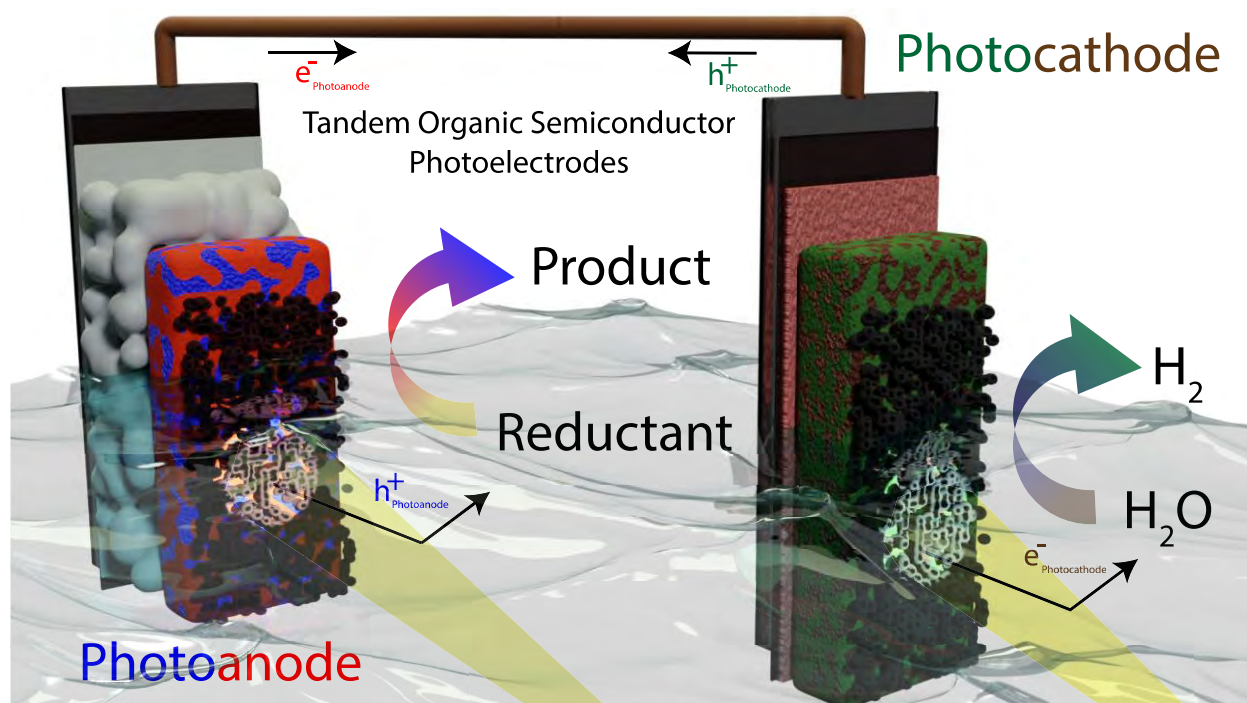


Figure 7.1.1: Tandem OSC based photoelectrodes in aqueous electrolytes.

While the high performance **P2:A2** demonstrate good stability, due to the low LUMO levels of **A2** the photoanode was shown to not work in a wide range of pH and cause issues of charge injection into the ETL in neutral-alkaline pH, besides causing loss of photovoltage. Additionally, **A2** tends to self-aggregate, leading to issues of large-scale device fabrication and charge recombination if additional overlayers like co-catalysts or HTLs would be used. Hence, there is a need to look at alternate acceptors, capable of forming BHJ with **P2** to drive electrolyte oxidation.

7.2. BHJ (re-)optimization

7.2.1. Acceptor modification

From Chapter 5, an extended RDI, **A4b** was synthesized and characterized, which is a dehalogenated dimer of **A2**. It can be seen from the energy level scheme (Figure 7.2.1b) that the LUMO of **A4b** is comparable with that of **A1**, which functions well in a wide pH range without issues of electron injection into the ETL. Moreover, **A4b** also absorbs a greater fraction of NIR light, as can be seen from the solid-state absorption spectra in Figure 7.2.1a.

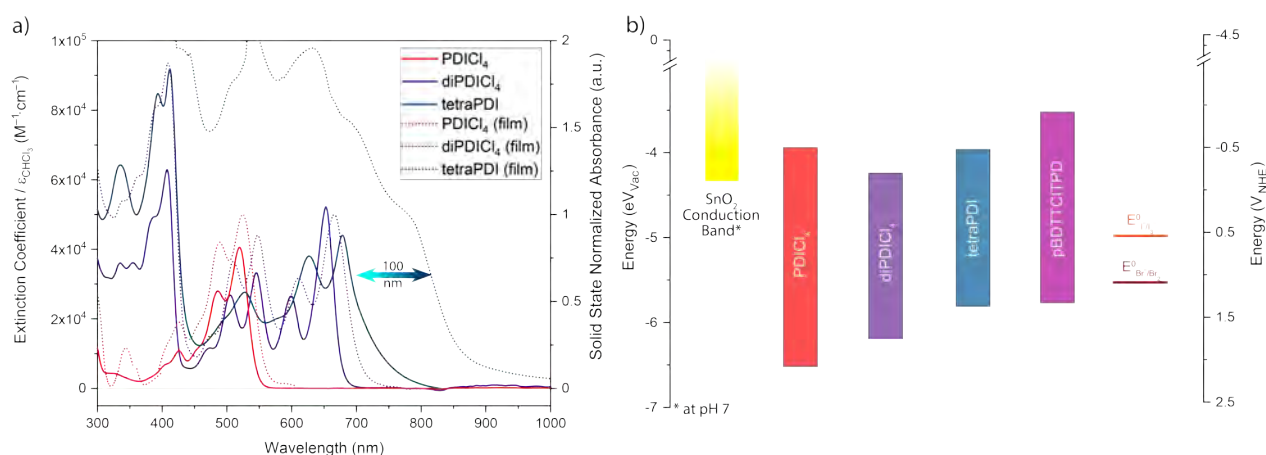


Figure 7.2.1: a) UV-Vis absorption spectra of the acceptors, b) Energy levels for OSCs, comparing **A1**, **A2**, and **A4b** with the donor **P2**.

Besides offering an electrochemical advantage, **A4b** also causes fewer aggregates compared to **A2**, in a BHJ film with **P2**. The **P2:A4b** thin films demonstrate smaller, well-ordered domains on annealing, as can be seen from the bright field spots from AFM topographic and phase images (Figure 7.2.2).

7.2.2. SAM modification

For reasons of smooth film formation and energetics, the ETL was treated with an electron donating organic compound, *cyclohexylamine*, before the BHJ spin-coating process. Surface potential maps by Kelvin Probe Force Microscopy, or KPFM (Figure 7.2.3) are a representation of the electronic fermi levels of the examined ETLs. It is evident that the use of an electron withdrawing organic substituent *benzoic acid*,^[2] which was used in earlier photoanodes greatly destabilizes the surface potential (-0.249 V) while an electron donating substituent, *cyclohexylamine* slightly stabilizes tin oxide's surface potential ($+0.235$ V). This results in greater driving force for electron injection from acceptors at a given pH and applied potential.

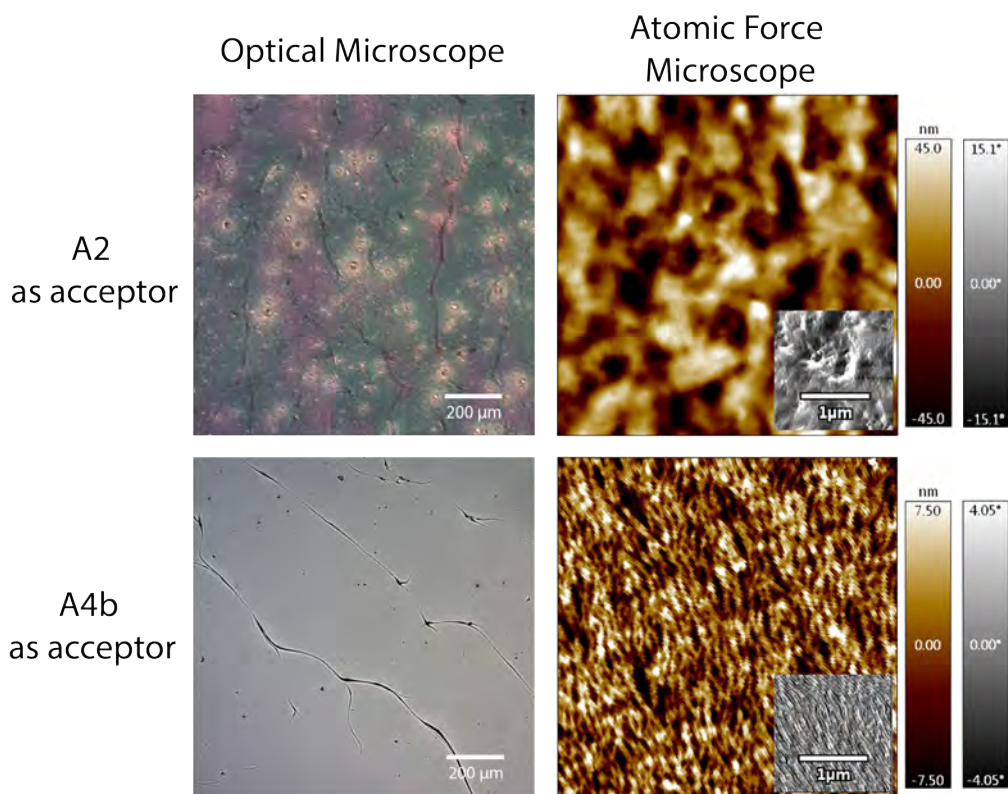


Figure 7.2.2: Optical microscope and AFM images comparing thin film BHJ of **P2**:Acceptor combination, under similar processing and annealing conditions.

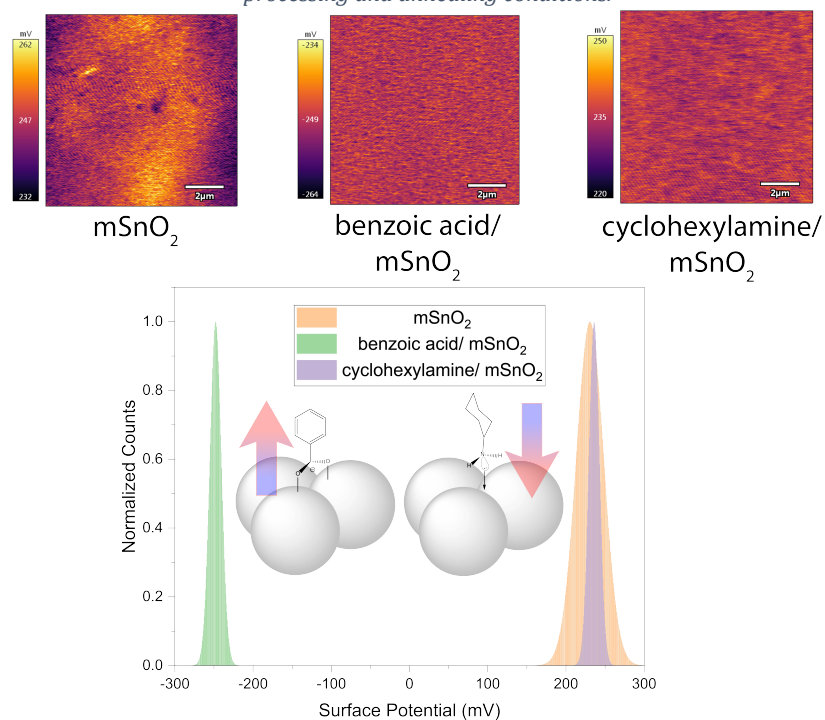


Figure 7.2.3: Kelvin probe force microscopy image maps of bare and SAM treated tin oxides. Note the use of benzoic acid destabilizes, while cyclohexylamine slightly stabilizes the tin oxide surface potential.

The effect of the using an electron donating SAM can also be seen in the difference in PEC performance for halide oxidation, elaborated in the next sub-section.

7.3. Halide PEC oxidation

For a complete PEC reaction, the oxidation half reaction is of importance as it determines the working parameters of the electrode. The focus can now shift from a sacrificial reductant oxidation (sulfite) to halide oxidation. The pH dependence of the halide oxidation potential is mapped in Figure 7.3.1, showing that the reaction itself does not have a pH dependence, and the redox potential remains constant irrespective of the electrolyte's pH (in the acidic to neutral range) at +0.54 V_{NHE} for iodide and +1.09 V_{NHE} for bromide.^[3,4] With a lower redox potential and a two-electron oxidation, on contrast with water oxidation reaction, these reactions also offer the economic advantage of iodine or bromine production, useful in the chemical, pharma industries.

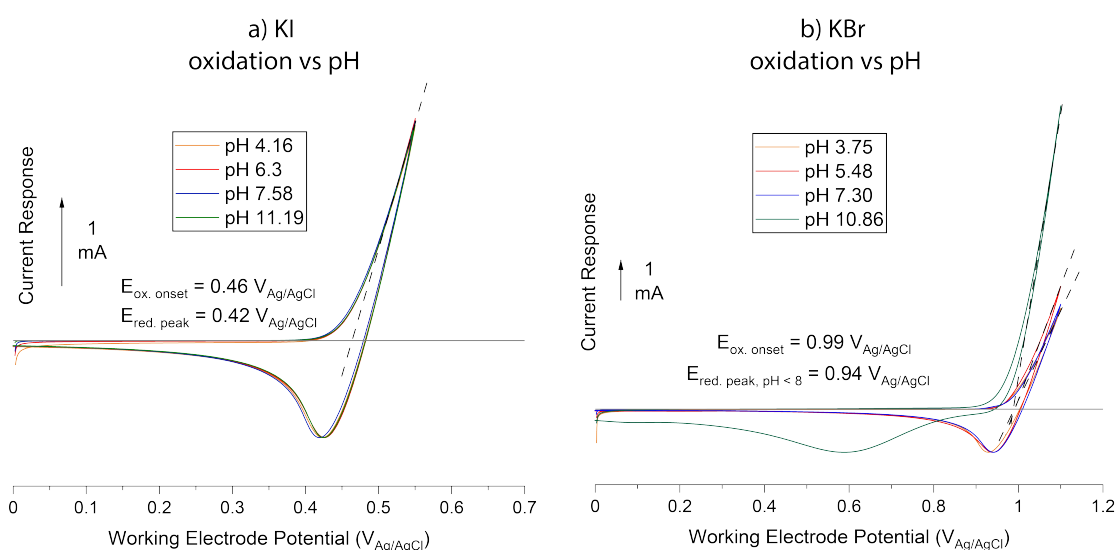


Figure 7.3.1: CV on FTO substrates immersed in 1 M KI/KBr electrolytes buffered at different pH (1 M KPi) showing pH insensitivity for halide oxidation.

7.3.1. PEC Performance

LSV curves under constant simulated 1 sun illumination and in dark conditions were collected and subtracted to give J_{ph} at different applied potentials, as shown in Figure 7.3.2b,c. For iodide oxidation, the resulting J_{ph} when applied potential equals the iodide redox potential (+0.54 V_{NHE}) is $\sim 3.7 \text{ mA}\cdot\text{cm}^{-2}$ at pH 1.2, while it reduces to $\sim 1.95 \text{ mA}\cdot\text{cm}^{-2}$ at pH 6.2. On the other hand, for bromide oxidation, the performance is modest, possibly due to reduced thermodynamic driving force (the difference between donor_{HOMO} and halide redox potentials) for hole transfer to the electrolyte (+0.79 eV for iodide oxidation vs. +0.24 eV for bromide oxidation). When the applied potential equals bromide redox potential (+1.09 V_{NHE}), the J_{ph} is $\sim 0.25 \text{ mA}\cdot\text{cm}^{-2}$ at pH 1.2, while it reduces to $\sim 0.03 \text{ mA}\cdot\text{cm}^{-2}$ at pH 6.4. These are also probably the first few examples of an OSC based photoanode

demonstrating PEC oxidation of iodides and bromides at acidic and near neutral pH without catalysts.^[5]

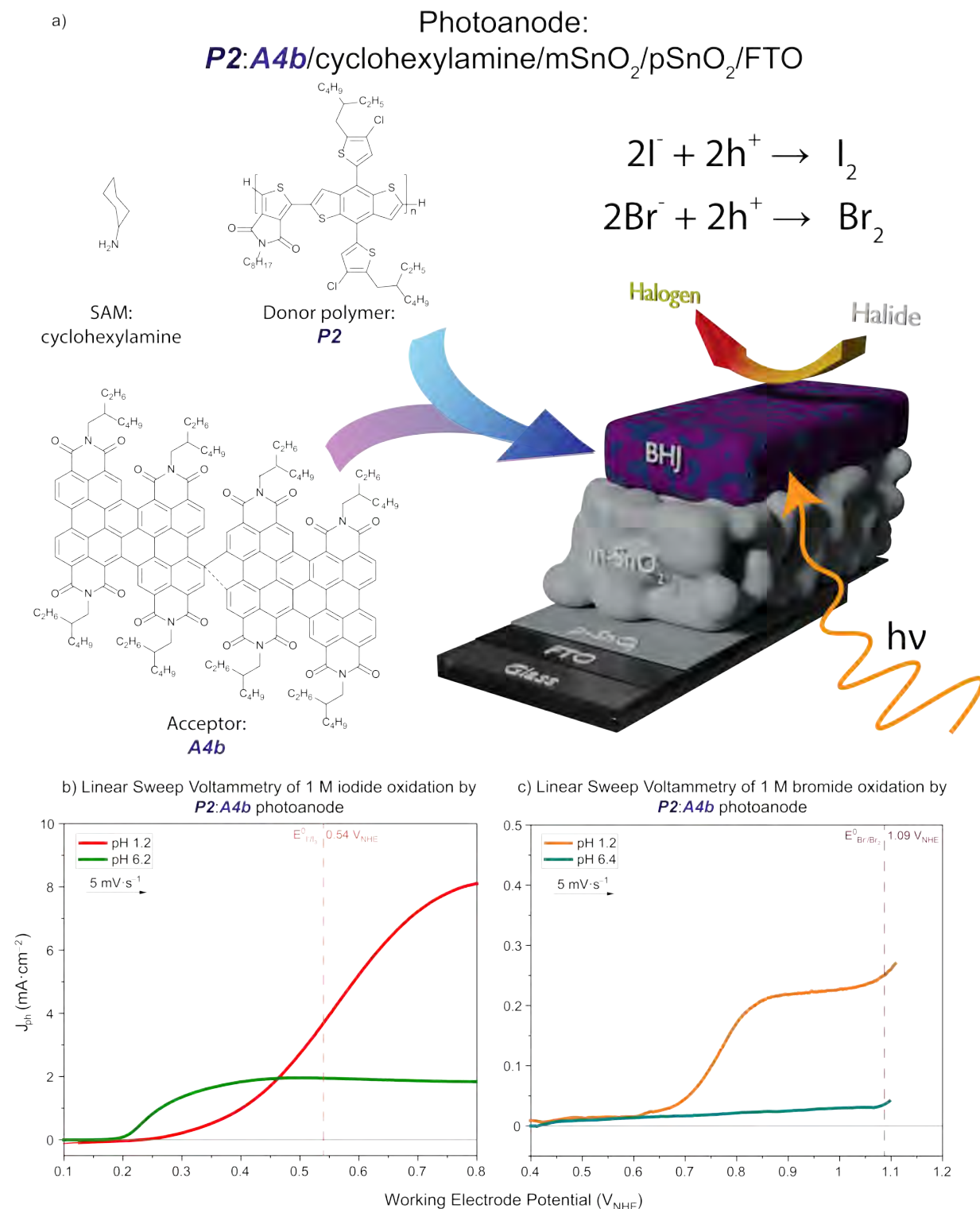


Figure 7.3.2: a) Chemical structures of OSC components in photoanode with reaction scheme and illustration, b) 1 M iodide, c) 1 M bromide aqueous photoelectrochemical oxidation, linear sweep voltammetry at pH 1.2 and pH 6.2-6.4.

The pH dependence in these photoanodes is studied by plotting a dynamic potential-pH diagram, like the earlier chapters (Figure 7.3.3). A clear advantage of using cyclohexylamine treated ETLs is seen, over benzoic acid treated ETLs. Under the same pH

and working electrode potential, cyclohexylamine treated ETLs show higher J_{ph} with **P2:A4b** BHJ.

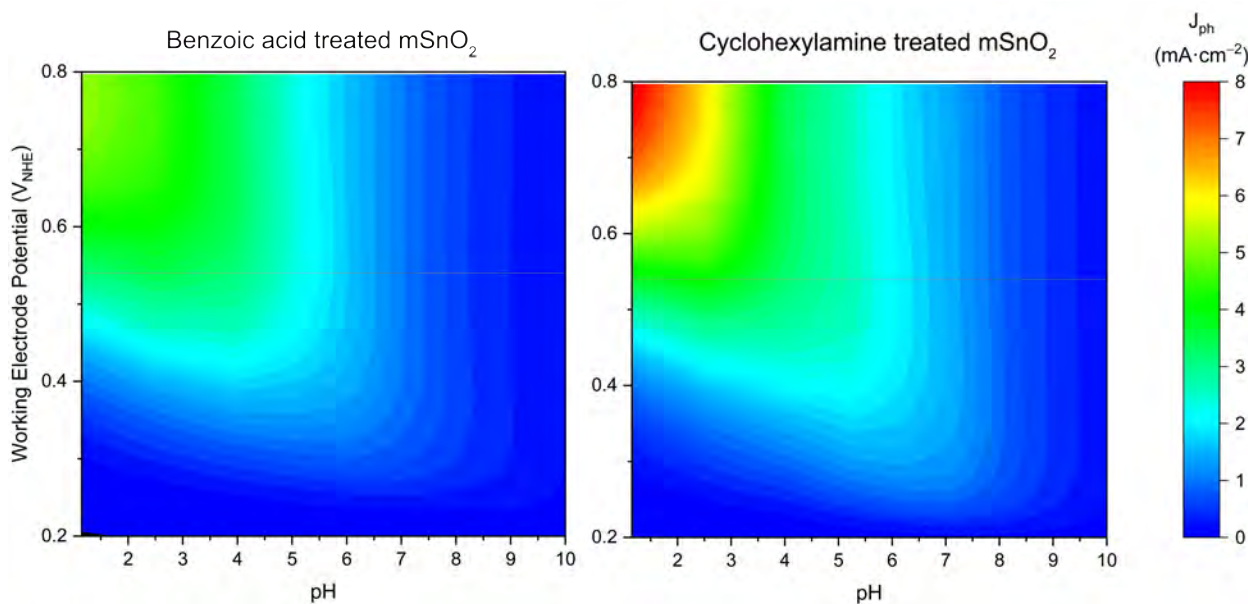


Figure 7.3.3: Dynamic potential-pH diagrams showing J_{ph} under different applied potentials and electrolytic pH. Cyclohexylamine treated ETLs show higher J_{ph} than benzoic acid treated ETLs under similar conditions.

These photoanodes are also quite stable in the hour-scale periods, as observed from CA when applied potential equals the halide redox potentials (Figure 7.3.4b). Even after 10 h of operation, the maximum loss in J_{ph} for the photoanode in different electrolytes is <10%. Note that all these experiments are performed with a graphite rod counter electrode (Figure 7.3.4a), and the next section deals with unassisted tandem electrolyte splitting using all OSC based photoelectrodes.

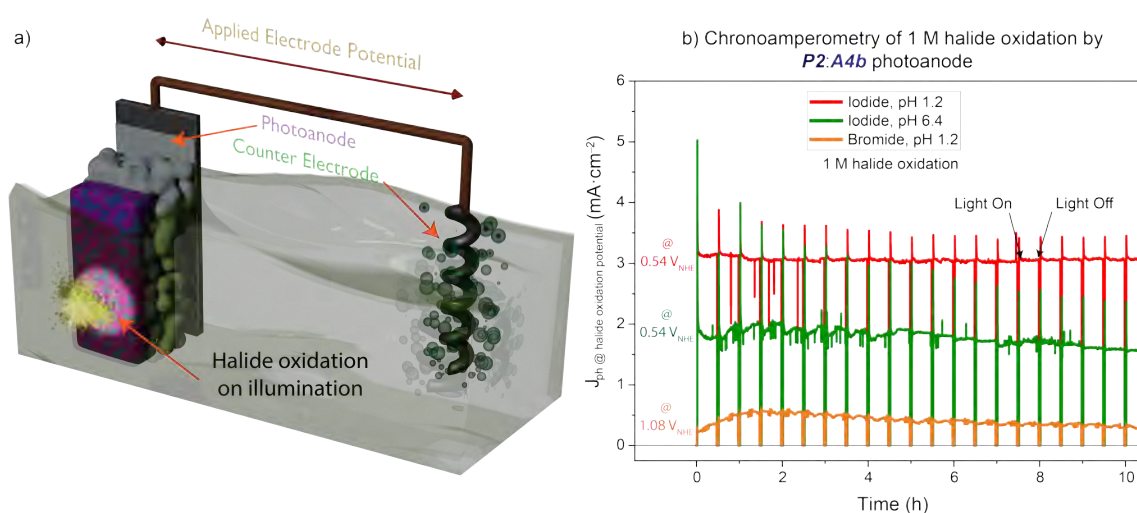


Figure 7.3.4: Scheme of PEC cell for photoanode characterization, b) CA of photoanodes showing hour-scale stability for halide oxidation.

7.3.2. Tandem PEC for HI splitting

The **P2:A4b** photoanodes are coupled directly to an OSC based photocathode whose configuration and components are derived from works^[6] with modifications to the BHJ used, and is elaborated in 7.6.Supporting Information. The energetic scheme of such a tandem system, along with the redox potentials, half reactions and equilibrium reactions^[7] are shown in Figure 7.3.5.

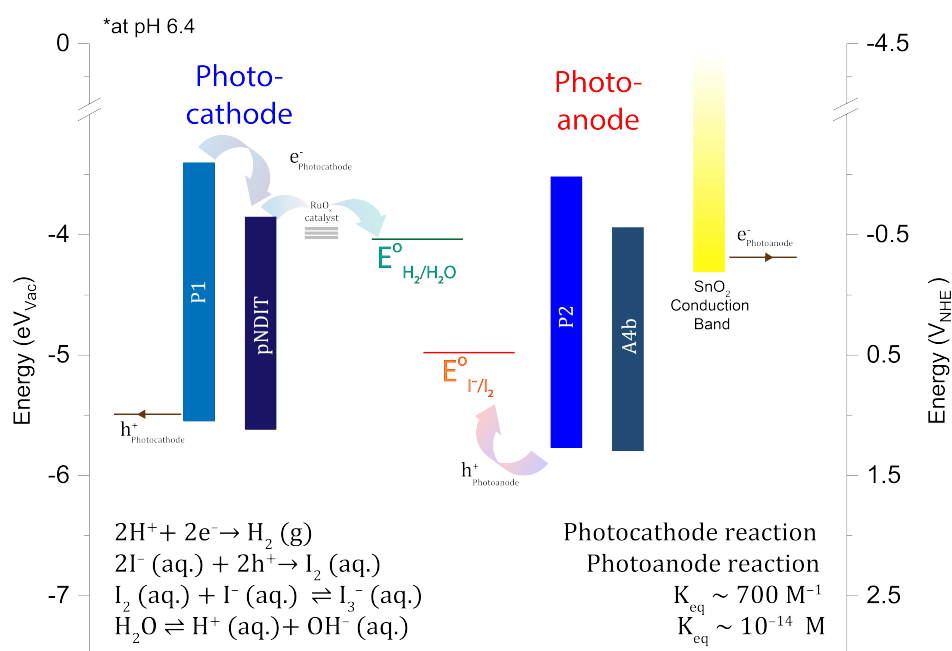


Figure 7.3.5: Energy scheme for a tandem BHJ based PEC system for HI splitting at near neutral pH. The redox half reactions, and other equilibrium reactions occurring simultaneously are also mentioned.

From Figure 7.3.2 and Figure 7.6.1, due to poor overlap of the j-V curves for the two photoelectrodes in acidic pH, the tandem system is demonstrated only in near neutral pH, as the photocathode reaction depends on pH due to the redox potential for water reduction decreasing with increase in pH. Besides, the BHJ photocathode also shows poor operation stability in acidic conditions.

For tandem systems, the configuration determines the incoming solar irradiation percentage received by each electrode. In the following large area tandem experiments, $\sim 2 \text{ cm}^2$ of the photoelectrodes are immersed in the electrolyte and the photocathode first receives irradiation, while transmitted irradiation is absorbed by the photoanode (scheme and photograph of the tandem PEC cell in Figure 7.3.6a,b). This is evident from the LSV curves of the photoelectrodes. The LSV curve (Figure 7.3.6c) of the photoanode with the photocathode blocking the irradiation shows a drastic decrease in J_{ph} compared to direct irradiation. Under the dynamic conditions of the LSV, it is estimated that the working conditions of the tandem cell should be close to the

operating parameters of 0.46 mA at 0.47 V_{NHE}. However, under steady-state, long term CA measurements with no applied bias (Figure 7.3.6d), this initial photocurrent value drops to ~0.2 mA within a few seconds, but stays relatively stable for over 11 h of operation, only interrupted by the regular light chopping for a few minutes. Over time, the photocathode surface evolves bubbles of hydrogen gas, and the electrolyte turns dark yellow-red indicating the formation of triiodide by the photoanode. This is one of the first demonstrations of hour-scale all OSC based tandem photoelectrode system splitting an electrolyte.

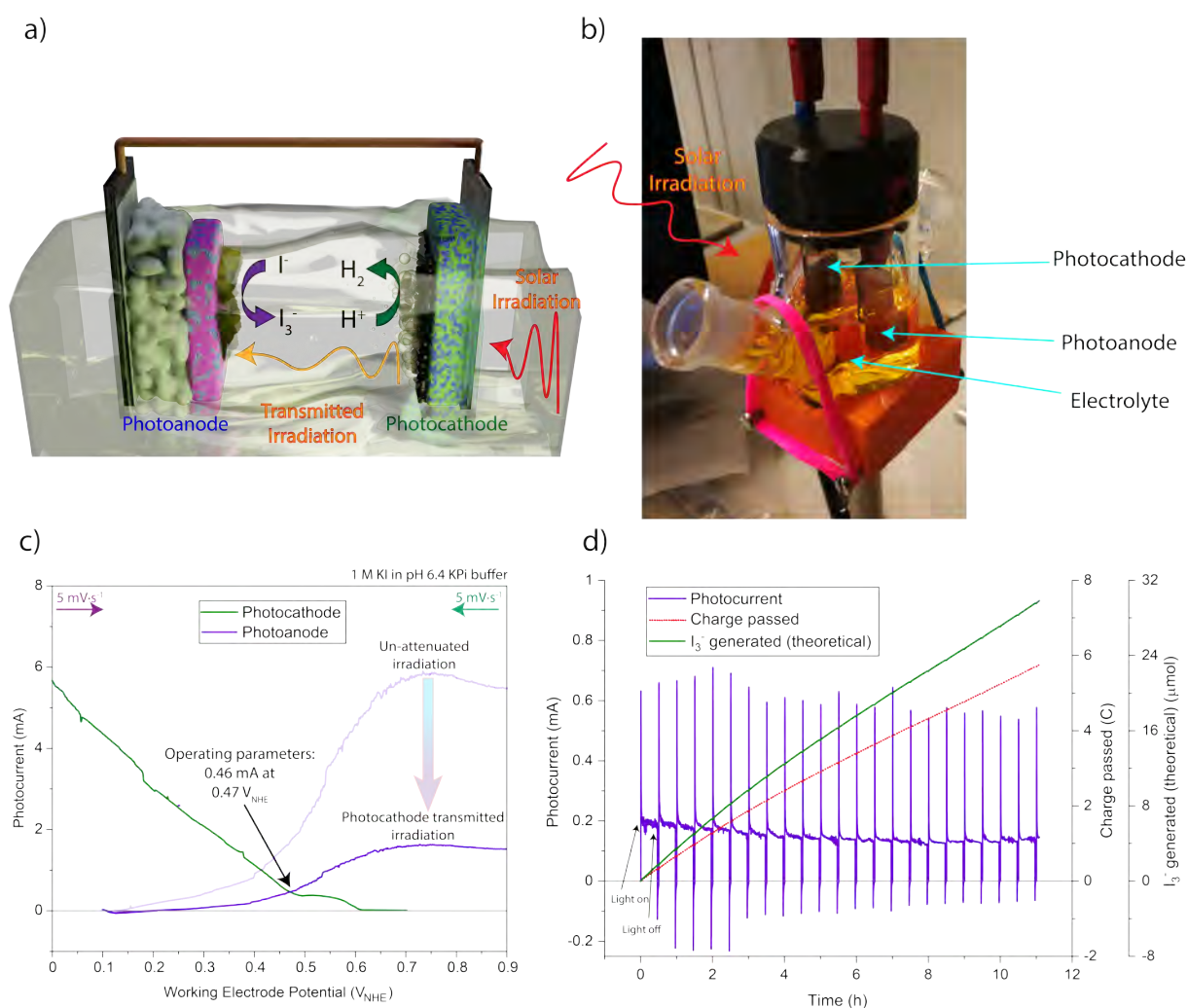


Figure 7.3.6: Large area tandem photocathode-photoanode PEC cell a) illustration, b) photograph, c) LSVs, d) CA in 1 M KI, KPi at pH 6.4.

7.3.3. Faradaic Efficiency Calculations

While the photoanode oxidizes the iodide to iodine, due to the large equilibrium constant and high iodide concentration (1 M), triiodide is generated instantaneously due to the *Le Chatelier's* principle. The amount of triiodide observed using absorption of the electrolyte is compared against the total charge passed through the PEC cell to calculate

the faradaic efficiency of triiodide generation (Figure 7.3.7 and Figure 7.3.8). In the large area tandem experiment, after 11 h, while 5.753 C of charges passed through the cell, which corresponds to 29.813 μmol I_3^- formed, only 25.113 μmol was detected by UV-Vis spectroscopy, resulting in an overall faradaic efficiency of 84.23% for triiodide production.

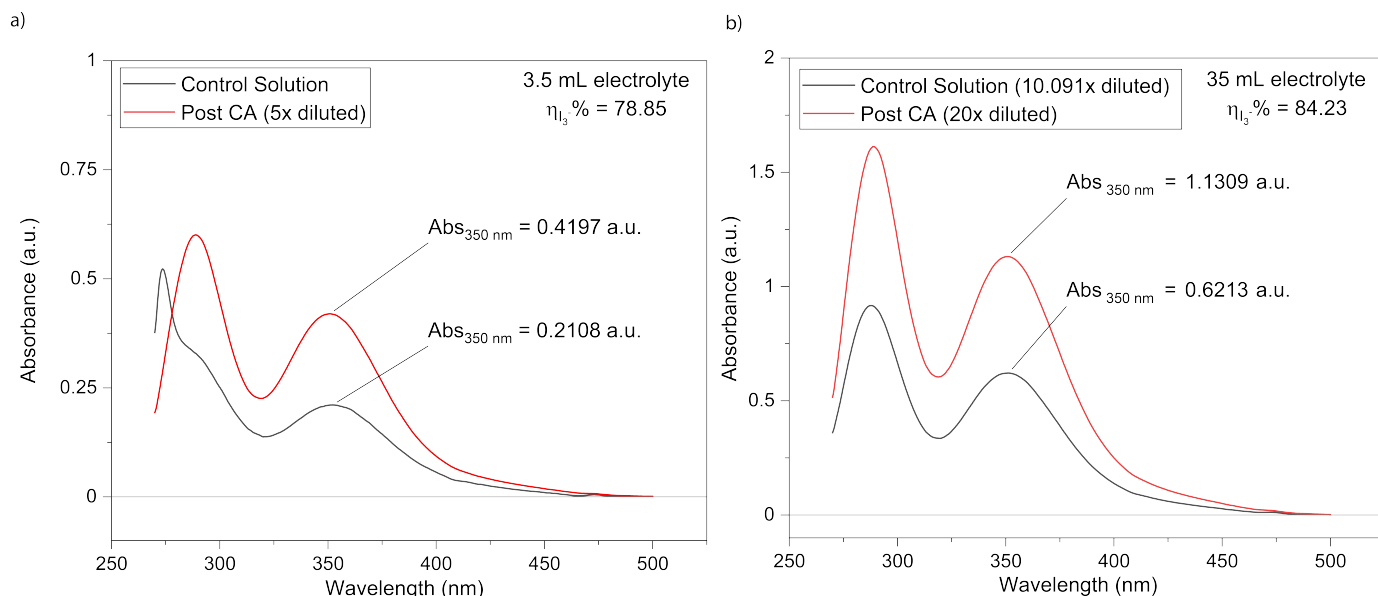


Figure 7.3.7: The UV-Vis absorption spectra of the diluted control solution and diluted electrolyte post CA in, a) small area PEC-GC cell, b) large area PEC cell.

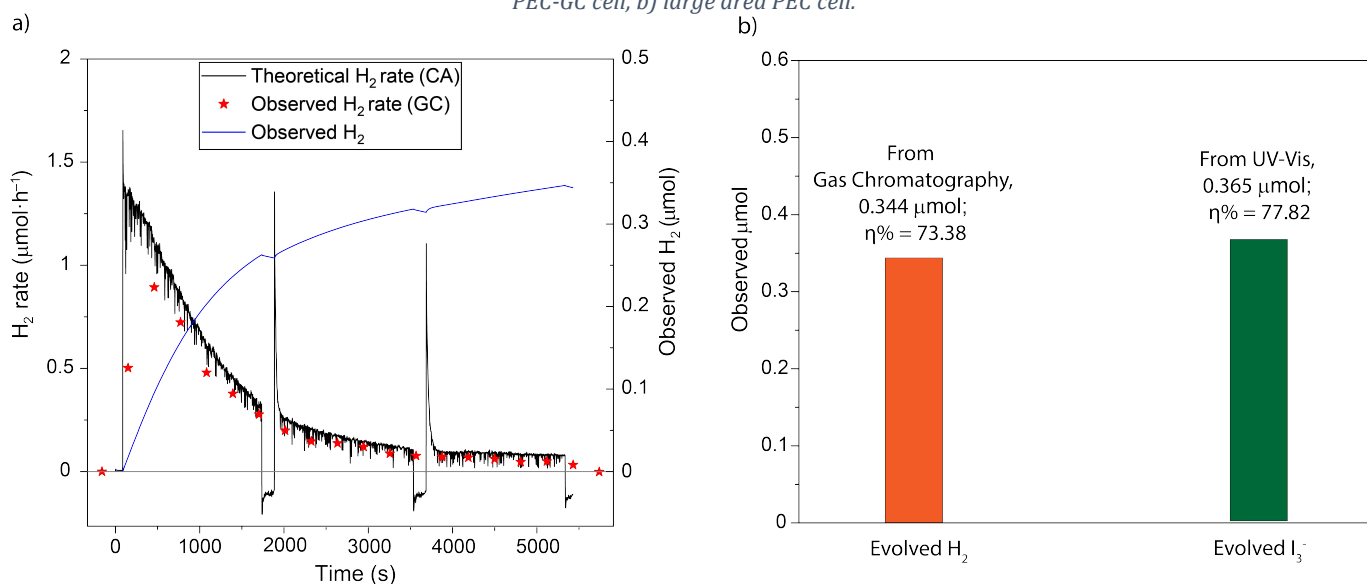


Figure 7.3.8: Small area tandem photocathode-photoanode PEC cell connected to GC: a) comparing hydrogen evolution rates, b) box plots showing overall hydrogen evolved and triiodide generated during the CA.

Similarly, the evolved gases from the photocathode were also subjected to analysis by the gas chromatograph (GC) at regular intervals. However, for this an airtight PEC cell was used, with smaller dimensions and immersed/irradiated area ($\sim 0.25 \text{ cm}^2$). The theoretical hydrogen evolution rate corresponds to the J_{ph} measured and is compared with the observed hydrogen rate from the GC. Over the course of ninety minutes of CA, the

average faradaic efficiency for hydrogen evolution in the small area cell amounts to 73.38%. At the same time, the triiodide evolved is also quantified at 77.82% from UV-Vis absorption.

Table 7.1: Table for calculation of triiodide generation faradaic efficiency for two different tandem PEC measurements: a large area (~2 cm²) demonstration and another connected to the GC (~0.25 cm²) for measuring hydrogen evolution. The absorbance values in a.u. are at 350nm, while the relation between absorbance and concentration is taken from the Beer-Lambert plot, see 7.6.Supporting Information. The large area PEC demonstrates higher faradaic efficiencies than the smaller PEC cell.

	Condition	Absorbance (a.u.)	Aliquot I ₃ ⁻ Concentration (μM)	Dilution factor	Bulk I ₃ ⁻ Concentration (μM)	ΔConcentration (μM)	Measured ΔI ₃ ⁻ (μmol)	Theoretical ΔI ₃ ⁻ (μmol) from CA	Faradaic efficiency, η (%)
Large area PEC (35 mL)	Control Electrolyte	0.6213	32.8307	x10.091	331.2916				
	Post CA Electrolyte	1.1309	52.4402	x20	1048.804	717.5084	25.1128	29.813	84.23
GC-PEC (3.5 mL)	Control Electrolyte	0.2108	16.1503	x1	16.1503				
	Post CA Electrolyte	0.4197	24.0800	x5	120.4001	104.2498	0.3649	0.4689	77.82

The inconsistencies between the large area and small area PEC cell faradaic efficiencies can be attributed to the use of a single chamber cell without membrane separation, a large distance between the photoelectrodes and constant stirring in the large area cell, which prevents the photocathode to reduce iodine/triiodide instead of water.

7.4. Water Oxidation – Catalysts

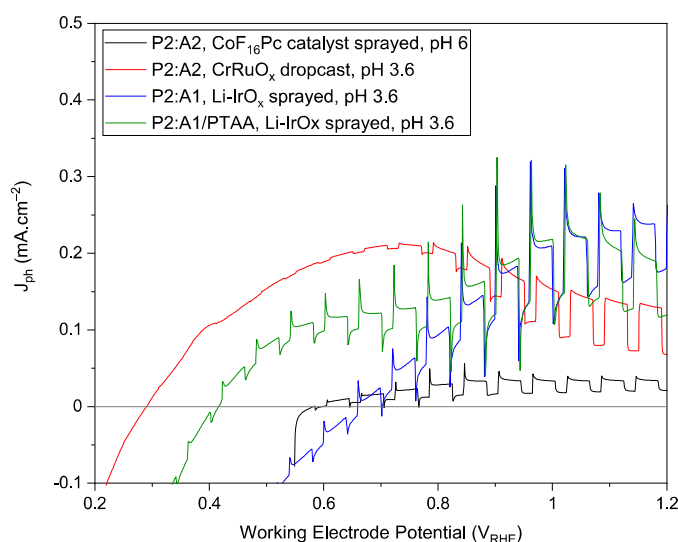


Figure 7.4.1: LSVs with various catalyst overlayers.

Post photoanode optimization, the inorganic catalysts, which would extract holes from the anode and oxidize water had to be looked at. However, despite best efforts, using mSnO₂ based OSC photoanodes only led to poor photocurrents (LSV curves in Figure 7.4.1).

The issues faced and bottlenecks are currently looked at. This might call for better catalyst design, better electronic interface between the organic/catalyst layers etc.

7.5. Conclusion

From the earlier chapters, the electrode was constructed in a bottom-up manner, and this chapter is focused towards applying these electrodes for hydrogen evolution using a completely unassisted solar PEC system. The problems faced with respect to onset potentials overlap, and catalysts for water oxidation are discussed briefly. The outlook for this field is positive, as there is significant scope for improvement, as was seen in the OPV field, where the current state-of-the-art devices touch 17% PCE. In this field, once the catalyst design and deposition are optimized, the transfer of holes from the anode to oxidize the water molecules can be facilitated, and stable, high performance photoanodes can be obtained.

7.6. Supporting Information

7.6.1. Photocathode description

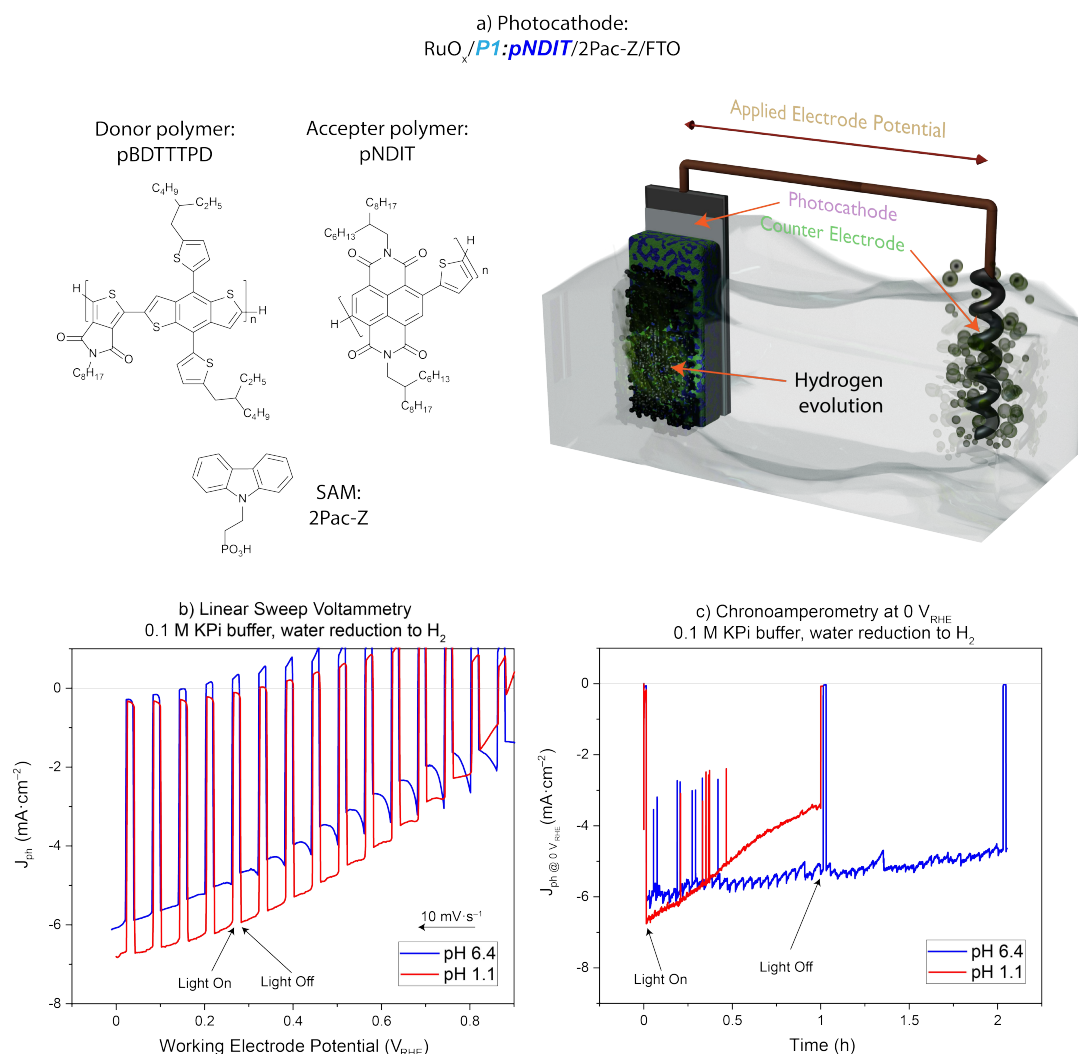


Figure 7.6.1: a) Chemical structures of donor:acceptors in photocathode and its schematic diagram, b) LSV and c) CA of the BHJ photocathode for water reduction at different pH conditions. The pH dependence of the LSV curves is accounted for in the Reversible Hydrogen Electrode (RHE) scale.

The photocathode is a BHJ consisting of **P1** as the donor^[10] and **pNDIT** as the acceptor.^[11] No hole transport underlayers are used, and the FTO is covered with a SAM with 2PAC-z molecule. After annealing, the water reduction catalyst RuO_x is sprayed onto the photocathode and re-annealed before use. This system was optimized by a colleague (Dan Zhang, LIMNO, EPFL) as a part of her thesis, and was used without modification for the tandem HI splitting system. The OSC components used and photocathodic performance for water reduction is illustrated in Figure 7.6.1.

7.6.2. UV-Vis Calibration of Triiodide Solutions

A stock solution of dilute iodine is prepared in a 1 M KI solution. Ensuring a 2500% mol. excess of iodide, this stock solution is diluted to known concentrations and the UV-Vis absorption spectra of triiodide at the known concentrations are measured. At 350 nm, the

absorbance values of the solutions are plotted against the concentration to obtain a linear fit of a Beer-Lambert relation for aqueous triiodide (Figure 7.6.2).

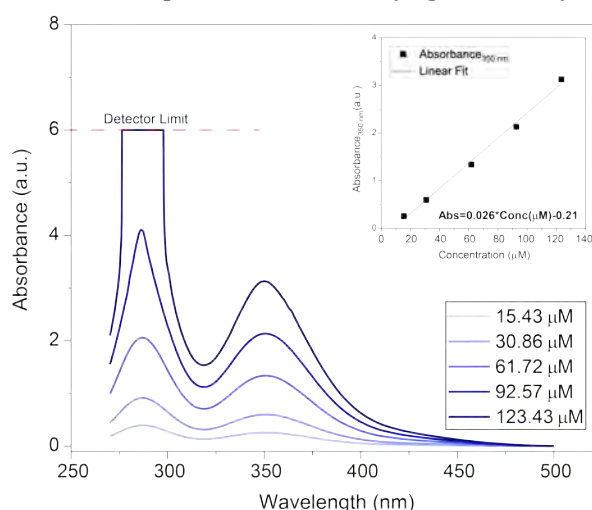


Figure 7.6.2: Calibration UV-Vis curves for various triiodide concentrations. For the calculations, absorbance values at 350 nm are considered. The Beer-Lambert linear equation is $Abs = 0.02634 \cdot Conc(\mu M) - 0.2146$; r^2 (coefficient of determination) = 0.995.

7.7. References

- [1] L. Yao, Y. Liu, H.-H. Cho, M. Xia, A. Sekar, B. Primera Darwich, R. A. Wells, J.-H. Yum, D. Ren, M. Grätzel, N. Guijarro, K. Sivula, *Energy Environ. Sci.* **2021**, 10.1039/D1EE00152C, DOI: 10.1039/D1EE00152C.
- [2] Y. E. Ha, M. Y. Jo, J. Park, Y.-C. Kang, S. I. Yoo, J. H. Kim, *J. Phys. Chem. C* **2013**, 117, 2646, DOI: 10.1021/jp311148d.
- [3] Y. Zhao, S. Gu, K. Gong, J. Zheng, J. Wang, Y. Yan, *J. Electrochem. Soc.* **2017**, 164, E138, DOI: 10.1149/2.0461707jes.
- [4] M. Küttinger, J. K. Wlodarczyk, D. Daubner, P. Fischer, J. Tübke, *RSC Adv.* **2021**, 11, 5218, DOI: 10.1039/D0RA10721B.
- [5] S. Berardi, S. Caramori, E. Benazzi, N. Zabini, A. Nioiretini, A. Orbelli Biroli, M. Pizzotti, F. Tessore, G. Di Carlo, *Appl. Sci.* **2019**, 9, 2739, DOI: 10.3390/app9132739.
- [6] L. Yao, N. Guijarro, F. Boudoire, Y. Liu, A. Rahmanudin, R. A. Wells, A. Sekar, H.-H. Cho, J.-H. Yum, F. Le Formal, K. Sivula, *J. Am. Chem. Soc.* **2020**, 142, 7795, DOI: 10.1021/jacs.0c00126.
- [7] D. A. Palmer, R. W. Ramette, R. E. Mesmer, *J. Solut. Chem.* **1984**, 13, 673, DOI: 10.1007/BF00650374.
- [8] J. Gao, C.-Q. Xu, S.-F. Hung, W. Liu, W. Cai, Z. Zeng, C. Jia, H. M. Chen, H. Xiao, J. Li, Y. Huang, B. Liu, *J. Am. Chem. Soc.* **2019**, 141, 3014, DOI: 10.1021/jacs.8b11456.
- [9] Y. Lin, Z. Tian, L. Zhang, J. Ma, Z. Jiang, B. J. Deibert, R. Ge, L. Chen, *Nat. Commun.* **2019**, 10, 162, DOI: 10.1038/s41467-018-08144-3.
- [10] H.-H. Cho, L. Yao, J.-H. Yum, Y. Liu, F. Boudoire, R. A. Wells, N. Guijarro, A. Sekar, K. Sivula, *Nat. Catal.* **2021**, 4, 431, DOI: 10.1038/s41929-021-00617-x.

[11] Y. Kim, J. Hong, J. H. Oh, C. Yang, *Chem. Mater.* **2013**, 25, 3251, DOI: 10.1021/cm401829x.

Chapter 8. Conclusion

8.1. Final Overview

A brief overview of this thesis includes an introduction dealing with the theory behind PEC, its advantages and significance of using OSCs. The limited number of previously published, peer-reviewed results are discussed, highlighting the OSCs and the catalysts.

Based on the rationale of using ladder like molecules, which can be solution processed, the relatively unexplored *QDI* molecule was selected due to various reasons. However, the photoanode fabricated showed significant instability during PEC oxidation of sacrificial reductants. Despite structural modifications, not a lot could be done to make viable photoanodes. The OSC eventually degrades/dissolves from the ETL, leading to drop in performance.

As using multi-OSC devices with BHJ structures are a step forward in terms of charge separation, these devices could possibly last longer as photoanodes. The possible candidates for donors and acceptors were zeroed in. Due to energetic reasons, a low HOMO level was required to oxidize the electrolyte, and TPD based donors *P1* and *P2* were synthesized, analyzed and electrochemically and optically characterized. Similarly, acceptors to complement these donors were synthesized and characterized: *A1* and *A2*. The scope of Ullmann reactions to obtain such similar laterally expanded RDIs were also explored to synthesize novel acceptors.

BHJs made with these OSCs were then analyzed and photoanodes using these were fabricated and optimized for sulfite oxidation. The various parameters involving BHJ thin film formation were analyzed, optimized and studied. The photoanodic performance observed was then analyzed with respect to these parameters and factors, resulting in the BHJ photoanodes with *P2:A2* with the highest performance for sulfite PEC oxidation. Traditional polymer donors and fullerene acceptors were also evaluated as photoanodes for reference and the novel BHJ outperforms them in terms of J_{ph} and stability.

For the real-world application, a *P2:A4b* photoanode driving the oxidative half-reaction is coupled with a high performance OSC based photocathode to drive water reduction. The resulting unassisted solar PEC cell then proceeds to split the electrolyte,

containing iodide at a near neutral pH. The photoanodes themselves are also capable of oxidizing iodide and bromide ions in water in acidic and neutral pH. Towards the end of the thesis, elementary attempts at water oxidation by combining these BHJ anodes with electrocatalysts were also studied.

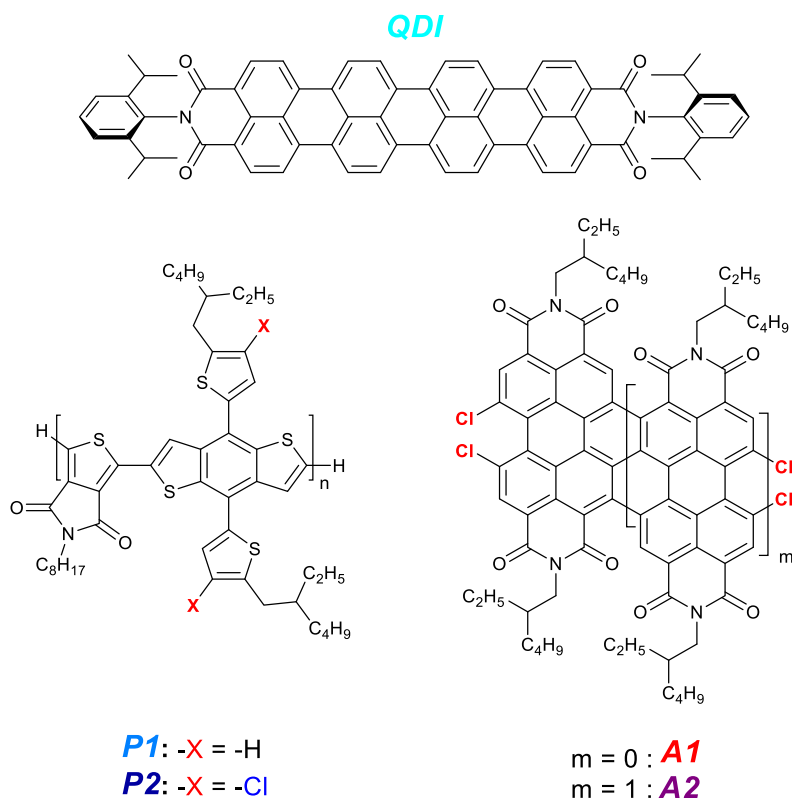


Figure 8.1.1: A few OSCs studied as photoanodes in this thesis.

The overall outlook is very positive for this field, as currently, it is at its nascent stage. The bottom line is that the traditional OSCs, which are used in high performance OPVs probably cannot be used due to energy level mismatch, and sensitivities to thermal annealing, as overlayers like hole transport layers and catalysts need to be deposited. There exists a need to look at OSCs with appropriate energy levels to favor the thermodynamic oxidation of electrolytes and this is achieved with OSCs having stabilized HOMO levels (Figure 8.1.1). With such encouraging results, hopefully other research groups all over the world pick up this interesting area of OSC based PEC applications.

Curriculum Vitae

Academic Background

École Polytechnique Fédérale de Lausanne

Lausanne, Switzerland

MSc in *Molecular & Biological Chemistry*. (CGPA: 5.48/6.00)

Thesis: Synthesis of All Conjugated Block Copolymer for use in Solar Cells.

(September 2015-Present Date)

Indian Institute of Technology Guwahati

Guwahati, India

B.Tech in *Chemical Science & Technology*.Ranked 1st in the Department. (CGPA: 9.11/10.00)

Thesis: Synthesis & Fabrication of Dye Sensitized Solar Cells.

(August 2011-April 2015)

Research Projects

Organic Semiconductors (OSC) for Solar Fuels (Doctoral Thesis)

Prof. Kevin Sivula, The Laboratory for Molecular Engineering of Optoelectronic Nanomaterials (LIMNO), EPFL (Switzerland)

OSCs in Photoelectrodes to split water into hydrogen & oxygen. (May '17-Ongoing)

All-Conjugated Block Copolymers for Organic Photovoltaics (Master's Thesis)

Prof. Kevin Sivula, The Laboratory for Molecular Engineering of Optoelectronic Nanomaterials (LIMNO), EPFL (Switzerland)

Method to utilize step growth polymerization to synthesize multiblock copolymers from donor & acceptor macro-monomer blocks was being explored. (September '16 – May '17)

Synthesis of Donor Segments & Compatibilizers (Semester Project)

*Prof. Kevin Sivula, The Laboratory for Molecular Engineering of Optoelectronic Nanomaterials (LIMNO), EPFL (Switzerland)*Diketopyrrolopyrrole (DPP) based donors & fullerene based (PC₆₁BM) acceptors were synthesized and aliphatically linked. Effect of its on morphology in the solar cells was explored. (February – June, '16)

Synthesis & fabrication of Dye Sensitized Solar Cells (Bachelor's thesis project)

Prof. P.K.Iyer, Department of Chemistry, IITG (India)

Different organic dyes were simulated for band gap optimization & the ideal aromatic dyes were synthesized in the lab & used to fabricate solar cells. (August, '14-April, '15)

In-situ polymerized "PEDOT: tosylate" for Organic Electrochemical Transistors (OECT)

Prof. Fabio Cicoira, Laboratory of Organic Iontronics, Polytechnique Montreal (Canada)

The objective was to obtain highest conductivity thin films of vapor phase polymerized PEDOT. Long term stability & its use in OECT devices were then investigated. (May – July, '14)

Publications

Co-authored/ Authored:

- “Effect of channel thickness, electrolyte ions, and dissolved oxygen on the performance of organic electrochemical transistors” (*Appl. Phys. Lett.* 107, 053303 (2015)) [10.1063/1.4927595](https://doi.org/10.1063/1.4927595)
- “Morphology stabilization strategies for small-molecule bulk heterojunction photovoltaics” (*J. Mater. Chem. A*, 2017, 5, 17517-17524) [10.1039/C7TA05405J](https://doi.org/10.1039/C7TA05405J)
- “Melt-processing of small molecule organic photovoltaics via bulk heterojunction compatibilization” (*Green Chem.*, 2018, 20, 2218-2224) [10.1039/C8GC00335A](https://doi.org/10.1039/C8GC00335A)
- “Catalyst-Free, Fast, and Tunable Synthesis for Robust Covalent Polymer Network Semiconducting Thin Films” (*Adv. Funct. Mater.* 2018, 28, 1706303) [10.1002/adfm.201706303](https://doi.org/10.1002/adfm.201706303)
- “Fully Conjugated Donor–Acceptor Block Copolymers for Organic Photovoltaics via Heck–Mizoroki Coupling” (*ACS Macro Lett.* 2019, 8, 2, 134–139) [10.1021/acsmacrolett.8b00932](https://doi.org/10.1021/acsmacrolett.8b00932)
- “Establishing Stability in Organic Semiconductor Photocathodes for Solar Hydrogen Production” (*J. Am. Chem. Soc.* 2020, 142, 17, 7795–7802) [10.1021/jacs.0c00126](https://doi.org/10.1021/jacs.0c00126)
- “A hybrid bulk-heterojunction photoanode for direct solar-to-chemical conversion” (*Energy Environ. Sci.*, 2021, 14, 3141–3151) [10.1039/D1EE00152C](https://doi.org/10.1039/D1EE00152C)
- “Organic Semiconductors as Photoanodes for Solar-driven Photoelectrochemical Fuel Production” (*CHIMIA* 2021, 75, No. 3) [10.2533/chimia.2021.169](https://doi.org/10.2533/chimia.2021.169)
- “A semiconducting polymer bulk heterojunction photoanode for solar water oxidation” (*Nature Catalysis*, 4, 431–438 (2021)) [10.1038/s41929-021-00617-x](https://doi.org/10.1038/s41929-021-00617-x)

Awards & Academic Achievements

- 3 subsequent years (2012-2015) recipient of **Institute Merit Scholarship**, meant for year-wise department toppers of engineering streams in IIT Guwahati, India.
- Awarded the **RQMP-GCM Yelon-Brebner Scholarship** to work in Montreal in 2014.
- Awarded **KVPY Fellowship** (Administered by Indian Institute of Science to around 300 students in India) in 2010 for proficiency in Basic Sciences.
- Secured an All India Rank of 3378 out of 485,000 students (the top 0.7%) who appeared for Indian Institute of Technology Joint Entrance Examination (IITJEE, 2011).

Conferences

Oral contribution at *13th International Conference on Hybrid and Organic Photovoltaics (HOPV21)*, titled “Organic Semiconductors for Photoelectrochemical Applications”

[Proceedings of 13th Conference on Hybrid and Organic Photovoltaics \(HOPV21\)](#)

References

Prof. Kevin Sivula

Associate Professor

The Laboratory for Molecular Engineering of Optoelectronic Nanomaterials (LIMNO),

École Polytechnique Fédérale de Lausanne

kevin.sivula@epfl.ch

Dr. Nestor Guijarro

Ramón y Cajal Research Professor & ERC StG fellow

University of Alicante

nestor.guijarro@ua.es

Dr. Shaik Mohammed Zakeeruddin

Senior Scientist

Laboratory of Photonics & Interfaces (LPI.)

École Polytechnique Fédérale de Lausanne

shaik.zakeer@epfl.ch

Résumé

Arvinth Sekar

Organic & Polymer Chemist | Electrochemist

Synthetic organic chemist with 5+ years of experience in laboratory scale reactions for applications in Organic Photovoltaics and Photoelectrodes for solar fuel generation. Specialized expertise in conjugated organic polymer synthesis, analytical characterization, and electrochemistry.

Experience

2016/March
– Ongoing

Research Assistant

The Laboratory for Molecular Engineering of Optoelectronic Nanomaterials (LIMNO), EPFL, Switzerland

Responsibilities & Outcomes

- MSc thesis on synthesizing block copolymers with alternating copolymers as macromonomers for OPVs.
- PhD thesis on solar fuel generation, using organic semiconductors as photoelectrodes.
- 8 scientific publications co-authored.
- Supervised MSc students' theses.
- Gained proficiency in electrochemistry, polymer syntheses & characterization.

2014/May
– 2014-July

Research Intern

Laboratory of Organic Iontronics, EPM, Canada

Responsibilities & Outcomes

- Vapor phase polymerization to obtain conjugated polymers for Organic Electrochemical Transistors.
- 1 scientific publication co-authored.

Education

2015-2017

MSc in Chemistry & Chemical Engineering
École Polytechnique Fédérale de Lausanne, Switzerland

Specialized in courses of Organic Chemistry, Energy Applications & Analytical Chemistry.

2011-2015

B.Tech in Chemical Science & Technology
Indian Institute of Technology Guwahati, India

Graduated with a minor in Chemical Engineering & excelled with Institute Merit Scholarship for 3 years with the highest grade in the course.

Personal Information

Phone

+41 788 92 93 55

e-mail

arvinthsekar@gmail.com

arvinth.sekar@epfl.ch

LinkedIn

[linkedin.com/in/arvinth-sekar-3161b8aa/](https://www.linkedin.com/in/arvinth-sekar-3161b8aa/)

Skills

Organic Synthesis ★★★★★☆

Homogeneous Catalysis ★★★★★☆

Polymer Chemistry ★★★★★★

Electrochemistry ★★★★★☆

Analytical Chemistry

GPC/HPLC ★★★★★☆

NMR ★★★★★★

MALDI-TOF ★★★★★★

Communication ★★★★★☆

Efficiency ★★★★★☆

Softwares

MS Office ★★★★★☆

Illustrator ★★★★★☆

Blender ★★★★★☆

Igor ★★★★★☆

Origin ★★★★★★

Languages

Native Proficiency

Hindi, Tamil, Telugu

English ★★★★★★

German ★★★★★☆

French ★☆☆☆☆

Programming

C++ ★★★★★☆

FORTAN ★★★★★☆